Universität der Bundeswehr München
Fakultät für Bauingenieurwesen und Umweltwissenschaften
Institut für Mathematik und Bauinformatik

Joule Heating in Connecting Structures of Automotive Electric Devices

–

Modelling, Simulation and Optimization

Florian Peter Loos
geboren in Nürnberg

Vollständiger Abdruck der von der Fakultät für Bauingenieurwesen und Umweltwissenschaften der Universität der Bundeswehr München zur Erlangung des akademischen Grades eines

Doktors der Ingenieurwissenschaften (Dr.-Ing.)

genehmigte Dissertation.

Vorsitzender des Promotionsausschusses: Prof. Dr.-Ing. S. Holzer

1. Gutachter der Dissertation: Prof. Dr.-Ing. H.-D. Ließ
2. Gutachter der Dissertation: Prof. Dr. rer. nat. habil. T. Apel
3. Gutachter der Dissertation: Prof. Dr. rer. nat. habil. H. Harbrecht

Die Dissertation wurde am 31. März 2014 bei der Universität der Bundeswehr München eingereicht und durch die Fakultät für Bauingenieurwesen und Umweltwissenschaften am 4. Juni 2014 angenommen. Die mündliche Prüfung fand am 5. Juni 2014 statt.

Zusammenfassung

Während die Anzahl elektrischer Verbraucher in modernen Fahrzeugen, vor allem in Elektro- und Hybridautos, stetig anwächst, bleibt der verfügbare Platz gleich oder wird mitunter sogar geringer. Verknüpft mit dieser Entwicklung ist der Anstieg an elektrischen Verbindungsstrukturen wie Kabeln, Kabelbündeln, Stromschienen und Stromverteilerboxen. Da all diese Geräte und Verbindungen bei Stromfluss aufgrund des Joule-Effekts Wärme erzeugen, erweist sich die thermische Belastbarkeit bei Dimensionierungsfragen häufig als Flaschenhals. Einerseits möchten Hersteller Kabelquerschnitte und elektrisch leitendenes Material reduzieren, um Kosten, Gewicht und Platz zu sparen und um den CO_2-Ausstoß zu verringern, auf der anderen Seite dürfen die Komponenten wegen der Gefahr von Überhitzung und Hotspot-Bildung sowie des Anstiegs der thermischen Verlustleistung nicht zu klein dimensioniert werden.

Deshalb sind in der Automobilindustrie und bei ihren Zulieferern derzeit einige Änderungen im Gange. Über viele Jahre eingesetzte Normen müssen wegen der neuen Gegebenheiten überarbeitet werden. Bei der Frage nach der richtigen Dimensionierung von Kabeln und anderer Verbindungsstrukturen wurde bislang fast ausschließlich auf Erfahrungswerte und aufwändige Messungen zurückgegriffen. Erfahrungswerte können bei vielen Neuentwicklungen jedoch nur bedingt weiterhelfen, Messungen sind extrem teuer und bieten lediglich ein sehr beschränktes Spektrum an Untersuchungsmöglichkeiten. Finite Elemente Simulationen kommen in vielen Firmen zum Einsatz, sind aber mitunter auch so aufwändig, dass ihre Verwendung in diesem Bereich häufig nicht rentabel genug ist. Ein weiteres, nicht zu unterschätzendes Hindernis stellen, insbesondere in der Kabelindustrie, mangelnde Kenntnisse über passende Modellierungen und die entscheidenden bzw. vernachlässigbaren Einflüsse dar.

Die vorliegende Arbeit präsentiert neue, problemspezifische Verfahren zur adäquaten Berechnung thermischer Belastungen in Verbindungsstrukturen. Die Simulation mit Finiten Elementen ist dabei wesentlicher Bestandteil, vorwiegend werden aber Simulationsmethoden entwickelt, die eine vereinfachte thermische Analyse erlauben. Sie zeichnen sich durch einen weit geringeren Berechnungsaufwand aufgrund qualifizierter Reduktion von Eingabedaten und geschickter Diskretisierungsstrategien aus. Es werden Modellierungs- und Berechnungsansätze für einfache, isolierte Kabel, abgeschirmte Leitungen der Automobil-Hochvolttechnik, Leitungsbündel, Stromschienen und Sicherungen hergeleitet. Vergleiche mit Finite Elemente Rechnungen liefern Abschätzungen zur Genauigkeit der Methoden und helfen mögliche Schwächen der Ansätze zu identifizieren. Zur Sicherstellung der praktischen Anwendbarkeit werden Messungen herangezogen und Übereinstimmung bzw. Diskrepanzen dieser mit den Simulationen aufgezeigt.

An einer Vielzahl von Beispielen wird demonstriert, wie Hersteller von Kabeln und anderer Komponenten die problemspezifisch entwickelten Methoden gewinnbringend einsetzen und damit den zeitlichen und materiellen Aufwand drastisch reduzieren können. Optimierung der Leitungsquerschnitte, der Stromschienendicken und Anordnung von Einzelleitungen in Leitungsbündeln sind dabei wesentliche Themen. Des Weiteren soll ein Designvorschlag das Auslöseverhalten von Schmelzsicherungen hinsichtlich präziserer Voraussagbar-

keit verbessern. Auf thermische Wechselwirkungen zwischen verschiedenen Komponenten wie Stromschienen und Leitungen oder Leitungen und Sicherungen wird ebenso eingegangen wie auf Fragen nach Konvergenz und mathematischer Plausibilität der Verfahren. Dabei ergibt sich ein direkter Zusammenhang zwischen der Existenz einer Lösung der Problemklasse und der Konvergenz von darauf angewandten Iterationsverfahren.

Abstract

The amount of electric consumers in modern automobiles, especially in hybrid and electric cars, is growing more and more in the recent years, whereas the available space remains the same or even decreases. Closely related is the increase of connecting structures like cables, cable bundles, current bars and current distribution boxes. As all these devices and their connections generate heat by the Joule effect, thermal loads often represent a bottleneck in the dimensioning of components. On the one hand, manufacturers would like to reduce cable diameters and the amount of electric conducting material to save costs, weight and space and to decrease CO_2 emission. On the other hand, they must not design them too small due to the danger of overheating and hotspot generation as well as the rise of thermal losses.

For these reasons, car industry and automotive suppliers are faced with numerous changes at the moment. Old norms used for the layout of components for many years are called into doubt due to the recent developments. The question of how to correctly dimension cables and other connecting structures has mostly been answered with the help of past experience and very elaborative measurements. Experience can hardly help in many cases concerning new developments; measurements are extremely expensive and offer only a limited spectrum of investigation opportunities. Finite element simulations are used in some companies, but due to the great effort involved, their application is often not sufficiently profitable. Moreover, there often exists, especially in the cable industry, a lack of necessary knowledge for adequate modelling and of the decisive or negligible influences.

The goal of the present work is to develop new specific methods for the computation of thermal loads in electric connecting structures. Although the simulation with finite elements constitutes an important part of this thesis, calculation methods that allow a simplified thermal analysis and excel by an enormous decrease of computational efforts thanks to qualified reduction of input data and smart discretization strategies represent the core issue. Problem specific modelling and computational approaches for insulated single-core cables, shielded cables of the automotive high voltage technology, cable bundles, current bars and fuses are derived. To obtain estimations for the accuracy respectively for possible weaknesses of the approaches, they are compared to finite element simulations. In order to ensure practical applicability, external measurements for each considered connection type are provided and accordance respectively discrepancies of those to simulations are analysed.

In addition, we demonstrate on a large number of examples how manufacturers can apply the developed methods in a profitable way and thus may reduce the amount of time and material. Optimization of cable cross sections, thickness of current bars and configuration of single cables in cable bundles are the main subjects of this thesis. Moreover, a design improvement of fuses that results in a more accurate and reliable blowing mechanism is proposed. We answer questions on thermal interaction between different components like current bars and wires or wires and fuses as well as on convergence and mathematical plausibility of our methods. It turns out that there is a close relation between the existence of solutions to the specific problems and the convergence of applied iterative methods.

Acknowledgements

This thesis has been prepared at the Institute of Mathematics and Applied Computer Science at the Faculty of Civil Engineering and Environmental Science of the Universität der Bundeswehr München for receiving the Ph.D. degree. The work presented in this thesis has been carried out from March 2009 to March 2014.

First of all, I would like to thank my supervisor Prof. Dr. Hans-Dieter Ließ for the opportunity to work at his group, to do research on subjects closely related to industry and to take actively part in international conferences. His interest on the progress of my research work, supervision and provided support had been valuable help for me.

I wish to express my deep gratitude to Prof. Dr. Thomas Apel who kindly agreed to co-supervise my Ph.D. dissertation. Moreover, he gave our group the possibility to continue the work in progress by providing offices and for me in particular to take part at the teaching activities.

For all his help and discussions concerning shape optimization, for two interesting research journeys at the Universität Basel and his contribution as third reviewer of this work, I would like to thank Prof. Dr. Helmut Harbrecht.

Moreover, I would like to thank Prof. Dr. Stefan Holzer for his contribution as the chairman of the examination committee.

Furthermore, I wish to acknowledge valuable discussions and fruitful cooperation with Dr. Karl Dvorsky, that will hopefully continue in the future by founding our own company together with Prof. Ließ. Despite (or actually due to) our different manners of working and interests, our research subjects have always complemented one another very well.

The colleagues of Thomas Apel's research group, namely Dr. Thomas Flaig, Dr. Johannes Pfefferer, Dr. Dieter Sirch and Max Winkler, as well as Carsten Riker, I deeply thank for the pleasant working atmosphere, the nice evenings we spent together, the (occasionally exhausting) discussions, useful hints to dealing with Latex and technical support.

A special thank is for the student assistants and interns Ronny Radke, Manuel Stahl, Ségolène Dessort, Adil Teffal, Céline Yüksel and in particular for Benjamin Nolet and Benoît Philippe who supported me and our group by doing many different jobs like programming, taking measurements, translating, creating graphical user interfaces, etc.

Last, but not least, I would like to thank my parents Helga and Wolfgang Loos for their everlasting support and my wife Nicole for encouraging me during the last years, for her love and all the things we share.

Contents

1 Introduction

1.1 Problem Definition

In 1905, Nikola Tesla claimed that in future, communication and electric energy would be transmitted through air without material [126]. Obviously, e.g. in telecommunications, his hypothesis can be confirmed to the largest extent. In contrast, in the domain of energy transport in on-board systems of vehicles, we definitively still have to deny his assertion [46]. In today's cars, more and more electric components exist which have to be supplied by electric current (cf. Figure 1.1). Newer product innovations like advanced driver assistance systems, novel drive concepts and recent comfort or security functions increase this development. Thus, completely equipped vehicles can contain more than 2.5 kilometres of wire in the harness with a weight of more than 100 kilograms [93].

The trend of car electrification is reinforced in hybrid and electric cars where electric current is indispensable even for the main drive. The proportion of electrical systems in present vehicles, driven by a combustion engine, is, dependent on the vehicle category, already between $20 - 35\,\%$. For electric cars, this value rises up to $70\,\%$ [9]. Despite the continuous growth of the amount of electrical systems, the available space remains the same or even decreases. Both tendencies – increase of electrical components on the one hand, shortage of available space on the other hand – result in a higher risk to exceed permitted temperatures in connecting structures. They possibly contribute to the generation of hotspots and overheating of essential components, which could result in irreparable damages.

Consequently, thermal energy management is one of the most important aspects in the production of cars. The two keywords *downsizing* and *rightsizing*, used by the Leoni AG [37], describe the challenges manufacturers are faced with today. The term downsizing means to reduce technical quantities (e.g. weight or cylinder capacity) and costs of the systems while maintaining equal efficiency and capability. The correct design and positioning of all components without affecting security and proper functioning is summarised in the word rightsizing. Both strategies have to be considered in order to reduce material, volume and weight and thus to save costs and energy.

Additionally to the right dimensioning and composition of the entire systems, an adequate design of the single components is of great importance. Apart from cables, cable bundles and cable harnesses, hubs of the on-board power supply like current distribution boxes and current bars (cf. Figure 1.2) have to sustain high currents. Their correct dimensioning is directly related to the cable designs and has to be considered in a holistic approach for thermal car management.

Another group of components that plays a major role in the heat generation of vehicles are fuses. Although e.g. semiconductor fuses have the advantage to be usable several times, their production costs are comparatively high. In this work, we restrict to investigations on fuses that interrupt the circuit due to a partially higher resistance in a thinner interior fuse element. This fuse element melts in case of too intense electric loads before damages at other components are caused by too high temperatures. Hence, the blowing characteristics of fuses have to be adapted to the properties of attached devices, wires and cable bundles.

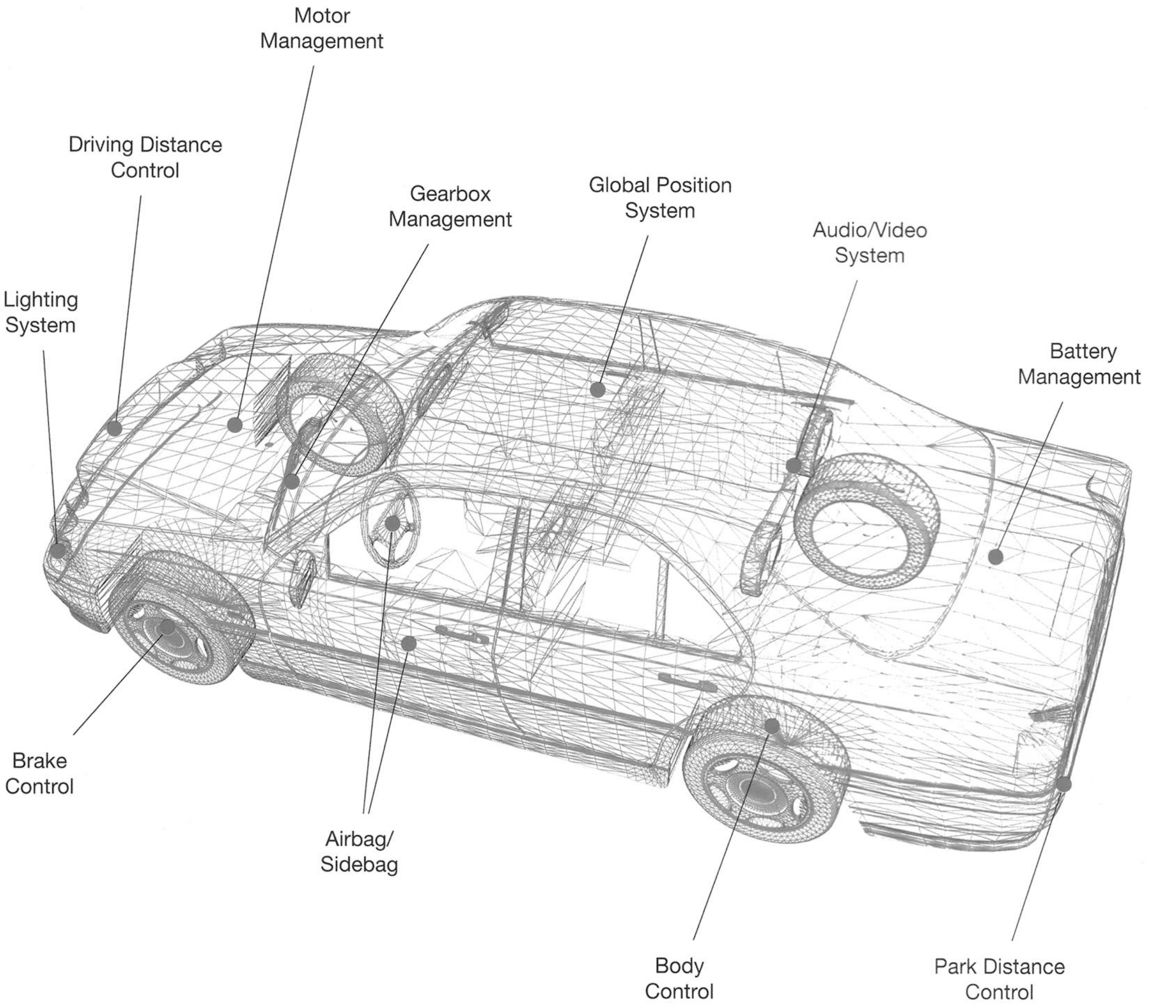

Fig. 1.1: *Modern car and its main electric components (image source: Coroplast Leitungskatalog [21]).*

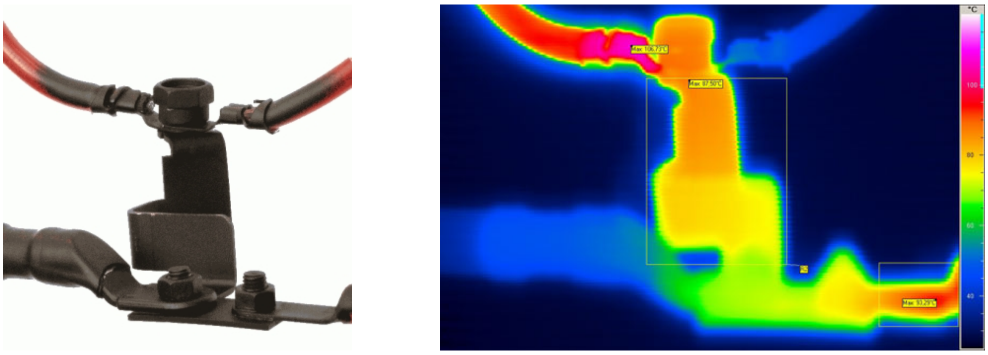

(a) Current bar. **(b)** Thermal image.

Fig. 1.2: *Current bar with four attached cables and thermal image of the current bar with electric loads (image source: Dräxlmaier Elektrotechnik GmbH).*

The aforementioned developments by electrification lead to a rethinking in the automotive industry. Whereas hardly any importance was attached to the design of cables, cable harnesses and connecting structures some years ago, it is now one of the essential parts in construction of vehicles. Moreover, measurements and experiments have formerly been performed nearly exclusively to investigate the (thermal) influence of connecting structures and to dimension those appropriately. Since measurements are very time-consuming, costly and rather limited concerning the spectrum of investigations, computational methods and simulations gain more and more importance. The complex physical and mathematical contexts represent a problem in this subject, because they require deeper insight to find adequate models, simulations and optimization strategies. Especially the described development to electric cars and, associated, the change from low to high voltage technology make old norms and standards obsolete. Consequently, we are forced to revise old methods and instructions, using appropriate models and sophisticated simulation and optimization methods. This is the point where the present work targets to.

Before going into detail about the main objectives of this work, we summarize general results of existing literature to the present topic. Literature to specific subjects is indicated at the beginning of each chapter and at corresponding points in the text.

The first mentionable calculations on heat transfer in electrical power cables were published by Neher and McGrath [101] in 1957 which form the fundamentals of many cable application guidelines and regulations. Based on Simmons' introductory work on underground cables [121], they describe a method to estimate the steady state temperature in underground cables. In 1964, Neher expanded his findings to corresponding transient computations [100]. The IEC Standards 60 287 [60–64] and 60 853 [65, 66], based on the work of Neher and McGrath, serve throughout the world as references for stationary respectively dynamic cable ratings. They provide principles of heat transfer for buried cables and equations for their computations. Many of them were developed empirically. But there is, to the largest extent, a lack of explicit derivations, explanations and numerical methods for their solution.

Anders' textbooks [3, 4] allow a deeper understanding of the basic theory behind the computing of cable ratings. They describe fundamental approaches for modelling these problems and analytical respectively numerical methods to solve corresponding equations or systems of equations. Thus, these works represent main sources and reference books for our calculations. Further profound knowledge to principle modelling and computation of temperatures is explained in [104, 124, 127]. In contrast to Anders, these presentations are not specific to cable ratings, but kept general for the calculation of heat transfer processes. Moreover, the references [68, 83, 128, 134] explain heat transfer by conduction, convection and radiation, presented in a physical and engineering way. The VDI Wärmeatlas [131] is essential in this context, since it provides formulas and empirical data for the determination of a temperature dependent heat transfer coefficient. The procedure is explained in detail in Section 2.3.

The Ph.D. theses of Dvorsky [35], Ilgevicius [67] and Schulz [118] mainly influenced the present work. Whereas Schulz and Ilgevicius describe first engineering approaches to compute heat transfer in certain connecting structures, Dvorsky mathematically analyses assumptions often made for thermo-electric calculations. Especially [35] and [67] are cited several times, as the direct cooperation with both authors inspired the present work.

1.2 Objective of this Work

In this work, we are interested in providing and evaluating models, methods and algorithms to perform thermal analysis of essential connecting structures, used in modern cars. These methods have mainly been implemented in calculation tools for dimensioning of cables and cable related components. Thus, one objective of these considerations is to show advantages and drawbacks, possibilities and limitations of our computations.

The practical applicability always represents one of the main aspects. Nevertheless, most of the problems and their numerical solution are also considered from a mathematical point of view. We investigate different electric components and model, simulate and/or optimize their structure concerning thermal aspects. To guarantee transferability on real world processes, most simulations are validated by comparison to measurements. Based on fundamental physical and mathematical principles, we derive appropriate algorithms. If further assumptions and simplifications are applied, we try to estimate their influence as far as possible.

The main objective is finally to improve the production and dimensioning procedure of manufacturers, working in the automotive sector. Thus, as one of the primary industrial needs is a high computational speed, we develop efficient calculation methods that are reliable in their specific application area. Furthermore, our algorithms help manufacturers to choose – in a thermal sense – the right cable types and their cross sections and to optimize dimensions of cable related components. One question often discussed in this context at present is whether to prefer aluminium or copper cables [112, 125]. With the aid of our algorithms, this question can be answered concerning thermal aspects.

Moreover, this thesis can also be considered as a preliminary work for the automatic dimensioning of complex on-board supply systems. To estimate the thermal loads of e.g. current distribution boxes with several electrical inputs and divers exterior influences is even more difficult. We illustrate fundamental components of the on-board system and show their thermal and electrical interaction.

Most of the findings in this work have been gained as a result of the cooperation with our project partners Acome GmbH, Autecto GmbH, Coroplast GmbH, Daimler AG, Dräxlmaier GmbH, IAV GmbH, Labco GmbH, Leoni AG, Nexans AG, Systech GmbH and VW AG.

1.3 Scientific Novelty

Of course, the thermal analysis of electric components in the automotive sector is not new. The papers of Neher and McGrath [100, 101] and the IEC norms [60–66] show that the subject has been of interest for several years, albeit in weakened form than today. The difference of our work compared to other articles is the more profound analysis of the problem with an engineering and mathematical insight. Whereas the approaches of mentioned textbooks remain general and in consequence often superficial, we try to derive our systems of formulas as far as possible rigorously and to provide suitable numerical methods. Nevertheless, practical applicability remains a primary objective. For most applications, we present a suggestion how to optimize the involved components.

Further novelties of the present work are listed below:

1. To analyse the problem of Joule heating by electric current, we state general problem formulations for domains consisting of one homogeneous material and for domains composed of several subdomains. A particularity of the problems represents

the consideration of the influence by surrounding air with temperature dependent heat transfer coefficients. Using available literature allows to state a so-called subresonance condition which implies the existence and uniqueness of a weak solution of the general problems.

2. We derive a fixed point scheme for the determination of temperatures at characteristic points of insulated single-core and shielded cables. It turns out that the condition for the convergence of an applied fixed point iteration is related to the mentioned subresonance condition. Moreover, we present a fast and simple algorithm that enables to create ambient temperature–electric current diagrams based on the fixed point iteration scheme to characterize the thermal loading capacities of different cable types.

3. Our computational approach for transient temperature evolution in insulated single-core and shielded cables has not been published, yet. Assuming that the ratio of temperatures in the cable core and the exterior insulation remains approximately constant over time, we derive a fast computational scheme for the transient calculation of temperatures at relevant points in the cable. It is of special interest for cables of the high-voltage industry, since there exist many current profiles that vary quickly over time.

4. Nearly all publications to the present topic suppose an infinite length of cables, which simplifies the computations. In fact, this reduction is not always adequate. In case of short cables, attached objects influence the cable temperature immensely, whereas long cables can be located in different sections of the car with large differences in the ambient temperature. We introduce a computational approach that takes the axial temperature dependency into account by subdivision of the cable into three sections.

5. The calculation of heat generation in cable bundles has only been possible in the last years since suitable models were developed. However, they have never been compared in detail and tested, e.g. concerning the influence of cable positions. We show when and why different approaches are applicable and which advantages respectively disadvantages they have.

6. A main result of the analysis of cable bundles is that the positioning of the single cables has an essential influence on the temperature distribution. In order to optimize the cable layout, which allows estimation of worst and best cases, we derive an optimization algorithm that combines a gradient based strategy with a genetic algorithm for shape optimization.

7. The linking of several cables by current bars requires the knowledge of temperature distributions in cables and in the current bars themselves. There is a lack in the literature for the computation of this application, which is filled by this thesis.

8. The last components analysed in this work are fuses. Many approaches have been applied to compute their blowing characteristics. With the help of experiments, we observe that, dependent on the amount of the current load, different physical and chemical processes essentially influence the blowing times. We present computational methods to determine those a priori, depending on the material and on attached cables. Furthermore, we propose a design extension that enables more precise predictions.

1.4 Outline

The next chapter, *Chapter 2*, starts with the physical and mathematical basics necessary for a thermo-electrical analysis of connecting structures. Based on the law of conservation of energy, power balances and partial differential equations (PDEs) respecting the Joule effect in electric components are derived. Appropriate boundary, interface and initial conditions enable to formulate general problems for the stationary and transient case. Notes about existence and uniqueness of a solution for each problem complete the modelling and analysis.

Numerical methods to solve the presented problems are introduced in *Chapter 3*. Application of the finite element method is explained, as well as further numerical procedures to solve problem specific equations.

As the optimization of connecting structures is one of the main aspects of this work, we give an introduction to (mathematical) optimization and provide basics for shape optimization and a genetic algorithm in *Chapter 4*.

Chapter 5 is dedicated to the investigation of insulated single-core cables. Taking advantage of the rotational symmetry and supposing infinite length of the cable, our fundamental procedures for thermal analysis of electric components are introduced.

In *Chapter 6*, we consider shielded cables of finite length. In contrast to insulated single-core cables, they possess a further metallic layer in the insulation that carries electric currents. Those cables are widely used in the field of high-voltage technology. As quickly varying current profiles are common in that area, a specific approach for the transient analysis which also respects axial temperature dependency in the cable core is proposed.

Several insulated cables packed together are called a cable bundle, which is subject of *Chapter 7*. As the concrete positions of the single cables are not known a priori, we present two different approaches for their simulation and compare them. It turns out that the positioning of the single cables has an influence on the temperature distribution. An algorithm to optimize cable bundles is derived and applied to several examples.

In order to connect different cables, current bars are used. To dimension them correctly, an adequate simulation method is introduced in *Chapter 8*. Contact resistances are respected as well as the influence of length, height and width of each subsection of the current bar on the internal heat distribution.

To ensure that cables and connected devices are not overloaded, fuses are widely used. In *Chapter 9*, we investigate their blowing characteristics, directly coupled to the thermodynamic processes taking place in attached cables. Apart from reduced simulation approaches involving modelling assumptions, we present finite element simulations that allow estimations of influences by the fuse design and by the environment. Furthermore, we propose an improved fuse design to optimize the predictions about the time when fuses blow.

Finally, we summarize the results of our work and give an outlook to potential future work in *Chapter 10*. Moreover, each chapter is concluded by a brief discussion of the proposed techniques.

1.5 Research Approval and Publications

Most parts of this thesis have been presented at the following international conferences:

- K. Dvorsky, F. Loos, H.-D. Ließ, *Simulation der elektrischen Belastbarkeit von Bordnetzen und ihrer Komponenten*, Bordnetzkongress 2013, Landshut, Germany, 2013;

- H.-D. Ließ, K. Dvorsky, F. Loos, *Thermal analysis of electric components: New developments*, Workshop, Automotive Cabling 2013, Stuttgart, Germany, 2013;
- F. Loos, H. Harbrecht, *Shape optimization of current carrying multicables*, GAMM 2013, Novi Sad, Serbia, 2013;
- F. Loos, *Two approaches for heat transfer simulation of current carrying multicables*, ECCOMAS 2012, Vienna, Austria, 2012;
- F. Loos, H.-D. Ließ, B. Philippe, *Comparison of two different approaches for the simulation of the triggering behaviour of safety fuses*, NHT 2012, Wroclaw, Poland, 2012;
- F. Loos, H. Harbrecht, *Shape optimization of current carrying multicables*, ICCAM 2012, Gent, Belgium, 2012;
- F. Loos, H. Harbrecht, *Shape optimization of current carrying multicables*, 17th International Conference on Mathematical Modelling and Analysis, Tallinn, Estonia, 2012;
- F. Loos, H.-D. Ließ, B. Philippe, *Transient Analysis of the Triggering Behaviour of Safety Fuses*, COMSOL Conference 2011, Stuttgart, Germany, 2011;
- F. Loos, H.-D. Ließ, K. Dvorsky, *Simulation Methods for Heat Transfer Processes in mechanical and electrical Connections*, 1st International Electric Drives Production Conference, Nuremberg, Germany, 2011;
- F. Loos, H.-D. Ließ, *Numerical Simulation of the Heat Distribution in electrical Devices*, 16th International Conference on Mathematical Modelling and Analysis, Sigulda, Latvia, 2011;
- F. Loos, H.-D. Ließ, *Numerical Simulation of Heat Distribution in a current-carrying Multi Wire*, 15th International Conference on Mathematical Modelling and Analysis, Druskininkai, Lithuania, 2010.

The author published/submitted six articles in/to journals and contributed to three further papers as co-author:

- F. Loos, K. Dvorsky, H.-D. Ließ, *Two approaches for heat transfer simulation of current carrying multicables*, Mathematics and Computers in Simulation, Elsevier, `http://www.sciencedirect.com/science/article/pii/S0378475414000500`, published online, 2014;
- K. Dvorsky, H.-D. Ließ, F. Loos, *Simulation der elektrischen Belastbarkeit von Bordnetzen und ihrer Komponenten*, Proceedings of Bordnetzkongress 2013;
- F. Loos, K. Dvorsky, H.-D. Ließ, *Determination of temperature in high-voltage cables of finite length with dynamic current profiles*, Mathematical and Computer Modelling of Dynamical Systems, Taylor & Francis, `http://www.tandfonline.com/doi/abs/10.1080/13873954.2013.833120#.Urf-LfuQOF8`, published online, 2013;
- F. Loos, H. Harbrecht, *Optimization of Current Carrying Multicables*, submitted to Computational Optimization and Applications, Springer, 2013;

- C. Holyk, H.-D. Ließ, S. Grondel, H. Kanbach, F. Loos, *Simulation and measurement of the stationary temperature in multi-conductor cables for hybrid and electric vehicles*, submitted to Electric Power Systems Research, Elsevier, 2013;
- F. Loos, K. Dvorsky, H.-D. Ließ, *Determination of Stationary Temperature Distribution in Shielded Cables of Finite Length*, International Review of Mechanical Engineering (IREME), Praise Worthy Prize, Vol. 7, n. 2, pp. 282-292, 2013;
- F. Loos, H.-D. Ließ, B. Philippe, *Transient Analysis of the Triggering Behaviour of Safety Fuses*, Proceedings of the COMSOL Conference 2011, Conference-CD, 2011;
- F. Loos, H.-D. Ließ, K. Dvorsky, *Simulation Methods for Heat Transfer Processes in mechanical and electrical Connections*, Proceedings of 1st International Electric Drives Production Conference 2011 (EDPC), pp. 214-220, 2011;
- C. Fischer, F. Loos, R. Süß-Wolf, H.-D. Ließ, J. Franke, *Integration von Makro-MID-Technologie im PKW*, HNI-Verlagsschriftenreihe, Vol. 294, pp. 39-56, 2011.

Most of the mentioned articles are available as preprints at `https://www.unibw.de/bauv1/personen/loos`.

2 Modelling and Analysis

In this chapter, thermal processes in connecting structures carrying electric currents are described. They are modelled in two different ways in this work, both based on the *law of conservation of energy*. On the one hand, we derive partial differential equations for stationary and transient problems, describing the full problem on three-dimensional domains, on the other hand, we introduce reduced computational models for different applications in Sections 5-9, yielding simplified (systems of) equations on one- or two-dimensional domains. Heat generated by Joule losses in the considered components dissipates from solid material to surrounding air by convection and radiation. Both processes are summarized in a heat transfer coefficient which represents a main ingredient of the governing nonlinear boundary condition. Interface conditions and initial conditions for the time-dependent case are introduced and allow to state general formulations for stationary and transient problems. Finally, we analyse the general problems mathematically and examine existence and uniqueness of solutions.

2.1 Energy Balance

In physics, the law of conservation of energy is one of the main principles. We consider a closed system, e.g. a small cable section or a volume element. At any time, there holds a balance for the amount of (thermal) energy. The energy E_{in} entering the system and E_{g} generated inside by Joule losses must be equal to the energy E_{out} which dissipates by conduction, convection and radiation and the change of energy ΔE_{st}[1] stored within the system [3, 68, 128]. Thus, we obtain

$$E_{\mathrm{in}} + E_{\mathrm{g}} = E_{\mathrm{out}} + \Delta E_{\mathrm{st}}, \tag{2.1}$$

with $\Delta E_{\mathrm{st}} > 0$ representing an increase, $\Delta E_{\mathrm{st}} < 0$ a decrease in energy of the system in the time interval Δt. For the stationary case, there holds $\Delta E_{\mathrm{st}} = 0$. This energy balance is fundamental for our reduced modelling approaches and also for the derivation of the PDEs.

2.2 Governing Equations

We derive the governing equations which determine the temperature of devices carrying electric currents. In contrast to the standard Poisson and heat equation, an additional energy source term is incorporated which depends on the temperature itself. It involves the rise of electrical resistivity for increasing temperatures in conductive material [71, 127].

Consider the heat conduction problem in a three-dimensional, bounded domain $\Omega \subseteq \mathbb{R}^3$ and time $t \geq 0$ for the temperature $T = T(\mathbf{x}, t) = T(x_1, x_2, x_3, t)$ with space dimensions x_1, x_2, x_3. On the cylinder $\mathcal{Q} = V \times \Delta t^*$ consisting of the volume element $V \subseteq \Omega$ with

---

[1] Note that in this context, the symbol Δ does not represent the Laplacian, but the change of a quantity which is not necessarily infinitesimal.

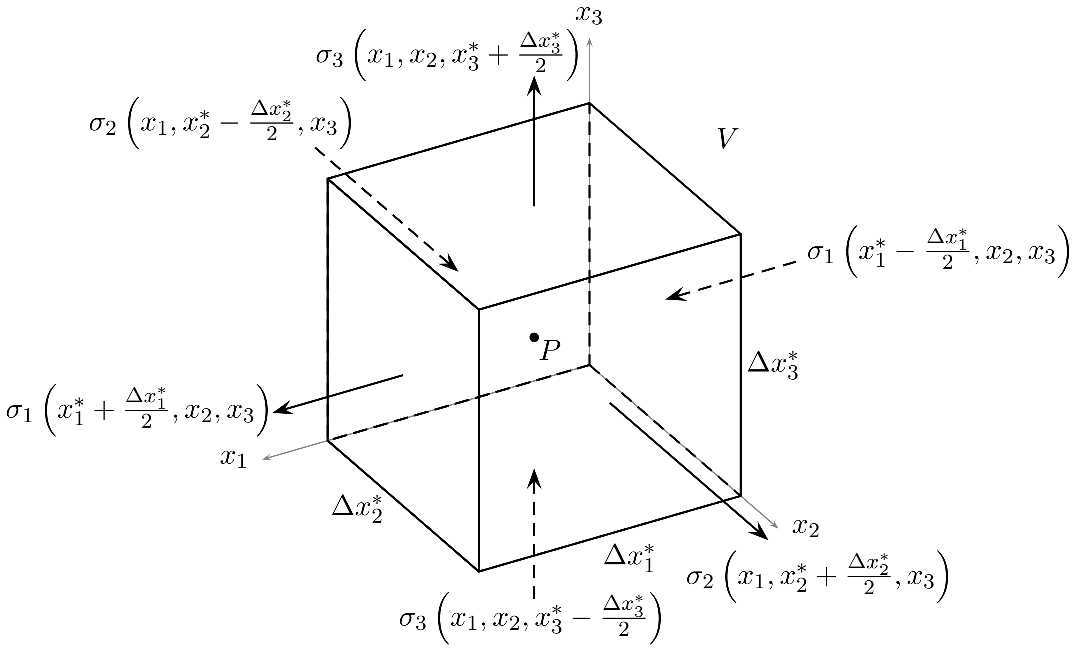

Fig. 2.1: *Heat power balance in a volume element* $V = \Delta x_1^* \times \Delta x_2^* \times \Delta x_3^*$.

centre $P = (x_1^*, x_2^*, x_3^*)$ and edge lengths Δx_1^*, Δx_2^*, Δx_3^* (cf. Figure 2.1) respectively the time interval $\Delta t^* = [t_1, t_2]$, $t_1, t_2 \geq 0$, the equation of heat balance holds:

$$\Delta E_{\mathrm{st}} = -E_{\mathrm{surf}} + E_{\mathrm{g}}. \tag{2.2}$$

The quantity ΔE_{st} denotes the amount of change of heat energy in $\mathcal{Q}$. It depends on the specific heat capacity $\gamma(\mathbf{x})$ per volume, i.e. the product of the specific heat capacity $c(\mathbf{x})$ per weight and the density $\varrho(\mathbf{x})$, and the change of temperature in all points $\mathbf{x} \in V$ in time:

$$\Delta E_{\mathrm{st}} = \int\limits_V \gamma(\mathbf{x}) \left(T\left(\mathbf{x}, t_2\right) - T\left(\mathbf{x}, t_1\right)\right) \mathrm{d}\mathbf{x}. \tag{2.3}$$

The heat energy $E_{\mathrm{surf}} := E_{\mathrm{out}} - E_{\mathrm{in}}$ flowing across the boundary $S = \partial V$ in the time interval Δt^* summarizes the entire heat energy entering and leaving the volume element during Δt^*. According to Fourier's law[2], the heat flux σ_i, $i = 1, 2, 3$, in direction x_i is

$$\sigma_i = -\lambda_i \frac{\partial T}{\partial x_i},\ i = 1, 2, 3.$$

We assume V to be of homogeneous, isotropic material. Thus, the heat conductivities are $\lambda_1 = \lambda_2 = \lambda_3 =: \lambda$ and

$$E_{\mathrm{surf}} = -\int\limits_{t_1}^{t_2} \int\limits_S \lambda \frac{\partial T}{\partial x_i} \,\mathrm{d}\mathbf{s}\,\mathrm{d}t = -\int\limits_{t_1}^{t_2} \int\limits_S \left(\lambda \nabla T\right) \cdot \mathbf{n} \,\mathrm{d}\mathbf{s}\,\mathrm{d}t,$$

---

[2] We suppose the considered volume element to be an *inner* cubic without free surfaces. Hence, all energy is supplied respectively emitted via conduction instead of convection and radiation.

with $\mathbf{n}$ the outer normal to S in the corresponding points. Application of Gauss' theorem yields

$$E_{\mathrm{surf}} = -\int\limits_{t_1}^{t_2}\int\limits_{V} \nabla\cdot(\lambda\nabla T)\,\mathrm{d}\mathbf{x}\,\mathrm{d}t. \tag{2.4}$$

Heat energy in conductive material is generated by the Joule effect due to resistive losses. We assume the current density in V to be constant. Thus, the heat energy E_{g} generated by the electric current I flowing through V with electrical resistance R is, according to Joule's first law,

$$E_{\mathrm{g}} = \int\limits_{t_1}^{t_2}\int\limits_{V} \frac{R\cdot I^2}{V}\,\mathrm{d}\mathbf{x}\,\mathrm{d}t. \tag{2.5}$$

The rise of electrical resistivity ρ for increasing temperatures is taken into account by a linear approximation via the temperature coefficient α_ρ, starting from the resistivity ρ_0 at reference temperature T_0. Furthermore, the electrical resistance R depends on the length ℓ and the cross sectional area A of the electro-conductive material

$$R = \rho\cdot\frac{\ell}{A} = \rho_0\left(1+\alpha_\rho\left(T-T_0\right)\right)\frac{\ell}{A}. \tag{2.6}$$

We obtain

$$E_{\mathrm{g}} = \int\limits_{t_1}^{t_2}\int\limits_{V}\left(\rho_0\,\alpha_\rho\left(\frac{I}{A}\right)^2 T + \rho_0\left(1-\alpha_\rho\,T_0\right)\left(\frac{I}{A}\right)^2\right)\mathrm{d}\mathbf{x}\,\mathrm{d}t. \tag{2.7}$$

Furthermore, we assume $\lambda\in C^1(\Omega)$, $\lambda>0$, const., $T\in C^1([0,\infty),C^2(\Omega))$ and replace ΔE_{st}, E_{surf} and E_{g} according to (2.3), (2.4) and (2.7) in (2.2). Multiplying by $\frac{1}{\Delta t^*}$ and $\frac{1}{\Delta x_1^*\,\Delta x_2^*\,\Delta x_3^*}$, taking Δt^* to zero ($\Delta t^*\to 0$), contracting V to the point P ($\Delta x_1^*\to 0$, $\Delta x_2^*\to 0$, $\Delta x_3^*\to 0$) and applying the mean value theorem for a function of several variables provides

$$\gamma(\mathbf{x}^*)\,\frac{\partial T(\mathbf{x}^*,t^*)}{\partial t} = \nabla\cdot\left(\lambda\,\nabla T(\mathbf{x}^*,t^*)\right)+\rho_0\,\alpha_\rho\left(\frac{I}{A}\right)^2 T(\mathbf{x}^*,t^*)+\rho_0\;\left(1-\alpha_\rho\,T_0\right)\left(\frac{I}{A}\right)^2 \tag{2.8}$$

with $\mathbf{x}^* = (x_1^*, x_2^*, x_3^*)$. To simplify the notation, we replace $\mathbf{x}^*$ by $\mathbf{x}$, t^* by t and leave out the dependency of the functions on space and time. At first, the domain Ω is supposed to consist of homogeneous material with equal parameter values on the entire domain. Since (2.8) is valid for all $\mathbf{x}\in\Omega$ and $t\in[0,t_{\max}]$ with $t_{\max}$ the last time of consideration, we finally obtain the *heat equation with a source* on the cylinder $\Omega\times[0,t_{\max}]$ [110]:

$$\boxed{\gamma\,\frac{\partial T}{\partial t} = \nabla\cdot(\lambda\nabla T)+\rho_0\,\alpha_\rho\left(\frac{I}{A}\right)^2 T+\rho_0\left(1-\alpha_\rho\,T_0\right)\left(\frac{I}{A}\right)^2 \quad \text{in } \Omega\times[0,t_{\max}].} \tag{2.9}$$

Neglecting the dependency of the temperature on the time ($\frac{\partial T}{\partial t}=0$, $t\to\infty$) yields the *inhomogeneous Helmholtz equation* on the domain Ω:

$$\boxed{\nabla\cdot(\lambda\nabla T)+\rho_0\,\alpha_\rho\left(\frac{I}{A}\right)^2 T = -\rho_0\left(1-\alpha_\rho\,T_0\right)\left(\frac{I}{A}\right)^2 \quad \text{in } \Omega\,.} \tag{2.10}$$

If the domain $\Omega = \cup_{k=1}^{N} \Omega_k$ consists of N subdomains, the parameters γ, λ, ρ_0, α_ρ, I, A are defined piecewise. Using the indicator function

$$\mathbb{I}_{\Omega_k} = \begin{cases} 1 & \text{if } \mathbf{x} \in \Omega_k, \\ 0 & \text{else,} \end{cases}$$

we define e.g. the heat conductivity by $\lambda := \bigcup_{k=1}^{N} \lambda_k \mathbb{I}_{\Omega_k}$. Appropriate interface conditions between different subdomains are given in Section 2.3.2.

2.3 Boundary and Initial Conditions

In order to determine a (unique) solution of (2.9) and (2.10), we define adequate boundary conditions describing the physical processes at the surface of our simulated objects. Furthermore, for the transient case, suitable initial conditions need to be introduced.

2.3.1 Exterior Boundary Condition

The surrounding media in our applications is air, so the condition

$$-\lambda_{\mathrm{ex}} \frac{\partial T}{\partial \mathbf{n}} = \alpha \cdot (T - T_{\mathrm{amb}}) \quad \text{on } \Gamma^{\mathrm{ex}} \tag{2.11}$$

describes the heat transfer at the exterior boundary $\Gamma^{\mathrm{ex}} = \partial\Omega$. We identify λ_{ex} with the heat conductivity of the (exterior) solid, $\partial T / \partial \mathbf{n}$ with the derivative of T in direction of the outer normal $\mathbf{n}$, T_{amb} with the ambient temperature and α with the heat transfer coefficient.

In many simulations of engineering, the nonlinear quantity α is estimated a priori by a fixed value and supposed to be constant. However, especially for higher temperatures, it is indispensable to respect the dependency of α on the temperature, since a wrong value for α can completely falsify the results. We demonstrate this by an insulated single-core cable with core of copper and an exterior diameter of 7.75 mm, which carries an electric current of 55.29 A. The simulation results obtained with constant heat transfer coefficients varying from $\alpha = 5 - 30\,\mathrm{W}/(\mathrm{K} \cdot \mathrm{m}^2)$ are compared to those computed with a temperature dependent one.

Figure 2.2 shows that the maximum temperatures in the cable vary from 92.3 °C ($\alpha = 30\,\mathrm{W}/(\mathrm{K} \cdot \mathrm{m}^2)$) to 289.8 °C ($\alpha = 5\,\mathrm{W}/(\mathrm{K} \cdot \mathrm{m}^2)$) for constant and fixed values of α, whereas the temperature in the core for a temperature dependent α is 106.8 °C (black dotted, vertical line in Figure 2.2). Since its actual value is unknown a priori, we have to apply appropriate formulas which are presented in the following. Thus, condition (2.11) becomes nonlinear by

$$-\lambda_{\mathrm{ex}} \frac{\partial T}{\partial \mathbf{n}} = \alpha(T) \cdot (T - T_{\mathrm{amb}}) \quad \text{on } \Gamma^{\mathrm{ex}}. \tag{2.12}$$

CFD simulations are subject of many research projects. They can give precise information about fluid behaviour and thermal extension. As we do focus on the heat generated inside of the electric devices, we use the simplified, but established concept of heat transfer coefficients that summarize the effects of convection by α_{conv} and radiation by α_{rad} [59, 67, 83]:

$$\alpha = \alpha_{\mathrm{conv}} + \alpha_{\mathrm{rad}}\,. \tag{2.13}$$

Since the temperature on the exterior boundary Γ^{ex} is not always constant, the heat transfer coefficient implicitly depends on the position. For a local heat transfer coefficient, we use

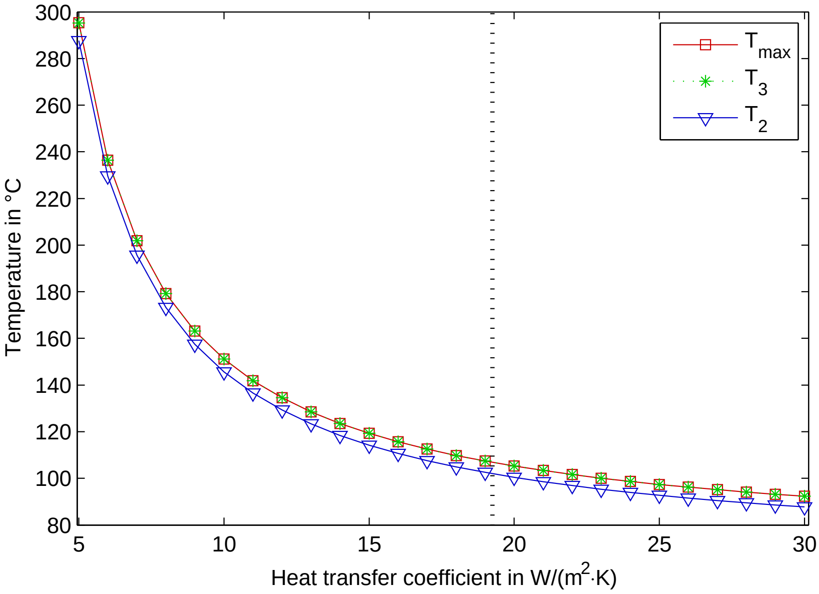

Fig. 2.2: *Influence of the heat transfer coefficient α on the maximum temperature (T_{max}), the temperature (T_3) in the core and the temperature (T_2) at the exterior surface of an insulated single-core cable (cf. Section 5). The black dotted line shows the value for a temperature dependent α ($\approx 19.25\ W/(m \cdot K)$ in this specific scenario), using the formulas presented in the following paragraphs and evaluating the numerical value a posteriori, after having computed the temperature distribution.*

the same formulas as for the global one, but the temperature at every evaluation point as well as the ambient temperature is considered for each position of the boundary $\mathbf{x} \in \Gamma^{\mathrm{ex}}$.

Determination of Convective Heat Transfer Coefficients

Although fluids do not conduct heat very well, they transport it by thermal convection. Convection is defined as transfer of thermal energy from one place to another by the movement of molecules in fluids. Heat transfer by free convection is caused by density differences as consequence of temperature differences. In our simulations, heat is transported from a (normally hotter) boundary surface of solid material by a fluid in motion [43, 68].

To describe convective heat transfer, we summarize the formulas in [8, 17, 18, 113] and mainly [131]. As the exact mathematical determination is complicated and not always possible, we make use of *similitude* where experimental data and formulas are transformed from simpler geometries to more complex ones. Based on dimensionless quantities, Nusselt's similitude enables to give a statement about the fluid behaviour without solving a coupled system of partial differential equations, namely the Navier-Stokes equations. Similitude of the two systems, original and model, is only possible if geometrical similitude of the systems, the physical processes and all involved quantities in spaces and time, is fulfilled [118].

First, we introduce the dimensionless quantities

- Nusselt number $Nu = \dfrac{\alpha_{\mathrm{conv}}}{\lambda_a} \cdot \ell_0 = f(Gr, Pr)$,
- Grashof number $Gr = \dfrac{g\,\ell_0^3}{\nu^2} \cdot \beta \Delta T$,

- Rayleigh number $Ra = Pr \cdot Gr$.

The Nusselt number represents the ratio of the convective to conductive heat transfer across the boundary of length ℓ_0 with the convective heat transfer coefficient α_{conv} and the heat conductivity λ_a of the fluid. It depends on the Grashof number and the Prandtl number Pr of air. The Grashof number is influenced by the gravitational acceleration $g\,(= 9.81\,\text{m/s}^2)$, the kinematic viscosity ν of air, the thermal extension coefficient β of air and the temperature difference ΔT between the temperature T at the boundary of the solid and the temperature T_{amb} of the surrounding fluid. The Rayleigh number Ra allows to distinguish between a laminar and turbulent surrounding airflow.

In general, there are different geometrical forms of boundaries which influence the calculation procedure of the heat transfer coefficient. The most important ones are

- vertical surfaces,
- horizontal surfaces, subdivided in upper and lower sides, and
- horizontal cylinders.

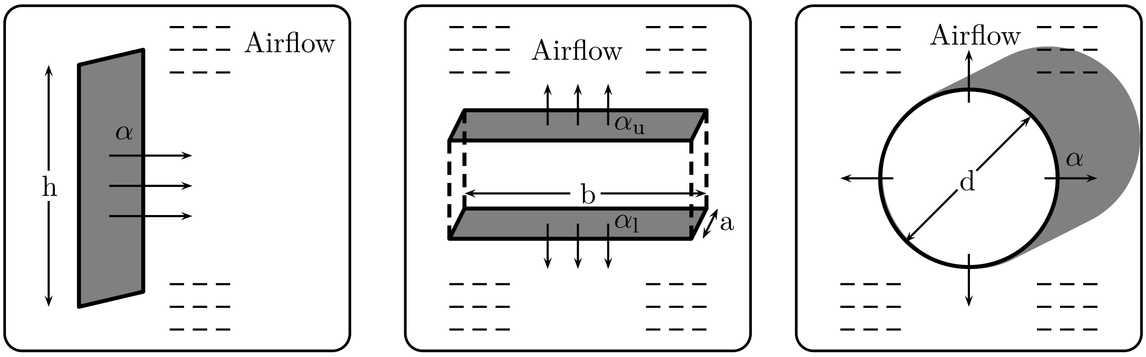

(a) Vertical surfaces. **(b)** Horizontal surfaces. **(c)** Horizontal cylinders.

Fig. 2.3: *Surface types for the computation of heat transfer coefficients.*

For each case, another function f and a characteristic length ℓ_0 are defined. The characteristic length possesses the dimension of a length, indeed it represents in general the three dimensional geometry of the considered system.

Vertical Surfaces

The Nusselt number for vertical surfaces, surrounded by either **laminar** or **turbulent** airflows ($0.1 \leq Ra \leq 10^{12}$), is given by

$$Nu = \left\{ 0.825 + 0.387 \left\{ \frac{Pr \cdot Gr}{\left[1 + \left(\frac{0.492}{Pr}\right)^{\frac{9}{16}}\right]^{\frac{16}{9}}} \right\}^{\frac{1}{6}} \right\}^2 .$$

Resolving the Nusselt number for the heat transfer coefficient, we obtain

$$\alpha_{\text{conv}} = \left\{ 0.825 \sqrt{\frac{\lambda_a}{\ell_0}} + 0.387 \sqrt{\lambda_a} \left\{ \frac{\beta\, g\, Pr}{\nu^2 \left[1 + \left(\frac{0.492}{Pr}\right)^{\frac{9}{16}}\right]^{\frac{16}{9}}} \right\}^{\frac{1}{6}} \sqrt[6]{\Delta T} \right\}^2 . \tag{2.14}$$

The characteristic length ℓ_0 corresponds to the height h of the vertical surface (cf. Figure 2.3a).

Horizontal Surfaces

To describe the heat transfer coefficient for horizontal surfaces, we have to distinguish between upper and lower sides. For upper sides, different formulas for laminar and turbulent flow need to be applied. The condition

$$\beta\,\ell_0^3\,(T - T_{\mathrm{amb}}) \leq 4.5e\text{-}5 \tag{2.15}$$

allows to check for practical applications whether the flow is laminar or turbulent [17].

In case of **laminar** flow at the **upper** side, the Nusselt number is

$$Nu = 0.766 \left\{ \frac{Pr \cdot Gr}{\left[1 + \left(\frac{0.322}{Pr}\right)^{\frac{11}{20}}\right]^{\frac{20}{11}}} \right\}^{\frac{1}{5}}$$

and the convective term corresponds to

$$\alpha_{\mathrm{conv}} = 0.766\,\lambda_a \left\{ \frac{\beta\,g\,Pr}{\nu^2 \left[1 + \left(\frac{0.322}{Pr}\right)^{\frac{11}{20}}\right]^{\frac{20}{11}}} \right\}^{\frac{1}{5}} \sqrt[5]{\frac{\Delta T}{\ell_0^2}}. \tag{2.16}$$

For **turbulent** flow at the **upper** side, we have

$$Nu = 0.150 \left\{ \frac{Pr \cdot Gr}{\left[1 + \left(\frac{0.322}{Pr}\right)^{\frac{11}{20}}\right]^{\frac{20}{11}}} \right\}^{\frac{1}{3}}$$

and

$$\alpha_{\mathrm{conv}} = 0.150\,\lambda_a \left\{ \frac{\beta\,g\,Pr}{\nu^2 \left[1 + \left(\frac{0.322}{Pr}\right)^{\frac{11}{20}}\right]^{\frac{20}{11}}} \right\}^{\frac{1}{3}} \sqrt[3]{\Delta T}. \tag{2.17}$$

At the **lower** side, only formulas for **laminar** flow are available and necessary, by

$$Nu = 0.600 \left\{ \frac{Pr \cdot Gr}{\left[1 + \left(\frac{0.492}{Pr}\right)^{\frac{9}{16}}\right]^{\frac{16}{9}}} \right\}^{\frac{1}{5}}$$

and

$$\alpha_{\mathrm{conv}} = 0.600\,\lambda_a \left\{ \frac{\beta\,g\,Pr}{\nu^2 \left[1 + \left(\frac{0.492}{Pr}\right)^{\frac{9}{16}}\right]^{\frac{16}{9}}} \right\}^{\frac{1}{5}} \sqrt[5]{\frac{\Delta T}{\ell_0^2}}. \tag{2.18}$$

The characteristic length for horizontal surfaces, both upper and lower sides, is computed by $\ell_0 = \frac{A}{U}$ with A the surface area of the considered object and U its perimeter. Thus, there holds

$$\ell_0 = \frac{a \cdot b}{2\,(a+b)} \quad \text{respectively} \quad \ell_0 = \frac{d}{4}$$

for rectangular respectively circular surfaces. The quantities a and b represent the length and width of the rectangle (cf. Figure 2.3b), d the diameter of the circle.

Horizontal Cylinders

The Nusselt number for horizontal cylinders reads as

$$Nu = \left\{ 0.752 + 0.387 \left\{ \frac{Pr \cdot Gr}{\left[1 + \left(\frac{0.559}{Pr}\right)^{\frac{9}{16}}\right]^{\frac{16}{9}}} \right\}^{\frac{1}{6}} \right\}^2 .$$

Thus, the convective heat transfer coefficient is

$$\alpha_{\text{conv}} = \left\{ 0.752 \sqrt{\frac{\lambda_a}{\ell_0}} + 0.387 \sqrt{\lambda_a} \left\{ \frac{\beta\, g\, Pr}{\nu^2 \left[1 + \left(\frac{0.559}{Pr}\right)^{\frac{9}{16}}\right]^{\frac{16}{9}}} \right\}^{\frac{1}{6}} \sqrt[6]{\Delta T} \right\}^2 \tag{2.19}$$

and

$$\ell_0 = \frac{d}{2}\pi,$$

with d the diameter of the cylinder (cf. Figure 2.3c).

Approximation of Temperature Dependent Quantities

Obviously, the thermal extension coefficient β, the heat conductivity λ_a, the kinematic viscosity ν and the Prandtl number Pr of air mainly determine the convective heat transfer coefficient. All these quantities are temperature dependent and only empirical data are provided in [131]. In order to obtain adequate formulas for these quantities, we fit the empirical data by polynomials of fourth degree or lower. A similar procedure was first performed in [67], but different fitting formulas were applied. In the following, the parameter T_m denotes the average value of the temperature T at the corresponding position on the boundary and the temperature T_{amb} of the surrounding fluid ($T_m = (T + T_{\text{amb}})/2$):

$$\begin{aligned}
\beta(T_m) &= \tfrac{0.993048}{T_m + 273.15}, \\
\lambda_a(T_m) &= -1.0648e\text{-}14\, T_m^4 + 3.1098e\text{-}11\, T_m^3 - 4.0303e\text{-}8\;\; T_m^2 + 7.6575e\text{-}5\, T_m + 2.4340e\text{-}2, \\
\nu(T_m) &= 1.3466e\text{-}17\, T_m^4 - 4.0352e\text{-}14\, T_m^3 + 1.0979e\text{-}10\, T_m^2 + 8.8761e\text{-}8\, T_m + 1.3520e\text{-}5, \\
Pr(T_m) &= 2.1796e\text{-}13\, T_m^4 - 6.1980e\text{-}10\, T_m^3 + 5.8848e\text{-}7\;\; T_m^2 + 1.5775e\text{-}4\, T_m + 7.1091e\text{-}1.
\end{aligned}$$

Determination of Radiative Heat Transfer Coefficients

In contrast to conduction and convection, thermal radiation requires no matter. Consequently, heat transfer in a vacuum is possible by radiation. Heat from a hotter to a colder body is transferred by electromagnetic waves, emitted from a heat or light source as a consequence of its temperature [120, 134]. The radiation rate q_r per unit surface area and unit time is, according to the Stefan-Boltzmann law,

$$q_r = \epsilon_{\mathrm{r}}\, \sigma \cdot \left(T_{2K}^4 - T_{1K}^4\right) \ . \tag{2.20}$$

Therein, we denote T_{1K}, T_{2K} the absolute temperatures[3] of the surface and ambient air, σ the Stefan-Boltzmann constant ($\sigma = 5.67e\text{-}8\,\frac{\mathrm{W}}{\mathrm{m^2K^4}}$) and ϵ_{r} the emissivity of the radiating element. Furthermore, Equation (2.20) can be expressed with the help of the radiative heat transfer coefficient α_{rad}, which allows to summarize the convective and radiative heat transfer according to (2.13) by

$$\begin{aligned} q_r &= \epsilon_{\mathrm{r}}\, \sigma \cdot \left(T_{2K}^2 + T_{1K}^2\right)\left(T_{2K}^2 - T_{1K}^2\right) \\ &= \underbrace{\epsilon_{\mathrm{r}}\, \sigma \cdot \left(T_{2K}^2 + T_{1K}^2\right)\left(T_{2K} + T_{1K}\right)}_{=\alpha_{\mathrm{rad}}}\underbrace{\left(T_{2K} - T_{1K}\right)}_{=T-T_{\mathrm{amb}}} \end{aligned}$$

$$\Rightarrow \quad q_r = \alpha_{\mathrm{rad}}\left(T - T_{\mathrm{amb}}\right) \ . \tag{2.21}$$

Both effects, convection and radiation, have to be taken into account simultaneously. Normally, for lower temperatures of surface and environment ($\leq 100\,°\mathrm{C}$), the convective term is more relevant. As both temperatures affect the radiative heat transfer coefficient in power of three, radiation dominates for higher values. In forced convection of gases, α_{conv} might well be larger and α_{rad} is negligible. As in our considerations the convection is natural, we always include both terms [83].

2.3.2 Interface Conditions

The set of interface boundaries at the transition of two different materials and subdomains is denoted by $\Gamma^{\mathrm{int}} \subset \Omega$. The notation $[\cdot]_\pm$ abbreviates the difference of the traces of a function at an interface boundary, approaching the boundary from exterior and interior respectively. On $\iota \in \Gamma^{\mathrm{int}}$, there hold the conditions

$$\left[\lambda \frac{\partial T}{\partial \mathbf{n}}\right]_\pm = 0 \quad \text{on } \ \iota \in \Gamma^{\mathrm{int}}, \tag{2.22}$$

$$[T]_\pm = 0 \quad \text{on } \ \iota \in \Gamma^{\mathrm{int}}. \tag{2.23}$$

Equation (2.22) reflects the equality of heat fluxes, Equation (2.23) the equality of temperatures on both sides of the interface. We point to the jump of the temperature gradient on $\iota \in \Gamma^{\mathrm{int}}$ that is of special interest for the optimization of multicables in Section 7.

Equation (2.23) is valid for perfect thermal contacts [68, 104] which we suppose in this work if not mentioned otherwise. At the point where different (metallic) materials meet, an electric contact resistance R_c may appear. The heat power P_c generated at the contact by Joule losses is

$$P_c = R_c(T)\, I^2 = R_{c,0}\, \left[1 + \alpha_{\rho_c}(T - T_0)\right] I^2,$$

---

[3] The absolute temperatures are indicated in K, all other temperatures in °C.

with electric current I crossing the contact of cross sectional area A_c [40]. The decrease of the electrical resistance $R_{c,0}$ at reference temperature T_0 for higher temperatures is approximated linearly by the temperature coefficient α_{ρ_c}. Adding the heat power term to (2.22) yields

$$\left[\lambda \frac{\partial T}{\partial \mathbf{n}}\right]_{\pm} = \frac{P_c}{A_c} \quad \text{on } \iota \in \Gamma^{\text{int}}. \tag{2.24}$$

2.3.3 Initial Condition

The temperature distribution at the initial time $t_0 = 0$ is specified for transient processes by

$$T = T_{\text{init}} \ \text{ in } \ \Omega \times \{0\}\,. \tag{2.25}$$

This condition is required to obtain a unique solution of the transient boundary value problem. In our simulations, we normally require the known temperature T_{init} to correspond to the ambient temperature T_{amb} on the entire domain Ω [68, 104]. If the ambient temperature varies for different subsections, e.g. in shielded cables of finite length in Section 6, a continuous initial temperature profile is applied.

2.4 General Problem Formulations

General boundary value problems (BVP) for the thermal analysis of connecting structures that carry electric currents are stated in this paragraph. We distinguish between stationary and transient considerations as well as domains that are either homogeneous or composed of several subdomains (of possibly different materials). As contacts between different metallic materials appear only in a few of our considered applications, boundary condition (2.24) is not part of the general problem formulations. Where necessary (e.g. in current bars in Section 8), it is mentioned explicitly.

2.4.1 General Problem Formulation for Homogeneous Domains

We first assume the entire domain to consist of only one conductive material. Then, the temperature in the stationary state is determined by the following PDE and exterior boundary condition:

$$\boxed{\begin{aligned} -\nabla \cdot (\lambda \nabla T) - \rho_0\, \alpha_\rho \left(\frac{I}{A}\right)^2 T &= \rho_0\, (1 - \alpha_\rho\, T_0) \left(\frac{I}{A}\right)^2 && \text{in } \ \Omega, \\ -\lambda_{\text{ex}} \frac{\partial T}{\partial \mathbf{n}} &= \alpha(T) \cdot (T - T_{\text{amb}}) && \text{on } \ \Gamma^{\text{ex}}. \end{aligned}} \tag{2.26}$$

For time-dependent problems on homogeneous domains, the constituting PDE is expanded by an additional term and we require an initial condition:

$$\boxed{\begin{aligned} \gamma \frac{\partial T}{\partial t} = \nabla \cdot (\lambda \nabla T) + \rho_0\, \alpha_\rho \left(\frac{I}{A}\right)^2 T + \rho_0\, (1 - \alpha_\rho\, T_0) \left(\frac{I}{A}\right)^2 \quad & \text{in } \ \Omega \times [0, t_{\max}], \\ -\lambda_{\text{ex}} \frac{\partial T}{\partial \mathbf{n}} = \alpha(T) \cdot (T - T_{\text{amb}}) \quad & \text{on } \ \Gamma^{\text{ex}}, \\ T = T_{\text{amb}} \quad & \text{on } \ \Omega \times \{0\}\,. \end{aligned}} \tag{2.27}$$

2.4.2 General Problem Formulation for Composed Domains

Now, we suppose the entire domain to be composed of several subdomains $\Omega = \bigcup_{k=1}^{N} \Omega_k$ and the values of parameters to vary for different subdomains.
Due to discontinuous parameters, the temperature profile has kinks at the interfaces $\iota \in \Gamma^{\text{int}}$ of different materials (cf. Figure 2.4 with interface boundaries Γ_k^e and Γ_k^i at the exterior and interior boundary of subdomain Ω_k). Although an explicit mentioning of these conditions is not necessary for a concise problem presentation, we state them as they are essential for the Hadamard presentation of the shape gradient for multicables in Section 7. Thus, the entire problem for stationary considerations reads as follows:

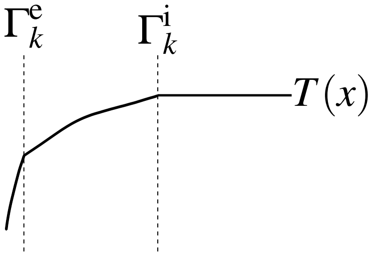

Fig. 2.4: *Continuous temperature profile with kinks at interface boundaries.*

$$
\begin{aligned}
-\nabla \cdot (\lambda \nabla T) - \rho_0\, \alpha_\rho \left(\frac{I}{A}\right)^2 T &= \rho_0\, (1 - \alpha_\rho\, T_0) \left(\frac{I}{A}\right)^2 && \text{in } \Omega \setminus \Gamma^{\text{int}}, \\
-\lambda_{\text{ex}} \frac{\partial T}{\partial \mathbf{n}} &= \alpha(T) \cdot (T - T_{\text{amb}}) && \text{on } \Gamma^{\text{ex}}, \\
\left[\lambda \frac{\partial T}{\partial \mathbf{n}}\right]_{\pm} &= 0, \quad [T]_{\pm} = 0 && \text{on } \iota \in \Gamma^{\text{int}}.
\end{aligned}
\tag{2.28}
$$

We emphasize once more that all parameters, including e.g. I and ρ_0, are defined seperately on each subdomain.

In case of transient considerations on composed domains, we apply

$$
\begin{aligned}
\gamma \frac{\partial T}{\partial t} &= \nabla \cdot (\lambda \nabla T) + \rho_0\, \alpha_\rho \left(\frac{I}{A}\right)^2 T + \rho_0\, (1 - \alpha_\rho\, T_0) \left(\frac{I}{A}\right)^2 && \text{in } \Omega \setminus \Gamma^{\text{int}} \times [0, t_{\max}], \\
-\lambda_{\text{ex}} \frac{\partial T}{\partial \mathbf{n}} &= \alpha(T) \cdot (T - T_{\text{amb}}) && \text{on } \Gamma^{\text{ex}}, \\
\left[\lambda \frac{\partial T}{\partial \mathbf{n}}\right]_{\pm} &= 0, \quad [T]_{\pm} = 0 && \text{on } \iota \in \Gamma^{\text{int}}, \\
T &= T_{\text{amb}} && \text{on } \Omega \times \{0\}\,.
\end{aligned}
\tag{2.29}
$$

2.5 Existence and Uniqueness of a Solution

The primary objective of this work is to simulate heating processes in electric connections. Nevertheless, mathematical considerations are indispensable in the field of simulations and application of numerical methods. Thus, we state main results about existence and uniqueness of a solution of the problems. Deeper insight and analysis are subject of Dvorsky's thesis [35].

As mentioned, the stationary problems (2.26) and (2.28) are of Helmholtz type with nonlinear boundary conditions on the exterior insulation. A proof of existence and uniqueness of a strong solution of problem (2.28) goes beyond the scope of this thesis. Instead, we investigate a weak formulation which is easier to handle.

First, we suppose Ω to be of homogeneous and to have constant material parameters in the entire domain. Using standard notation for Sobolev spaces [1], we introduce the Hilbert space $H^1(\Omega)$ of functions with square integrable weak derivatives. To simplify notation, we define

$$\tilde{c} := \rho_0\, \alpha_\rho \left(\frac{I}{A}\right)^2, \quad \tilde{\gamma}(T) := \alpha(T)\,(T - T_{\text{amb}}), \quad \tilde{f} := \rho_0\,(1 - \alpha_\rho\, T_0) \left(\frac{I}{A}\right)^2.$$

After multiplication with test functions $v \in H^1(\Omega)$ and integration over Ω, a weak formulation of (2.26) reads as follows:

Find $T \in H^1(\Omega)$ such that

$$a(T, v) = b(v) \quad \forall v \in H^1(\Omega) \tag{2.30}$$

with

$$a(T, v) := \int\limits_{\Omega} \Big[\lambda\, \nabla T \cdot \nabla v \;-\; \tilde{c}\, T\, v\Big]\, \mathrm{d}\mathbf{x} + \int\limits_{\Gamma^{\text{ex}}} \tilde{\gamma}\,(T)\; v\; \mathrm{d}\mathbf{s},$$

$$b(v) := \int\limits_{\Omega} \tilde{f}\, v\, \mathrm{d}\mathbf{x}\,.$$

We truncate the monotone and continuous heat transfer coefficient α in our problem by

$$\tilde{\alpha}(T) \;:=\; \begin{cases} \alpha_l & \text{if } T < T_l \\ \alpha\,(T) & \text{if } T \geq T_l \end{cases}, \tag{2.31}$$

where $0 < \alpha_l = \alpha\,(T_l)$ is a lower bound for the heat transfer coefficient, determined by a fixed temperature T_l (for applications, normally $T_l = T_{\text{amb}}$). According to [35], there exists a unique solution $T \in H^1(\Omega)$ of problem (2.30), if

$$\alpha_\rho \left(\frac{I}{A}\right)^2 < \frac{\alpha_l}{\rho_0\, d_{\text{ex}}}\,. \tag{2.32}$$

The parameter $d_{\text{ex}} = \max\limits_{\mathbf{x},\mathbf{y} \in \Omega} |\mathbf{x} - \mathbf{y}|$ denotes the maximum distance of two arbitrary points $\mathbf{x}, \mathbf{y} \in \Omega$ in the considered domain. The sufficient condition (2.32) is called a *subresonance condition*. It might be surprising that for heat transfer processes, the term 'resonance' is employed. In physics, resonance is the response of a system that develops oscillations with large amplitudes under certain characteristic frequencies. In this setting, we use the term resonance as a criterion which distinguishes between well posed and ill posed problems in the theory of elliptic partial differential equations [22, 35, 76, 90]. The subresonance condition (2.32) ensures that a unique solution of our considered problem exists.

We denote the current for which the subresonance condition is fulfilled with equality the *limiting current*. There might exist cases with a unique solution for higher currents than the limiting current. Thus, we additionally introduce a *resonance current*, denoting the lowest known current load for which no stationary temperatures are attained.

Additionally, condition (2.32) ensures the existence and uniqueness of a time-dependent evolution of T, converging to the solution of the stationary problem. Therein, a constant current profile over the entire time horizon is supposed. For currents varying in time, a successive interpolation scheme is introduced in Section 6.4, taking advantage of the uniqueness of a stationary solution lower than the limiting current. However, for even higher currents, we cannot guarantee the existence of a unique solution.

If the domain $\Omega = \bigcup_{k=1}^{N} \Omega_k$ consists of several subdomains and the parameters are defined piecewise with index k in the subdomain Ω_k, the subresonance condition has to be formulated more restrictively. We recall an adapted theorem in [35] whose proof exploits the main theorem on monotone operators by Browder and Minty [141][4]:

Theorem 1. *Let $\alpha_{\rho,k}\,(\frac{I_k}{A_k})^2 < \frac{\alpha_l}{\rho_{0,k}\,d_{ex}}$ hold for all $k = 1, \ldots, N$. Then there exists a unique solution $T \in H^1(\Omega)$ of problem (2.30).*

Analogously to a homogeneous domain Ω, a time-dependent evolution of T to the solution of the stationary problem is given for composed domains if Theorem 1 is fulfilled for each subsection. Assume that condition $\alpha_{\rho,k}\,(\frac{I_k}{A_k})^2 < \frac{\alpha_l}{\rho_{0,k}\,d_{\mathrm{ex}}}$ holds for all k, a limiting current

$$I_{\mathrm{lim},k} = A_k \sqrt{\frac{\alpha_l}{\rho_{0,k}\,d_{\mathrm{ex}}\,\alpha_{\rho,k}}}$$

can be defined locally for each subdomain.

---

[4] Note that if a so called scaling condition is not fulfilled, the subresonance condition has to be slightly modified [35]. As these cases are far from practical relevance, we restrict to the situations fulfilling the condition, without explicitly mentioning it.

3 Simulation Methods

This chapter is dedicated to simulation methods necessary to solve heat transfer problems in electric connections. Since analytical and numerical approaches are applied in this work, advantages and drawbacks of both types are discussed.

Most of our computations are either performed or at least verified by finite elements (FE). We give a short introduction to the principles of the finite element method (FEM) as well as the finite difference method (FDM) and their application to our concrete problems. Due to the nonlinearity in the exterior boundary condition, iterative techniques have to be applied for both – the numerical solution by FEM and for adequate simplified approaches. We show basics of the employed methods, namely the Newton-Raphson method and fixed point iteration.

3.1 Analytical versus Numerical Methods

To solve heat transfer problems in electric connections, in particular (2.28) and (2.29), one can either use numerical or, with some simplifications, analytical methods. Analytical methods have been applied more frequently in the present field for several reasons. Mentionable in this context is a historical one, as most calculations are based on the analytical formulas of Neher and McGrath [100, 101] and the standard IEC norms (e.g. [60]). With growing computation powers, numerical methods have been gaining more importance [3, 4].

Analytical methods excel in general by

- shorter calculation times because no iterations are necessary to solve (nonlinear) systems and no expensive geometry or mesh generations as with e.g. FEM is needed,
- more manageable storage of information, since an extensive amount of data is avoided,
- better visualizability of physical laws that describe the processes and
- easier recognizability of new (scientific) contexts and correlations.

In contrast, the advantages of numerical methods are

- higher precision, since e.g. more (nonlinear) effects can be respected and
- greater flexibility concerning the consideration of complex geometries.

In this work, we never use solely analytical methods because of the nonlinearity on the exterior boundary condition. This requires the application of iterative methods. Nevertheless, we always simplify the equations of the model as far as possible and adapt our specific problems by analytical means. We have to keep in mind that our methods shall be applied in industry where saving time represents a main objective. Hence, finite elements often serve to validate whether assumptions and analytical formulations hold or to carry out investigations that are not possible with simplified approaches.

3.2 Solution Methods for Nonlinear Systems

The (discretized) nonlinear systems obtained in this work are solved via a fixed point iteration or the Newton-Raphson method which can also be interpreted as a fixed point iteration. They represent standard methods and are introduced briefly in the following section.

3.2.1 Fixed Point Iteration

There is often no possibility to solve nonlinear systems by elimination techniques. Thus, we have to apply another solution strategy, the concept of iteration [23]. An initial step in this context is to formulate a corresponding *fixed point equation*. Instead of searching the root $\mathbf{x}^*$ of a function $\mathbf{F} : \mathbb{R}^n \to \mathbb{R}^n$, the problem $\mathbf{F}(\mathbf{x}) = 0$ is reformulated equivalently by

$$\mathbf{x} = \widetilde{\mathbf{F}}(\mathbf{x}). \tag{3.1}$$

The following procedure enables to determine a solution $\mathbf{x}^*$ of Equation (3.1). Therein, we denote $i_{\max}$ the maximum number of iterations and $\epsilon > 0$ a small real constant:

Algorithm 1

```
(* Fixed point iteration *)
Input: $\widetilde{\mathbf{F}}$, $\epsilon$, $i_{\max}$
Output: $\mathbf{x}^*$
Choose an initial guess $\mathbf{x}^{(0)}$ (in the vicinity of $\mathbf{x}^*$) and set $i = 0$.
while $|\widetilde{\mathbf{F}}(\mathbf{x}^{(i)}) - \mathbf{x}^{(i)}| > \epsilon$ and $i < i_{\max}$
    Set $\mathbf{x}^{(i+1)} = \widetilde{\mathbf{F}}(\mathbf{x}^{(i)})$.
    Set $i = i + 1$.
return $\mathbf{x}^{(i)}$
```

Application of Algorithm 1 generates a sequence $(\mathbf{x}^{(i)})_{i \le i^*}$ with i^* representing the minimum of $i_{\max}$ and the smallest iteration number i, for which the condition $|\widetilde{\mathbf{F}}(\mathbf{x}^{(i)}) - \mathbf{x}^{(i)}| \le \epsilon$ holds. The convergence of the sequence $(\mathbf{x}^{(i)})_{i \in \mathbb{N}}$ to a fixed point of the mapping $\widetilde{\mathbf{F}}$ of (3.1) is ensured in a general setting by

Theorem 2 (Banach's Fixed Point Theorem)**.** *Let $(\mathbf{X}, d)$ be a complete metric space with a contraction mapping $\widetilde{\mathbf{F}} : \mathbf{X} \to \mathbf{X}$, i.e. there exists $0 \le q < 1$ such that $d(\widetilde{\mathbf{F}}(\mathbf{x}), \widetilde{\mathbf{F}}(\mathbf{y})) \le q\, d(\mathbf{x}, \mathbf{y})$ for all $\mathbf{x}, \mathbf{y} \in \mathbf{X}$. Then, there holds:*
a) The mapping $\widetilde{\mathbf{F}}$ has a unique fixed point $\mathbf{x}^* \in \mathbf{X}$.
b) For every initial value $\mathbf{x}^{(0)} \in \mathbf{X}$, the iterative sequence $(\mathbf{x}^{(i)})_{i \in \mathbb{N}}$ converges by

$$\mathbf{x}^{(i+1)} = \widetilde{\mathbf{F}}(\mathbf{x}^{(i)}), \quad i = 0, 1, 2, \ldots$$

to the fixed point $\mathbf{x}^*$.
c) For the speed of convergence, there holds

$$d(\mathbf{x}^{(i)}, \mathbf{x}^*) \le \frac{q^i}{1 - q}\, d(\mathbf{x}^{(1)}, \mathbf{x}^{(2)}).$$

Proof. Cf. [119, 141].

3.2.2 Newton-Raphson Method

Another iterative procedure to solve nonlinear systems is the widely used Newton-Raphson method. It is based on the idea of linear approximation and shows, if applicable, faster convergence properties than the previously presented fixed point iteration. For its implementation, we need information about the derivatives of the function $\mathbf{F} : \mathbb{R}^n \to \mathbb{R}^n$. A more detailed description in the context of finite elements can be found in e.g. [77, 119].

We begin with the (nonlinear) system $\mathbf{F}(\mathbf{x}) = 0$, $\mathbf{x} \in \mathbb{R}^n$. Furthermore, let an approximation $\mathbf{x}^{(i)}$ of the solution of $\mathbf{F}$ be given by $\mathbf{x}^*$. It is the objective to find an improved approximation $\mathbf{x}^{(i+1)}$ of the solution $\mathbf{x}^*$ of the system of nonlinear equations. The idea of the Newton-Raphson method consists in approximating $\mathbf{F}(\mathbf{x})$ in the vicinity of $\mathbf{x}^{(i)}$ ($\mathbf{F}(\mathbf{x}^*) \approx \mathbf{M}(\mathbf{x}^*; \mathbf{x}^{(i)})$) such that the system $\mathbf{M}(\mathbf{x}^*; \mathbf{x}^{(i)}) = 0$ represents an equation or a system of equations that is solved easily. The solution of this system yields the improved approximation $\mathbf{x}^{(i+1)}$ of the solution of the original system $\mathbf{F}(\mathbf{x}) = 0$. If no termination criterion like e.g. $\left\|\mathbf{x}^{(i+1)} - \mathbf{x}^{(i)}\right\| \leq \epsilon$ with a given norm $|| \cdot ||$ and tolerance $\epsilon > 0$ is fulfilled, $\mathbf{x}^{(i+1)}$ plays the role of $\mathbf{x}^{(i)}$ and represents the new initial approximating of the next iteration step.

The system $\mathbf{F}(\mathbf{x}) = 0$ is approximated in the vicinity of $\mathbf{x}^{(i)}$ by a linear function $\mathbf{M}(\mathbf{x}; \mathbf{x}^{(i)})$:

$$\mathbf{M}(\mathbf{x}; \mathbf{x}^{(i)}) = \mathbf{F}(\mathbf{x}^{(i)}) + \mathbf{J}(\mathbf{x}^{(i)}) \cdot (\mathbf{x} - \mathbf{x}^{(i)}),$$

with $\mathbf{J} \equiv \nabla \mathbf{F}$ the Jacobian of $\mathbf{F}$. With $\mathbf{F} = (F_1, \ldots, F_n)^t$ and $\mathbf{x} = (x_1, \ldots, x_n)^t$, the entry (u, v) of $\mathbf{J}$ corresponds to the expression $\partial F_u / \partial x_v$. Thus, to determine a further approximation $\mathbf{x}^{(i+1)}$ via $\mathbf{M}(\mathbf{x}^{(i+1)}; \mathbf{x}^{(i)})$, a linear system with $\mathbf{J}$ as coefficient matrix has to be solved.

Summarized, this yields the following algorithm:

Algorithm 2
(∗ Newton-Raphson method ∗)
Input: $\mathbf{F}$, ϵ, $i_{\max}$
Output: $\mathbf{x}^*$

```
Choose an initial guess $\mathbf{x}^{(0)}$ (in the vicinity of $\mathbf{x}^*$) and set $i = 0$.
while $||\mathbf{F}(\mathbf{x}^{(i)})|| > \epsilon$ and $i < i_{\max}$
    Solve the linear system $\mathbf{J}(\mathbf{x}^{(i)})\, \delta\mathbf{x}^{(i+1)} = -\mathbf{F}(\mathbf{x}^{(i)})$ w.r.t. $\delta\mathbf{x}^{(i+1)}$.
    Set $\mathbf{x}^{(i+1)} = \mathbf{x}^{(i)} + \delta\mathbf{x}^{(i+1)}$.
    Set $i = i + 1$.
return $\mathbf{x}^{(i)}$
```

The Newton-Raphson method belongs to the class of fixed point iterations because the inner core of Algorithm 2 can be formulated equivalently (if J is regular) by

$$\mathbf{x}^{(i+1)} = \mathbf{x}^{(i)} - \mathbf{J}^{-1}(\mathbf{x}^{(i)})\, \mathbf{F}(\mathbf{x}^{(i)}).$$

Thus, we have a fixed point mapping

$$\widetilde{\mathbf{F}}(\mathbf{x}) := \mathbf{x} - \mathbf{J}^{-1}(\mathbf{x})\, \mathbf{F}(\mathbf{x}) \;\text{ with }\; \widetilde{\mathbf{F}}(\mathbf{x}^*) = \mathbf{x}^*.$$

The drawback of the Newton-Raphson method is that, in contrast to the general fixed point iteration, we have to determine the Jacobian of $\mathbf{F}$ and must solve a linear system (instead of computing the inverse of $\mathbf{J}$) in every iteration step. A main advantage of the Newton-Raphson method is a better convergence speed given by

Theorem 3. *Let in a vicinity* U *of* $\mathbf{x}^*$ *the function* $\mathbf{F}$ *be twice continuous differentiable and* $\mathbf{F}(\mathbf{x}^*) = \mathbf{0}$, $\mathbf{J}(\mathbf{x}^*)$ *regular. Then, for* $\mathbf{x}^{(i)} \in U$ *and* $\mathbf{x}^{(i+1)} := \mathbf{x}^{(i)} - \mathbf{J}^{-1}(\mathbf{x}^{(i)})\,\mathbf{F}(\mathbf{x}^{(i)})$*, there holds with* $\xi^{(i)} \in U$ *and* $\mathbf{H}$ *the Hessian of* $\mathbf{F}$*:*

$$\mathbf{x}^{(i+1)} - \mathbf{x}^* = \frac{1}{2}\,\mathbf{J}^{-1}(\mathbf{x}^{(i)})\,\mathbf{H}(\xi^{(i)})\,(\mathbf{x}^{(i)} - \mathbf{x}^*)^2.$$

This means that the convergence of the Newton-Raphson method is locally quadratic.

Proof. Cf. [23, 119].

3.3 Numerical Methods for Heat Transfer Simulation

To solve the full BVPs (2.28) and (2.29) without reduction, numerical standard methods can be applied. The most important ones in this context are

- Finite Differences,
- Finite Volumes,
- Finite Elements,
- Boundary Elements.

All have in common that an infinite set of values of the solution is transformed to a finite set of values by *discretization*. These are finally obtained by solving a system of algebraic equations.

The idea of **Finite Differences** is to approximate a differential operator by a difference quotient. Introducing a *mesh* or *grid* yields nodal points and values of the sought-for function at the nodes. They represent the unknowns of the discretized problem. Finite differences are easy to understand and to implement, even for complicated equations. Disadvantages are that the application of standard finite difference techniques is cumbersome in domains of complex shape, especially the treatment of boundary conditions on curved boundaries. Moreover, problems arise for steep gradients, especially for discontinuities. Finite differences are often used for the discretization of time in parabolic or hyperbolic systems, combined with other numerical methods for the space discretization as e.g. in the *methods of lines*. Further information about finite differences, also in context of heat transfer, can be found in the relevant literature [47, 105].

The **Finite Volume** Method (FVM) is the most natural discretization scheme of the mentioned methods, because it makes use of the conservation laws in integral form. Subdividision of the domain into cells (finite volumes) and application of the conservation rule to every finite volume cell yields the set of algebraic equations with respect to the nodal values of the field. In contrast to finite differences, finite volumes are conservative, as the flux entering a given volume is identical to that leaving the adjacent volume. Therefore, it is more adequate from a physical point of view and widely used in the field of computational fluid dynamics. Furthermore, it is easily formulated on unstructured meshes and discontinuities can be handled with less difficulties. The disadvantage compared to finite differences is, of course, that the implementation is more complex [38, 80, 106].

In addition to the decomposition of the domain into smaller subdomains, the field of interest is, in the **Finite Element** Method (FEM), approximated by a linear combination of known functions, the *test*, *ansatz* or *trial functions*. The unknowns of the algebraic systems are the coefficients of the ansatz functions. We describe the finite element method with more details and specific to our problem in the next subsection. Like finite volumes, finite elements excel by a great flexibility in the discretization of complex geometries. Due to the use of integral formulations and the reduced requirements on the regularity, it provides a more natural treatment of Neumann, Robin and nonlinear boundary conditions as well as discontinuous source terms. On the other hand, its implementation is the most complex and expensive one of the presented methods. And it is still a comparatively slow process due to the need to define and redefine meshes in the domain under study. Of the seemingly endless wealth of literature, we mention books of introductory character [11, 71, 74, 77, 104].

Instead of discretizing the entire domain, **Boundary Element** techniques restrict to the surface. Thus, the dimension of the problem is reduced by one. Formulating BVPs as boundary integral equations describes problems only by equations with known and unknown boundary states. A basic feature of all boundary element methods is their use of fundamental solutions, which are analytical solutions of the governing differential equation. Boundary element methods have emerged as a powerful alternative to finite elements, particularly in cases where the domain extends to infinity, e.g., acoustics or soil-structure interaction. Due to the fact that creation and modification of the meshing of the complete domain is not necessary, time can be saved for complex geometries. It is often more effective in terms of computational resources for problems where there is a small surface/volume ratio or if minor design changes take place. On the other hand, boundary element formulations typically give rise to fully populated and non-symmetric matrices. This means that the storage requirements and computational times tend to grow with the square of the problem size. Furthermore, boundary element methods depend on the knowledge of a suitable fundamental solution which is not always obtainable. And, the treatment of inhomogeneous and nonlinear problems often requires meshing of more than the surface, which can neglect the main advantage of boundary element methods. We refer to [5, 58, 115, 139] for deeper insight to boundary methods.

In this work, we mainly use finite elements and, in parts, finite differences. We give short introductions to both methods.

3.3.1 Finite Differences

Finite differences are used within this work in two different contexts. Firstly, they help to control the correctness of gradients for shape optimization in Section 7.6.4 by an auxiliary method. Secondly, we use them for discretization of time in transient problems, e.g. to compute the non-stationary temperature and blowing characteristics of fuses in Section 9. Forward, backward and central differences are presented in the following paragraph and application to general time discretization is demonstrated.

Forward, Backward and Central Differences

Let a function $T : \mathbb{R}^n \to \mathbb{R}$, $T \in C^1$, depending on the (space) variable $\mathbf{x}$, be given. The (partial) derivative of T to x_i – the i-th component of $\mathbf{x}$ – is defined by

$$\frac{\partial}{\partial x_i} T(\mathbf{x}) := \lim_{h \to 0} \frac{T(\mathbf{x} + h\,\mathbf{e}_i) - T(\mathbf{x})}{h}, \tag{3.2}$$

with $\mathbf{e}_i$ the unit vector pointing in direction of the i-th coordinate axis. The first kind of finite difference class we introduce is the so called *forward difference approximation of first order*. It approximates the derivative defined in (3.2) by

$$\frac{\partial}{\partial x_i} T(\mathbf{x}) \approx \frac{T(\mathbf{x} + h\,\mathbf{e}_i) - T(\mathbf{x})}{h} =: \left(D_i^+ T\right)(\mathbf{x}), \tag{3.3}$$

with $h > 0$ the step length of the discretization and D_i^+ the corresponding *difference operator*.

Further approximations of the first derivative and corresponding difference operators are given by the *backward difference approximation of first order*

$$\frac{\partial}{\partial x_i} T(\mathbf{x}) \approx \frac{T(\mathbf{x}) - T(\mathbf{x} - h\,\mathbf{e}_i)}{h} =: \left(D_i^- T\right)(\mathbf{x}) \tag{3.4}$$

and the *central difference approximation of second order*

$$\frac{\partial}{\partial x_i} T(\mathbf{x}) \approx \frac{T(\mathbf{x} + h\,\mathbf{e}_i) - T(\mathbf{x} - h\,\mathbf{e}_i)}{2\,h} =: \left(D_i^0 T\right) = \frac{1}{2}\left(D_i^+ T + D_i^- T\right) . \tag{3.5}$$

Derivatives of higher order can also be approximated by finite differences. We renounce their explicit introduction and refer to [79].

Derivation of Finite Difference Methods and Local Errors

The basis for the derivation of the stated finite difference approximations is the Taylor expansion of the function T. As known, the function value T at the points $\mathbf{x} + h\mathbf{e}_i$ and $\mathbf{x} - h\mathbf{e}_i$ can be computed by

$$T(\mathbf{x} + h\mathbf{e}_i) = T(\mathbf{x}) + \frac{h}{1!}\frac{\partial T(\mathbf{x})}{\partial x_i} + \frac{h^2}{2!}\frac{\partial^2 T(\mathbf{x})}{\partial x_i^2} + \ldots \tag{3.6}$$

$$T(\mathbf{x} - h\mathbf{e}_i) = T(\mathbf{x}) - \frac{h}{1!}\frac{\partial T(\mathbf{x})}{\partial x_i} + \frac{h^2}{2!}\frac{\partial^2 T(\mathbf{x})}{\partial x_i^2} \mp \ldots\ . \tag{3.7}$$

Reordering (3.6) provides

$$\frac{\partial T(\mathbf{x})}{\partial x_j} = \frac{T(\mathbf{x} + h\mathbf{e}_i) - T(\mathbf{x})}{h} + \left(-\frac{h}{2!}\frac{\partial^2 T(\mathbf{x})}{\partial x_i^2} - \frac{h^2}{3!}\frac{\partial^3 T(\mathbf{x})}{\partial x_i^3} - \ldots\right). \tag{3.8}$$

Summarizing the terms including derivatives of second or higher by $\mathcal{O}(h)$, one obtains

$$\frac{\partial}{\partial x_i} T(\mathbf{x}) \approx \frac{T(\mathbf{x} + h\,\mathbf{e}_i) - T(\mathbf{x})}{h} + \mathcal{O}(h), \tag{3.9}$$

the formula for a finite difference approximation of first order. Decisive for the size of $\mathcal{O}(h)$ is the step length h and its power in the dominant term of the rest, denoted by the *local error order* $\mathcal{O}_{loc}$. For that reason, the method has the local error order $\mathcal{O}_{loc}(h)$.

The local error of the backward finite difference procedure is of the same order, obtainable by an analogous derivation, starting from (3.7). The error order of the central difference approximation is, as already mentioned, one degree higher. We get the formula by subtracting (3.7) from (3.6) and solving the resulting equation with respect to the first partial derivative of T to x_i:

$$\frac{\partial T(\mathbf{x})}{\partial x_i} = \frac{T(\mathbf{x} + h\mathbf{e}_i) - T(\mathbf{x} - h\mathbf{e}_i)}{2\,h} + \mathcal{O}(h^2). \tag{3.10}$$

Time Discretization and Line Methods

As mentioned, we apply finite differences for time discretization of transient problems like (2.29). The time intervall $[0, t_{\max}]$ is divided equidistantly into $n_t + 1$ time steps and n_t intervals $[t_j, t_{j+1}]$, $j = 0, \ldots, n_t - 1$, with $t_0 = 0$ respectively $t_{n_t} = t_{\max}$.

For example, if a backward difference approximation is applied to $\partial T / \partial t$, we have to solve a sequence of elliptic boundary value problems with unknown (continuous) functions $T^{(j)}(\mathbf{x})$ in time step j. The described procedure corresponds to a *horizontal method of lines*.

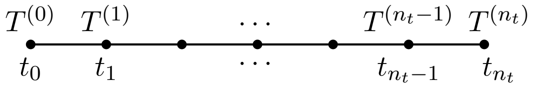

Fig. 3.1: *Time discretization scheme.*

In contrast, applying the *vertical method of lines* provides a system of ordinary differential equations (ODEs), as the system of equations is discretized in the space variable $\mathbf{x}$. Finally, equations depending solely on the time t remain [15, 47]. We show the application of the vertical method of lines in the next section.

The horizontal method of lines (often denoted by *Rothe's method*) is commonly combined with the θ-rule. The equation $\partial T / \partial t = G$ is approximated by

$$\frac{T^{(j)} - T^{(j-1)}}{\delta} = \theta\, G^{(j)} + (1-\theta)\, G^{(j-1)}, \quad 0 \leq \theta \leq 1,$$

with $\delta = t_j - t_{j-1}$ the time step size, $T^{(j)}$ abbreviating $T(\mathbf{x}, t_j) = T(\mathbf{x}, j\,\delta)$ and $G^{(j)}$ respectively $G^{(j-1)}$ the value of function G at time step t_j respectively t_{j-1}.

Obviously, for special values of θ, we obtain different procedures:

- $\theta = 0$: *explicit Euler method* (forward Euler method),
- $\theta = 0.5$: *Crank-Nicolson method* (midpoint rule),
- $\theta = 1$: *implicit Euler method* (backward Euler method).

Note that the explicit Euler method can entail stability problems. Hence, the value $\theta = 0$ should be chosen with caution. In contrast, the backward Euler and Crank-Nicolson schemes are unconditionally stable[1]. An additional advantage of the Crank-Nicolson method is that the error in the time approximation is of order δ^2, whereas it is of one order lower for the other schemes [77].

3.3.2 Finite Elements

Explaining the Finite Element Method in detail lies beyond the scope of this thesis. Nevertheless, basic ideas and notations will be highlighted and the effects of particularities of our model problems are presented.

Solving BVPs like (2.28) analytically is often too difficult. Instead, one tries to find a discrete solution of a corresponding *weak formulation*. The approximation of the (infinite dimensional) solution is described with a finite number of parameters, the so-called *degrees of freedom* (DOFs). The insertion of the approximated solution in the weak form finally generates a system of algebraic equations for the DOFs [95].

---

[1] For $\theta = 0.5$, unconditional stability is only guaranteed in the Euclidean norm. In the maximum norm, further conditions concerning space and time discretization have to be fulfilled [6].

Starting from a variational formulation of the classical problem like in (2.30), we apply Ritz-Galerkin's idea of replacing the infinite dimensional space of test functions respectively the set of feasible solutions V (here: $V = H^1(\Omega))^2$ by a finite dimensional subspace $V_h \subset V$:

$$V_h := \left\{ v_h \,:\, v_h(\mathbf{x}) = \sum_{j=1}^{N} v_j \, \varphi_j(\mathbf{x}) \right\}.$$

Note that the prescribed *ansatz functions* $\{\varphi_j\}_{j=1}^N$ represent a basis of V_h. Characteristic for the finite element method is to choose for V_h a function space consisting of piecewise polynomial functions. Thus, if T is approximated by

$$T \approx T_h = \sum_{j=1}^{N} T_j \, \varphi_j(\mathbf{x}),$$

we have to solve the following discrete problem w.r.t. the coefficients T_j, $j = 1, \dots, N$:

$$\boxed{\text{Find } T_h \in V_h \text{ such that } a(T_h, v_h) = b(v_h) \;\; \forall v_h \in V_h\,. \qquad (3.11)}$$

If $a(\cdot,\cdot)$ were a bilinear form, we could explicitly state the corresponding Galerkin system of our problem at this stage. Due to the nonlinearities in $a(\cdot,\cdot)$, caused by $\alpha(T)$, it is more complex. We examine the system of equations in detail later.

First, we note that for solving the system (3.11), it is of advantage to apply functions φ_j with a small local support

$$\operatorname{supp} \varphi_j := \overline{\{\mathbf{x} \in \Omega : \varphi_j(\mathbf{x}) \neq 0\}}.$$

It results in a sparse (stiffness) matrix and the entries of the matrix and right hand side can be evaluated element by element [71]. To this end, we divide the domain Ω into a finite number of subdomains respectively elements M (e.g. Figure 3.2 shows a triangulation of the cross section of an insulated single-core cable). Triangular and quadrilateral elements are usually used for two dimensional geometries, tetrahedrons, hexahedrons, prisms, or pyramids in three dimensions. The corresponding finite element mesh $\mathcal{M}_h$ consists of non-overlapping elements M such that the following conditions hold:

$$\overline{\Omega} = \bigcup_{M \in \mathcal{M}_h} \overline{M}, \; M_k \cap M_l = \emptyset \, \forall \, M_k, M_l \in \mathcal{M}_h, k \neq l.$$

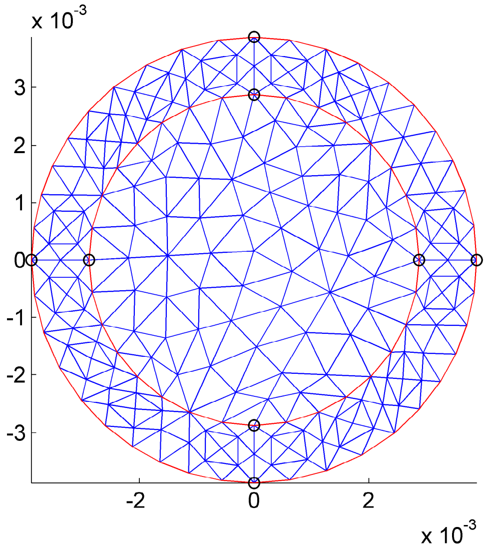

Fig. 3.2: *Triangulation of the cross section of an insulated single-core cable.*

In general, continuous, piecewise polynomial ansatz functions are applied which fulfil [77]:

---

[2] In general, the set of test functions and feasible solutions may be different. As in our model problem they are equal, we restrict to this special case.

1. φ_i is polynomial over each element and uniquely determined by its value at the nodes.
2. $\varphi_i(\mathbf{x}^{[j]}) = \delta_{ij}$.

Therein, $\mathbf{x}^{[j]}$ denotes the j-th node of the finite element mesh and δ_{ij} represents Kronecker's delta. The second property implies that the variable T_i corresponds to the value of T_h at node i:

$$T_h(\mathbf{x}^{[i]}) = \sum_{j=1}^{N} T_j\, \varphi_j(\mathbf{x}^{[i]}) = \sum_{j=1}^{N} T_j\, \delta_{ij} = T_i.$$

Throughout this work, we use linear or quadratic triangular Lagrange elements (cf. Figure 3.3 in two dimensions). In case of linear Lagrange elements, piecewise polynomials of first degree are used on mesh elements of the form depicted in Figure 3.3a; for quadratic Lagrange elements, piecewise polynomials of second degree are applied on mesh elements depicted in Figure 3.3b.

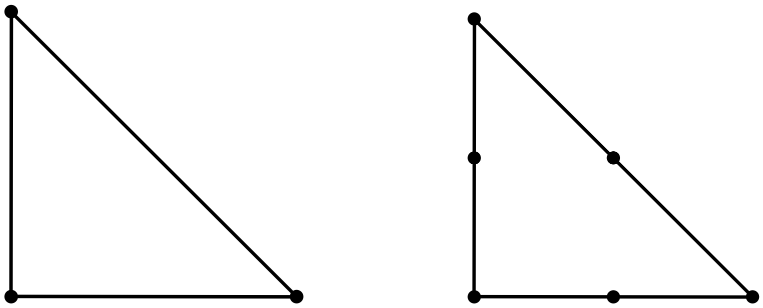

(a) Triangular Lagrange reference element of order 1.

(b) Triangular Lagrange reference element of order 2.

Fig. 3.3: *Triangular Lagrange reference elements of first and second order.*

For further details about the finite element method like numerical integration to evaluate matrices and right hand sides, mapping between local and global coordinates in mesh elements, assembling, isoparametric elements for curved shapes, convergence properties, etc., we refer to [11, 12, 47, 71, 77].

We return to the fact that $a(\cdot,\cdot)$ is not a bilinear form, but only linear in the second component. As mentioned, nonlinear problems are solved by application of iterative methods. Concretely, we use the Newton-Raphson method introduced in Section 3.2.2. As $\{\varphi_i\}_{i=1}^{N}$ represents a basis of V_h, it is sufficient to have one equation with test function φ_i in (3.11) for each basis function. Thus, we obtain a nonlinear system

$$F_i(T_1, \dots, T_N) = 0, \quad i = 1, \dots, N \tag{3.12}$$

with

$$\begin{aligned} F_i &= \int_\Omega \lambda\, \nabla\Big(\sum_{j=1}^{N} T_j\, \varphi_j\Big) \cdot \nabla\varphi_i - \tilde{c} \sum_{j=1}^{N} T_j\, \varphi_j\, \varphi_i \, \mathrm{d}\mathbf{x} + \int_{\Gamma^{\mathrm{ex}}} \tilde{\gamma}(T_h)\, \varphi_i \, \mathrm{d}\mathbf{s} - \int_\Omega \tilde{f}\, \varphi_i \, \mathrm{d}\mathbf{x} && (3.13) \\ &= \sum_{j=1}^{N} K_{ij} T_j - \tilde{c} \sum_{j=1}^{N} M_{ij} T_j + \int_{\Gamma^{\mathrm{ex}}} \tilde{\gamma}(T_h)\, \varphi_i \, \mathrm{d}\mathbf{s} - \int_\Omega \tilde{f}\, \varphi_i \, \mathrm{d}\mathbf{x}, && (3.14) \end{aligned}$$

where

$$\begin{aligned} K_{ij} &= \int\limits_{\Omega} \lambda \nabla\varphi_i \cdot \nabla\varphi_j \,\mathrm{d}\mathbf{x}\,, \\ M_{ij} &= \int\limits_{\Omega} \varphi_i\,\varphi_j \,\mathrm{d}\mathbf{x}. \end{aligned} \tag{3.15}$$

The matrix M_{ij} is often called the *mass matrix.* It is the objective to solve the equations $F_i = 0,\ i = 1, \dots, N$, w.r.t. the coefficients $T_1, \dots, T_N$. We denote $T_j^{(k)}$ the approximation of T_j in the k-th iteration of the Newton iteration, corresponding $T_h^{(k)}$ the approximation of T_h with

$$T_h^{(k)} = \sum_{j=1}^{N} T_j^{(k)}\,\varphi_j.$$

In each iteration, the (Newton) corrections $\delta\,T_1^{(k+1)}, \dots, \delta\,T_n^{(k+1)}$ are obtained by solving a linear system. When evaluating the Jacobian J_{ij} and $-F_i$ as indicated in Section 3.2.2, the previous iteration $(T_j^{(k)})$ is employed. The entries in the Jacobian are

$$\boxed{\begin{aligned} J_{ij} = \frac{\delta F_i}{\delta T_j} &= \int\limits_{\Omega} \lambda\,\nabla\varphi_i \cdot \nabla\varphi_j - \tilde{c}\,\varphi_i\,\varphi_j \,\mathrm{d}\mathbf{x} + \int\limits_{\Gamma^{\mathrm{ex}}} \frac{\mathrm{d}\tilde{\gamma}}{\mathrm{d}T_h}(T_h^{(k)})\,\frac{\mathrm{d}T_h}{\mathrm{d}T_j}\,\varphi_i \,\mathrm{d}\mathbf{x} \\ &= \int\limits_{\Omega} \lambda\,\nabla\varphi_i \cdot \nabla\varphi_j - \tilde{c}\,\varphi_i\,\varphi_j \,\mathrm{d}\mathbf{x} + \int\limits_{\Gamma^{\mathrm{ex}}} \frac{\mathrm{d}\tilde{\gamma}}{\mathrm{d}T_h}(T_h^{(k)})\,\varphi_i\,\varphi_j \,\mathrm{d}\mathbf{x}. \end{aligned}} \tag{3.16}$$

The formula for the right-hand side is simply $-F_i$ with T_h replaced by $T_h^{(k)}$. Obviously, J_{ij} is in each iteration a sparse, symmetric matrix due to $\frac{\partial F_i}{\partial T_j} = \frac{\partial F_j}{T_i}$ (cf. Figure 3.4). This is of great advantage for the solution of the linear system.

The application of finite elements within this work for two and three dimensional simulations is done with the help of COMSOL Multiphysics 3.5a and 4.1-4.3 [95]. With these commercial software tools, we can generate precise geometries via a graphical interface or Matlab scripts. Furthermore, it allows to automatically create meshes and adaptive refinements, to adjust nonlinear solvers (based on a modified Newton method [28]) as well as to choose different linear solvers. Various direct and iterative solvers are available within the programmes. As in all our simulations, there are less than one million DOFs and sufficient memory is available, we apply the direct solvers UMFPACK [24, 25] or PARDISO [48, 116].

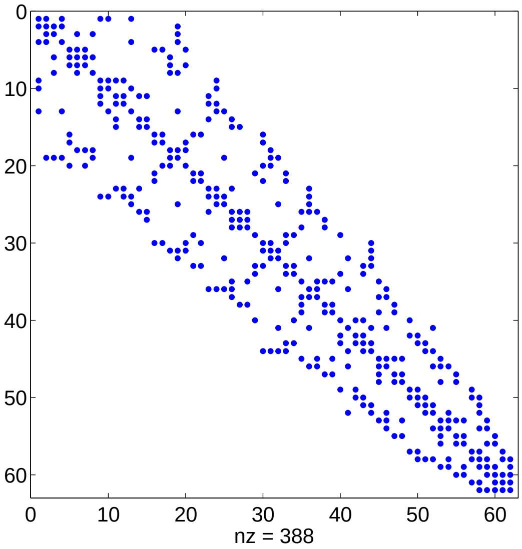

Fig. 3.4: *Sparsity pattern of a symmetric matrix with 388 non-zero elements, obtained in the Newton-Raphson iteration to perform the FE analysis for an insulated single-core cable.*

Solving time-dependent problems with FEM

In COMSOL Multiphysics, time-dependent problems like (2.29) are discretized via the vertical method of lines, mentioned in Section 3.3.1. We apply finite elements to the transient problem, which results in a system of ODEs. Multiplication of (2.29) by test functions $\{\varphi_i\}_{i=1}^N$, integration over Ω, application of integration by parts and approximation of T by T_h with

$$T(\mathbf{x},t) \approx T_h(t) = \sum_{j=1}^{N} T_j(t)\,\varphi_j(\mathbf{x})$$

yields, analogously to the stationary case, a *system of spatially discretized and time-dependent equations:*

$$\boxed{\gamma \sum_{j=1}^{N} M_{ij}\dot{T}_j(t) = \sum_{j=1}^{N} K_{ij}T_j(t) - \tilde{c}\sum_{j=1}^{N} M_{ij}T_j(t) + \int\limits_{\Gamma^{\mathrm{ex}}} \tilde{\gamma}(T_h(t))\,\varphi_i \,\mathrm{d}\mathbf{s} - \int\limits_{\Omega} \tilde{f}\,\varphi_i \,\mathrm{d}\mathbf{x}, \quad i = 1,\dots,N \qquad (3.17)}$$

Therein, the matrices M_{ij} and K_{ij} are defined identically as in (3.15) and we denote $\dot{T}_j(t)$ the derivative of function T_j to t.

Now, we can either continue with discretization by the θ-rule and afterwards solve a completely algebraic systems, or apply other methods for the solution of ODEs. In COMSOL, the two solvers IDA[3] [14, 56] and generalized-α [16, 70] are available. IDA uses backward differentiation formulas (BDF), whereas generalized-α is an implicit, second-order method. Throughout this work, we apply IDA coupled with the Newton-Raphson method.

---

[3] Implicit differential-algebraic solver.

4 Optimization

Optimization of components, especially of cable bundles, is a main subject of this thesis. Thus, we give a short overview of optimization by mathematical means. This includes the presentation of *shape optimization* and *genetic algorithms*.

4.1 General Optimization Problem

Most (mathematical) optimization problems can be formulated as special case of the following *general optimization problem*[1] [42]:

Definition 4. (General optimization problem)
Let $\mathbf{X}$ *be an arbitrary set and* $\mathbf{K_1} \subseteq \mathbf{X}$*,* $f : \mathbf{X} \to \mathbb{R}$ *a functional,* $\mathbf{Z}$ *an arbitrary set and* $\mathbf{K_2} \subseteq \mathbf{Z}$*,* $\mathbf{g} : \mathbf{X} \to \mathbf{Z}$ *a mapping. An optimization problem for the data is given by*

$$\boxed{\begin{aligned} &\underset{\mathbf{x}}{\textit{Minimize}} && f(\mathbf{x}) \\ &\textit{subject to} && \mathbf{x} \in \mathbf{K_1}, \;\; \mathbf{g}(\mathbf{x}) \in \mathbf{K_2}. \end{aligned}} \tag{4.1}$$

In (4.1), the function f is called *objective function*, the mapping $\mathbf{g}$ *mapping of restrictions*, the condition $\mathbf{x} \in \mathbf{K_1}$ *implicit restriction* or *restriction set* and the restriction $\mathbf{g}(\mathbf{x}) \in \mathbf{K_2}$ *explicit restriction.* The set

$$\mathbf{S} := \{\mathbf{x} \in \mathbf{X} \,:\, \mathbf{x} \in \mathbf{K_1},\, \mathbf{g}(\mathbf{x}) \in \mathbf{K_2}\}$$

is called *feasible set.* Each $\mathbf{x} \in \mathbf{S}$ corresponds to a *feasible solution.* Furthermore, we call

$$w := \inf\,\{f(\mathbf{x}) \,:\, \mathbf{x} \in \mathbf{K_1},\, \mathbf{g}(\mathbf{x}) \in \mathbf{K_2}\}$$

minimum value of the problem and $\mathbf{x}^*$ *optimal solution*, if $\mathbf{x}^*$ is feasible and

$$\begin{aligned} f(\mathbf{x}^*) &= \inf\{f(\mathbf{x}) \,:\, \mathbf{x} \in \mathbf{K_1},\, \mathbf{g}(\mathbf{x}) \in \mathbf{K_2}\} \\ &= \min\{f(\mathbf{x}) \,:\, \mathbf{x} \in \mathbf{K_1},\, \mathbf{g}(\mathbf{x}) \in \mathbf{K_2}\}. \end{aligned}$$

There exist various types of optimization problems summarized in (4.1), e.g. shape optimization problems (cf. Section 4.2), as well as a great number of optimization methods. In general, we distinguish between gradient based and non-gradient based strategies. Basics for gradient based shape optimization are introduced in Section 4.2 and a general non-gradient based strategy via a genetic algorithm is explained in Section 4.3.

---

[1] We restrict to minimization problems. Maximization problems can be transformed to equivalent minimization problems by multiplying f with -1.

4.2 Shape Optimization

A part of the important branch of computational mechanics called *structural optimization* is shape optimization. It is the objective of structural optimization problems to improve the behaviour of a structure until optimal (desired) properties are achieved [52].

A general shape optimization problem looks as follows:

$$\boxed{\begin{aligned} &\underset{\Omega\in\mathcal{O}_{\mathrm{ad}}}{\text{Minimize}} \quad J\left(\Omega\right) = \int\limits_{\Omega} j_1\big(\mathbf{x}, T\left(\mathbf{x}\right), \nabla T\left(\mathbf{x}\right)\big)\,\mathrm{d}\mathbf{x} + \int\limits_{\Gamma} j_2\big(\mathbf{x}, T\left(\mathbf{x}\right), \nabla T\left(\mathbf{x}\right)\big)\,\mathrm{d}\sigma \\ &\text{subject to} \quad \mathcal{A}T = f_1 \ \text{ in } \ \Omega, \quad \mathcal{B}T = f_2 \ \text{ on } \ \Gamma. \end{aligned}} \tag{4.2}$$

Herein, the functional J represents the function to be optimized, dependent on the domain Ω which is contained in the set of admissible domains $\mathcal{O}_{\mathrm{ad}}$. The function $T : \Omega \to \mathbb{R}$ is the solution to the PDE with the (second order) differential operator $\mathcal{A}$ and the boundary condition described by the operator $\mathcal{B}$. The functions $j_1, j_2 : D\times\mathbb{R}\times\mathbb{R}^n \to \mathbb{R}$, $f_1, f_2 : D \to \mathbb{R}$ are sufficiently smooth, and the set $D \subseteq \mathbb{R}^n$ is called the holdall which is assumed to always contain the (varying) domain Ω. For a general overview on shape calculus, we refer the reader to [26, 109, 122].

As the roots of the gradient of the objective function J taken to zero yield stationary points and thus candidates for local minima, we have to determine the corresponding gradient. In order to compute the derivative of a function with respect to the geometry, we apply the *perturbation of identity* [98]. A bounded reference domain Ω_{ref} is fixed and $\Omega \in \mathcal{O}_{\mathrm{ad}}$ correspond to transformations of Ω_{ref}.

For a smooth perturbation field $\mathbf{V} : D \to \mathbb{R}^n$, we consider the perturbed domain

$$\Omega_\epsilon[\mathbf{V}] := \{\mathbf{x} + \epsilon\mathbf{V}(\mathbf{x}) : \mathbf{x} \in \Omega\},$$

with $\epsilon > 0$ sufficiently small [98] (cf. Figure 4.1). This enables the definition of the *shape derivative* of the shape functional J at Ω in direction of a vector field $\mathbf{V}$ by

$$\delta J(\Omega)\left[\mathbf{V}\right] := \lim_{\epsilon\to 0} \frac{J\left(\Omega_\epsilon\left[\mathbf{V}\right]\right) - J\left(\Omega\right)}{\epsilon}. \tag{4.3}$$

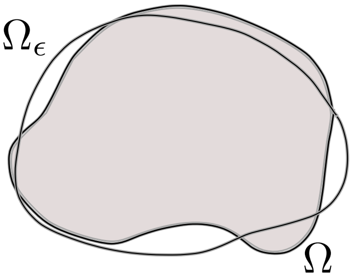

Fig. 4.1: *An arbitrary domain Ω and a corresponding perturbed domain Ω_ϵ.*

The shape functional J is shape differentiable at Ω, if the Eulerian derivative $\delta J(\Omega)\left[\mathbf{V}\right]$ exists for all directions $\mathbf{V}$ and the mapping $\mathbf{V} \mapsto \delta J(\Omega)\left[\mathbf{V}\right]$ is linear and continuous. In the following, we abbreviate the scalar product in $\mathbb{R}^n$ by $\langle\cdot,\cdot\rangle$. To compute the shape derivative efficiently, we state the Hadamard-Zolésio structure theorem [26, 117, 122]:

Theorem 5 (Hadamard-Zolésio structure theorem)**.** *Let J be shape differentiable according to definition (4.3) and $\Gamma \in C^{k+1}$, $k \geq 0$. Then, the relation*

$$\delta J(\Omega)[\mathbf{V}] = \delta J(\Gamma)\left[\langle \mathbf{V}, \mathbf{n}\rangle \, \mathbf{n}\right]$$

holds for all vector fields $\mathbf{V} \in C^k(\bar{D}; \mathbb{R}^n)$.

Proof. Cf. [122], proposition 2.26, pages 59–60. ☐

In the following, we explain the notation $\delta J(\Gamma)\left[\langle \mathbf{V}, \mathbf{n}\rangle \, \mathbf{n}\right]$, with $\mathcal{D}^{-k}(\cdot)$ the function space of scalar distributions:

Remark 6. *In reference [122], the Hadamard-Zolésio theorem actually states the existence of a scalar distribution*

$$g(\Gamma) \in \mathcal{D}^{-k}(\Gamma),$$

such that the shape gradient $G(\Omega) \in \mathcal{D}^{-k}(\Omega, \mathbb{R}^n)$ is given by

$$G(\Omega) = \gamma_\Gamma^*(g \cdot \mathbf{n}),$$

where γ_Γ^* is the adjoint of the trace operator on Γ. Here, however, it is always assumed that $G(\Omega)$ is an integrable function, i.e. Ω has piecewise smooth boundaries. Then, the shape gradient g is much more conveniently expressed by

$$\delta J(\Omega)[\mathbf{V}] = \int\limits_\Gamma \langle \mathbf{V}, \mathbf{n}\rangle \, g \, d\sigma.$$

Furthermore, we shall introduce the local shape derivative $\delta T = \delta T[\mathbf{V}]$ that describes the sensitivity of the PDE solution with respect to domain variations. It is defined pointwise by

$$\delta T[\mathbf{V}](\mathbf{x}) := \lim_{\epsilon \to 0} \frac{T_\epsilon(\mathbf{x}) - T(\mathbf{x})}{\epsilon}, \quad \mathbf{x} \in \Omega \cap \Omega_\epsilon,$$

with the solution of the boundary value problem on the perturbed domain denoted by T_ϵ.

The local shape derivative $\delta T = \delta T[\mathbf{V}]$ and the shape gradient $\delta J(\Omega)\,[\mathbf{V}]$ are essential for the sensitivity analysis of the problem of an optimal multicable in Section 7.6.3.

4.3 Genetic Algorithm

A certain class of optimization methods is summarized in the term *genetic algorithm*. We describe how a genetic algorithm generally works, based on [52, 53, 92].

A genetic algorithm is a stochastic method that can be used to approximately solve optimization problems, e.g. to find a function's minimum. However, it is not as precise as a gradient based method, as it does not study the function to be minimized. It only evaluates the function for a given number of optimization variable values (individuals).

The algorithm employs the concept of natural evolution (cf. Figure 4.2): an initial population of individuals evolves in several generations, using the simulated genetic operations *crossover* and *mutation*, which let the fittest individuals survive and reproduce. The initial population is made up of the M individuals, obtained e.g. via specific heuristics, and can be completed by random individuals.

We evaluate the fitness (i.e. the value of the corresponding objective function) of each individual in order to determine which individuals are the 'better' ones. To simulate the transition from one generation to the next, we use the following steps:

- The reproduction is subject to the fitness: the k best individuals are directly transmitted to the next generation as *elite* and the parents are selected stochastically or by a certain strategy in the current population.
- Some parents are *crossed* and *mutated* to produce the 'children'.
- The new population replaces the old one.

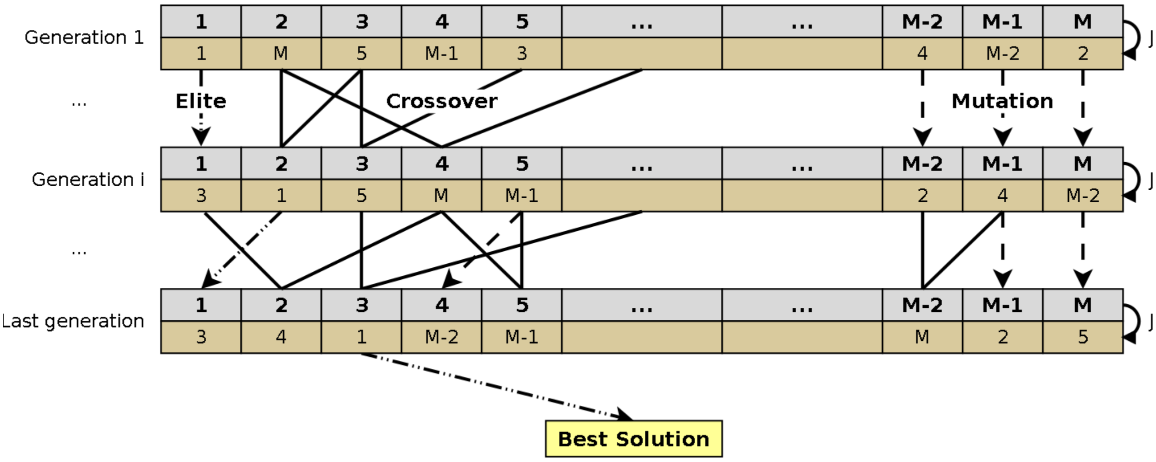

Fig. 4.2: *Diagram of the general procedure of a genetic algorithm.*

Crossover

Crossover children are created by combining a pair of parents: we randomly select components from both parents (here: p_1 and p_2) and create the child (here: k) with these components. For example, for two parents

$$p_1 = [1, 2, 3, 4, 5, 6, 7]$$
$$p_2 = [a, b, c, d, e, f, g],$$

one child could be

$$k = [1, 2, c, 4, e, f, 7].$$

Mutation

Mutation children are created by randomly modifying a certain number of components of the parent. We pick some components of the parent and take the average of these components with a random number r_i. For example, a mutation of

$$p = [a, b, c, d, e, f, g] \quad \text{could be} \quad k = \left[a, \frac{b + r_1}{2}, c, d, \frac{e + r_2}{2}, \frac{f + r_3}{2}, g\right].$$

Each created individual (by crossover or mutation) has to be tested to ensure that it respects the constraints of the optimization problem. If however it does not, we have to modify it until it respects the given criteria, or if adaptation fails, the non-conform individual is erased and a new one is created.

Stopping criterion

Since there is no natural stopping criterion for this algorithm, it is interrupted in general either after a certain number of generations or if there is no improvement in the fitness of the best individual in the population for several steps.

5 Insulated Single-Core Cables

Our first application considered in the context of Joule heating of connecting structures is an insulated single-core cable. We show the principles of our calculations of temperature in cables, using problem specific approaches and validate those by finite elements and measurements. In all following chapters, we present computations of temperatures that refer to those of insulated single-core cables. In case of shielded cables and cable bundles, the computational models are reduced to that of an insulated single-core cable, in case of current bars and fuses, single cables are attached and thus, they have a direct impact on the heat distribution in the devices.

5.1 Problem Formulation

Since cables are often quite long such that the ratio length to diameter of the cable is huge, we suppose the cable to have infinite length with equal heat distribution in each cross section. Hence, we neglect temperature differences in axial direction. This enables a reduction to a two dimensional problem.

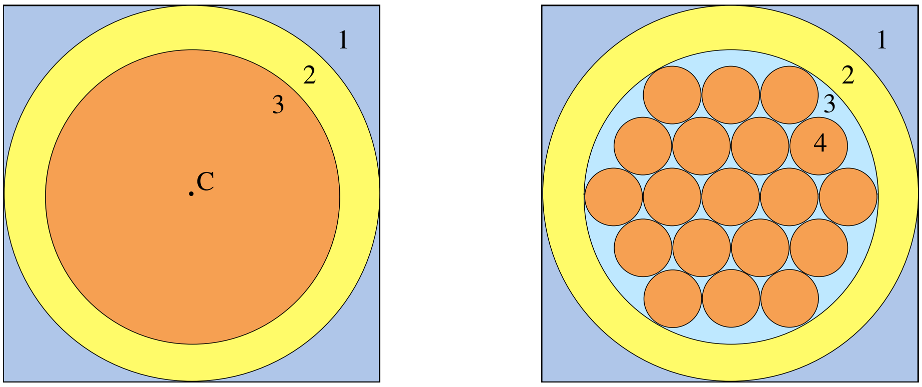

(a) Insulated single-core cable with a massive core.

(b) Insulated single-core cable consisting of several conductors.

Fig. 5.1: *Massive and composed cross sections of insulated single-core cables.*

In Figure 5.1, two cross sections of insulated single-core cables are depicted. On the left, there is an insulated cable with a massive cable core, on the right, the cable core consists of several metallic conductors of the same diameter. By introducing a filling factor β_f that indicates the ratio of the sum of conductor cross sectional areas to the cross sectional area of the entire core, we transform a cable of n_c conductors into a cable with a massive core. Hence, the cable on the left can be interpreted to have a filling factor $\beta_f = 100\,\%$, consisting of $n_c = 1$ conductor.

Throughout this thesis, we index quantities specific to cables from exterior to interior in ascending order, starting with '1' for the ambience and '2' for the exterior insulation. In case of a massive cable core, '3' represents the core, whereas for cables consisting of several conductors, '3' denotes the area between the conductors (air or a solid insulation material) and '4' the conductors themselves. Index '0' is always used for the reference temperature T_0 that has a standard value of 20 °C.

It is the objective of this chapter to provide formulas to calculate temperatures in the cable core and in the insulation. We suppose the insulated cable to be suspended in free air and the current to be equally distributed in the core. Possible imbalances of the current distribution – e.g. by the skin effect [75] – that occur frequently in the high voltage area, especially for alternating currents, are not respected. Thus, we assume the heat distribution to be rotationally symmetric, which allows a further reduction of the problem to only one dimension. In fact, it is even sufficient to determine the temperatures T_2 at the exterior insulation boundary respectively T_3 at the interface of cable core and insulation. Cables must not exceed the melting point of the insulation material and the temperature in the insulation normally decreases for larger distances from the centre of the cable. Hence, the most interesting quantity for cable manufacturers concerning thermal loads is the temperature T_3 which normally represents the hottest one in the entire insulation. As the heat conductivity of the core is huge, the temperature profile in the core can be considered as approximately constant. The ambient temperature T_1 is given, so we determine T_2 and T_3 dependent on the parameters

- electric current I,
- heat conductivities λ_2, λ_3,
- diameters d_2, d_3,
- electrical resistivities ρ_3, $\rho_{0,3}$,[1]
- linear temperature coefficient of electrical resistivity α_ρ,
- specific heat capacities γ_2, γ_3 per volume (solely transient case).

Note that like in (2.6), the temperature dependency of the electrical resistivity is linearly approximated by

$$\rho_3 = \rho_{0,3}\left(1 + \alpha_\rho\left(T_3 - T_0\right)\right). \tag{5.1}$$

For the transformation of a cable with core consisting of n_c conductors into a massive one, we additionally introduce the heat conductivity λ_4, the diameter d_4, the specific heat capacity γ_4 per volume and the electric resistivities ρ_4 respectively $\rho_{0,4}$ of each of the (equal) conductors. At first, we restrict to the stationary case, secondly, we apply an interpolative recursive scheme for transient computations.

Transformation of a Composed to a Massive Cable Core

As mentioned, the cable core consists in most cases of several metallic conductors to guarantee a better mechanical flexibility. The rest of the core is filled with air or solid insulation material. We define a physical cross sectional area A_3^{ph} and a geometrical cross sectional area A_3^{ge} of the core by

$$A_3^{\mathrm{ph}} := n_c\,(\frac{d_4}{2})^2\,\pi, \quad A_3^{\mathrm{ge}} := (\frac{d_3}{2})^2\,\pi. \tag{5.2}$$

---

[1] In spite of the electrical resistivity ρ, we sometimes indicate the electric conductivity κ. It is converted one to another by $\rho = 1/\kappa$.

Thus, we introduce the filling factor [67]

$$\beta_f := \frac{A_3^{\mathrm{ph}}}{A_3^{\mathrm{ge}}} = n_c \, (\frac{d_4}{d_3})^2, \tag{5.3}$$

that indicates a measure for the packing density of the cable core.

In the problems (2.28) and (2.29), the filling factor has an influence on the squared current density $(I/A_3)^2$ and the heat conductivity λ_3 of the core. We replace A_3^2 in the current density term by $A_3^{\mathrm{ph}} \cdot A_3^{\mathrm{ge}}$. In the derivation of this term, the cross sectional area refers in one case to the area A_3^{ph} carrying electric current, in the other case to the area A_3^{ge} conducting heat. Furthermore, we apply an appropriate heat conductivity of the core (including air gaps) by

$$\lambda_3 = \beta_f \, \lambda_4 + (1 - \beta_f) \, \lambda_{\mathrm{air}}, \tag{5.4}$$

with λ_{air} denoting the heat conductivity of the air gaps[2]. In case of transient considerations, we propose to neglect the influence of air on the specific heat capacity γ_3 per volume of the core and to restrict to the solid part.

Since the filling factor of insulated single-core cables is usually large ($\geq 75\,\%$), we do not always state it explicitly. To keep the notation easier, we generally use the variable A_3 for the physical cross sectional area of the cable.

5.2 Heat Power Balance Approach

Based on Equation (2.1), we establish heat power balances for insulated single-core cables and derive formulas to compute temperatures at essential points for the stationary and non-stationary case.

5.2.1 Stationary Computations

At first, we state formulas for temperatures in the cable for the stationary case that are solved by a fixed point iteration. Its convergence is ensured under certain conditions, specified in the following section. Finally, we provide an algorithm to create a diagram indicating how intensively a cable may be loaded with electric currents for given ambient temperatures and a maximum temperature of the insulation.

In the stationary case, the rate of change of energy $\Delta E_{st} = 0$ vanishes. Consequently, by cancelling out Δt for the remaining terms, the energy balance is equivalent to the heat power balance

$$P_{\mathrm{in}} + P_{\mathrm{g}} = P_{\mathrm{out}}, \tag{5.5}$$

with heat power P_{in} entering into, heat power P_{out} emitted from and heat power P_{g} generated in the system. First, we derive formulas for the temperature T_2, stating a heat power balance for the cross section of the entire cable at the exterior insulation boundary. The heat power emitted via the surface on a reference length ℓ reads as

$$P_{out} = \alpha(T_2) \, d_2 \, \pi \, (T_2 - T_1) \, \ell. \tag{5.6}$$

Since the outer surface is part of the insulation and consequently does not carry any current, $P_g = 0$ applies inhere for the generated heat power. Furthermore, the heat power entering

---

[2] For solid insulation material between the conductors instead of air, a corresponding heat conductivity for the filling material has to be applied.

each insulation ring around the centre C of the cable (cf. Figure 5.1) and thus the exterior insulation boundary, is equal to the heat power generated in the core

$$P_{in} = R\, I^2 = \rho_3 \frac{\ell}{A_3} I^2 = \rho_{0,3}\, (1 + \alpha_\rho\, (T_3 - T_0)) \frac{\ell}{A_3}\, I^2. \tag{5.7}$$

Replacing the heat power terms in (5.5) by (5.6) respectively (5.7) and reorganizing yields the implicit equation

$$T_2 = T_1 + \frac{\rho_{0,3}\, (1 + \alpha_\rho\, (T_3 - T_0))\, I^2}{\pi\, A_3\, \alpha(T_2)\, d_2}. \tag{5.8}$$

If we consider an arbitrary circle inside the insulation around the cable centre C, there applies $P_g = 0$ for the generated heat. Moreover, according to Fourier's law, for the heat power entering the considered surface in the insulation at distance s from the cable centre C by conduction, it holds

$$P_{in} = -2\, s\, \pi\, \ell\, \lambda_2 \frac{\mathrm{d}T}{\mathrm{d}s}. \tag{5.9}$$

Reorganizing, replacing P_{in} by (5.7) and integrating both sides from $d_3/2$ to $d_2/2$ provides

$$\int\limits_{d_3/2}^{d_2/2} \frac{\mathrm{d}T}{\mathrm{d}s}\, \mathrm{d}s = -\int\limits_{d_3/2}^{d_2/2} \frac{\rho_{0,3}\, \left(1 + \alpha_\rho\, (T_3 - T_0)\right)\, I^2}{2\, \lambda_2\, \pi\, A_3\, s}\, \mathrm{d}s = -\Big[\frac{\rho_{0,3}\, \left(1 + \alpha_\rho\, (T_3 - T_0)\right)\, I^2}{2\, \lambda_2\, \pi\, A_3} \ln s\Big]_{d_3/2}^{d_2/2}. \tag{5.10}$$

Finally, we obtain

$$T_3 = T_2 + \frac{\rho_{0,3}\, \left(1 + \alpha_\rho\, (T_3 - T_0)\right)\, I^2}{2\, \lambda_2\, \pi\, A_3} \ln(d_2/d_3). \tag{5.11}$$

We summarize the nonlinear system for the determination of T_2 and T_3 by

$$\boxed{\begin{aligned} T_2 &= T_1 + \frac{\rho_{0,3}\, (1 + \alpha_\rho\, (T_3 - T_0))\, I^2}{\pi\, A_3\, \alpha(T_2)\, d_2}, \\ T_3 &= T_2 + \frac{\rho_{0,3}\, \left(1 + \alpha_\rho\, (T_3 - T_0)\right)\, I^2}{2\, \lambda_2\, \pi\, A_3} \ln(d_2/d_3). \end{aligned}} \tag{5.12}$$

Fixed Point Iteration for the Computation of Characteristic Temperatures

In order to determine the temperatures $\mathcal{T} = (T_2, T_3)^t$ by a vector valued fixed point iteration, we define the temperature mapping $\mathbf{h} \in C^1(\mathbb{R}^2, \mathbb{R}^2)$ by

$$\mathbf{h}(\mathcal{T}) := \left(\begin{array}{c} T_1 + \frac{\rho_{0,3}\, (1+\alpha_\rho\, (T_3 - T_0))\, I^2}{\pi\, A_3\, \alpha(T_2)\, d_2}, \\ \\ T_2 + \frac{\rho_{0,3}\, (1+\alpha_\rho\, (T_3 - T_0))\, I^2}{2\, \lambda_2\, \pi\, A_3} \ln(d_2/d_3) \end{array} \right), \tag{5.13}$$

with corresponding Jacobian $\nabla\mathbf{h} = (\mathbf{h}_{uv})_{1 \le u,v \le 2}$ and $\mathbf{h}_{uv}(\mathcal{T}) = \frac{\partial\, \mathbf{h}_u(\mathcal{T})}{\partial\, \mathcal{T}_v}$. Furthermore, we set the iterative sequence $(\mathcal{T}^{(i)})_{i \in \mathbb{N}}$ by

$$\mathcal{T}^{(i+1)} = \mathbf{h}\left(\mathcal{T}^{(i)}\right) \tag{5.14}$$

with $\mathcal{T}^{(i)} = \left((T_2)^{(i)}, (T_3)^{(i)}\right)^t$, the matrix norm $\|\nabla\mathbf{h}(\mathcal{T})\| := \sup\limits_{\mathbf{x} \in \mathbb{R}^2 \setminus \{0\}} \frac{|\nabla\mathbf{h}(\mathcal{T}) \cdot \mathbf{x}|}{|\mathbf{x}|}$ and apply a variant of Banach's fixed point theorem.

Theorem 7. *Suppose that* $q := \sup\limits_{\mathcal{T}^{(1)},\mathcal{T}^{(2)}\in\mathbb{R}^2} \left\| \int\limits_0^1 \nabla\mathbf{h}(\mathcal{T}^{(1)} + s\,(\mathcal{T}^{(2)} - \mathcal{T}^{(1)}))\,ds \right\| < 1\,.$ *Then, the following assertions hold:*

1. *There exists a unique solution* $\mathcal{T}^* \in \mathbb{R}^2$ *of* $\mathbf{h}(\mathcal{T}) = \mathcal{T}$*.*
2. *For every initial vector* $\mathcal{T}^{(1)} \in \mathbb{R}^2$*, the recursively defined sequence* $\mathcal{T}^{(i+1)} = \mathbf{h}(\mathcal{T}^{(i)})$*,* $i \in \mathbb{N}$*, converges to the solution* $\mathcal{T}^*$ *with the following rate of convergence:*

$$\left|\mathcal{T}^{(i)} - \mathcal{T}^*\right| \le \frac{q^i}{1-q}\left|\mathcal{T}^{(2)} - \mathcal{T}^{(1)}\right|.$$

Proof. The Mean Value Theorem for vector valued mappings implies

$$\mathbf{h}(\mathcal{T}^{(2)}) - \mathbf{h}(\mathcal{T}^{(1)}) = \left(\int\limits_0^1 \nabla\mathbf{h}(\mathcal{T}^{(1)} + s\,(\mathcal{T}^{(2)} - \mathcal{T}^{(1)}))\,\mathrm{d}s\right)\cdot(\mathcal{T}^{(2)} - \mathcal{T}^{(1)})$$

and application of the Cauchy-Schwarz inequality yields

$$\left|\mathbf{h}(\mathcal{T}^{(2)}) - \mathbf{h}(\mathcal{T}^{(1)})\right| \le q\left|\mathcal{T}^{(2)} - \mathcal{T}^{(1)}\right|.$$

Thus, with $q < 1$, the assertions follow by Banach's fixed point theorem. □

At this stage, two difficulties remain. We have to identify q with physical quantities and have to examine, when the condition $q < 1$ holds. To this end, we provide a sufficient condition for the convergence of $(\mathcal{T}^{(n)})_{n\in\mathbb{N}}$ in physical terms and determine an upper bound for the constant of contraction q, depending explicitly on the essential quantities.

Let $T_{\min}$ and $T_{\max}$ denote lower and upper bounds for the temperatures in the insulated cable, set a priori. We truncate the heat transfer coefficient α by (2.31) with $T_l = T_{\min}$ and P_{in} in (5.7) at $T_3 = T_{\max}$ with the upper bound $P_{in}(T_{\max})$. Using these quantities for the fixed point mapping $\mathbf{h}$ in (5.13), we obtain

Proposition 8. *If* $\frac{\rho_{0,3}\,\alpha_\rho\,I^2}{A_3} < \pi\,d_2\,\alpha_l$*, the mapping* $\mathbf{h}$ *is contractive with the constant of contraction*

$$q = \frac{\rho_{0,3}\,\alpha_\rho\,I^2}{\pi\,A_3\,\alpha_l\,d_2}. \tag{5.15}$$

Proof. We define an auxiliary fixed point mapping

$$\bar{\mathbf{h}}(\mathcal{T}) := \begin{pmatrix} T_1 + \frac{\rho_{0,3}\,(1+\alpha_\rho\,(T_3-T_0))\,I^2}{\pi\,A_3\,\alpha(T_{\min})\,d_2}, \\ T_2 + \frac{\rho_{0,3}\,(1+\alpha_\rho\,(T_{\max}-T_0))\,I^2}{2\,\lambda_2\,\pi\,A_3}\ln(d_2/d_3) \end{pmatrix} \tag{5.16}$$

which provides an upper bound on the Lipschitz constant of $\mathbf{h}$.[3] In the first component, we replace $\alpha(T_2)$ by the smallest heat transfer coefficient $\alpha_l = \alpha(T_{\min})$, in the second, we evaluate the heat power term P_{in} for $T_3 = T_{\max}$. Due to the monotonicity of P_{in} in T_3 and

---

[3] Note that at this point, a rigorous justification is outstanding. We give a sketch of the plausibility of our Proposition.

α in T_2, these replacements yield a larger iterative rise of the components of $\bar{\mathbf{h}}$. Hence, for $\bar{q} := \sup\limits_{\mathcal{T}^{(1)},\mathcal{T}^{(2)} \in \mathbb{R}^2} \left\| \int\limits_0^1 \nabla\bar{\mathbf{h}}(\mathcal{T}^{(1)} + s\,(\mathcal{T}^{(2)} - \mathcal{T}^{(1)}))\,\mathrm{d}s \right\|$, there holds $q \leq \bar{q}$.

The definition of $\bar{\mathbf{h}}$ in (5.16) implies

$$\nabla\bar{\mathbf{h}} = \begin{pmatrix} 0 & C_{\bar{h}} \\ 1 & 0 \end{pmatrix} \quad \text{with} \quad C_{\bar{h}} = \frac{\rho_{0,3}\,\alpha_\rho\,I^2}{\pi\,A_3\,\alpha_l\,d_2}.$$

Observe that $\nabla\bar{\mathbf{h}}$ is constant and diagonalizable. The eigenvalues of $\nabla\bar{\mathbf{h}}$ are $\lambda_{1,2} = \pm\sqrt{C_{\bar{h}}}$ and there holds $\mathbb{R}^2 = E_{\lambda_1} \oplus E_{\lambda_2}$, with E_λ the eigenspace to the eigenvalue λ. Consequently, each vector $\mathbf{x} \in \mathbb{R}^2 \setminus \{0\}$ represents an eigenvector, either belonging to λ_1 or λ_2. Thus, we obtain

$$\bar{q} = \|\nabla\mathbf{h}(\mathcal{T})\| = \sup_{\mathbf{x}\in\mathbb{R}^2\setminus\{0\}} \frac{|\nabla\mathbf{h}(\mathcal{T})\,\cdot\,\mathbf{x}|}{|\mathbf{x}|} = \max_{\lambda\in\{\lambda_1,\lambda_2\}} \frac{|\lambda\cdot x|}{|x|} = \max_{\lambda\in\{\lambda_1,\lambda_2\}} |\lambda| = \lambda_1.$$

Consequently, the constant of contraction $\bar{q}$ is given by the largest eigenvalue of $\nabla\bar{\mathbf{h}}$, which reads as $\bar{q} = \sqrt{C_{\bar{h}}}$. Identifying q with the upper bound $\bar{q}$ yields the result. ☐

The sufficient condition for the contractivity of $\mathbf{h}$ in Proposition 8 is already implied by the subresonance condition (2.32):

Proposition 9. *Suppose that the subresonance condition (2.32) is fulfilled. Then there holds $q < 1$, i.e. the fixed point iteration in Theorem 7 converges to the unique solution $\mathcal{T}^*$ of $\mathbf{h}(\mathcal{T}) = \mathcal{T}$.*

Proof. The subresonance condition (2.32) applied to an insulated single-core cable reads as $\frac{\rho_{0,3}\,\alpha_\rho\,I^2}{A_3\,A_3^{\mathrm{ge}}} < \frac{\alpha_l}{d_2}$ and the contractivity of $\mathbf{h}$ is ensured by $\frac{\rho_{0,3}\,\alpha_\rho\,I^2}{\pi\,A_3\,d_2^2} < \frac{\alpha_l}{d_2}$. Since $d_2^2\,\pi = 4\,A_2 > A_3^{\mathrm{ge}}$, there holds

$$\frac{\rho_{0,3}\,\alpha_\rho\,I^2}{\pi\,A_3\,d_2^2} < \frac{\rho_{0,3}\,\alpha_\rho\,I^2}{A_3\,A_3^{\mathrm{ge}}} < \frac{\alpha_l}{d_2},$$

which implies the assertion. ☐

Remark 10. *For applications, it makes sense to set $T_{min} = T_1$ and $T_{max} \leq 200\,°\mathrm{C}$ because the cables normally are at least as hot as the environment and insulation parts do not sustain temperatures higher than $200\,°\mathrm{C}$.*

Determination of an Ambient Temperature versus Current Diagram

Car manufacturers are often interested in knowing how intensely cables may be loaded for different ambient temperatures or inversely, which ambient temperatures are acceptable for given currents. To this purpose, cables are characterized by a curve illustrating ambient temperatures versus electric current loads, the T_1-I-diagram. In contrast to the task in (5.12), the temperature T_3 in the core, which then corresponds to the maximum temperature the cable can endure, is fixed. Normally, it is set slightly below the melting point of the insulation. We provide a simple algorithm for the determination of the T_1-I-curve.

Rearranging Equation (5.11) yields

$$\frac{\rho_{0,3}\,(1+\alpha_\rho\,(T_3-T_0))\,I^2}{\pi\,A_3}=\frac{(T_3-T_2)\,2\,\lambda_2}{\ln\left(d_2/d_3\right)}, \tag{5.17}$$

and replacing the left hand side in (5.17) by the corresponding term in equation (5.8) provides

$$T_1=T_2-\frac{(T_3-T_2)\,2\,\lambda_2}{\ln\left(d_2/d_3\right)\alpha(T_2,T_1)\,d_2}. \tag{5.18}$$

Note that Equation (5.18) is implicit for the determination of T_1 because the heat transfer coefficient α depends on the ambient temperature. To emphasize this, we exceptionally mention this dependency explicitly in (5.18).

Solving the fixed point equation (5.18) is essential to obtain the T_1-I-curve of a given cable type in the current interval $\mathcal{I} := [I_{min}, I_{max}]$ with $\mathcal{T}_1 := [T_1(I_{min}), T_1(I_{max})]$:

```
Algorithm 3
(* DetermineT1IDiagram *)
Input: $\mathcal{I}$, $T_3$, $n_d$
Output: $T_1$-$I$-diagram
1. Discretize $\mathcal{I}$ equidistantly in $n_d$ points to obtain the set of currents $\mathcal{I}_d$.
2. for $I_j \in \mathcal{I}_d$
3.         Determine $(T_2)_j$ by solving Equation (5.11).
4.         Solve the fixed point equation (5.18) iteratively to obtain $(T_1)_j$.
5. Interpolate between the values $(I_j, (T_1)_j)$, $j = 1, \ldots, n_d$.
```

Application of Algorithm 3 with melting temperature $T_{\mathrm{melt}} = T_3 = 120\,^\circ\mathrm{C}$ of the insulation yields the following T_1-I-curves for the cable types FLRY-B 4, FLRY-B 6, FLRY-B 10 and FLRY-B 16:

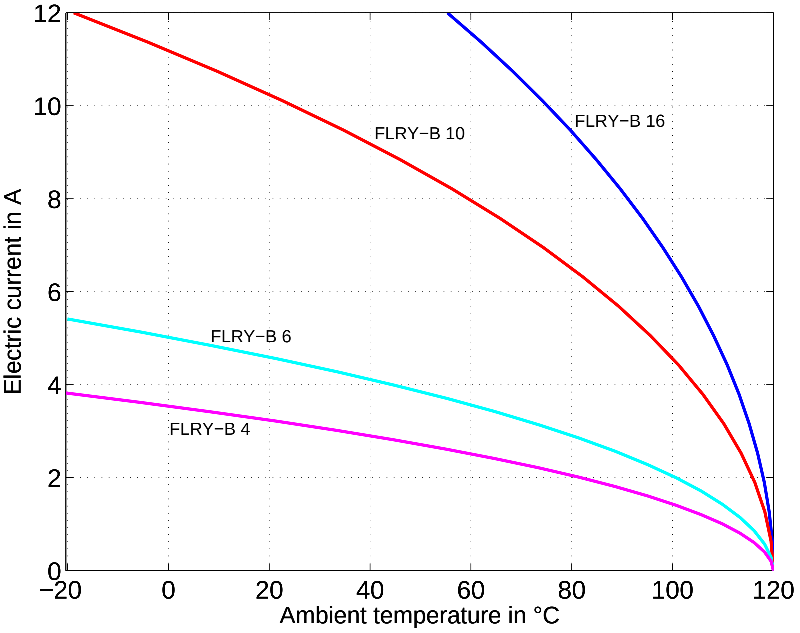

Fig. 5.2: *T_1-I-diagram of cable types FLRY-B 4, FLRY-B 6, FLRY-B 10 and FLRY-B 16.*

The number in the designation of each cable type indicates the nominal cross sectional area of the cable core, which corresponds approximately to the physical cross sectional area.

5.2.2 Transient Computations

The objective of this section is to derive formulas for the temperature evolution in insulated single-core cables over time $t \in [0, t_{max}]$. Herein, we suppose the electric current to be constant, thus I is independent of t. In Section 6.4.2, we introduce a calculation scheme for the determination of temperatures in shielded cables with current loads varying over time. This could be transferred to insulated single-core cables with only minor modifications. To compute the transient temperature profile, we introduce a *resonance current* that allows to distinguish between *quasi-stationary* and *instationary dynamics*[4]. Dynamics converging to a stationary state are denoted by quasi-stationary within this thesis, dynamics exceeding any upper temperature limit are called instationary.

Time Discretization

As described in Section 3.3.1, the interval $[0, t_{max}]$ is divided equidistantly into $n_t + 1$ time steps $0 = t_0 < t_1 < \ldots < t_{n_t}$, with $t_j = j \, \frac{t_{max}}{n_t}$, $j = 0, \ldots, n_t$, and time step size $\delta = \frac{t_{max}}{n_t}$. The temperature at the exterior boundary of the insulator at time step j is abbreviated by $T_2^{(j)} := T_2(t_j)$, the corresponding temperature in the core by $T_3^{(j)} := T_3(t_j)$, $j = 0, \ldots, n_t$. The ambient temperature T_1 is supposed to be constant in time.

In this context, we apply the explicit Euler. By experience, it works well for the consideration of the cross section of insulated single-core cable, as no fine discretization in space is required.

Definition of the Resonance Current

We remind to the formulas (5.8) and (5.11) for the determination of the temperatures T_2 of the exterior cable insulation and T_3 of the cable core in the stationary case. Resolving Equation (5.8) into I^2 yields

$$I^2 = \frac{\pi \, A_3 \, \alpha(T_2) \, (T_2 - T_1) \, d_2}{\rho_{0,3} \, (1 + \alpha_\rho \, (T_3 - T_0))} \, . \tag{5.19}$$

Replacing $\frac{\rho_{0,3} \, (1+\alpha_\rho \, (T_3 - T_0)) \, I^2}{\pi \, A_3}$ in (5.11) by the corresponding term in (5.8) provides an explicit form for the core temperature

$$T_3 = T_2 + \frac{\alpha(T_2) \, (T_2 - T_1) \, d_2 \, \ln(d_2/d_3)}{2 \, \lambda_2} . \tag{5.20}$$

We define $P_\alpha^{'}(T_2) := \alpha(T_2) \, (T_2 - T_1) \, d_2$ and state

$$\lim_{T_2 \to \infty} P_\alpha^{'}(T_2) = \infty \ \text{ as well as } \ \lim_{T_2 \to \infty} \frac{T_2}{P_\alpha^{'}(T_2)} = 0 \, .$$

Both assertions are obvious, since the radiative heat transfer coefficient α_{rad} (cf. (2.13)) depends on T_2 in the power of three due to the Stefan-Boltzmann law.

---

[4] Both terms – quasi-stationary and instationary – refer to non-stationary temperature evolutions. As we derive different computational approaches for currents below and above the resonance current, we introduce this terminology.

Inserting Equation (5.20) into (5.19) yields the dependency of the electric current on the temperature of the exterior insulation

$$I(T_2) = \sqrt{\frac{\pi\, A_3\, P'_\alpha(T_2)}{\rho_{0,3}\, \left(1 + \alpha_\rho\, (T_2 - T_0 + \frac{\ln{(d_2/d_3)}}{2\,\lambda_2}\, P'_\alpha(T_2))\right)}}. \tag{5.21}$$

Finally, we define the limit of $I(T_2)$ for $T_2 \to \infty$ by the resonance current

$$I_{\text{res}} := \sqrt{\frac{2\,\pi\, A_3\, \lambda_2}{\rho_{0,3}\, \alpha_\rho\, \ln{(d_2/d_3)}}}\,. \tag{5.22}$$

Hence, the current I_{res} is the smallest for which no stationary temperatures exist. For $I < I_{\text{res}}$, the temperature profile converges to the distribution of the steady state which is attained approximately after sufficiently long time. In the present situation, we have a necessary and sufficient condition for the convergence of the temperature to a stationary state.

Quasi-Stationary Dynamics

If $I < I_{\text{res}}$, we obtain stationary temperatures T_2^s and T_3^s at the exterior boundary of the outer insulation and in the core. We define a temperature ratio for the stationary case by

$$\eta_s := \frac{T_2^s - T_1}{T_3^s - T_1} = \frac{1}{1 + \alpha(T_2^s)\, d_2\, \frac{\ln{(d_2/d_3)}}{2\,\lambda_2}}\,. \tag{5.23}$$

Furthermore, we suppose the temperature ratio to be invariant in time, formulated by

Assumption 11. *Let η_s be given as the temperature ratio of the exterior insulation and the core in the stationary state by (5.23). For the transient temperature ratio $\eta(t) := \frac{T_2(t)-T_1}{T_3(t)-T_1}$, we postulate*

$$\eta(t) \equiv \eta_s \;\; \forall\, t \in [0, t_{max}]\,.$$

The range of validity of this assumption for practical applications is discussed in detail in the Sections 5.3 and 6.4.3 as well as in [36]. Therein, we show that it holds especially well for thin insulation layers and not too small time intervals.

The energy balance in the cable reads for an infinitesimal period of time $\mathrm{d}t$ as

$$\mathrm{d}E_{\text{st}}^{\text{is}} + \mathrm{d}E_{\text{st}}^{\text{co}} = P_{\text{g}}\,\mathrm{d}t - P_{\text{out}}\,\mathrm{d}t, \tag{5.24}$$

with $\mathrm{d}E_{\text{st}}^{\text{is}} = \gamma_2\, A_2\, \ell\, \mathrm{d}T_2$ and $\mathrm{d}E_{\text{st}}^{\text{co}} = \gamma_3\, A_3\, \ell\, \mathrm{d}T_3$ the increase of stored energy in the insulation and in the core and γ_2, γ_3 the corresponding specific heat capacities per volume. The heat power generated in the core is $P_{\text{g}} = \frac{\rho_3\, I^2\, \ell}{A_3}$ and the heat power emitted via the surface is again given by formula (5.6). Herein, the temperatures T_2 and T_3 are time-dependent, in contrast to the previous considerations. Thus, we obtain

$$\gamma_2\, A_2\, \mathrm{d}T_2 + \gamma_3\, A_3\, \mathrm{d}T_3 = \left(\frac{\rho(T_3(t))\, I^2}{A_3} - \alpha(T_2(t))(T_2(t) - T_1)\pi\, d_2\right)\mathrm{d}t. \tag{5.25}$$

Applying an explicit discretization scheme yields

$$\gamma_2\, A_2\, \left(T_2^{(j+1)} - T_2^{(j)}\right) + \gamma_3\, A_3\, \left(T_3^{(j+1)} - T_3^{(j)}\right) = \left(\frac{\rho(T_3^{(j)})\, I^2}{A_3} - \alpha\left(T_2^{(j)}\right)\left(T_2^{(j)} - T_1\right)\pi\, d_2\right)\delta \tag{5.26}$$

for $j = 0, \dots, n_t - 1$ and $T_2^{(0)} = T_3^{(0)} = T_1$. Moreover, we define

$$\eta^{(j)} := \eta\,(t_j) = \eta_s,\ \ j \geq 0.$$

Since $\eta^{(j+1)} = \eta^{(j)}$, $j = 0, \dots, n_t - 1$, there holds for $\eta^{(j)} \neq 0$ and $T_3^{(j+1)} \neq T_1$:

$$T_3^{(j+1)} - T_3^{(j)} = \frac{1}{\eta^{(j)}} \left(T_2^{(j+1)} - T_2^{(j)} \right) . \tag{5.27}$$

Reordering the definition of $\eta^{(j)}$ yields

$$T_3^{(j)} = \frac{T_2^{(j)}}{\eta^{(j)}} + \left(1 - \frac{1}{\eta^{(j)}} \right) T_1. \tag{5.28}$$

We summarize (5.26) and (5.28) in an explicit recursion scheme for $j = 0, \dots, n_t - 1$:

$$\boxed{\begin{aligned} T_2^{(j+1)} &= T_2^{(j)} + \frac{\frac{\rho\left(\Phi(T_2^{(j)})\right) I^2}{A_3} - \alpha\left(T_2^{(j)}\right)\left(T_2^{(j)} - T_1\right) \pi\, d_2}{\gamma_2\, A_2 + \frac{\gamma_3\, A_3}{\eta^{(j)}}}\ \delta, \\ T_3^{(j+1)} &= \frac{T_2^{(j+1)}}{\eta^{(j+1)}} + \left(1 - \frac{1}{\eta^{(j+1)}} \right) T_1. \end{aligned}} \tag{5.29}$$

Since the electric current is supposed to be constant over time in this setting, we could replace $\eta^{(j)}$ and $\eta^{(j+1)}$ by η_s. As mentioned, the calculation rule could be applied with minor changes for electric currents varying over time. Then, the value of the temperature ratio η could change from one time step to the next.

Instationary Dynamics

For $I \geq I_{\text{res}}$, no stationary temperatures T_2 and T_3 exist. Consequently, the quasi-stationary assumption $\eta^{(j+1)} = \eta^{(j)} = \eta_s,\ j \geq 0$, cannot be applied in this situation. In practical applications, electric currents higher than I_{res} can only occur for very short times because else, temperatures high above the upper limit of the materials are exceeded, immediately. In this context, estimations with shorter heating times than those obtained respecting all quantities are sufficient. Hence, we neglect the capacity term of the insulation, namely $\mathrm{d}E_{\text{st}}^{\text{is}}$ and the emission via the surface $P_\alpha\, \mathrm{d}t$. Thus, we obtain a simply integrable equation $\mathrm{d}E_{\text{st}}^{\text{co}} = P_{\text{g}}\, \mathrm{d}t$ respectively $\gamma_3\, A_3^2\, \mathrm{d}T_3 = \rho_{0,3}\ (1 + \alpha_\rho (T_3 - T_0))\, I^2 \mathrm{d}t$. Separation of variables and integration of both sides yields an estimate for the heating time by

$$t_{j+1} - t_j = \frac{\gamma_3\, A_3^2}{\rho_{0,3}\, \alpha_\rho\, I^2} \ln \left(\frac{\rho_{0,3}(1 + \alpha_\rho(T_3^{(j+1)} - T_0))}{\rho_{0,3}(1 + \alpha_\rho(T_3^{(j)} - T_0))} \right),\ j = 0, \dots, n_t - 1. \tag{5.30}$$

With $T_3^{(0)} = T_1$, we obtain the explicit heating evolution by

$$T_3^{(j+1)} = \frac{1}{\alpha_\rho} \left(\left(1 + \alpha_\rho\ (T_3^{(j)} - T_0) \right) \exp\left(\frac{\rho_{0,3}\, \alpha_\rho\, I^2}{\gamma_3\, A_3^2} (t_{j+1} - t_j) \right) - 1 \right) + T_0\,. \tag{5.31}$$

Since for currents higher than the resonance current no stationary temperatures exist, no η_s is available. To get at least an orientation for the temperature at the surface of the insulation, we define a temperature ratio η_{res} for currents higher than the resonance current at current $I^* := 0.99 \cdot I_{\text{res}}$ and set

$$T_2^{(j+1)} = \eta_{\text{res}}\, T_3^{(j+1)}. \tag{5.32}$$

In summary, we apply the following mapping in the instationary case for $j = 0, \dots, n_t - 1$:

$$\boxed{\begin{aligned} T_3^{(j+1)} &= \frac{1}{\alpha_\rho} \left(\left(1 + \alpha_\rho \, (T_3^{(j)} - T_0)\right) \exp\left(\frac{\rho_{0,3}\, \alpha_\rho\, I^2}{\gamma_3\, A_3^2} (t_{j+1} - t_j) \right) - 1 \right) + T_0, \\ T_2^{(j+1)} &= \eta_{\text{res}}\, T_3^{(j+1)}. \end{aligned}} \tag{5.33}$$

We suppose that the temperature ratio for a current slightly below the resonance current yields a better approximation of the actual temperature ratio for an electric current above the resonance current than that of a small electric current. Hence, we choose I^* as indicated for the determination of the temperature ratio in case of currents larger than or equal to the resonance current. However, improving this formula will be a subject of future research.

Summary of the Transient Computation Scheme

We summarize our explicit calculation scheme for arbitrary, constant currents I as follows:

$$\boxed{\begin{aligned} &\text{If } I < I_{\text{res}} = \sqrt{\frac{2\,\pi\, A_3\, \lambda_2}{\rho_{0,3}\, \alpha_\rho\, \ln(d_2/d_3)}} : \\ &\quad T_2^{(j+1)} = T_2^{(j)} + \frac{\frac{\rho\left(\Phi(T_2^{(j)})\right) I^2}{A_3} - \alpha\left(T_2^{(j)}\right)\left(T_2^{(j)} - T_1\right) \pi\, d_2}{\gamma_2\, A_2 + \frac{\gamma_3\, A_3}{\eta^{(j)}}}\, \delta, \\ &\quad T_3^{(j+1)} = \frac{T_2^{(j+1)}}{\eta^{(j+1)}} + \left(1 - \frac{1}{\eta^{(j+1)}}\right) T_1, \\ &\text{else}: \\ &\quad T_3^{(j+1)} = \frac{1}{\alpha_\rho} \left((1 + \alpha_\rho \, \left(T_3^{(j)} - T_0\right)) \exp\left(\frac{\rho_{0,3}\, \alpha_\rho\, I^2}{\gamma_3\, A_3^2} (t_{j+1} - t_j) \right) - 1 \right) + T_0, \\ &\quad T_2^{(j+1)} = \eta_{\text{res}}\, T_3^{(j+1)}, \qquad\qquad j = 0, \dots, n_t - 1. \end{aligned}} \tag{5.34}$$

5.3 Comparison to Finite Element Simulations

In order to validate our cable specific approaches for heat distributions in insulated single-core cables, we first compare our computational results to calculations with finite elements, afterwards in Section 5.4, to measurements performed by the Leoni AG [138].[5]

Since no analytical means to evaluate the error of our η_s calculation have been applied yet, we use finite element computations, supposing they are sufficiently accurate in this context.

For numerical experiments with finite elements, we apply linear Lagrange elements, the standard Newton-Raphson solver with relative accuracy $\epsilon = 1.0e\text{-}6$ respectively maximum

---

[5] Note that the measurements and computations of this section refer to the same scenarios.

number of iterations $i_{\max} = 25$ in Algorithm 2, UMFPACK as linear solver and, for the non-stationary case, IDA with step size $\delta = 1s$ for time discretization.

In Tables 5.1 and 5.2, the parameter values used in the computations, explicitly given in [78, 138], are summarized. The time-dependent measurements were performed with a constant electric current below the resonance current and were interrupted when a stationary state had been approximately reached.

Tab. 5.1: *Parameter values in computations of temperatures in insulated single-core cables.*

Parameter name	Symbol	Value	Unit
Heat conductivity of the exterior insulation	λ_2	0.23	$\mathrm{W/(m \cdot K)}$
Heat conductivity of the metallic conductors	λ_4	386	$\mathrm{W/(m \cdot K)}$
Heat conductivity of air	λ_{air}	2.61e-2	$\mathrm{W/(m \cdot K)}$
Electr. resistivity of the conductors resp. core at reference temperature	$\rho_{0,3}, \rho_{0,4}$	1.75e-8	$\Omega \cdot \mathrm{m}$
Temperature coefficient of the electr. resistivity of the core	α_ρ	3.93e-3	1/K
Specific heat capacity per volume of the insulation	γ_2	1.82e6	$\mathrm{J/(K \cdot m^3)}$
Specific heat capacity per volume of the cable core resp. conductors	γ_3, γ_4	3.50e6	$\mathrm{J/(K \cdot m^3)}$
Emission coefficient	ϵ_{r}	0.93	
Ambient temperature	T_1	25	°C

Tab. 5.2: *Properties of insulated single-core cable types and specific parameters of performed scenarios.*

Cable type	d_2 (mm)	d_3 (mm)	d_4 (mm)	n_c	I (A)	$t_{\max}$ (s)
FLRY-A 0.35	1.40	0.80	0.26	7	10	220
FLRY-B 2.5	3.00	2.20	0.26	50	40	430
FLY 4	4.40	2.75	0.30	56	50	800
FLY 6	5.00	3.30	0.30	84	65	800
FLY 10	6.50	4.50	0.37	77	69	740
FLY 16	7.30	6.30	0.37	128	108	1 400
FLY 25	10.0	7.80	0.37	200	144	5 200
FLY 35	11.3	9.00	0.37	276	184	3 500
FLY 50	13.9	10.5	0.37	400	228	4 000

The computed resonance current I_{res}, the stationary temperatures T_2 and T_3, the temperature ratio η_s and the constant of contraction q are listed in Table 5.3. Figure 5.3 shows that, although our approaches based on energy balances use some heuristics, their results correspond nearly perfectly to those obtained with finite elements. In all cases, the temperature curves nearly coincide or the heat power balance approach (in the following abbreviated by HBA) provides slightly higher temperatures and shorter heating times. The difference in temperature between both approaches is for all cable types and at any time never larger than 2 K and the relative deviation is always less than 5 %. This allows to conclude that the proposed simplified approach is very adequate in the context of thermal analysis of insulated single-core cables with currents below the resonance current. Moreover, the computation times are extremely fast (< 1 s in Matlab, version 7.10.0.499, on an Intel Core 2 Duo processor with 2.67 GHz and 3.00 GB RAM) and hence, several times faster than the finite element calculations (> 5 s with COMSOL on the same system).

The constant of contraction q is in all cases small enough (≤ 0.519) to guarantee a fast convergence of the method. This is due to the fact that all applied currents are quite low, far from the resonance current I_{res}. It might be surprising that the resonance current of cable type FLY 16 is higher than that of FLY 25, although the metallic cross sectional area is larger. Considering Equation (5.22), we can explain it by the ratio d_2/d_3 that mainly influences the resonance current and this ratio is for FLY 16 much smaller than for FLY 25.[6]

Tab. 5.3: *Computational results for insulated single-core cables.*

Cable type	I_{res} (A)	T_2 (°C)	T_3 (°C)	η_s	q
FLRY-A 0.35	116.4	69.5	71.7	0.953	0.352
FLRY-B 2.5	417.7	86.4	89.3	0.955	0.519
FLY 4	414.4	74.7	79.2	0.918	0.419
FLY 6	539.8	75.9	80.4	0.919	0.429
FLY 10	714.2	56.1	58.8	0.921	0.255
FLY 16	1 417	68.1	69.8	0.961	0.361
FLY 25	1 328	65.6	69.1	0.921	0.333
FLY 35	1 674	66.2	69.8	0.920	0.336
FLY 50	1 768	64.1	69.0	0.888	0.313

To investigate the validity of η_s for different heating times, we take one specific scenario and compare the results obtained by FEM to those computed via the HBA. In Figure 5.4, the temperatures in the stationary state, after ten seconds and after one second are depicted for different constant current loads. The considered cable is of type FLY 16 and the ambient temperature $T_1 = 25\,°\text{C}$. We notice that the accordance in the stationary state is excellent, for T_3 as well as for T_2 (cf. Figures 5.4a and 5.4b). Whereas for T_3 the agreement in case of electric current during ten seconds is nearly perfect, we have a discrepancy in T_2 (cf. Figures 5.4c and 5.4d). This discrepancy is even more obvious for one second with very large electric currents. In this case, the computation of T_2 is no more adequate (cf. Figures 5.4e and 5.4f). For currents below the resonance current, our HBA corresponds very well to the finite element simulations concerning T_3. At the transition of quasi-stationary to instationary case, we have a jump in temperature, which is non-physical. Moreover, the temperatures computed for current loads higher than the resonance current are overestimated.

We conclude that our specific computational approaches yield good results for 'normal' currents below the resonance current. Checked by finite elements, the proposed methods work perfectly if the considered heating times are not too small. For currents above the resonance current, we obtain temperatures T_3 hotter than those of the finite element calculation. Thus, they provide an orientation. The formulas for T_2 concerning short time heating must be improved, but since the most important quantity our interest is T_3, it is not subject of this thesis.

5.4 Comparison to Measurements

To show the validity of our calculation approaches for practical applications, we validate the computations with experimental data. We use the same parameters as given in Tables 5.1 and 5.2. Since in the measurements only the temperatures of the core were measured, we renounce indicating the temperature T_2 and restrict to T_3.

Figure 5.5 depicts the heat evolution of measurements and simulations for nine different cable types. The qualitative shape of the curves are very similar, except for the cable types

---

[6] The same argumentation is applicable for the resonance currents of cable types FLRY-B 2.5 and FLY 4.

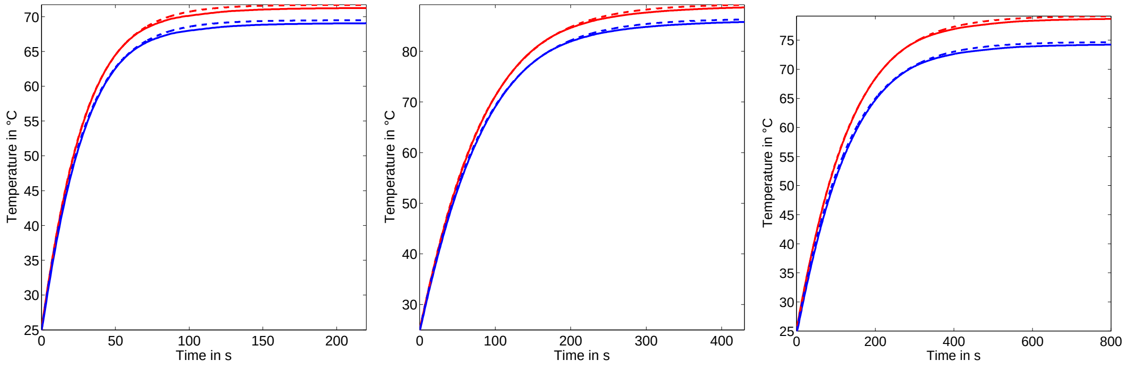

(a) FLRY-A 0.35. **(b)** FLRY-B 2.5. **(c)** FLY 4.

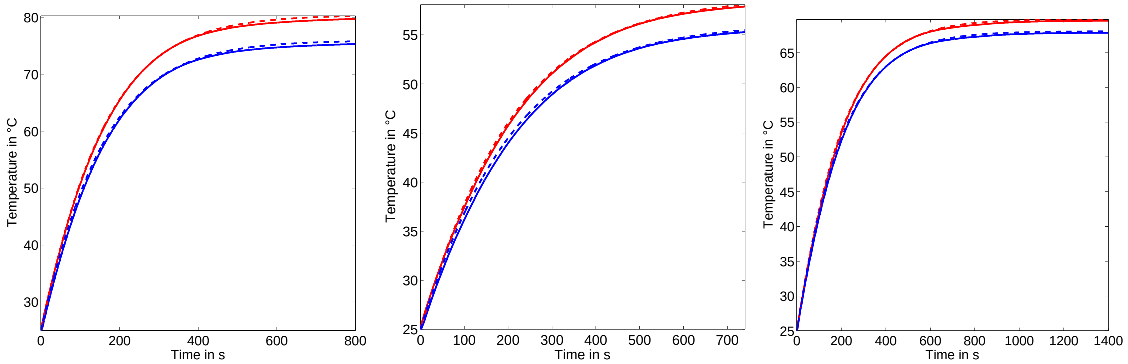

(d) FLY 6. **(e)** FLY 10. **(f)** FLY 16.

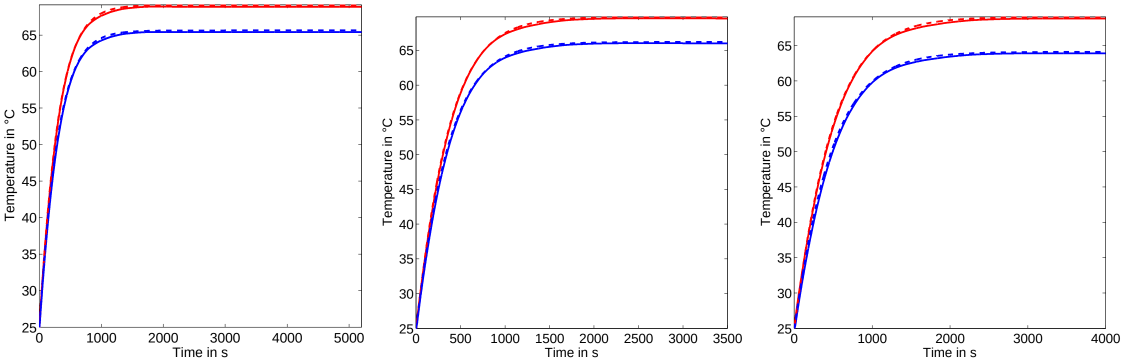

(g) FLY 25. **(h)** FLY 35. **(i)** FLY 50.

Fig. 5.3: *Comparison of computed temperature evolutions for different cable types. In each subfigure, the blue lines show the temperatures T_2 and the red ones T_3. The dashed lines represent the calculations via the HBA, the solid lines depict the results of the finite element approach.*

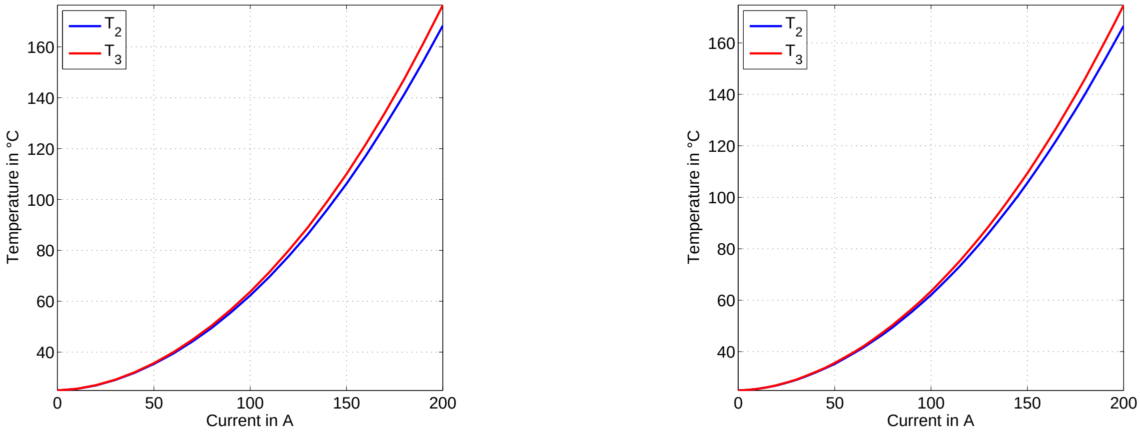

(a) Stationary temperatures over current loads, obtained via the HBA.

(b) Stationary temperatures over current loads, obtained via the FE approach.

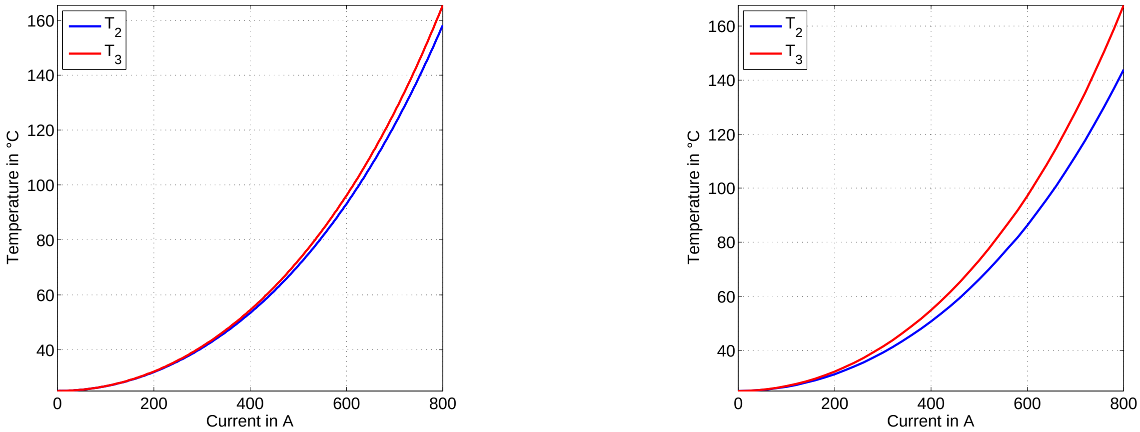

(c) Temperatures after 10 seconds over current loads, obtained via the HBA.

(d) Temperatures after 10 seconds over current loads, obtained via the FE approach.

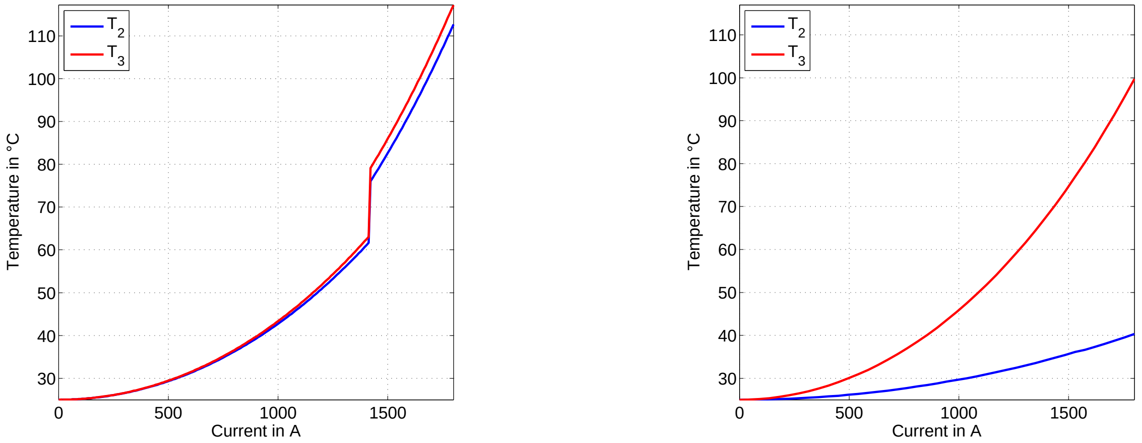

(e) Temperatures after 1 second over current loads, obtained via the HBA.

(f) Temperatures after 1 second over current loads, obtained via the FE approach.

Fig. 5.4: *Comparison of stationary temperatures and temperatures after 10 seconds respectively 1 second for different currents, obtained via the HBA (left) and the finite element approach (right) for cable type FLY 16.*

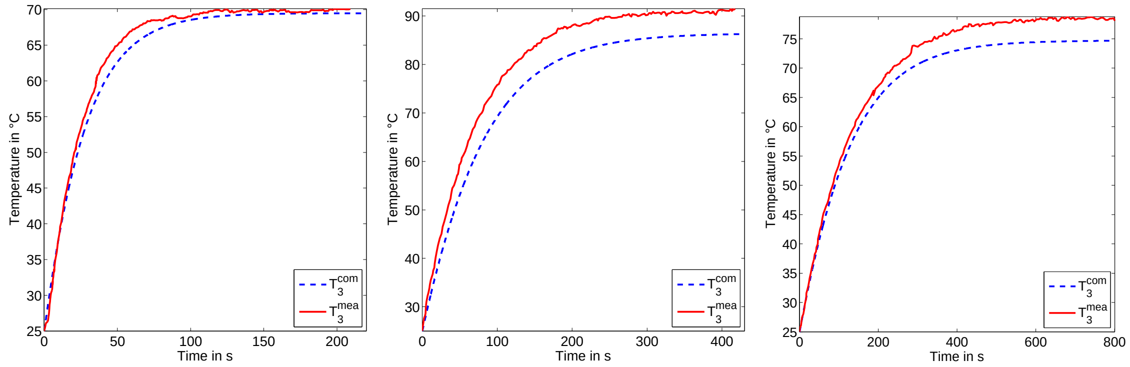

(a) FLRY-A 0.35. **(b)** FLRY-B 2.5. **(c)** FLY 4.

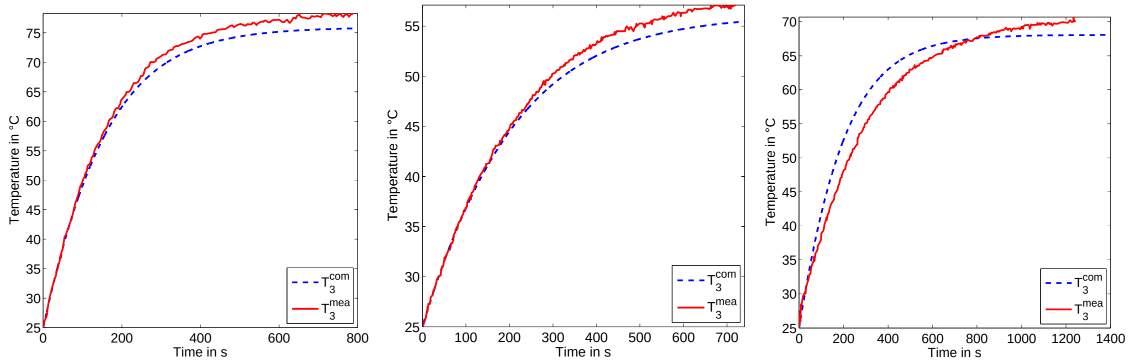

(d) FLY 6. **(e)** FLY 10. **(f)** FLY 16.

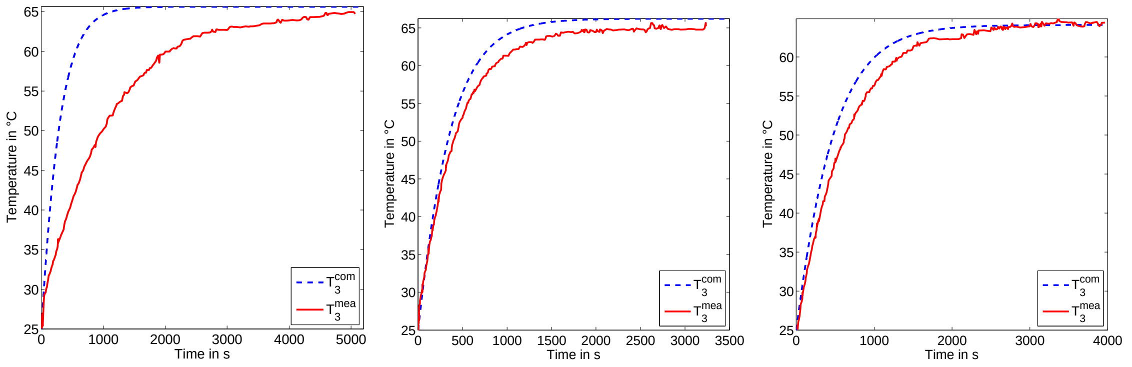

(g) FLY 25. **(h)** FLY 35. **(i)** FLY 50.

Fig. 5.5: *Comparison of temperature evolutions for different cables measured in the laboratories (red lines) and computed via the HBA (blue lines).*

FLY 16 and FLY 25. The maximum deviations in temperatures over time remain below 8 K and the relative errors below 10 %. We need to mention that an accordance of 100 % cannot be expected in this framework due to several reasons, explained later in this section. Thus, we claim that the simulations are to the largest extent confirmed by the measurements.

Some observations and particularities of the computational and measuring results are listed in the following:

- The discrepancy between simulation and measurement for the cable types FLRY-B 2.5 and FLY 4 is quite large ($> 5\,\mathrm{K}$) concerning the maximum temperature after sufficiently long times. Even though in the derivation of the computational approach all reduction were applied such that higher maximum temperatures and shorter heating times might be expected, we obtain lower temperatures and longer heating times in the computations for these examples.
- The curves belonging to cable type FLY 16 show an unusual behaviour by crossing after about 800 s. The computed stationary temperature lies beneath the maximum temperature of the experiment, however, the computed heating times are shorter in the beginning of the calculations.
- In the graphs for FLY 25, the heating times differ significantly, although the final temperatures correspond well within the limits of numerical accuracy. Whereas in the simulations, the stationary state is reached within an accuracy of 5 % after less than 2000 s, the temperature in the measurement still increases after more than 4000 s.
- By tendency, we notice that for thinner cable types, in particular for FLRY-B 2.5, FLY 4 and FLY 10, the maximum temperatures in the simulations are underestimated, whereas for thicker ones, they represent an upper bound (cf. FLY 25, FLY 35) or correspond very well (cf. FLY 50).

Possible reasons for our observations are:

- As mentioned, our specific approaches include some computational simplifications, especially the introduction and application of the temperature ratio η_s is rather heuristic. Nevertheless, we showed in the previous section that the results coincide very well with those obtained via FEM. Consequently, the influence due to the simplified simulation approach is estimated to be rather small in the context of low current loads as they are applied in the present scenarios.
- Simulation results always depend on the quality of the material parameters. The employed parameter values in our computations represent standard values of the corresponding materials. It is often hard or impossible to say, if the materials are completely pure and if their state is as good as supposed for the parameter value. Differences between the assumed material parameters and their real values could result in larger deviations. Especially the progress of the curve in FLY 25 allows to draw the conclusion that the supposed heat capacities in the simulation are too small. This would explain the much faster convergence to the stationary temperatures than in the measurements.
- In addition to the previous argument, the data provided by cable manufacturers are often not very precise. Wongyala [138] already noticed in his work that the conductor diameters in reality sometimes deviate more than 10 % from the information given

by the cable manufacturers. Since the cross sectional areas represent an essential part of the source term in our equations, these variances have a strong impact on the simulation results.

- A further reason which may not be forgotten in this context is that the measurements are not free of inaccuracies and errors, too. The integration of thermocouples into the experimental setup falsifies the real temperature evolutions and the accuracy of measurement devices is limited.

5.5 Choosing the Best Cable

A question currently often discussed in the on-board supply industry is whether to replace copper by aluminium cables [112, 125]. In fact, the price of copper has increased much faster in the recent years than the price of aluminium (cf. Figure A.1). Furthermore, the price of copper (5 396.2 €/LME Rolling[7]) is at the moment nearly four times higher than that of aluminium (1 376.1 €/LME Rolling[7] [10]). On the other hand, copper excels by good physical properties like the electrical conductivity ($\kappa_0 \approx 5.7e7\,\mathrm{S/m}$ in contrast to $3.5e7\,\mathrm{S/m}$ of aluminium). We demonstrate a study which explains how car producers can apply our simulation approaches in order to choose the 'right' cable.

Given a specific scenario - a worst case scenario - in which the manufacturer has to choose between several available cable types. We restrict the stock of cable types to the size of eight – four cable types with core of copper (FLY 16, FLY 25, FLY 35, FLY 50, cf. Table 5.2), four cable types with core of aluminium (denoted by FLY 16-Al, FLY 25-Al, FLY 35-Al, FLY 50-Al[8]). The scenario is the same as presented in Section 5.3 for cable type FLY 50 with ambient temperature 25 °C and electric current $I = 228\,\mathrm{A}$. Furthermore, we assume that the melting point of the insulation must not be exceeded, else the corresponding cable is not adequate in this situation. The aluminium cables have the same insulation materials and diameters like their copper pendants, but the parameter values of the core are

- heat conductivity of the conductors $\lambda_4 = 235\,\mathrm{W/(m \cdot K)}$,
- electrical resistivity of the core at reference temperature $\rho_{0,3} = \rho_{0,4} = 2.65e\text{-}8\,\Omega \cdot \mathrm{m}$,
- temperature coefficient of electrical resistivity $\alpha_\rho = 4.04e\text{-}3\,\mathrm{K}^{-1}$,
- specific heat capacity per volume of the cable core $\gamma_3 = \gamma_4 = 2.42e6\,\mathrm{J/(kg \cdot m^3)}$.

If we suppose the melting temperature of the insulation to be 130 °C, too high temperatures would definitely be generated in cables of types FLY 16 and FLY 16-Al (cf. Figure 5.6a). In contrast, the diameters of cable types FLY 50 and FLY 50-Al (cf. Figure 5.6d) are far too large and thus, these cable types would be too expensive in this context. FLY 25-Al must also be rejected for the first reason (cf. Figure 5.6b), FLY 35 for the second (cf. Figure 5.6c). Consequently, there only remain the cable types FLY 25 and FLY 35-Al. In a cable FLY 25, the metallic part in each cross section amounts according to [78] about $21.5\,\mathrm{mm}^2$, in FLY 35-Al about $31.3\,\mathrm{mm}^2$. Thus, the copper cable would be 2.69 times more expensive ($2.69 \approx \frac{21.5\,\mathrm{mm}^2}{31.3\,\mathrm{mm}^2} \cdot \frac{5\,396.2\,€}{1\,376.1\,€}$), if we just consider the metallic part.

From this point of view, we would recommend the manufacturer to employ the aluminium cable FLY 35-Al because it is much cheaper. On the other hand, we may not forget to take into account that aluminium has other 'worse' properties than copper, e.g. less mechanical stability, lower tensile strength and, from a practical point of view, it is more complicated

---

[7] State: 27th September 2013 [10], LME Rolling: London Metal Exchange - indicator for price of metals.

[8] These cable types of aluminium do not really exist, at least they do not have these names. We introduce them just for our theoretical study.

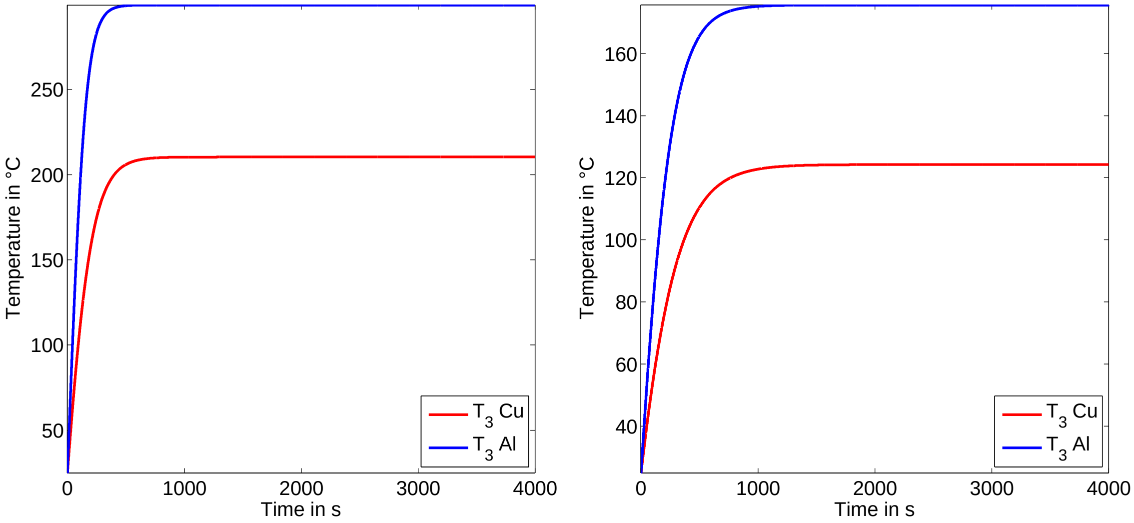

(a) FLY 16, FLY 16-Al. **(b)** FLY 25, FLY 25-Al.

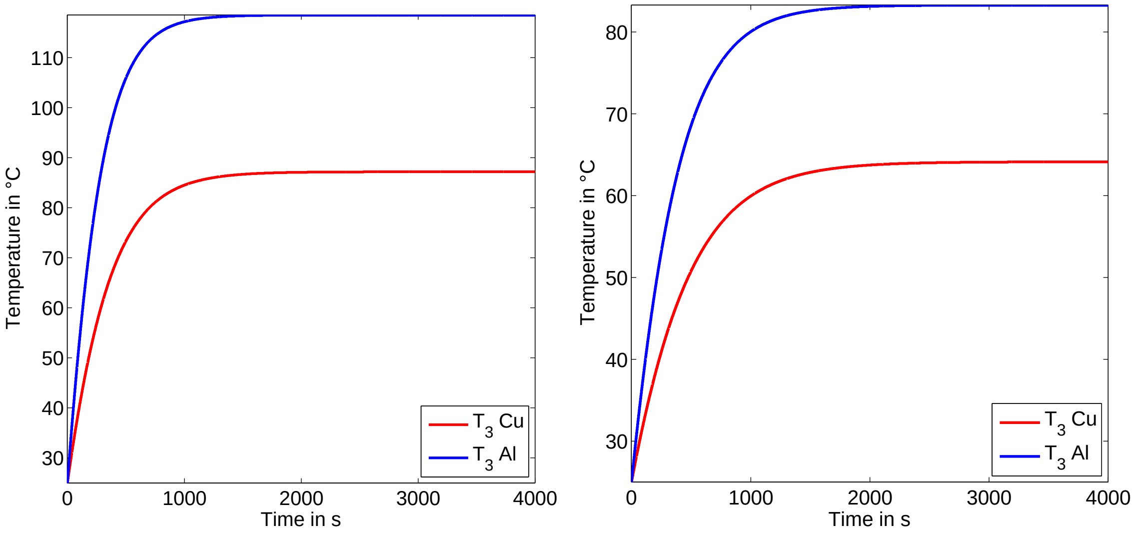

(c) FLY 35, FLY 35-Al. **(d)** FLY 50, FLY 50-Al.

Fig. 5.6: *Comparison of temperature evolutions for different cable types at a specific scenario, each time depicted the maximum temperature* T_3 *in the copper (Cu) or aluminium (Al) core.*

for soldering [112]. Our hypothesis confines to the fact that, taking thermal aspects and costs into account, it would definitely make sense for this scenario to replace copper cables by thicker aluminium wires. Furthermore, the weight would decrease, since aluminium has a more than three times smaller density than copper (2 700 kg/m^3 vs. 8 920 kg/m^3), but the volume would of course increase.

It is difficult to give a general answer to this question. In cars, the available space is often rare and the circumstances avoid an integration of thicker cables. Hence, this question can only be answered for specific cases as shown by our example.

5.6 Conclusion

In this chapter, we proposed computational approaches (called HBA) specific to the determination of temperatures in insulated single-core cables. The derived system of equations to calculate temperatures at essential positions in the cable is nonlinear and solved via a fixed point iteration. It was shown that for certain conditions and currents below the resonance current, the existence of a unique solution for the stationary case is ensured. Furthermore, we compared the solutions of our HBA to measurements and simulation results obtained via finite elements. Whereas some acceptable discrepancies to the measurements exist due to uncertainties of parameter values, measurement inaccuracies and simplifications in the computations, the accordance to finite elements is excellent for current loads of lower and normal intensity. Nevertheless, improvements for short times and very high currents have to be added in future investigations.

Moreover, useful operations like creating diagrams that ilustrate the properties of cables and comparison of different cable types concerning heat generation can be performed easily by the given approaches. The introduced computational methods can now be applied to other cable types and connecting structures.

6 Shielded Cables

Shielded cables, i.e. wires with a metallic, current carrying layer in the insulation, find practical use in the high frequency technology, especially in high voltage on-board systems. In the automotive context, the term 'high voltage' refers to voltages above 60 V DC [37]. It is the task of the shielding to 'separate' the cable from the environment, regarding both, the radiation from exterior into the cable and from inside to outside. Radiation like electromagnetic induction by alternating current or radio waves is concerned.

We present specific approaches, developed in cooperation with our industrial partners, to compute the main temperatures in shielded cables of finite length for stationary and transient considerations. Therein, we respect different ambient temperatures in subsections of the cable and influences of connected objects. Our approaches are validated by comparison to measurements and finite element simulations. Some methods trace back to the computational approaches for insulated single-core cables. Moreover, we show how cable manufacturers can apply our methods for right dimensioning of shielded cables.

6.1 Problem Formulation

There exists a great number of publications concerning shielded cables, e.g. [31–33]. Most of them are focused on other aspects than the thermal analysis, especially electromagnetic compatibility (EMC) is the subject of many investigations. However, the importance of the heat generation in shielded cables has increased over the last years because today, cable cores and sometimes shieldings carry higher currents in the high voltage technology.

Our aim is to approximate the axial temperature distribution at characteristic points in shielded cables of finite length. These temperatures are essentially determined by the electric currents in the core (I) and shielding (I_3), the material of the cable and its dimensions. Moreover, the attached devices at the ends of the cable and the ambient temperatures in different subsections influence the temperature profile. Figure 6.1a shows the cross section of a shielded cable in radial direction with its main physical and cable specific parameters.

In order to be applicable to very short cables of only a few centimetres of length and also to longer wires of several metres distributed over the entire car, we keep our computational methods general. For shorter conductors, the temperatures of attached devices play a main role, whereas for longer cables varying ambient conditions in different cable subsections essentially influence the temperature profile. We first confine to the stationary case with a constant direct current over the complete time period, afterwards we investigate the transient one. In our non-stationary considerations of this chapter, the current loads vary, in contrast to Section 5.2.2, in time, meaning that the current $I(t)$ in the core depends on time $t \in [0, t_{\max}]$.

The entire chapter has been published in two articles of scientific journals. The first concerns the stationary case [86], the second describes the transient [85].

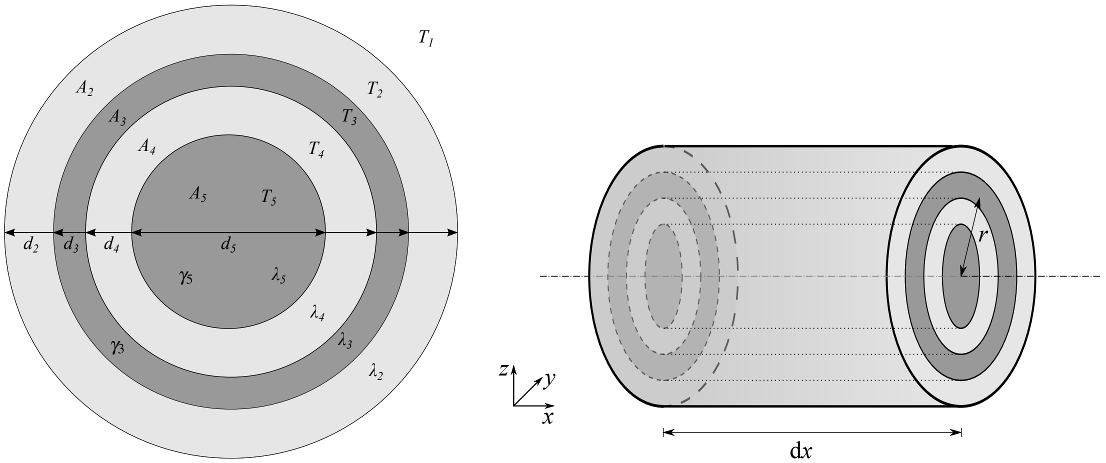

(a) Radial cross section of a shielded cable. **(b)** Volume element of length dx.

Fig. 6.1: *Radial cross section and volume element of a shielded cable.*

6.2 Notation and Annotations

Throughout this chapter, the temperatures and material parameters for the different cable cross section areas are indexed by 1 for the environment, 2 for the exterior insulation, 3 for the shielding, 4 for the inner insulation and 5 for the core.

We denote T_1 the ambient temperature, T_2 the temperature at the exterior boundary of the outer insulation layer, T_3 the temperature in the shielding, T_4 the temperature in the inner insulation layer and T_5 the temperature in the core[1]. Since T_5 is the main quantity of our interest, it is abbreviated by T later in this chapter.

The geometrical properties of the cable cross section are determined by the diameters d_i, $i = 2, \ldots, 5$, and the cross sectional areas A_i, $i = 2, \ldots, 5$. The thermal identification of the system requires the heat conductivities λ_i, $i = 2, \ldots, 5$ and specific heat capacities γ_3, γ_5 per volume for core and shielding (see all parameters describing the cable in Figure 6.1a). Furthermore, the important electric quantities are the electrical resistivity ρ_0 of the core at reference temperature T_0, the temperature coefficient α_ρ of the electrical resistivity for the cable core and the resistivity ρ_3 of the shielding. The rise of the electrical resistance in the cable core for higher temperatures is approximated linearly by

$$\rho = \rho_0 \left[1 + \alpha_\rho \left(T_5 - T_0\right)\right]. \tag{6.1}$$

The temperature of attached devices can either be known, which finally results in a Dirichlet boundary condition, or the heat flux is approximated by an approach presented in Section 6.3.2 (Boundary and Interface Conditions), yielding a Robin boundary condition. For the first case, depicted in Figure 6.2a, the fixed temperatures T^l at the left and T^r at the right end are given. The attached objects in the second case, cf. Figure 6.2b, are characterized by the heat conductivities λ^l_{ad} respectively λ^r_{ad}, the asymptotic temperatures T^l_{ad} respectively T^r_{ad} and the contact resistances R^l_k respectively R^r_k. This general model for attached components allows to take a great number of devices into account. However,

---

[1] The temperature in the core in radial direction is approximately constant because of the large heat conductivity of metals.

each has to be identified by the mentioned quantities, which is not always elementary in practice, especially for complex geometries.

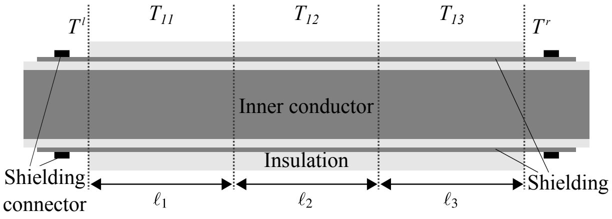

(a) Cable with fixed temperatures at both ends.

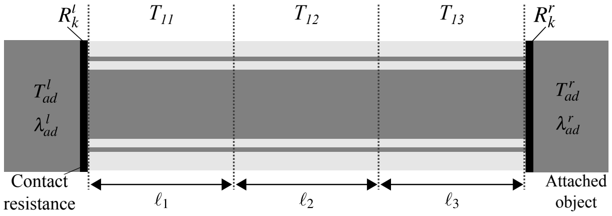

(b) Cable with attached objects at both ends.

Fig. 6.2: *Axial cross sections of shielded cables with different boundary conditions.*

A shielded cable can be placed in the entire car with varying ambient temperatures for different subsections. Herein, we restrict the model to three different sections, which is, according to our industrial partner, sufficient. An extension to more subsections is easily possible. The subsections with lengths ℓ_1, ℓ_2, ℓ_3 have the ambient temperatures T_{11}, T_{12}, T_{13}.

6.3 Stationary Case

We assume the electric current to be constant and the entire system to reach an equilibrium.

6.3.1 Heat Power Balance Approach

In order to derive appropriate equations for the stationary heat distribution in the shielded cable, we consider a volume element of infinitesimal length $\mathrm{d}x$, shown in Figure 6.1b.

An adapted heat power balance in the volume element reads as

$$\underbrace{\mathrm{d}P_k + \mathrm{d}P_s}_{\text{produced heat power}} = \underbrace{\mathrm{d}P_x + \mathrm{d}P_r}_{\text{conducted heat power}} \tag{6.2}$$

with $\mathrm{d}P_k$ the heat power generated by current flow in the core, $\mathrm{d}P_s$ the heat power produced in the shielding, $\mathrm{d}P_x$ the conducted heat power in axial direction and $\mathrm{d}P_r$ the heat power conducted in radial direction.

For $\mathrm{d}P_k$, there holds

$$\mathrm{d}P_k = \frac{\rho_0\, I^2\,(1+\alpha_\rho\,(T_5 - T_0))}{A_5}\,\mathrm{d}x. \tag{6.3}$$

To reduce the complexity of our system, we neglect the dependency of the electrical resistance of the shielding on the temperature T_3 and obtain

$$\mathrm{d}P_s = \frac{\rho_3\, I_3^2}{A_3}\, \mathrm{d}x. \tag{6.4}$$

This simplification is justified by significantly smaller current densities and consequently lower produced heat power in the shielding compared to the core. Indeed, the shielding mainly serves to avoid radiation, which is already fulfilled by low currents.[2]

We identify $\mathrm{d}P_x$ via Fourier's law by

$$\mathrm{d}P_x = -\sum_{j=2}^{5} \lambda_j A_j \frac{\mathrm{d}T_j}{\mathrm{d}x}. \tag{6.5}$$

Since the main contribution of $\mathrm{d}P_x$ is given by $\lambda_5\, A_5\, \frac{\mathrm{d}T_5}{\mathrm{d}x}$ because of the disproportionately greater heat conductivity and cross sectional area, it is reasonable to approximate $\frac{\mathrm{d}T_j}{\mathrm{d}x} = \frac{\mathrm{d}T_5}{\mathrm{d}x}$, $j = 2, \dots, 4$. Thus, we obtain

$$\mathrm{d}P_x = -\Lambda \frac{\mathrm{d}T_5}{\mathrm{d}x} \tag{6.6}$$

with $\Lambda := \sum_{j=2}^{5} \lambda_j\, A_j$. Assuming T_5 twice differentiable, we get

$$\frac{\mathrm{d}P_x}{\mathrm{d}x} = -\Lambda\, \frac{\mathrm{d}^2 T_5}{\mathrm{d}x^2} \quad \Rightarrow \mathrm{d}P_x = -\Lambda\, \frac{\mathrm{d}^2 T_5}{\mathrm{d}x}. \tag{6.7}$$

The heat power conducted in radial direction in a cable of length ℓ_x is also given by Fourier's law via

$$P_r \;=\; -\int\limits_{A_s} \lambda(s) \frac{\partial T}{\partial s}\, \mathrm{d}\sigma, \quad d_5/2 \le s \le d_2/2. \tag{6.8}$$

The quantity $A_s = 2\,\pi\, s\, \ell_x$ denotes the surface area with distance s to the centre of the conductor. Since we assume a constant temperature profile in the core ($0 \le s \le d_5/2$), the interval $(0, d_5/2)$ makes no heat power contribution in radial direction. The space dependent quantity $\lambda = \lambda(s)$ represents the different heat conductivities in the layers of the main, i.e.

$$\lambda(s) = \begin{cases} \lambda_4 & \text{for} \quad d_5/2 \le s \le d_4/2\,, \\ \lambda_3 & \text{for} \quad d_4/2 \le s \le d_3/2\,, \\ \lambda_2 & \text{for} \quad d_3/2 \le s \le d_2/2\,. \end{cases} \tag{6.9}$$

Rotational symmetry of the geometry and of the temperature profile yields

$$\begin{aligned} P_r &= -\, A_s\, \lambda(s)\, \frac{\partial T}{\partial s} \\ \Rightarrow \frac{\partial T}{\partial s} &= -\frac{P_r}{2\,\pi\, \lambda(s)\, s\, \ell_x}. \end{aligned} \tag{6.10}$$

---

[2] In the recent past, the shielding is sometimes 'abused' to carry high electric currents. The actual idea to prevent the generation of electric and magnetic fields is thus reduced to absurdity. The increase of electrical resistance for higher electric currents has to be taken into account for these cases, which will be subject of future investigations.

Integration over $s \in (d_5/2, d_2/2)$ provides

$$T_5 - T_2 \;=\; \frac{P_r}{\ell_x} \left(\sum_{j=2}^{4} \frac{1}{2\,\pi\,\lambda_j} \ln\left(\frac{d_j}{d_{j+1}}\right) \right) . \tag{6.11}$$

In order to respect the heat transfer from the surface of the insulation to the environment, we consider the difference of temperatures $T_2 - T_1$, given by

$$T_2 - T_1 = \frac{P_{\text{out}}}{\alpha\,\ell_x\,\pi\,d_2}, \tag{6.12}$$

where α denotes the heat transfer coefficient and P_{out} the heat power emitted to the environment. The second quantity is equal to the heat power P_r conducted from the centre to the surface. Hence, we get

$$T_5 - T_1 \;=\; \frac{P_r}{\ell_x} \left(\sum_{j=2}^{4} \frac{1}{2\,\pi\,\lambda_j} \ln\left(\frac{d_j}{d_{j+1}}\right) + \frac{1}{\alpha\,\pi\,d_2} \right) = \frac{P_r}{\pi\;\ell_x}\;\rho_w\,. \tag{6.13}$$

Therein, the parameter

$$\rho_w := \frac{1}{\alpha\,d_2} + \frac{1}{2} \sum_{j=2}^{4} \frac{1}{\lambda_j}\; \ln(d_j/d_{j+1}) \tag{6.14}$$

denotes the heat resistance of the core to the environment in radial direction.
Replacing ℓ_x in (6.13) by the infinitesimal length $\mathrm{d}x$, we finally obtain

$$\mathrm{d}P_r \;=\; \frac{\pi\,(T_5 - T_1)}{\frac{1}{\alpha\,d_2} + \frac{1}{2}\sum\limits_{j=2}^{4} \frac{1}{\lambda_j}\,\ln\left(\frac{d_j}{d_{j+1}}\right)}\;\mathrm{d}x = \frac{\pi\,(T_5 - T_1)}{\rho_w}\;\mathrm{d}x\,. \tag{6.15}$$

For simplification, we suppose constant values of α in the subsections ℓ_1, ℓ_2 and ℓ_3, which represents an idealizing assumption, enabling an explicit resolvability of (6.2). The heat transfer coefficients are determined by an a posteriori mean value iteration over the surface temperatures, described in Section 6.3.2 (Mean Value Iteration).

Replacement of the infinitesimal heat powers in (6.2), substitution of T_5 by T and division by $-\Lambda\,\mathrm{d}x$ provide the stationary equation for heat transfer in axial direction:

$$\boxed{\frac{\mathrm{d}^2 T(x)}{\mathrm{d}x^2} - B\,T(x) + C \;=\; 0,} \tag{6.16}$$

with

$$B = \frac{1}{\Lambda}\left(\frac{\pi}{\rho_w} - \frac{\rho_0\,\alpha_\rho\,I^2}{A_5}\right), \tag{6.17}$$

$$C = \frac{1}{\Lambda}\left(\frac{\pi\,T_1}{\rho_w} + \frac{\rho_0\,(1 - \alpha_\rho\,T_0)\,I^2}{A_5} + \frac{\rho_3\,I_3^2}{A_3}\right). \tag{6.18}$$

6.3.2 Computational Method

In the following, we divide the cable into three parts and assume piecewise constant coefficients. For the subsections of length ℓ_1, ℓ_2, ℓ_3 and ambient temperatures T_{11}, T_{12}, T_{13}, we define the axially variable core temperatures $T^{(1)}$, $T^{(2)}$, $T^{(3)}$.

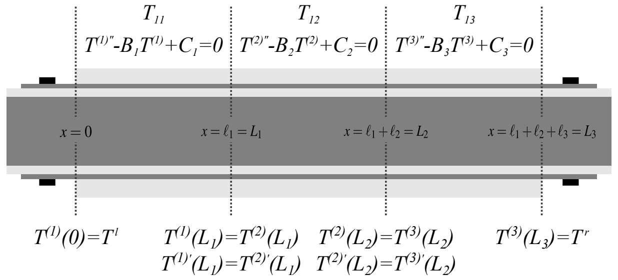

(a) Cable with fixed temperatures at both ends.

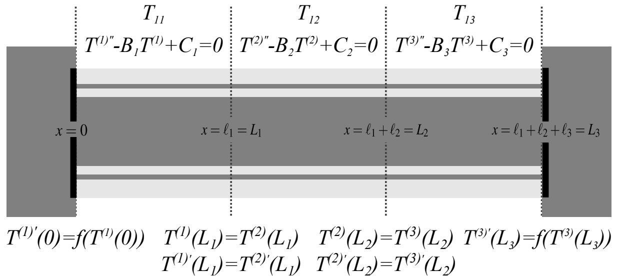

(b) Cable with attached objects.

Fig. 6.3: *Shielded cables with governing equations, boundary and interface conditions.*

Piecewise Constant Approximation of Equation Defining Coefficients

We refer to the coefficients B and C in (6.17) and (6.18) for each subsection by B_i and C_i:

$$B_i = B(\alpha_i) \quad \text{and} \quad C_i = C(T_{1i}), \quad i = 1, 2, 3.$$

A general solution of the inhomogeneous linear differential equation in (6.16) provides

$$\boxed{\begin{aligned} T^{(1)}(x) &= \vartheta_1 \exp(\sqrt{B_1}\,x) + \vartheta_2 \exp(-\sqrt{B_1}\,x) + \frac{C_1}{B_1}, \quad x \in (0, L_1),\\ T^{(2)}(x) &= \vartheta_3 \exp(\sqrt{B_2}\,x) + \vartheta_4 \exp(-\sqrt{B_2}\,x) + \frac{C_2}{B_2}, \quad x \in (L_1, L_2),\\ T^{(3)}(x) &= \vartheta_5 \exp(\sqrt{B_3}\,x) + \vartheta_6 \exp(-\sqrt{B_3}\,x) + \frac{C_3}{B_3}, \quad x \in (L_2, L_3), \end{aligned}} \tag{6.19}$$

with $\vartheta_1, \ldots, \vartheta_6$ to be determined and $L_i := \sum\limits_{j=1}^{i} \ell_j$.

Boundary and Interface Conditions

To get a unique solution of (6.19), appropriate boundary and interface conditions have to be formulated. As in some applications the temperatures of adjacent objects are known, we use Dirichlet boundary conditions for the first case (cf. Figure 6.3a). In the second case, we prescribe the heat flow at both ends of the cable by Robin boundary conditions (cf. Figure 6.3b).

The interface conditions read as

$$T^{(i)}(L_i) = T^{(i+1)}(L_i), \tag{6.20}$$

$$T^{(i)\prime}(L_i) = T^{(i+1)\prime}(L_i) \tag{6.21}$$

for $i = 1, 2$. Equation (6.20) represents the equality of the temperatures at the interface, Equation (6.21) is a result of the equality of the heat fluxes and equal heat conductivities at both sides of the interface.

The boundary conditions for the first case are

$$T^{(1)}(0) = T^l, \quad T^{(3)}(L_3) = T^r. \tag{6.22}$$

With (6.19), this results in a system of linear equations

$$\boxed{\mathbf{\Pi_1}\, \vartheta \;=\; \mathbf{b_1},} \tag{6.23}$$

with unknown vector $\vartheta = (\vartheta_1, \ldots, \vartheta_6)^T \in \mathbb{R}^6$, matrix $\mathbf{\Pi_1} \in \mathbb{R}^{6\times 6}$ respectively right hand side $\mathbf{b_1} \in \mathbb{R}^6$. Defining the abbreviations

$$\tau_{ij} := e^{\sqrt{B_i}\, L_j}, \qquad \tau_{-ij} := e^{-\sqrt{B_i}\, L_j},$$

$$\sigma_{ij} := \sqrt{B_i}\, \tau_{ij}, \qquad \sigma_{-ij} := \sqrt{B_i}\, \tau_{-ij},$$

the matrix $\mathbf{\Pi_1}$ and the right hand side $\mathbf{b_1}$ write as follows:

$$\mathbf{\Pi_1} = \begin{pmatrix} 1 & 1 & 0 & 0 & 0 & 0 \\ \tau_{11} & \tau_{-11} & -\tau_{21} & -\tau_{-21} & 0 & 0 \\ \sigma_{11} & -\sigma_{-11} & -\sigma_{21} & \sigma_{-21} & 0 & 0 \\ 0 & 0 & \tau_{22} & \tau_{-22} & -\tau_{32} & -\tau_{-32} \\ 0 & 0 & \sigma_{22} & -\sigma_{-22} & -\sigma_{32} & \sigma_{-32} \\ 0 & 0 & 0 & 0 & \tau_{33} & \tau_{-33} \end{pmatrix}, \tag{6.24}$$

$$\mathbf{b_1} = \left(T^l - \frac{C_1}{B_1}, \frac{C_2}{B_2} - \frac{C_1}{B_1}, 0, \frac{C_3}{B_3} - \frac{C_2}{B_2}, 0, T^r - \frac{C_3}{B_3} \right)^T. \tag{6.25}$$

For the second case, we consider contact resistances and the attached objects at the exterior boundary of the cable, i.e. at $x = 0$ and $x = L_3$, yielding the following power balance[3] (cf. Figure 6.4a):

$$P_{cab} - P^l_{ad} = P^l_k. \tag{6.26}$$

We denote P_{cab} the heat power emitted by the cable at the contact boundary, P^l_{ad} the heat power absorbed by the attached material and P^l_k the heat power generated by the contact resistance (the shielding current is excluded):

$$P_{cab} = -\Lambda\, T'(0), \tag{6.27}$$

$$P^l_{ad} = -\lambda^l_{ad}\, A_k\, T'_{ad}(0), \tag{6.28}$$

$$P^l_k = R^l_k\, I^2. \tag{6.29}$$

---

[3] We restrict to the boundary condition at $x = 0$. The one at $x = L_3$ is derived analogously.

Resolving (6.26) into $T'(0)$ provides

$$-T'(0) = \frac{P^l_{ad}}{\Lambda} + \frac{R^l_k\, I^2}{\Lambda}\,. \tag{6.30}$$

In order to formulate Equation (6.30) explicitly, we have to determine P^l_{ad} dependent on the asymptotic temperature T^l_{ad} and the temperature $T(0)$ at the contact. We suppose a spheric heat expansion in the attached material (cf. Figure 6.4b). Fourier's law implicates

$$P^l_{ad} \;=\; \lambda^l_{ad}\, A_R\, \frac{\mathrm{d}T^l_{ad}}{\mathrm{d}R}, \quad R \in (R_0, \infty)\,. \tag{6.31}$$

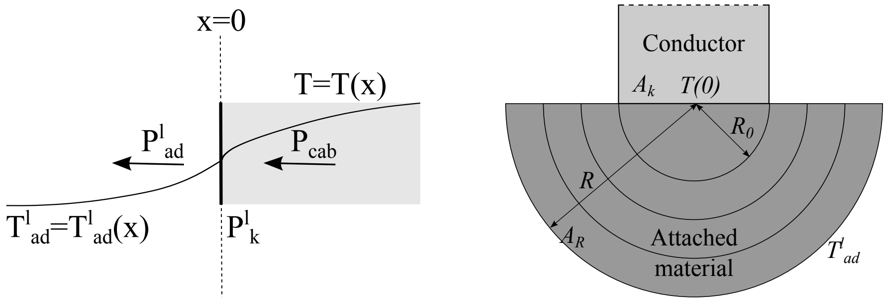

(a) Heat power balance at the left exterior boundary.

(b) Attached object characterized by λ^l_{ad} and T^l_{ad}.

Fig. 6.4: *Heat power balance and modelling of attached objects for shielded cables.*

Hence, the isotherms are located on hemispherical shells with $A_R = 2R^2\pi$. Separation of variables provides

$$\mathrm{d}T \;=\; \frac{-P^l_{ad}\,\mathrm{d}R}{2\pi\,\lambda^l_{ad}\,R^2} \tag{6.32}$$

and integration over $R \in (R_0, \infty)$ results in

$$\begin{aligned} T^l_{ad} - T(0) &= \frac{P^l_{ad}}{2\pi\lambda^l_{ad}\,R_0} \\ \Rightarrow P^l_{ad} \;&=\; 2\pi\lambda^l_{ad}\,R_0\,(T^l_{ad} - T(0))\,. \end{aligned} \tag{6.33}$$

Inserting (6.33) into (6.30), we obtain

$$T'(0) \;=\; \frac{2\pi\lambda^l_{ad}\,R_0}{\Lambda}\,(T(0) - T^l_{ad}) - \frac{R^l_k\,I^2}{\Lambda}. \tag{6.34}$$

Using a function f for the heat flux description at both ends (cf. Figure 6.3b) and $R_0 = d_2/2$, the boundary conditions read as follows:

$$f(T^{(1)}(0)) = \frac{\pi\,\lambda^l_{ad} d_2}{\Lambda}\left(T^{(1)}(0) - T^l_{ad}\right) - \frac{R^l_k\,I^2}{\Lambda}, \tag{6.35}$$

$$f(T^{(3)}(L_3)) = \frac{\pi\,\lambda^r_{ad} d_2}{\Lambda}\left(T^r_{ad} - T^{(3)}(L_3)\right) + \frac{R^r_k\,I^2}{\Lambda}. \tag{6.36}$$

Thus, the system of linear equations for the second case is

$$\boxed{\mathbf{\Pi_2}\,\vartheta \;=\; \mathbf{b_2},} \tag{6.37}$$

with

$$\mathbf{\Pi_2} = \begin{pmatrix} \Pi_{(11)} & \Pi_{(12)} & 0 & 0 & 0 & 0 \\ \tau_{11} & \tau_{-11} & -\tau_{21} & -\tau_{-21} & 0 & 0 \\ \sigma_{11} & -\sigma_{-11} & -\sigma_{21} & \sigma_{-21} & 0 & 0 \\ 0 & 0 & \tau_{22} & \tau_{-22} & -\tau_{32} & -\tau_{-32} \\ 0 & 0 & \sigma_{22} & -\sigma_{-22} & -\sigma_{32} & \sigma_{-32} \\ 0 & 0 & 0 & 0 & \Pi_{(65)} & \Pi_{(66)} \end{pmatrix}, \tag{6.38}$$

$$\mathbf{b_2} = \left(b_{(1)}, \frac{C_2}{B_2} - \frac{C_1}{B_1}, 0, \frac{C_3}{B_3} - \frac{C_2}{B_2}, 0, b_{(6)} \right)^T \tag{6.39}$$

and

$$\begin{aligned} \Pi_{(11)} &= \pi\, \lambda_{ad}^l\, d_2 - \Lambda\, \sqrt{B_1}, & \Pi_{(12)} &= \pi\, \lambda_{ad}^l\, d_2 + \Lambda\, \sqrt{B_1}, \\ \Pi_{(65)} &= \left(\pi\, \lambda_{ad}^r\, d_2 + \Lambda\, \sqrt{B_3} \right) \tau_{33}, & \Pi_{(66)} &= \left(\pi\, \lambda_{ad}^r\, d_2 - \Lambda\, \sqrt{B_3} \right) \tau_{-33}, \\ b_{(1)} &= R_k^l\, I^2 + \pi\, \lambda_{ad}^l\, d_2 \left(T_{ad}^l - \frac{C_1}{B_1} \right), & b_{(6)} &= R_k^r\, I^2 + \pi\, \lambda_{ad}^r\, d_2 \left(T_{ad}^r - \frac{C_3}{B_3} \right). \end{aligned}$$

By solving the linear system (6.23) respectively (6.37), we obtain $\vartheta_1, \ldots, \vartheta_6$ and determine the temperature profile in the core by $T^{(1)}$, $T^{(2)}$, $T^{(3)}$.

Mean Value Iteration

For an explicit solution of (6.16) in the three subsections, indexed by $i = 1, 2, 3$, we have to define a constant value for the heat transfer coefficient α in each subsection. To get adequate values α_1, α_2 and α_3, we compute

$$\begin{aligned} \bar{T}^{(i)} &= \frac{1}{\ell_i} \int\limits_{L_{i-1}}^{L_i} T^{(i)}(x)\, \mathrm{d}x \\ &= \frac{1}{\ell_i} \left(\frac{\vartheta_{2i-1}}{\sqrt{B_i}} \left(\tau_{ii} - \tau_{i(i-1)} \right) - \frac{\vartheta_{2i}}{\sqrt{B_i}} \left(\tau_{-ii} - \tau_{-i(i-1)} \right) \right) + \frac{C_i}{B_i} \end{aligned} \tag{6.40}$$

with $L_0 = 0$. This enables the determination of average temperatures at the exterior insulation according to [123] by

$$\bar{T}_2^{(i)} = \bar{T}^{(i)} - \frac{1}{2\pi} \left(\sum_{j=2}^{4} \frac{1}{\lambda_j} \ln \left(\frac{d_j}{d_{j+1}} \right) \right) \cdot \left(\frac{\rho_0\, (1 + \alpha_\rho(\bar{T}^{(i)} - T_0))\, I^2}{A_5} + \frac{\rho_3\, I_3^2}{A_3} \right) \tag{6.41}$$

and

$$\alpha_i = \alpha(\bar{T}_2^{(i)}). \tag{6.42}$$

Starting with $\bar{T}_{2,start}^{(i)}$, we solve the system of linear equations (6.23) respectively (6.37), obtaining the temperature profile defined piecewise in (6.19). The Equations (6.40), (6.41) and (6.42) then provide $\bar{T}_{2,1}^{(i)}$ respectively α_i. Repetition of this process leads to iteratively defined sequences $\big(\bar{T}_{2,k}^{(i)}\big)_{k\in\mathbb{N}}$, converging to final mean temperatures. The desired temperature profile is obtained as soon as the following stopping criterion with fixed $\epsilon > 0$ is fulfilled:

$$|\bar{T}_{2,k}^{(i)} - \bar{T}_{2,k-1}^{(i)}| < \epsilon. \tag{6.43}$$

To get favourable initial values for the fixed point iteration, we calculate asymptotic temperatures $\bar{T}_{2,start}^{(i)} := T_{2,as}^{(i)}$ at the surface by a procedure described in [123]. Therein, methods for the temperature determination of shielded cables without axial temperature profile are presented.

Convergence of the iterative procedure
We want to derive a sufficient condition for the convergence of the iterative procedure described in the previous paragraph. To this end, we define an auxiliary fixed point mapping $\mathbf{F}$ for the piecewise constant mean value temperatures $\bar{T}^{(i)}$ via the considerations in (6.3), (6.4) and (6.13) by

$$\bar{T}^{(i)} = T_{1i} + \frac{\rho_w^{(i)}}{\pi}\Big(p_k(\bar{T}^{(i)}) + p_s\Big) =: \mathbf{F}(\bar{T}^{(i)}), \tag{6.44}$$

with

$$p_k = \frac{\rho_0\, I^2\,(1+\alpha_\rho(\bar{T}^{(i)} - T_0))}{A_5}, \quad p_s = \frac{\rho_3\, I_3^2}{A_3} \tag{6.45}$$

and

$$\rho_w^{(i)} := \frac{1}{\alpha_l\, d_2} + \frac{1}{2}\sum_{j=2}^{4}\frac{1}{\lambda_j}\ln(d_j/d_{j+1}). \tag{6.46}$$

We identify $\rho_w^{(i)}$ by (6.14) in the subsection i, evaluated for the lowest heat transfer coefficient α_l, defined in (2.31). By analogy to (5.16), the function $\mathbf{F}$ provides an upper bound on the Lipschitz constant of the actual mapping of the mean value iteration with stopping criterion (6.43). The mapping $\mathbf{F}$ is a linear function in $\bar{T}^{(i)}$ with slope $\frac{\rho_0\,\alpha_\rho\, I^2\,\rho_w^{(i)}}{A_5\,\pi}$. Hence, the mapping $\mathbf{F}$ is contractive, if

$$\frac{\rho_0\,\alpha_\rho\, I^2}{A_5} < \frac{\pi}{\rho_w^{(i)}}, \tag{6.47}$$

i.e. if $B_i > 0$. On the other hand, $B_i > 0$ is the condition for a consistent evaluation of the temperature profiles in (6.19). Thus, by Banach's Fixed Point Theorem, $B_i > 0$ yields a sufficient condition for the convergence of the iterative procedure.

Following [35], Equation (6.47) is equivalent to a subresonance condition which ensures existence and uniqueness of solutions of the full stationary heat transfer problem. If condition (6.47) is not fulfilled, the electrical currents yield temperatures far from practical relevance in the stationary case. We explain this in detail in Section 6.4 and emphasize the similarity to our subresonance condition in (2.32).

6.3.3 Numerical Results

To check if our proposed computational approach is applicable in practice, we first perform a comparison to measurements. Afterwards, we present some examples on how to use it for thermal analysis. Finally, we show the validity and limitations of the approach in relation to finite elements.

Comparison of Measurements and Simulations

To test the calculation method concerning practical applicability, measurements were performed in the laboratories of the Labco GmbH. Therein, four different shielded cable types were loaded by constant electric currents in the core and the shielding for a sufficiently long time such that stationary temperatures were approximately attained. The four cable types with their geometrical, thermal and electrical properties are listed in Tables 6.1 and 6.2. They are labelled with respect to the cross sectional area of their core[4]. To compute the physical cross sectional area A_5^{ph} of the core and the geometrical A_5^{ge}, we introduce the diameter d_6 of the n_c conductors. This distinction is omitted for the shielding.

Tab. 6.1: *Properties of shielded cable types.*

Cable type	d_2 (mm)	d_3 (mm)	d_4 (mm)	d_5 (mm)	d_6 (mm)	n_c
FLR2GB2G 16	9.90	7.54	6.90	5.80	0.21	512
FLR2GB2G 25	11.90	9.34	8.50	7.20	0.21	790
FLR2GB2G 35	14.10	11.00	10.15	8.50	0.21	1070
FLR2GB2G 50	15.50	12.69	11.85	10.50	0.21	1600

Tab. 6.2: *Parameter values in computations of temperatures in shielded cables.*

Parameter name	Symbol	Value	Unit
Heat conductivity of the exterior and interior insulation	$\lambda_2,\ \lambda_4$	0.23	$\mathrm{W/(m \cdot K)}$
Heat conductivity of the shielding	λ_3	193	$\mathrm{W/(m \cdot K)}$
Heat conductivity of the cable core	λ_5	310	$\mathrm{W/(m \cdot K)}$
Electr. resistivity of the cable core at reference temperature	ρ_0	1.75e-8	$\Omega \cdot \mathrm{m}$
Temperature coefficient of the electr. resistivity in the cable core	α_ρ	3.93e-3	1/K
Electr. resistivity of the shielding	ρ_3	4.96e-8	$\Omega \cdot \mathrm{m}$
Specific heat capacity per volume of the conductors	γ_5	3.43e6	$\mathrm{J/(K \cdot m^3)}$
Specific heat capacity per volume of the shielding	γ_3	2.92e6	$\mathrm{J/(K \cdot m^3)}$
Emission coefficient	ϵ_r	0.93	
Ambient temperature	T_1	25	°C

Via thermocouples, temperatures of the core, the shielding and the environment were taken in the laboratories with $T_1 = T_{11} = T_{12} = T_{13} = 25\,^\circ\mathrm{C}$. An axial temperature distribution has not been measured, only temperatures at one position were examined. Thus, the comparison of our method is performed with a long cable ($> 10\,\mathrm{m}$) to neglect external influences by attached objects. Verifying the results of axial temperature distribution is subject of the next subsection (Comparison to Finite Element Simulations).

---

[4] The entire names of the cable tpyes are 'Coroplast $16\,\mathrm{mm}^2$ FLR2GB2G / T180', 'Coroplast $25\,\mathrm{mm}^2$ FLR2GB2G / T180', 'Coroplast $35\,\mathrm{mm}^2$ FLR2GB2G / T180' and 'Coroplast $50\,\mathrm{mm}^2$ FLR2GB2G / T180'.

	$I_3 = 0\,\mathrm{A}$				$I_3 = 20\,\mathrm{A}$			
I (A)	T^{me} (°C)	T^{com} (°C)	E (K)	e (%)	$T_{\mathrm{S}}^{\mathrm{me}}$ (°C)	$T_{\mathrm{S}}^{\mathrm{com}}$ (°C)	E (K)	e (%)
0	25	25	0	-	31	33	2	6.5
50	35	34	1	2.9	38	41	3	7.9
100	59	59	0	0.0	61	65	4	6.6
150	99	100	1	1.0	100	106	6	6.0
200	163	164	1	0.6	166	169	3	1.8
250	253	255	2	0.8	256	260	4	1.6

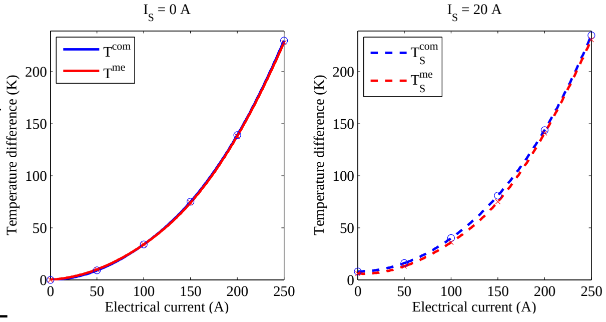

Fig. 6.5: *Measurements, calculations and deviations for FLR2GB2G 16.*

	$I_3 = 0\,\mathrm{A}$				$I_3 = 20\,\mathrm{A}$			
I (A)	T^{me} (°C)	T^{com} (°C)	E (K)	e (%)	$T_{\mathrm{S}}^{\mathrm{me}}$ (°C)	$T_{\mathrm{S}}^{\mathrm{com}}$ (°C)	E (K)	e (%)
0	25	25	0	-	28	30	2	7.1
80	36	37	1	2.8	37	41	4	10.8
160	69	72	3	4.4	70	75	5	7.1
240	129	133	4	3.1	132	137	5	3.8
295	196	196	0	0	198	199	1	0.5
345	286	270	16	5.6	287	273	14	4.9

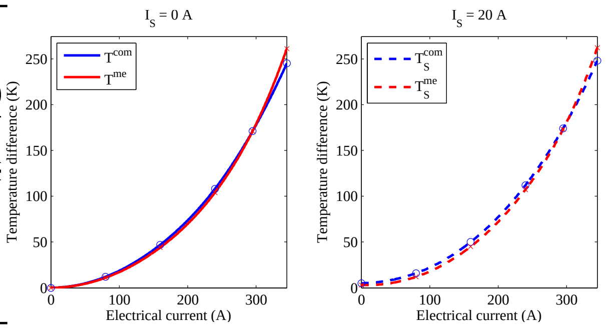

Fig. 6.6: *Measurements, calculations and deviations for FLR2GB2G 25.*

	$I_3 = 0\,\mathrm{A}$				$I_3 = 20\,\mathrm{A}$			
I (A)	T^{me} (°C)	T^{com} (°C)	E (K)	e (%)	$T_{\mathrm{S}}^{\mathrm{me}}$ (°C)	$T_{\mathrm{S}}^{\mathrm{com}}$ (°C)	E (K)	e (%)
0	25	25	0	-	27	29	2	7.4
87.5	33	35	2	6.1	36	38	2	5.6
175	57	63	6	10.5	60	66	6	10.0
262.5	100	111	11	11.0	104	113	9	8.7
350	172	186	14	8.1	177	188	11	6.2
400	233	243	10	4.3	237	246	9	3.8

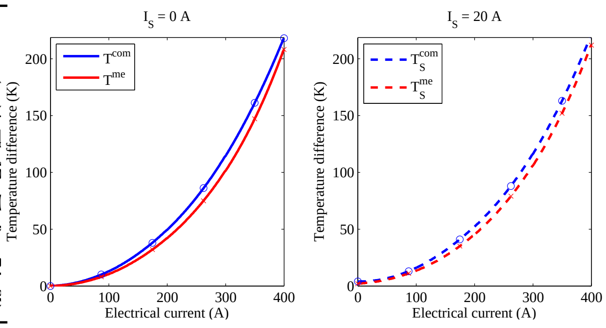

Fig. 6.7: *Measurements, calculations and deviations for FLR2GB2G 35.*

	$I_3 = 0\,\mathrm{A}$				$I_3 = 20\,\mathrm{A}$			
I (A)	T^{me} (°C)	T^{com} (°C)	E (K)	e (%)	$T_{\mathrm{S}}^{\mathrm{me}}$ (°C)	$T_{\mathrm{S}}^{\mathrm{com}}$ (°C)	E (K)	e (%)
0	25	25	0	-	27	28	1	3.7
125	34	37	3	8.8	37	40	3	8.1
250	65	71	6	9.2	68	73	5	7.4
375	122	132	10	8.2	124	134	10	8.1
500	220	228	8	3.6	227	230	3	1.3
535	261	263	2	0.8	268	265	3	1.1

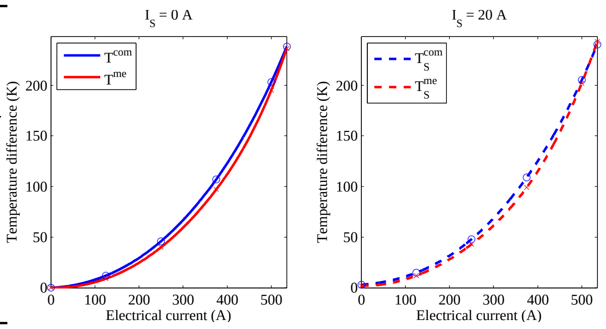

Fig. 6.8: *Measurements, calculations and deviations for FLR2GB2G 50.*

For comparison, we restrict to material parameters given by our industrial partners who have standard specifications for each cable type. All these material parameters have to be treated with caution. Consequently, relative errors of less than 10 % can hardly be expected.

Figures 6.5-6.8 show measurement and calculation results for the four cable types. Therein, we denote T^{me} the measured temperature, T^{com} the computed temperature, E the absolute difference between measurement and calculation and e the relative error[5]. Furthermore, $T_{\mathrm{S}}^{\mathrm{me}}$ represents the measured temperature in the core with a shielding carrying electric current and $T_{\mathrm{S}}^{\mathrm{com}}$ the corresponding computed temperature. The curves illustrate the differences of the measured and computed temperatures to the ambient temperature.

A maximum absolute difference of 16 K and a maximum relative error of 11 % confirm good accordance of the calculations and the measurements. As mentioned, an even better agreement cannot be expected because of the absence of exact material parameter values. Furthermore, the inaccuracies of the measurements essentially influence the listed errors.

By tendency, the calculated temperatures are higher than the measured ones, except for cable of cross sectional area $25\,\mathrm{mm}^2$ and $I = 345\,\mathrm{A}$. For this case, measurement problems or deviations of the actual conductor diameters to the indicated ones seem likely.

Further Calculation Results

To illustrate the possibilities our method offers, we calculate temperature profiles with varying parameters. First, we examine the influence of different electrical currents (cf. Figure 6.9). We suppose the temperatures of the attached objects to be $T^l = 80\,°\mathrm{C}$ and $T^r = 70\,°\mathrm{C}$ and the ambient temperatures $T_{11} = 60\,°\mathrm{C}$, $T_{12} = 10\,°\mathrm{C}$ and $T_{13} = 90\,°\mathrm{C}$ with cable lengths $\ell_1 = 1\,\mathrm{m}$, $\ell_2 = 1.50\,\mathrm{m}$ and $\ell_3 = 1\,\mathrm{m}$. The cable type is FLR2GB2G 16 and the shielding carries a current of $I_3 = 40\,\mathrm{A}$.

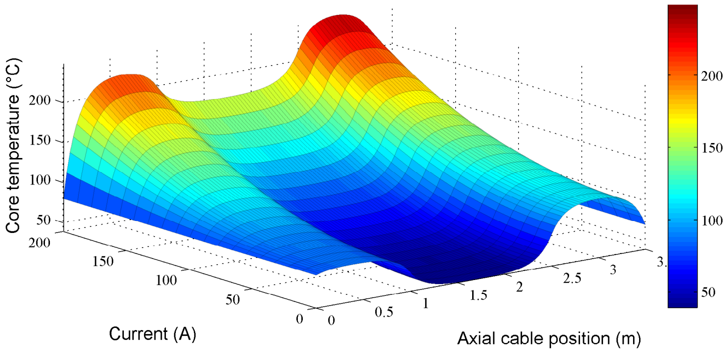

Fig. 6.9: *Axial core temperatures of a shielded cable for varying electric currents.*

Assumed that the cable would not endure temperatures above 200 °C, current loads higher than 170 A would be unfavourable for this type of cable and the specific scenario. Note that in the middle section with lower ambient temperature T_{12}, the cable is colder than in the other parts. Taking this into account is important in the dimensioning of concrete on-board systems and cable harnesses. Furthermore, upper bounds for electric current loads can be determined by these kinds of simulations.

---

[5] In this context, the measure e represents the ratio of the difference between measured and computed temperature in K to the measured temperature in °C.

We consider a second scenario. If the manufacturer wants to choose the appropriate cable type for fixed currents, the temperature distribution in different cable types can be compared (cf. Figure 6.10). We take the same parameters as in the precedent case with a fixed current of $I = 200\,\mathrm{A}$ in the core. As expected, the temperature increases for smaller cross sections of the cables. Supposed the temperature in the cable must not exceed the critical value of 150 °C – possibly corresponding to the melting temperature of the insulation – the manufacturer shall choose the cable type of cross sectional area $35\,\mathrm{mm}^2$.

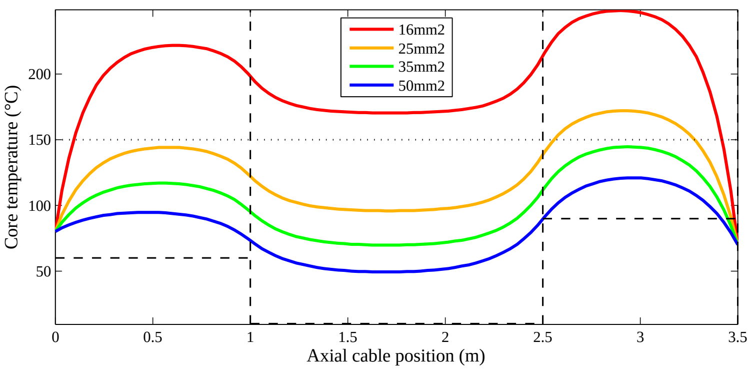

Fig. 6.10: *Temperature distribution in different types of shielded cables for an equal scenario with fixed boundary temperatures.*

Since the connected electric components only work at specific voltages, information about the voltage drop on the core of the cable is necessary. It is calculated via Ohm's law $\Delta U = R \cdot I$, with R denoting the temperature dependent resistance (cf. Equation (6.1) for its calculation). For the previous example and each cable type, the voltage drop is shown in Figure 6.11.

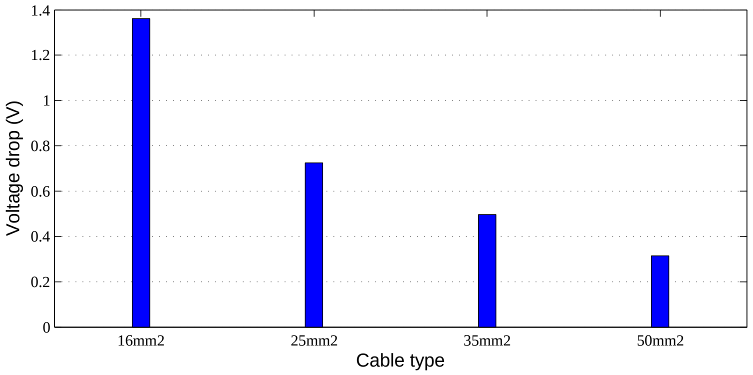

Fig. 6.11: *Voltage drop in different types of shielded cables for an equal scenario.*

Figures 6.12 and 6.13 show a variation of the temperature T^l at the left end in a longer and a shorter cable. Note that the parameter values are nearly the same as in the previous examples, except for the current $I_3 = 35\,\mathrm{A}$ in the shielding. This explains the slightly lower temperatures in the second part of the cable with entire length $\ell = 3.5\,\mathrm{m}$. Observe that the influence of the boundary temperature in the shorter cable is more significant, whereas the varying ambient temperature has a stronger impact on the heat distribution in the longer cable.

It is interesting that in Figure 6.12 the curves for different temperatures at the left end cross each other. This effect can be explained by the heat transfer coefficient. As mentioned in Subsection 6.3.2 (Mean Value Iteration), its value is computed depending on the mean temperature of the surface in each subsection. Thus, a lower temperature at the left end of the cable implies a lower mean temperature in this subsection and thus a smaller value of α. This in turn means that less energy can dissipate from the cable, resulting in higher temperatures. Near the left end, the effect of the smaller temperature at the boundary dominates, whereas at the right end of the cable section (in our example at $x = 1\,\mathrm{m}$), the second effect is more important.

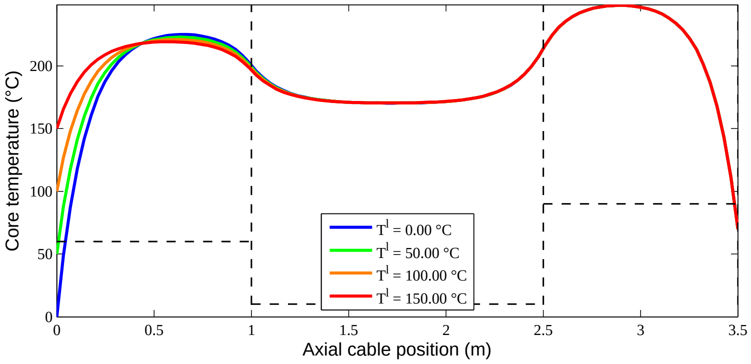

Fig. 6.12: *Variation of the temperature of the left object for a long shielded cable.*

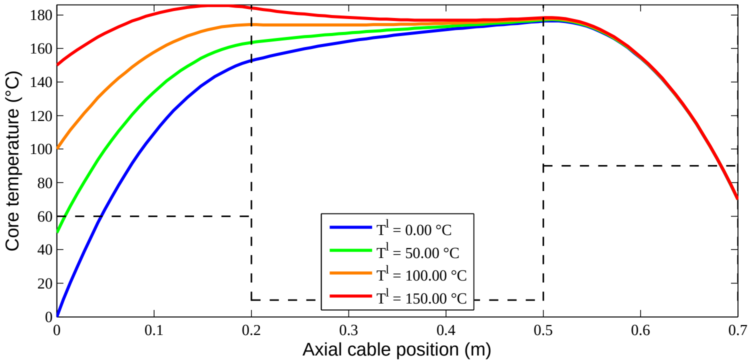

Fig. 6.13: *Variation of the temperature of the left object for a short shielded cable.*

One expects that higher current densities imply higher temperatures at the boundaries. Hence, the temperature profiles with Dirichlet conditions in Figure 6.10 are rather non-physical at the boundaries. Therefore, the same simulations are performed with respect to Robin boundary conditions discussed in Section 6.4.2.

In Figure 6.14, we apply asymptotic temperatures $T^l_{ad} = 80\,°\mathrm{C}$, $T^r_{ad} = 70\,°\mathrm{C}$, contact resistances $R^l_k = 1\,\mathrm{m}\Omega$, $R^r_k = 1\,\mathrm{m}\Omega$, and heat conductivities $\lambda^l_{ad} = 10\,\mathrm{W}/(\mathrm{m}\cdot\mathrm{K})$, $\lambda^r_{ad} = 10\,\mathrm{W}/(\mathrm{m}\cdot\mathrm{K})$, of the two attached objects. The modified boundary conditions hardly influence the inner temperature profile, but yield more realistic results at both ends of the cable. The reason for the minor influence in the middle section is the great length of the cable. Note that the resulting temperature at the point of contact is lower for the cable type of $16\,\mathrm{mm}^2$ than in the core of the cable, which results in decreasing temperatures towards

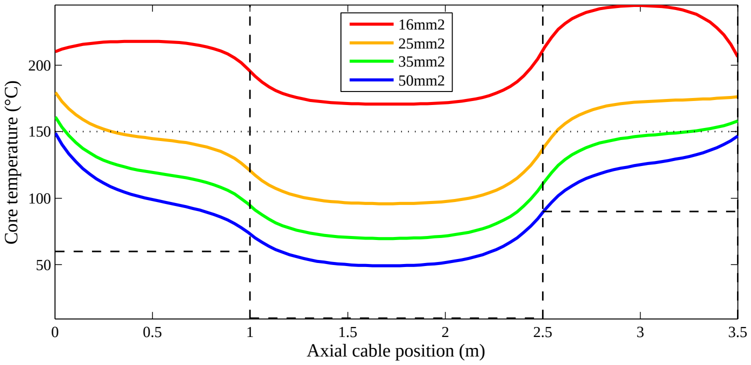

Fig. 6.14: *Temperature distribution in different types of shielded cables for an equal scenario with exterior Robin boundary conditions.*

the exterior ends. In contrast, the temperature at the point of contact is higher for the other cable types, which results in increasing temperatures towards the boundaries.

Comparison to Finite Element Simulations

In order to check the validity of our heat power balance approach (HBA), but also to demonstrate its limitations, we performed some numerical experiments with finite elements on the scenarios of the previous Paragraph 6.3.3 (Further Calculation Results). Special attention is paid to the question whether the axial temperature distribution in the core is modelled adequately.

For the finite element computations, we apply quadratic Lagrange elements, the standard Newton-Raphson solver with relative accuracy $\epsilon = 1.0e\text{-}6$ respectively maximum number of iterations $i_{\max} = 25$ in Algorithm 2. Moreover, we use the direct solver PARDISO for the solution of resulting systems of linear equations.

Figures 6.15a, 6.16a and 6.17a depict the simulation results obtained via FEM in solid lines and those computed via the HBA with dashed lines, Figures 6.15b, 6.16b and 6.17b show the deviations between the results of both computational methods.

The qualitative progressions of the heat distributions, obtained with the HBA and with finite elements, coincide well (cf. Figures 6.15 – 6.17). Nevertheless, some deviations are obvious. In Figure 6.15, the maximum deviation is more than 10 K. Apart from some computational simplifications like the equating of temperature gradients in axial direction (cf. Equation (6.6)), the main contribution to this error is the application of constant values for α in each subsection. If we consider cable type FLR2GB2G 16 in Figure 6.10, the maximum temperature (248.4 °C) in the third cable subsection is much higher than the lowest (70 °C at right end of the cable) and the mean value (219.4 °C). Since the heat transfer for fixed characteristic lengths and constant ambient temperatures is a monotonically increasing function with respect to the temperature at the surface, the *local* heat transfer coefficient (which is computed in the finite element simulations) at the position with maximum temperature has a higher value than the average heat transfer coefficient in the third subsection. Hence, in the finite element simulation, more heat power is emitted to the environment than in the simulation of the HBA, which finally yields lower (maximum) temperatures in the finite element calculations. Consequently, the temperatures in the third subsection are overestimated via the HBA. Obviously, the discrepancy in the second subsection is much lower due to a smaller difference between minimum and maximum temperature. A subdivision into

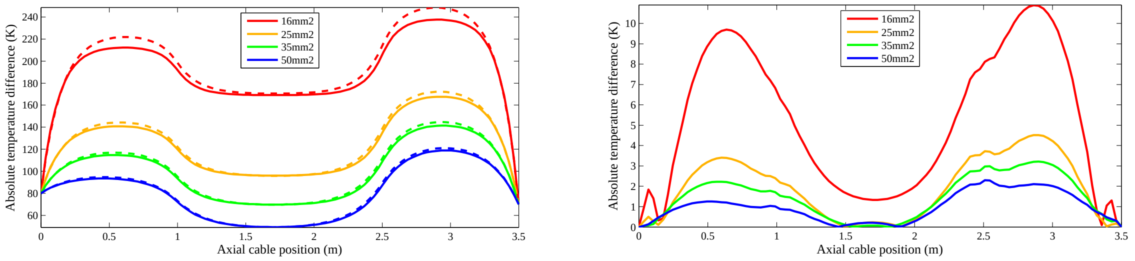

(a) Temperature distributions computed with finite elements for different types of shielded cables. The dashed lines show the temperatures obtained via the HBA (cf. Figure 6.10).

(b) Absolute temperature differences between the computations with finite elements and the HBA.

Fig. 6.15: *Temperature distribution computed with finite elements for the same current loads and exterior temperatures like in Figure 6.10, and absolute deviations to results of the HBA.*

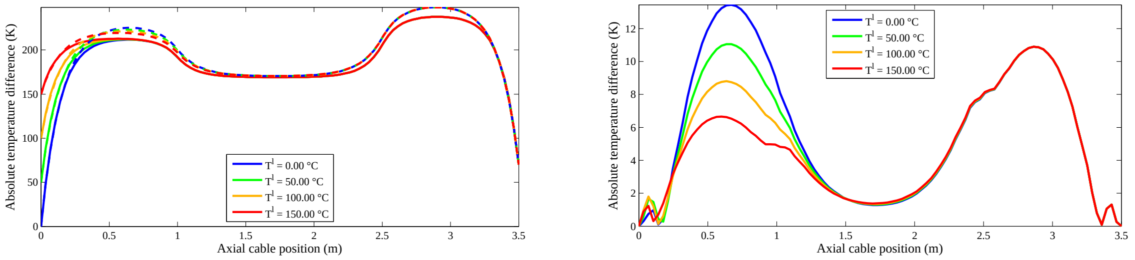

(a) Temperature distributions computed with finite elements for varying temperatures of the left object. The dashed lines show the temperatures obtained via the HBA (cf. Figure 6.12).

(b) Absolute temperature differences between the computations with finite elements and the HBA.

Fig. 6.16: *Temperature distribution computed with finite elements for the same current loads and exterior temperatures like in Figure 6.12, and absolute deviations to results of the HBA.*

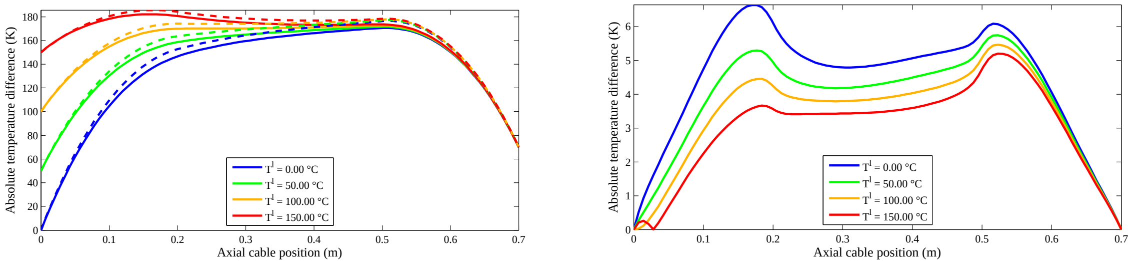

(a) Temperature distributions computed with finite elements for a short shielded cable. The dashed lines show the temperatures obtained via the HBA (cf. Figure 6.13).

(b) Absolute temperature differences between the computations with finite elements and the HBA.

Fig. 6.17: *Temperature distribution computed with finite elements for the same current loads and exterior temperatures like in Figure 6.13, and absolute deviations to results of the HBA.*

more subsections would reduce this error, but requires higher computational effort.

The mentioned effect is also observable in the first subsection of the cable in Figure 6.16. For a low temperature (e.g. $T^l = 0\,°\mathrm{C}$) at the left end of the cable, the temperature in the subsection varies more intensely than for a high one (e.g. $T^l = 150\,°\mathrm{C}$) and thus, a mean heat transfer coefficient is less adequate. The smaller deviations in Figure 6.17 with less than 7 K can be explained by the generally smaller temperatures in the shorter cable, but the relative error is approximately of the same magnitude.

6.4 Transient Case

In the following, we extend our computational model to the non-stationary situation. In contrast to the considerations in Section 5.2.2, the current in the core may be time-dependent. This requires some additional modifications, although we mostly resort to the previously introduced approaches.

6.4.1 General Modelling

Applying our model of (2.29) to a shielded cable, the evolution of temperature $T = T(\mathbf{x}, t)$ is determined by the following initial boundary value problem:

$$\gamma(\mathbf{x})\,\frac{\partial T}{\partial t} - \nabla\cdot(\lambda(\mathbf{x})\,\nabla T) = f(\mathbf{x},t) + r(\mathbf{x},T) \qquad \text{with } \mathbf{x}\in Z_2^L,\ t\in[0,t_{max}], \tag{6.48a}$$

$$-\lambda_2\,\frac{\partial T}{\partial \mathbf{n}} = \alpha(T)\,(T - T_1) \qquad \text{with } \mathbf{x}\in \partial B_{d_2}\times[0,L],\ t\in[0,t_{max}], \tag{6.48b}$$

$$T(\mathbf{x},0) = T_{\text{init}} \qquad \text{with } \mathbf{x}\in Z_2^L. \tag{6.48c}$$

Therein, the set $Z_2^L := B_{d_2}\times[0,L]$ represents the cable cylinder of length $L = \ell_1 + \ell_2 + \ell_3$ and diameter d_2. The temperature independent power densities in the core Z_5^L and the shielding $Z_3^L \setminus Z_4^L$ of the cable are defined piecewise by

$$f(\mathbf{x},t) := \frac{\rho_0\,I^2}{A_5^2}\,\mathbb{I}_{Z_5^L}(\mathbf{x}) + \frac{\rho_3\,I_3^2}{A_3^2}\,\mathbb{I}_{Z_3^L\setminus Z_4^L}(\mathbf{x}). \tag{6.49}$$

The temperature dependent part of the power density in the core[6] is

$$r(\mathbf{x},T) := \frac{\rho_0\,\alpha_\rho\,I^2(T-T_0)}{A_5^2}\,\mathbb{I}_{Z_5^L}(\mathbf{x}). \tag{6.50}$$

At $B_{d_2}\times\{0,L\}$, which represents the tails of the cylinder, the temperature T fulfils the boundary conditions specified in Section 6.3.2 (Boundary and Interface Conditions).

Remark 12. *Like in the stationary case, we neglect the temperature dependence of the resistivity of the shielding and with this, its temperature dependent part of the power density. This is admissible, since the heat produced in the shielding is low compared to the heat generated in the core. Furthermore, the shielding current is usually constant in time.*

---

[6] In contrast to the previous subsection, $r(\cdot,\cdot)$ now denotes a function and not a radius.

Remark 13. *The electrical currents in core and shielding are supposed to be equally distributed. Hence, we get a rotationally symmetric heat distribution, characterized by* $T_2(x,t)$*,* $T_3(x,t)$*,* $T_4(x,t)$*,* $T_5(x,t)$*. Note that the temperatures* $T_2, \dots, T_5$ *depend in space on the axial coordinate* $x \in [0, L]$*. As the temperature in the core is the most relevant in practice, we restrict to the computation of* T_5*.*

6.4.2 Computational Method

In order to distinguish between a quasi-stationary and instationary case, we first derive a limiting current I_{lim}. An efficient method to determine temperatures via interpolation in case of quasi-stationary dynamics is presented as well as an approach for the instationary dynamics. Both cases are summarized in a general recursive scheme. Finally, we specify the trisection of the cable and the boundary conditions at its tails.

Determination of the Limiting Current

Due to the specific form of the governing Equation (6.48a), there exist (constant) current loads for which no stationary temperature will be reached. Hence, there holds $\lim_{t\to\infty} T(t) = \infty$. According to the theory of elliptic PDEs [22, 76, 90], this is a resonance effect. Analogously to the definition (5.22) for insulated single-core cables, the resonance current I_{res} for shielded cables is given by

$$\rho_0 \, \alpha_\rho \, I_{\text{res}}^2 = \frac{\pi \, A_5}{\frac{1}{2} \sum_{i=2}^{4} \frac{1}{\lambda_i} \, \ln\left(d_i / d_{i+1} \right)} . \tag{6.51}$$

The resonance current, and in most cases (slightly) smaller currents, would not yield a reasonable solution for the temperature T in Equation (6.16). This is due to the fact that the solution depends on $\sqrt{B}$ (cf. (6.19)) with B introduced in (6.17). Thus, we define a limiting current $I_{\text{lim}} < I_{\text{res}}$ for which $B = 0$ holds. This is equivalent to

$$\rho_0 \, \alpha_\rho \, I_{\text{lim}}^2 = \frac{\pi \, A_5}{\frac{1}{\alpha \, d_2} + \frac{1}{2} \sum_{i=2}^{4} \frac{1}{\lambda_i} \, \ln\left(d_i / d_{i+1} \right)} . \tag{6.52}$$

Hence, the condition $I < I_{\text{lim}}$ yields a sufficient condition for the existence of a stationary temperature profile ($t \to \infty$) of (6.48). The condition $B = 0$ distinguishes between a concave ($B > 0$) and convex ($B < 0$) temperature evolution close to $t = 0$.

Quasi-Stationary Dynamics

First, we consider constant electric currents below the limiting current I_{lim}. In order to compute temperature evolutions in the core of shielded cables, we reduce the full problem to the core. Afterwards, we derive an interpolation approach for the calculation of temperatures.

Reduction of the Initial Boundary Value Problem to the Cable Core

We obtain stationary temperatures T_{s5} and T_{s2} in the core and at the exterior boundary of the outer insulation, if $I < I_{\mathrm{lim}}$ holds. Analogously to (5.23), we define a temperature ratio for the stationary case, with T_1 assumed to be constant:

$$\eta_s := \frac{T_{s2} - T_1}{T_{s5} - T_1}. \tag{6.53}$$

This temperature ratio is supposed to be invariant in time. Hence, for the transient temperature ratio $\eta(t) := \frac{T_2(t)-T_1}{T_5(t)-T_1}$, we postulate again $\eta(t) = \eta_s \ \forall\, t \in [0, t_{\max}]$. Note that at this stage, the electric current is supposed to be constant in time. Later, it will vary in time and thus, the value of $\eta(t)$ can change from one time step to the next.

Our assumption holds especially well for thin insulation layers. We discuss it in detail for shielded cables in Section 6.4.3 (Discussion). It allows a reduction of the full problem in (6.48) to the core Z_5^L of the cable. To this end, we transform the outer boundary condition in (6.48b) to a condition of the boundary of the core.

An entire heat power balance for insulation and shielding of a shielded cable is given by

$$\int\limits_{Z_3^L \setminus Z_4^L} \frac{\rho_3\, I_3^2}{A_3^2}\,\mathrm{d}\mathbf{x} + \int\limits_{\partial Z_5^L} \lambda_5\,\frac{\partial T}{\partial \mathbf{n}}\,\mathrm{d}\sigma \;=\; \int\limits_{\partial Z_2^L} \lambda_2\,\frac{\partial T}{\partial \mathbf{n}}\,\mathrm{d}\sigma + \int\limits_{Z_2^L \setminus Z_5^L} \gamma(\mathbf{x})\,\frac{\partial T(\mathbf{x},t)}{\partial t}\,\mathrm{d}\mathbf{x}. \tag{6.54}$$

As stated in Remark 12, the source term of the shielding does not depend on the temperature in our model. Hence, according to [35, p. 51–52], it is not relevant for the dynamics, and consequently, we neglect it. Furthermore, we do not take into account the capacitive absorption of the heat power. This yields an estimate from below for the corresponding heating times, relevant for applications. Thus, conservation of energy with the mentioned simplifications provides equality of the emitted heat power of the core and the exterior boundary of the outer insulation:

$$\int\limits_{\partial Z_5^L} \lambda_5\,\frac{\partial T}{\partial \mathbf{n}}\,\mathrm{d}\sigma \;=\; \int\limits_{\partial Z_2^L} \lambda_2\,\frac{\partial T}{\partial \mathbf{n}}\,\mathrm{d}\sigma. \tag{6.55}$$

We approximate the axial temperature profile by piecewise constant functions (which corresponds to a discrete L_1 approximation of the temperature profile) and state a heat power balance like (6.55) in each axial subsection. Summing up the heat power balances of all subsections yields[7]

$$\begin{aligned}
\pi\, d_5\, L\, \lambda_5\, \frac{\partial T}{\partial \mathbf{n}}\Big|_{\partial Z_5^L} = \pi\, d_2\, L\, \lambda_2\, \frac{\partial T}{\partial \mathbf{n}}\Big|_{\partial Z_2^L} &\overset{(6.48b)}{=} -\pi\, d_2\, L\, \alpha(T_2)\,(T_2 - T_1) \\
\Longleftrightarrow \quad -\lambda_5\,\frac{\partial T}{\partial \mathbf{n}} = \frac{d_2}{d_5}\,\alpha(T_2)\,(T_2 - T_1) &\quad \text{on} \ \ \partial Z_5^L.
\end{aligned}$$

The temperature ratio $\eta(t)$ provides a modification of (6.48b):

$$-\lambda_5\,\frac{\partial T}{\partial \mathbf{n}} = \frac{d_2}{d_5}\,\alpha\big(\eta(t)\,T_5 + (1-\eta(t))\,T_1\big)\,\eta(t)\,(T_5 - T_1) \quad \text{on} \ \ \partial Z_5^L. \tag{6.56}$$

We rewrite (6.56) with $\beta(T_5) := \alpha\big(\eta(t)\,T_5 + (1-\eta(t))\,T_1\big)\,\eta(t)$ by

$$-\lambda_5\,\frac{\partial T}{\partial \mathbf{n}} = \frac{d_2}{d_5}\,\beta(T_5)\,(T_5 - T_1) \quad \text{on} \ \ \partial Z_5^L.$$

---

[7] Note that the neglect of the axial dependence of the heat power change is only used to project the boundary condition of the insulation to the core. However, in the final formulas for the temperatures in the core, the axial dependency is respected.

Interpolation between Initial and Stationary Temperature

Problem (6.48) reduced to the core of the cable reads as

$$\begin{aligned} \gamma_5 \frac{\partial T}{\partial t} - \nabla \cdot (\lambda_5 \nabla T) &= \tilde{f} + \tilde{r}(T) && \text{with } \mathbf{x} \in Z_5^L,\ t \in [0, t_{max}], \\ \lambda_5 \frac{\partial T}{\partial \mathbf{n}} &= \beta(T)(T - T_1) && \text{with } \mathbf{x} \in \partial B_{d_5} \times [0, L],\ t \in [0, t_{max}], \\ T(\mathbf{x}, 0) &= T_{\text{init}} && \text{with } \mathbf{x} \in Z_5^L. \end{aligned} \tag{6.57}$$

Therein, we define $\tilde{r} := \frac{\rho_0\, \alpha_\rho\, I^2 (T - T_0)}{A_5^2}$ and $\tilde{f} := \frac{\rho_0\, I^2}{A_5^2}$. Thus, the stationary temperature in the core $T_{s5} =: T_s$ fulfils the equations

$$\begin{aligned} -\lambda_5\, \Delta T_s &= \tilde{f} + \tilde{r}(T_s) && \text{with } \mathbf{x} \in Z_5^L, \\ -\lambda_5 \frac{\partial T_s}{\partial n} &= \frac{d_2}{d_5}\, \beta\,(T_s)\,(T_s - T_1) && \text{with } \mathbf{x} \in \partial B_{d_5} \times [0, L]. \end{aligned} \tag{6.58}$$

Dvorsky's thesis [35, p. 54] provides the convergence of the dynamic solution of (6.57) to the stationary solution of (6.58) by

$$|T_s(x) - T(x,t)| \leq e^{-\tilde{\phi}\, t}\ |T_s(x) - T_{\text{init}}|\,, \quad x \in [0, L], \quad t \in [0, t_{max}], \tag{6.59}$$

with $\tilde{\phi} = \frac{1}{\gamma_5} \left(\frac{d_2\, \tilde{\beta}}{d_5^2} - \frac{\rho_0\, \alpha_\rho\, I^2}{A_5^2} \right)$, $\tilde{\beta} = \beta(T_s)$.

Remark 14. *We apply an interpolation factor*

$$\phi = \frac{1}{A_5\, \gamma_5} \left(\pi\, d_2\, \tilde{\beta} - \frac{\rho_0\, \alpha_\rho\, I^2}{A_5} \right) \tag{6.60}$$

that is larger than the interpolation factor $\tilde{\phi}$. It improves the rather pessimistic estimation of $\tilde{\phi}$ and is more relevant for practical applications. The formulas (6.12) and (6.13) of the stationary case for $T_{s2} - T_1$ and $T_{s5} - T_1$ yield

$$\eta_s = \left(1 + \alpha\, d_2\, \frac{1}{2} \sum_{i=2}^{4} \frac{1}{\lambda_i}\, \ln\left(d_i / d_{i+1} \right) \right)^{-1}. \tag{6.61}$$

This and B from (6.17) provide $\phi = \frac{\Lambda}{A_5\, \gamma_5} B$. Consequently, the enlargement of $\tilde{\phi}$ to ϕ is justified by the plausibility condition $\phi > 0 \Leftrightarrow B > 0$. The convergence to a stationary state is fulfilled ($\phi > 0$), if and only if a stationary state exists ($B > 0$).

Condition (6.59) yields an upper bound for the difference between the sought-for temperature $T(x,t)$ at time t and the temperature T_s for the stationary state. If we additionally assume that the temperature increases over time, we identify $T(x,t)$ by the following approximative interpolation:

$$T(x,t)\ =\ e^{-\phi\, t}\, T_{\text{init}}(x) + (1 - e^{-\phi\, t})\, T_s(x) \quad x \in [0, L],\ t \in [0, t_{max}]. \tag{6.62}$$

Hence, an interpolation in $[t_0, t_1] \subset [0, t_{max}]$, with $T(t_0) := T^{(0)}$, $T(t_1) := T^{(1)}$, yields

$$\boxed{T^{(1)}\ =\ e^{-\phi\, (t_1 - t_0)}\, T^{(0)} + (1 - e^{-\phi\, (t_1 - t_0)})\, T_s.} \tag{6.63}$$

Instationary Dynamics

For constant electric currents $I \geq I_{\text{lim}}$, the presented interpolation approach is no more reasonable, as the existence of a stationary temperature T_s in the core is not ensured. Due to very short heating times, we neglect the capacity term of the insulation and the heat power emitted via the surface of the cable. Furthermore, we set $\mathrm{d}T = \mathrm{d}T_5 = \mathrm{d}T_3$. Thus, we obtain

$$\mathrm{d}E_{\gamma_{3,5}} = \mathrm{d}P_{\rho_{3,5}}\,\mathrm{d}t \tag{6.64}$$

with the stored energy $\mathrm{d}E_{\gamma_{3,5}} := (\gamma_3\,A_3 + \gamma_5\,A_5)\,\mathrm{d}T$ and the generated heat power $\mathrm{d}P_{\rho_{3,5}} := \left(\frac{\rho_3\,I_3^2}{A_3} + \frac{\rho(T)\,I^2}{A_5}\right)$ in core and shielding during $\mathrm{d}t$. Finally, we only consider the two terms $\mathrm{d}E_{\gamma_{3,5}}$ and $\mathrm{d}P_{\rho_{3,5}}\,\mathrm{d}t$, as the energy stored in the core and the shielding as well as the energy generated by electric current in core and shielding represent the most relevant parts for the short time heating with intense currents.

Separation of variables and integration of (6.64) over $[t_0, t_1]$, $t_0, t_1 \in [0, t_{\max}]$, provide

$$t_1 - t_0 = (\gamma_3\,A_3 + \gamma_5\,A_5) \int\limits_{T^{(0)}}^{T^{(1)}} \frac{1}{\frac{\rho_3\,I_3^2}{A_3} + \frac{\rho(T)\,I^2}{A_5}}\,\mathrm{d}T. \tag{6.65}$$

Hence, we obtain

$$\frac{\rho(T^{(1)})\,I^2}{A_5} = \exp\left(\phi_{inst}(t_1 - t_0)\right)\left(\frac{\rho_3\,I_3^2}{A_3} + \frac{\rho(T^{(0)})\,I^2}{A_5}\right) - \frac{\rho_3\,I_3^2}{A_3}. \tag{6.66}$$

Therein, $\phi_{inst} := \frac{\rho_0\,\alpha_\rho\,I^2}{A_5\,(\gamma_3\,A_3 + \gamma_5\,A_5)}$ denotes the instationary interpolation factor. Consequently, we get

$$\boxed{T^{(1)} = \frac{\frac{A_5\,\rho_3\,I_3^2}{A_3\,\rho_0\,I^2}\,(e_1 - 1) + \left(1 + \alpha_\rho(T^{(0)} - T_0)\right)\,e_1 - 1}{\alpha_\rho} + T_0,} \tag{6.67}$$

with $e_1 := \exp\left(\phi_{inst}\,(t_1 - t_0)\right)$. The current $I = 0$ is excluded because of the condition for the instationary case $I \geq I_{\text{lim}} > 0$ as well as $\alpha_\rho = 0$, since there is no resonance effect.

Recursion for Arbitrary, Time-Dependent Current Loads

We consider an arbitrary electric current $I = I(t)$, $t \in [0, t_{\max}]$, in the core, a constant current I_3 in the shielding and a time-dependent temperature $T = T(x,t)$ in the core. We divide the interval $[0, t_{max}]$ equidistantly by $0 = t_0 < t_1 < \ldots < t_{n_t} = t_{\max}$ into n_t intervals $[t_{i-1}, t_i]$, $i = 1,..,n_t$. Thus, the length of the time steps is given by $\delta := t_i - t_{i-1} = {}^{t_{\max}}/_{n_t}$. We define the associated temperatures in the core by $T^{(i)} = T(x, t_i)$, $i = 0,..,n_t$. The current I is approximated by a piecewise constant current $\tilde{I}(t) = I^{(i)}$ for $t \in [t_{i-1}, t_i]$ with $I^{(i)} = I(t_{i-1})$, $i = 1, \ldots, n_t$.

Using (6.63) and (6.67), we now deploy a recursive scheme for the evolution of the core temperature $\left(T^{(i)}\right)_{i=0}^{n_t}$. We define the initial axial temperature profile $T^{(0)}$ with $I = 0$ according to the results of the stationary case. Then, the temperature profiles $\left(T^{(i)}\right)_{i=1}^{n_t}$ are given by the following recursion:

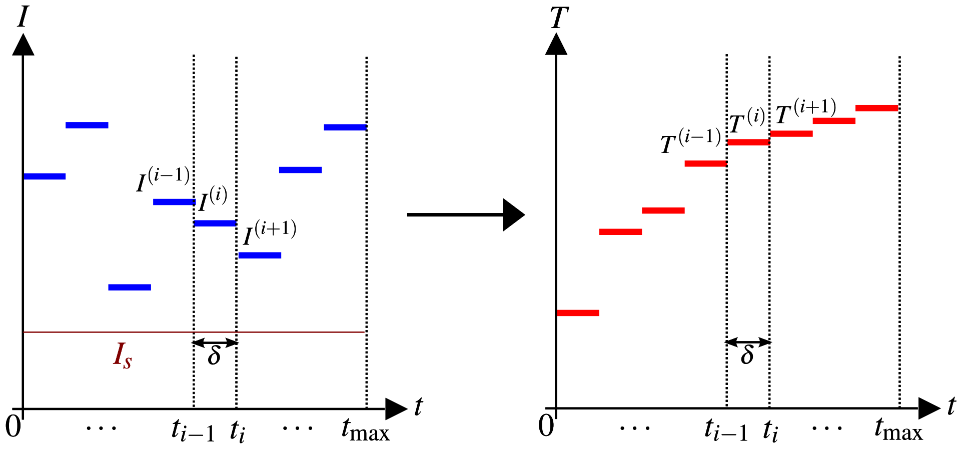

Fig. 6.18: *Recursive scheme for the calculation of temperatures with time-dependent currents.*

1. *Quasi-stationary case ($I^{(i)} < I_{lim}$):*

$$T^{(i)} = e^{-\phi_i \, \delta} \, T^{(i-1)} + (1 - e^{-\phi_i \, \delta}) \, T_s^{(i)}, \quad i = 1, .., n_t \tag{6.68}$$

with $\phi_i = \frac{1}{A_5 \, \gamma_5} \left(\pi \, d_2 \, \beta \left(T^{(i-1)} \right) - \frac{\rho_0 \, \alpha_\rho \, (I^{(i)})^2}{A_5} \right)$. Note that η, included in $\beta(\cdot)$, has to be evaluated for each current $I^{(i)}$.

2. *Instationary case ($I^{(i)} \geq I_{lim}$):*

$$T^{(i)} = \frac{\frac{A_5 \, \rho_3 \, (I_3^{(i)})^2}{A_3 \, \rho_0 \, (I^{(i)})^2} \left(e^{(i)} - 1 \right) + \left(1 + \alpha_\rho (T^{(i-1)} - T_0) \right) \, e^{(i)} - 1}{\alpha_\rho} + T_0, \quad i = 1, .., n_t \tag{6.69}$$

with $e^{(i)} = \exp\left(\delta \, \phi_{inst}^{(i)}\right)$ and $\phi_{inst}^{(i)} = \frac{\rho_0 \, \alpha_\rho \, (I^{(i)})^2}{A_5 \, (\gamma_3 \, A_3 + \gamma_5 \, A_5)}$.

Trisection and Boundary Conditions

The initial (stationary) temperature profile $T^{(0)} = T_{\text{init}}$ results from the calculation procedure for $I = 0$ presented in Section 6.3. Therein, the cable division in three sections is included. The temporal continuation of the trisection is given by the quasi-stationary (6.68) and instationary (6.69) interpolation for all $x \in [0, L]$.

Note that the distinction between quasi- and instationary case is given by $B > 0$ resp. $B \leq 0$ in (6.17). For each cable section, we have a specific B_j, $j = 1, 2, 3$. If $B_j \leq 0$ for at least one j, we apply the instationary recursion (6.69) for the entire cable. This ensures the continuity in space of the temperature profiles for every time step i.

The temperatures at the tails of the cable are well defined via the boundary conditions discussed in Section 6.3.2 (Boundary and Interface Conditions). Their evolution is given by the Equations (6.68) respectively (6.69).

6.4.3 Numerical Results

Comparison of Measurements and Simulations

In order to test our simulation method, the industrial partners performed measurements on several shielded cables with different current profiles. We compare these experimental results to our computations.

For four cable types (see physical properties in Table 6.1), the same as used in the comparison for the stationary case, simulations and temperature measurements were taken. Measuring the voltage drop in the core of the cable enables the identification of its electrical resistance and thus the experimental determination of present temperatures in the core.

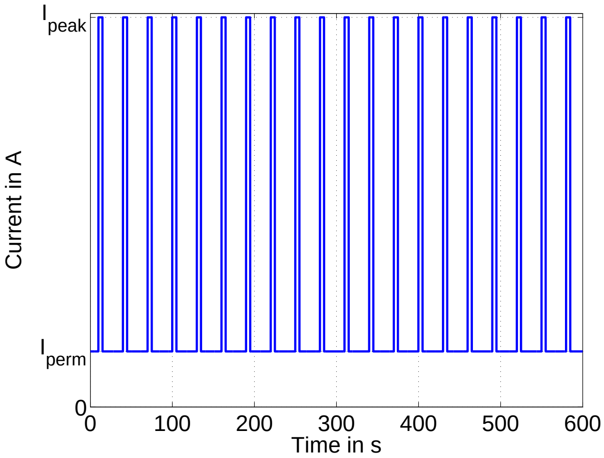

Fig. 6.19: *Schematic current profile for comparison of measurement and simulation results in the first 10 minutes with permanent current I_{perm} and peak current I_{peak}.*

We apply a specific current profile to the core of each cable, illustrated schematically in Figure 6.19. The current profile repeats with a period length of 30 s and includes a peak current after 10 s of each cycle, lasting 5 s. The intensity of the constant current I_{perm} is 50 A (for the cable type of cross sectional area 16 mm^2), 80 A (25 mm^2), 87 A (35 mm^2) and 125 A (50 mm^2); the strength of the peak current I_{peak} amounts to 350 A (16 mm^2), 400 A (25 mm^2), 500 A (35 mm^2) and 600 A (50 mm^2). All current profiles are chosen such that the constant current is below the cable's limiting current, the peak current above it. The current in the shielding remains constant for all cases with 400 mA.

In the measurements, the ambient temperatures were recorded and the electrical resistances of core and shielding were determined by the voltage drop on a length of 4 m for each cable. Moreover, the periodic current profile was repeated until the temperature change from one period to the five previous ones was lower than 2 K.

In the simulations, a length of 6 m was supposed for the cables such that the temperatures at the ends only have a minor influence. We compare the measured temperatures to those computed in the middle of our simulated cables. Measured ambient temperatures varying over time are also respected in the simulations. This explains the non-smooth behaviour of some computed curves, especially in Figure 6.21.

The crucial factor for the correct dimensioning of cables is the maximum temperature. We state the maximum temperatures obtained in our simulations and measurements as well as their deviations in Table 6.3. Therein, the quantity $T_{\max}^{\text{mes}}$ denotes the measured maximum temperature, $T_{\max}^{\text{com}}$ the computed maximum temperature, $\Delta T_{\max}$ the difference

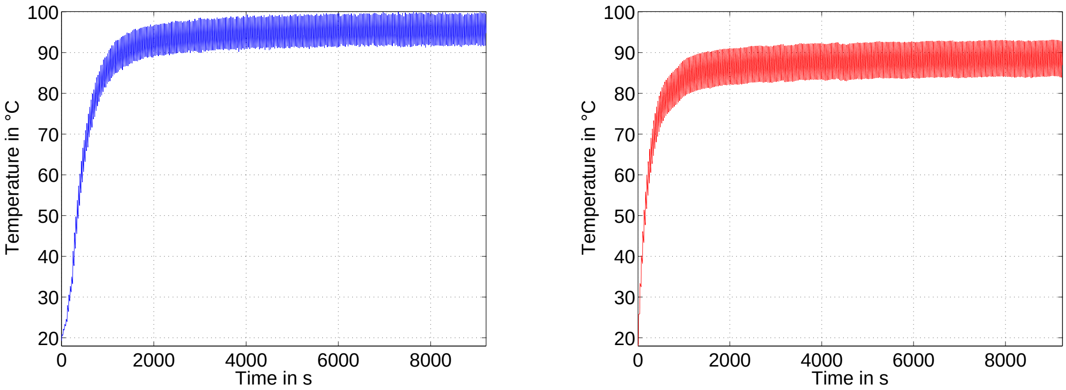

(a) Measured temperatures. **(b)** Computed temperatures.

Fig. 6.20: *Measured and computed temperatures of cable type FLR2GB2G 16.*

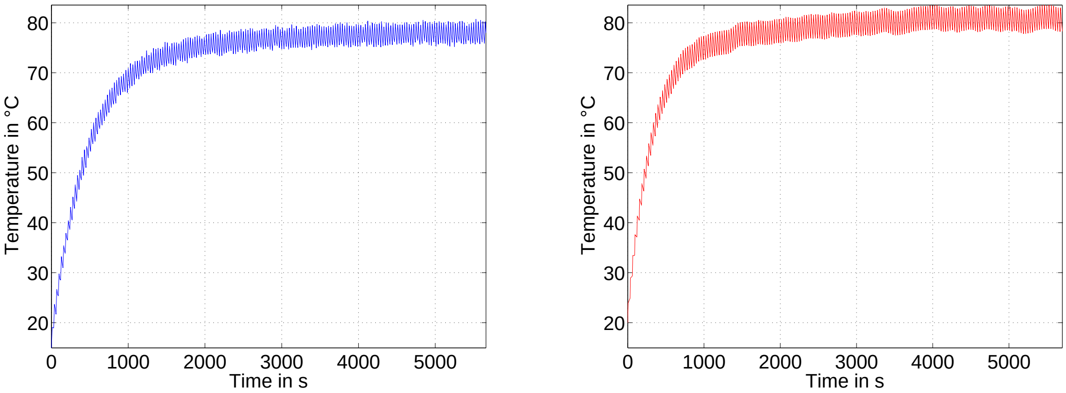

(a) Measured temperatures. **(b)** Computed temperatures.

Fig. 6.21: *Measured and computed temperatures of cable type FLR2GB2G 25.*

between both maximum temperatures and ϵ_{rel} their relative deviation compared to the absolute maximum temperature minus ambient temperature.

Tab. 6.3: *Measured and computed maximum temperatures in shielded cables.*

	Cross sectional area of cable type			
	$16\,\mathrm{mm}^2$	$25\,\mathrm{mm}^2$	$35\,\mathrm{mm}^2$	$50\,\mathrm{mm}^2$
$T_{\max}^{\mathrm{mes}}$ (°C)	100.1	80.7	80.1	76.9
$T_{\max}^{\mathrm{com}}$ (°C)	93.1	83.6	74.1	78.3
$\Delta T_{\max}$ (K)	7.0	2.9	6.0	1.4
ϵ_{rel} (%)	8.4	4.1	9.6	2.4

Furthermore, Figures 6.20-6.23 show the curves of temperature over time for our simulations and measurements. In each case, the curves of measurement and simulation have the same qualitative form and maximum temperatures do not differ vastly. The widths of

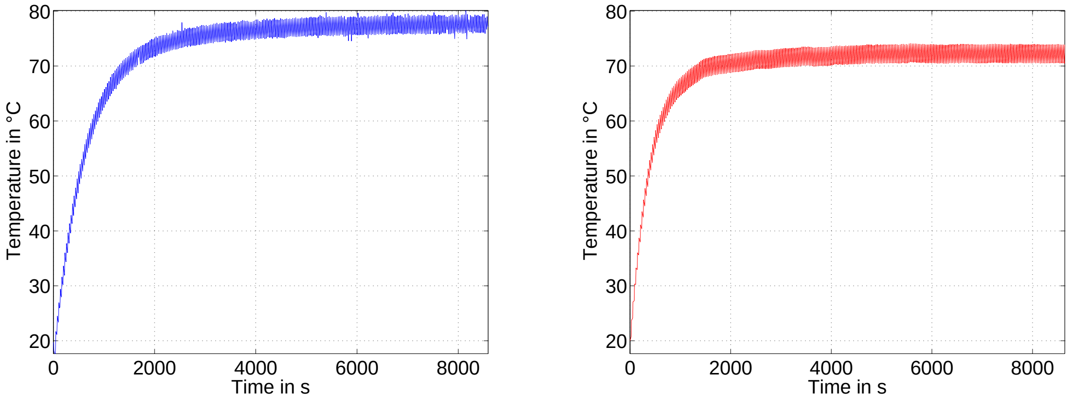

(a) Measured temperatures.

(b) Computed temperatures.

Fig. 6.22: *Measured and computed temperatures of cable type FLR2GB2G 35.*

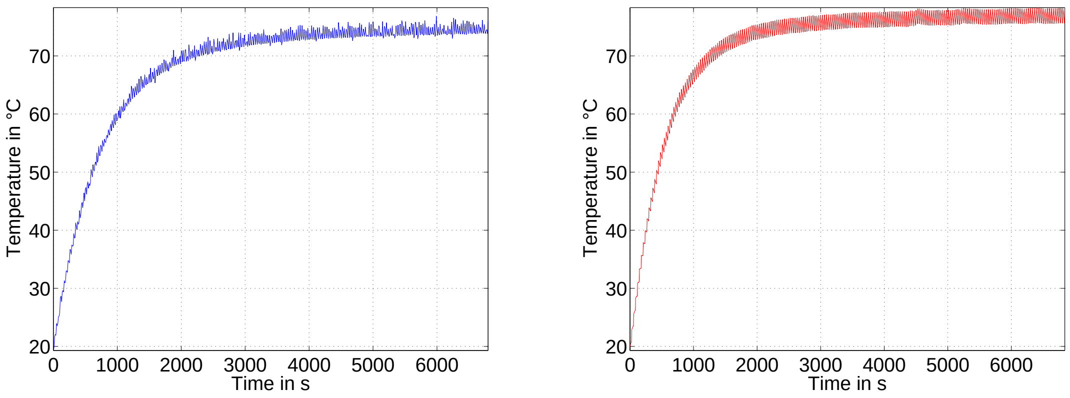

(a) Measured temperatures.

(b) Computed temperatures.

Fig. 6.23: *Measured and computed temperatures of cable type FLR2GB2G 50.*

oscillation also correspond well. Nevertheless, there are discrepancies as indicated in Table 6.3. For example, for the cable type of cross sectional area 16 mm^2, the deviation of maximum temperatures is 7.0 K, which means a relative error of 8.4 %. It is mainly explained by imprecise data distributed by the cable manufacturers. In particular, the core diameter of the cables is indicated with a tolerance of ±5 %. As the current density $J = {}^{I}\!/_{A}$ represents the main quantity for the produced heat power, these variations essentially influence the simulation results, especially the computed maximum temperatures.

Our computational approach reflects the inaccuracies of the given data and yields predictions that are reliable in a range of 10 %. In addition to the input errors, the output deviations are not only caused by the made assumptions and computational errors, but also by inaccuracies of the measurements. Nevertheless, the comparison of computations and measurements provides a positive conclusion if we keep the mentioned limitations in mind.

Further Calculation Results

In the following, we apply the presented approach in two examples. They show how the method could be used by manufacturers to dimension cables for given current loads and illustrate differences between the quasi-stationary and instationary case.

Example 1

We suppose the cable to have a length of $L = 4.0\,\text{m}$ with subsections of $\ell_1 = 0.5\,\text{m}$, $\ell_2 = 3.0\,\text{m}$ and $\ell_3 = 0.5\,\text{m}$. The ambient temperatures in the subsections are $T_{11} = 65\,°\text{C}$, $T_{12} = 85\,°\text{C}$ and $T_{13} = 55\,°\text{C}$. The attached device at the left end has a heat conductivity of $\lambda^l_{ad} = 150\,{}^{W}\!/_{\text{m}\cdot\text{K}}$, reaches an asymptotic temperature of $T^l_{ad} = 20\,°\text{C}$ and the contact resistance to the cable is $R^l_k = 5\,\text{m}\Omega$. At the right end, the attached device has a heat conductivity of $\lambda^r_{ad} = 300\,{}^{W}\!/_{\text{m}\cdot\text{K}}$, reaches an asymptotic temperature of $T^r_{ad} = 50\,°\text{C}$ and the contact resistance to the cable is $R^r_k = 10\,\text{m}\Omega$.

We compare the temperature evolution in four different types of cables. Their geometrical properties are summarized in Table 6.4, for the physical properties, we refer to Table 6.2. The current profile in the core is shown in Figure 6.24. It was provided by a car manufacturer and was recorded at a racing test. The current in the shielding is constant with 10 A.

Tab. 6.4: *Properties of further shielded cable types.*

Cable type	d_2 (mm)	d_3 (mm)	d_4 (mm)	d_5 (mm)	d_6 (mm)	n_c
FLR2GB2G 4	5.50	4.49	3.55	2.30	0.21	120
FLR2GB2G 6	6.25	5.06	4.15	2.84	0.21	183
FLR2GB2G 10	8.50	6.72	5.70	3.76	0.21	320
FLR2GB2G 12	9.20	7.32	6.20	4.09	0.21	380

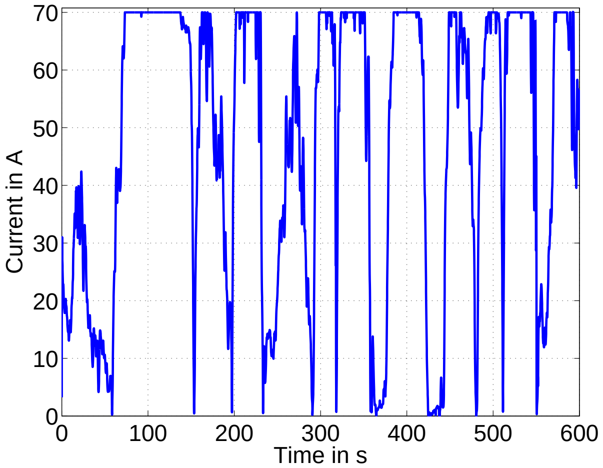

Fig. 6.24: *Current profile for a shielded cable in ten minutes of time.*

Figure 6.25 depicts the temperature distribution in the core over the length of 4.0 m and the time of 10 min for the indicated cable types. Furthermore, the temperature profile over the cable length is depicted at the moment when the global maximum temperature appears.

With the given current profile, the maximum temperature is reached after 546.9 s for the cables of cross sectional area 4 mm^2 and 6 mm^2, after 547.0 s for those of cross sectional area

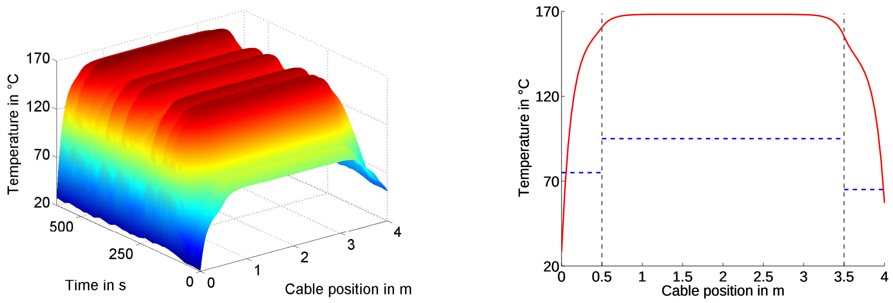

(a) Temperature profile over time and length for cable type FLR2GB2G 4.

(b) Temperature profile after 546.9 s for cable type FLR2GB2G 4.

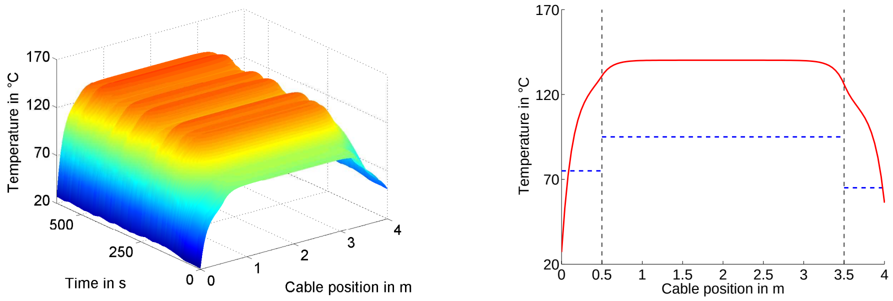

(c) Temperature profile over time and length for cable type FLR2GB2G 6.

(d) Temperature profile after 546.9 s for cable type FLR2GB2G 6.

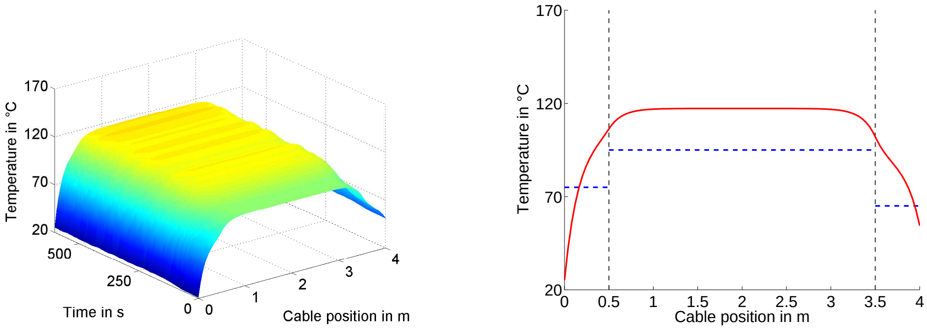

(e) Temperature profile over time and length for cable type FLR2GB2G 10.

(f) Temperature profile after 547.0 s for cable type FLR2GB2G 10.

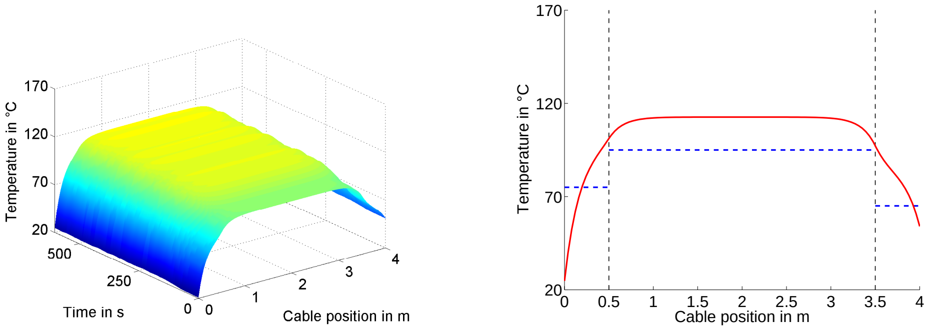

(g) Temperature profile over time and length for cable type FLR2GB2G 12.

(h) Temperature profile after 547.0 s for cable type FLR2GB2G 12.

Fig. 6.25: *Temperature profiles for cable types FLR2GB2G 4, FLR2GB2G 6, FLR2GB2G 10 and FLR2GB2G 12 over time and length of the cable for a specific scenario.*

$10\,\mathrm{mm}^2$ and $12\,\mathrm{mm}^2$. Its value is $168.2\,°\mathrm{C}$ ($4\,\mathrm{mm}^2$), $140.2\,°\mathrm{C}$ ($6\,\mathrm{mm}^2$), $117.3\,°\mathrm{C}$ ($10\,\mathrm{mm}^2$) respectively $112.6\,°\mathrm{C}$ ($12\,\mathrm{mm}^2$).

If we suppose the given situation to be a worst case scenario and the insulation to have a melting point of 130 °C, the manufacturer would have to choose the cable type FLR2GB2G 10. If the cable is able to sustain overheating for a short time, he could take the cable type FLR2GB2G 6. The types FLR2GB2G 4 and FLR2GB2G 12 have to be rejected in this context, as the first exceeds maximum temperatures the insulation could sustain, the second is too wide and thus too expensive.

Each of the presented computations took less than 10 s in Matlab, version 7.10.0.499, on an Intel Core 2 Duo processor with 2.67 GHz and 3.00 GB RAM. With time step size $\delta = 0.1\,\mathrm{s}$, the current profile consisted of 6 000 intervals. The space was discretized equidistantly in 100 points. Hence, the temperature was evaluated at $6\,001 \times 100 = 600\,100$ points.

Example 2

In the second example, we suppose the electric current in the core to be constant, but the ambient temperatures to vary significantly from one section to another. We first apply a constant current below the limiting current, afterwards one above it. The lengths of the three subsections are $\ell_1 = \ell_2 = \ell_3 = 1.0\,\mathrm{m}$ with ambient temperatures $T_{11} = 80\,°\mathrm{C}$, $T_{12} = 10\,°\mathrm{C}$ and $T_{13} = 40\,°\mathrm{C}$. The attached devices have the following properties:

- $\lambda^l_{ad} = 100\,{}^{W}\!/\mathrm{m{\cdot}K}$, $T^l_{ad} = 70\,°\mathrm{C}$ and $R^l_k = 5\,\mathrm{m}\Omega$,
- $\lambda^r_{ad} = 100\,{}^{W}\!/\mathrm{m{\cdot}K}$, $T^r_{ad} = 30\,°\mathrm{C}$ and $R^r_k = 5\,\mathrm{m}\Omega$.

The cable has a cross sectional area of $16\,\mathrm{mm}^2$ with properties listed in Table 6.1. The currents in core and shielding are constant in time $t \in [0, 2\,700]s$ with $I = 160\,\mathrm{A}$ and $I_3 = 5\,\mathrm{A}$.

Figure 6.26 illustrates the temperature distribution in the core over time and length. Obviously, the maximum temperature of 166.2 °C is reached in the first subsection with the highest ambient temperature. The temperature profile shows an asymptotic behaviour and converges to a stationary state.

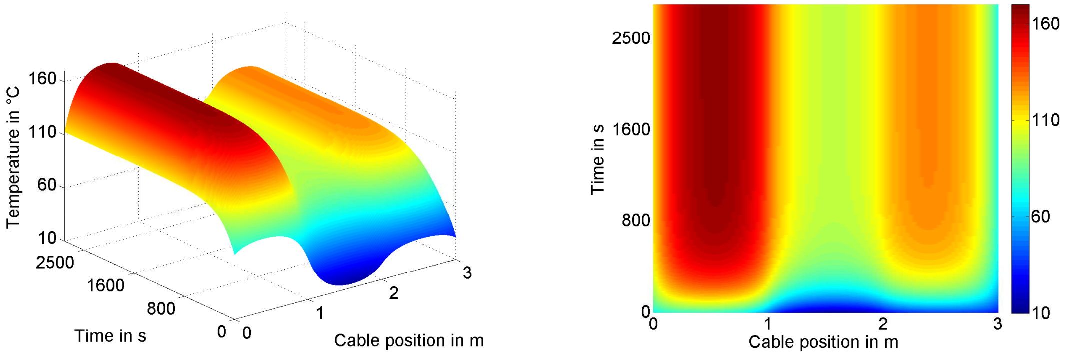

(a) Temperature profile in the first 2 700 s.

(b) Temperature profile in the first 2 700 s, view from above.

Fig. 6.26: *Temperature profiles for cable type FLR2GB2G 16 over time and length of the cable for a specific scenario in the quasi-stationary case.*

In contrast, the temperature profile in Figure 6.27 does not converge for time $t \to \infty$. The constant current in the core $I = 270\,\mathrm{A}$ is above the limiting current of $I_{\mathrm{lim}} = 267.3\,\mathrm{A}$. Figure 6.27a shows that after already 100 s, the cable heats up to a maximum temperature of $\approx 200\,°\mathrm{C}$. Opposed to the quasi-stationary case, there is no saturation. Hence, any desired temperature is exceeded after sufficiently long time. In Figure 6.27b, temperatures higher than 1 000 000 °C are obtained theoretically, which, of course, is no more realistic.

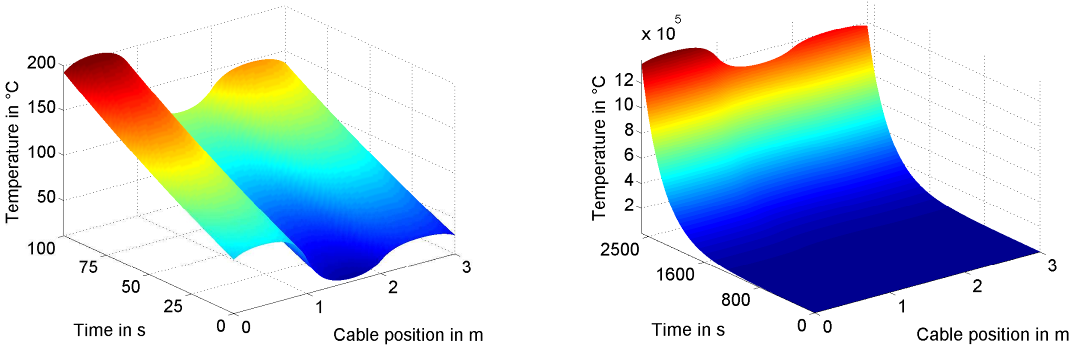

(a) Temperature profile in the first 100 s. **(b)** Temperature profile in the first 2 500 s.

Fig. 6.27: *Temperature profiles for cable type FLR2GB2G 16 over time and length of the cable for a specific scenario in the instationary case.*

As mentioned, one great advantage of our method is the short computational time. Each calculation took less than 10 s on the same computer system as described in the previous example. With time step size $\delta = 1\,\mathrm{s}$, the current profile consisted of 2 700 intervals for the quasi-stationary case. The space component was discretized equidistantly in 100 points. Thus, the temperature was evaluated at $2\,701 \times 100 = 270\,100$ points.

Discussion and Comparison to Finite Element Simulations

In this paragraph, we discuss some assumptions made in our heat power balance approach and compare our results to those of finite element simulations.

The main task of the shielding is to reduce electric and magnetic fields generated by the flow of electric current through the core. Small currents in the shielding, constant in time, are sufficient to fulfil this task. This justifies our simplification in Remark 12 to neglect the temperature dependency of the shielding and thus simplifies the derivation of the interpolation approach in (6.68) and (6.69).

The fundamental assumption concerning the interpolation approach represents the reduction of the full problem (6.48a) – (6.48c) to the core. It is motivated by much better approximation properties in (6.59) and (6.62) for homogeneous materials (cf. [35]) than for heterogeneous materials. For this reduction, the definition of the temperature ratio η_s in (6.53) respectively $\eta(t)$ is essential. The stationary ratio η_s is well defined by (6.61). In the following, we compute the evolution of temperatures $T_5(t)$ and $T_2(t)$ for varying initial temperatures via FEM for a specific scenario. We choose the cable type FLR2GB2G 6 and consider a single cross section with ambient temperature $T_1 = 40\,°\mathrm{C}$ and the constant current $I = 90\,\mathrm{A}$ (cf. Figure 6.28).

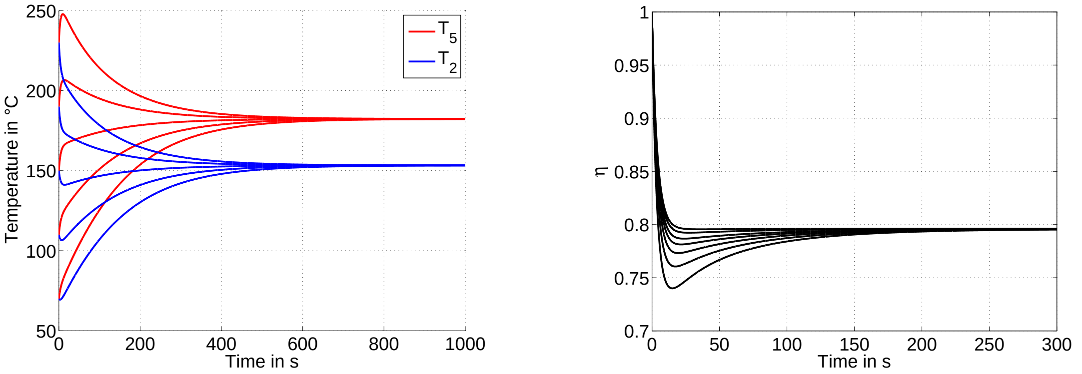

(a) Evolution of temperatures at the exterior insulation and the core for a usual insulation layer and initial temperatures varying from 70–230 °C in steps of 40 K.

(b) Evolution of corresponding temperature ratios for a usual insulation layer. The lowest curve is assigned to the initial temperature 70 °C, the topmost to 230 °C.

Fig. 6.28: *Evolution of temperatures and temperature ratios for cable type FLR2GB2G 6 with varying initial temperatures.*

Afterwards, we enlarge the exterior insulation of cable type FLR2GB2G 6 to a diameter $d_2 = 12\,\mathrm{mm}$. The same simulations are performed for this new (imaginary) cable and $\eta(t)$ is evaluated (cf. Figure 6.29).

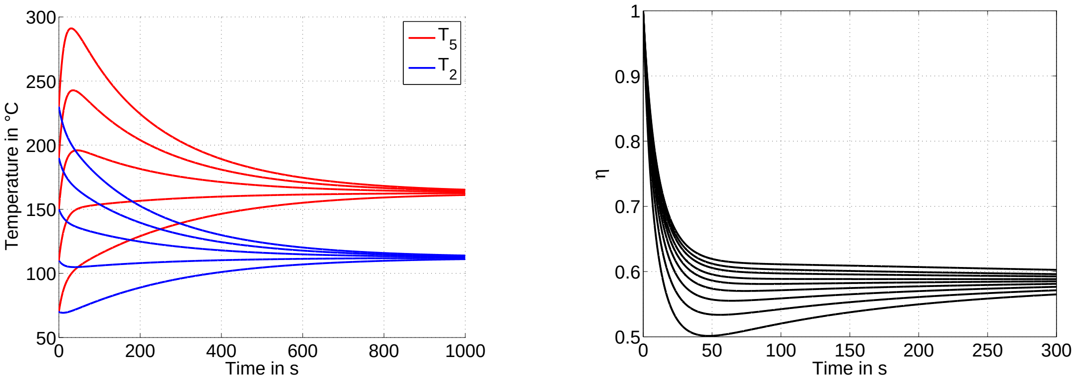

(a) Evolution of temperatures at the exterior insulation and the core for a thick insulation layer and initial temperatures varying from 70–230 °C in steps of 40 K.

(b) Evolution of corresponding temperature ratios for a thick insulation layer. The lowest curve is assigned to the initial temperature 70 °C, the topmost to 230 °C.

Fig. 6.29: *Evolution of temperatures and temperature ratios for modified cable type FLR2GB2G 6 of exterior diameter* 12 mm *with varying initial temperatures.*

Note that scenarios with $(d_2 - d_5)/2 > d_5$ are unusual (cf. Tables 6.1 and 6.4), hence the assumption $\eta(t) = \eta \;\forall\, t \in (0, t_{\max}]$ is admissible for most practical applications in this context.

Observe that for thin insulation layers which are common in applications, the value of

$\eta(t)$ hardly changes over time (cf. Figure 6.28b). However, for thick insulation layers (cf. Figure 6.29b), we have large deviations.

6.5 Conclusion

In this chapter, we presented new methods specific to the calculation of stationary and transient temperature profiles in shielded cables of finite length, applicable in the high voltage domain of electric and hybrid vehicles. In these approaches, the influence of varying ambient temperatures and attached objects is respected. The computational methods for the stationary and transient case work extremely fast – calculation times for the stationary case were less than one second, those for instationary scenarios less than ten seconds – and are very flexible. Changes in geometry can be handled much more easily compared to standard methods like e.g. the finite element method.

Good agreement between measurements and calculations was observed, which qualifies the methods for direct industrial application. The presented approaches have been applied in the implementation of a calculation tool. Despite some simplifications and heuristics, the approaches work well. This is not only confirmed by comparison of measurements and simulations, but also by the feedback of our industrial partners. Cables previously dimensioned with far too large diameters can now be reduced more easily. Moreover, costly measurements can be replaced to a great extend by the introduced calculation procedures.

7 Multicables

In this chapter, we present two approaches to simulate stationary Joule heating of current carrying multicables. Multicables are wires that consist of several single cables (see an example in Figure 7.1), which are stuck together by an exterior layer of insulation. Although the single cables might be insulated single-core cables or shielded cables, we restrict the multicable to contain exclusively insulated single-core cables in our considerations.

A main result of one simulation approach, confirmed by measurements, is that the positioning of the single cables has a significant effect on the heat distribution and especially on the maximum temperature in a multicable. Thus, we developed an optimization algorithm that minimizes the maximum temperature in a multicable by varying the positions of the single cables. The optimization algorithm is subject of the second part of this chapter.

Fig. 7.1: *Real multicable consisting of fifteen single cables.*

Both main parts of this chapter, the comparison of two simulation approaches [87] and the optimization of multicables [50], have been summarized in two research papers.

7.1 Problem Formulation

For the simulation, we use a stationary, two dimensional model of a cable. Due to the great length of the cables ($\ell \to \infty$) and the implicated minor temperature changes in axial direction, we consider the heat generation in a single cross sectional area $\Omega^{\mathrm{MC}} \subseteq \mathbb{R}^2$. Interested in the long time behaviour ($t \to \infty$) and the maximum temperatures, we investigate the stationary case. These equilibrium temperatures give an upper bound for the time-dependent case with constant currents.

One problem in the simulation of the heat distribution is that, by now, the cables are positioned more or less arbitrary during the production process. Consequently, it is difficult to forecast precisely how the multicable will be designed. We consider this aspect in our simulations and thus propose two different simulation approaches.

In the first approach, we simulate the production process of multicables, i.e. the squeezing of the cables until a fixed layout is obtained. We then calculate the temperature distribution $T(x)$, $x \in \Omega^{\mathrm{MC}}$, on the prescribed domain by solving numerically a nonlinear system of PDEs. With the help of finite elements, we determine an entire temperature profile with respect to the complex geometry of the cross section. Our second approach is again based on the law of conservation of energy. We apply a heat power conserving isotropization technique which allows to reduce the complex geometry to the simpler one of an insulated single-core cable. Afterwards, we apply a fast vector valued fixed point iteration.

Before going into detail, let us state some results from literature. In [34], a cable model and basic procedures for the analysis of currents and temperatures by using FEM are presented. Numerical and analytical approaches for the calculation of temperatures in electric power cables are subject of [84]. Both mentioned references give fundamental information about the computation of temperatures in cables, but their main focus is not to compute the heat distribution in multicables. Closer to our subject is the article [20]. It describes the practical problem of correct dimensioning of cable bundles, the occurring physical effects and a mathematical model for the instationary case, solved via a FVM. To determine the heat conductivity in the air gaps between the single cables, an inverse solution method is proposed additionally in [19].

A combination of analytical and numerical formulas is applied in [81], resulting in the possibility to reduce the great number of data necessary for the calculation of cables. These simplified formulas can describe the heat generation in cables with limitations, for example a temperature dependent heat transfer coefficient was not entirely respected. But this is the case for our two approaches. Motivated by the above-named works and the collaboration to cable manufacturers, it is our main interest to present opportunities and limitations of our methods.

This chapter is organized as follows: In Section 7.2, we define the physical problem and describe it mathematically by a corresponding model with PDEs. A cable squeezing algorithm (CSA) to set up the layout and finite elements to calculate the temperature profile are applied in Section 7.3. In Section 7.4, we derive formulas for temperatures at specific positions in the cable, based on the law of conservation of energy and evaluated by a fixed point iteration. Section 7.5 provides numerical results of both approaches and compares those to measurements, which were carried out on real multicables. Finally, we present an optimization algorithm for the design of multicables in Section 7.6, which combines gradient based shape optimization and a genetic algorithm.

7.2 PDE model

By introducing the physical problem with PDEs, varying parameter values for different subsections, boundary and interface conditions, we state the classical formulation of our model.

7.2.1 Notation and Governing Equations

Starting point of our considerations for the temperature T is the elliptic equation

$$-\nabla \cdot (\lambda \nabla T) = f \quad \text{in} \quad \Omega^{\mathrm{MC}}, \tag{7.1}$$

with heat conductivity λ and heat power density f varying for different subdomains of the two-dimensional domain Ω^{MC} of the cross section. All heat conductivities are assumed to be isotropic and not temperature dependent. Consequently, constant values for λ in the subdomains are adequate.

Figures 7.1 and 7.2 show cross sections of multicables. A multicable consists of N single cables, indexed by $k \in \{1, \dots, N\}$. In each single cable, metallic conductors (orange in Figure 7.2) and small air gaps (yellow) are surrounded by insulation (pink). The single cables are stuck together by an outer layer of insulation (grey). Spacing between single cables and outer insulation is filled by air or a solid insulation material (blue).

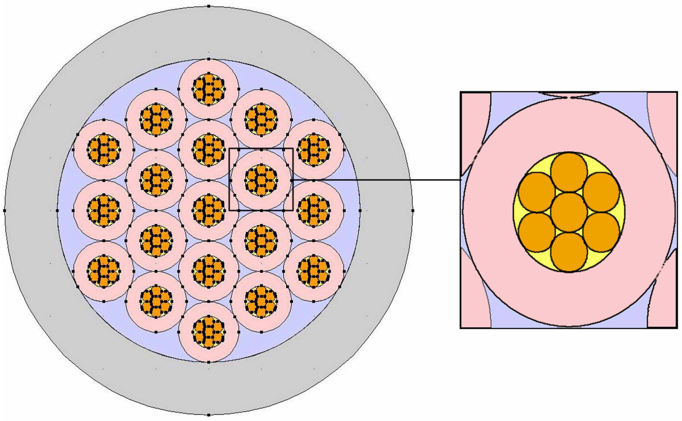

Fig. 7.2: *Schematic cross section of a multicable and a single cable.*

Consecutively, each quantity characterizing the k-th cable is indexed by k, e.g. Ω_k denotes the domain of the entire single cable k. We assume $\cdot$ to be an arbitrary quantity. If it concerns the metallic conductors (orange in Figure 7.2) of single cable k, it is denoted by $\cdot_k^{\mathrm{met}}$, for the inner part (orange and yellow) of single cable k by $\cdot_k^{\mathrm{core}}$, for the insulation (pink) of single cable k by $\cdot_k^{\mathrm{iso}}$, for the spacing between (blue) by $\cdot^{\mathrm{gaps}}$ and for the exterior insulation (grey) by $\cdot^{\mathrm{ex}}$. We omit the designation of quantities in ascending order from exterior to interior by numbers starting with 1, because it might be confusing in this context. Only the reference temperature T_0 and the ambient temperature T_1 retain their 'old' designation.

Modelling of Conductor Domains

Integration of the heat power density f over volume $V_k^{\mathrm{core}} := \Omega_k^{\mathrm{core}} \times [0, \ell]$ yields the electrical power $U_k \cdot I_k$, generated in single cable k on length ℓ. Application of Ohm's law results in

$$\int\limits_{V_k^{\mathrm{core}}} f \, dx = U_k I_k = R_k I_k^2 = \frac{\rho_k \, \ell}{A_k^{\mathrm{ph}}} I_k^2, \tag{7.2}$$

with physical cross sectional area A_k^{ph} denoting the sum of cross sectional areas of all metallic conductors in single cable k and A_k^{ge} the corresponding geometrical one.

Assuming a constant heat power density f in the core of single cable k, we obtain

$$f|_{\Omega_k^{\mathrm{core}}} = \frac{\rho_k \, \ell}{|V_k^{\mathrm{met}}| \cdot A_k^{\mathrm{ph}}} I_k^2 = \frac{\rho_k}{A_k^{\mathrm{ge}} \cdot A_k^{\mathrm{ph}}} I_k^2. \tag{7.3}$$

It remains to take into account the air gaps of a single cable with respect to the heat conductivity. A CFD analysis in this context is not worthwhile because the air gaps are too small. Instead, a filling factor β_k, proposed in [81], is introduced analogously to (5.3) for each single cable by

$$\beta_k := \frac{A_k^{\mathrm{ph}}}{A_k^{\mathrm{ge}}}, \quad 0 \leq \beta_k \leq 1, \tag{7.4}$$

and the core of a single cable including air gaps is treated like homogeneous material with heat conductivity

$$\lambda_k^{\mathrm{core}} := \beta_k \cdot \lambda_k^{\mathrm{met}} + (1 - \beta_k) \cdot \lambda_{\mathrm{air}}. \tag{7.5}$$

The metallic conductors are, in contrast to the single cables in a multicable, of identical material and have the same cross sections. The parameter λ_{air} identifies the heat conductivity of air. In summary, the equation describing the heat distribution in the core of single cable k is

$$-\nabla \cdot (\lambda_k^{\mathrm{core}} \nabla T) = \left(\frac{I_k^2}{A_k^{\mathrm{ge}} \cdot A_k^{\mathrm{ph}}} \right) (\rho_0)_k \left(1 + (\alpha_\rho)_k \left(T - T_0\right)\right) \text{ in } \Omega_k^{\mathrm{core}}. \tag{7.6}$$

Modelling of Insulation Domains

Insulation domains are source free, thus in the exterior insulation layer Ω^{ex} and in the insulation of all single cables Ω_k^{iso}, $k = 1, \ldots, N$, there holds

$$-\Delta T = 0 \text{ in } \Omega^{\mathrm{ex}} \cup \bigcup_{k=1}^{N} \Omega_k^{\mathrm{iso}}, \tag{7.7}$$

with Δ the Laplacian. Figure 7.1 shows that in practice, the single cables are often pressed together, such that the air gaps in between nearly disappear. Thus, convective and radiative effects are reduced enormously. The conductive effect of the air gaps depends on their size. Therefore, we also apply Equation (7.7) in the domain Ω^{gaps} of the air gaps with the heat conductivity approximated by

$$\lambda^{\mathrm{gaps}} := \frac{\lambda^{\mathrm{air}} \cdot |\Omega^{\mathrm{gaps}}| + \sum_{k=1}^{N} \lambda_k^{\mathrm{iso}} \cdot |\Omega_k|}{|\Omega^{\mathrm{MC}} \setminus \Omega^{\mathrm{ex}}|} \text{ in } \Omega^{\mathrm{gaps}}. \tag{7.8}$$

By this heuristic means, the size of the air gaps relative to that of solid domains is respected.

7.2.2 Boundary Conditions

The surrounding medium of a multicable is assumed to be air, so the condition governing heat transfer at the exterior boundary Γ^{ex} of the exterior insulation to ambience corresponds to (2.12).

7.2.3 Particularities of a Cylindrical Multicable

The general modelling in Section 7.2.1-7.2.2 does not make use of the round form of the cable cross section. Hence, application of the formulas to devices of different shape would be possible. In this context, the entire multicable and all single cables are cylindrical. Thus, introducing for single cable k the exterior diameter d_k^{ex}, the interior diameter d_k^{in} (without insulation), the number of metallic conductors n_k and their diameter δ_k, Equation (7.6) results in

$$-\nabla\cdot(\lambda_k^{\text{core}}\,\nabla T) = \frac{1}{n_k}\left(\frac{4I_k}{d_k^{\text{in}}\delta_k\pi}\right)^2 (\rho_0)_k\,(1+(\alpha_\rho)_k\,(T-T_0)) \;\text{ in }\; \Omega_k^{\text{core}},\;\; k=1,\dots,N, \tag{7.9}$$

and

$$\beta_k = \frac{A_k^{\text{ph}}}{A_k^{\text{ge}}} = n_k\left(\frac{\delta_k}{d_k^{\text{in}}}\right)^2. \tag{7.10}$$

Furthermore, for the heat transfer coefficient $\alpha(T)$, we apply the formulas for a horizontal cylinder of Section 2.3 (Horizontal Cylinders).

7.2.4 Classical Formulation

We summarize our boundary value problem:

Find a piecewise differentiable function $T \in C(\overline{\Omega^{\text{MC}}})$ such that

$$\begin{aligned}
&-\nabla\cdot(\lambda\,\nabla T) + c(T) = \tilde f \;\text{ in }\; \Omega^{\text{MC}}, \quad -\lambda^{\text{ex}}\,\frac{\partial T}{\partial n} = \tilde\gamma\,(T) \;\text{ on }\; \Gamma^{\text{ex}},\\
&\lambda := \sum_{k=1}^{N}\left(\lambda_k^{\text{core}}\,\mathbb{I}_{\Omega_k^{\text{core}}} + \lambda_k^{\text{iso}}\,\mathbb{I}_{\Omega_k^{\text{iso}}}\right) + \lambda^{\text{ex}}\,\mathbb{I}_{\Omega^{\text{ex}}} + \lambda^{\text{gaps}}\,\mathbb{I}_{\Omega^{\text{gaps}}},\\
&c(T) := -\sum_{k=1}^{N}\frac{1}{n_k}\left(\frac{4I_k}{d_k^{\text{in}}\delta_k\pi}\right)^2 (\rho_0)_k\,(\alpha_\rho)_k T\,\mathbb{I}_{\Omega_k^{\text{core}}},\; \tilde\gamma\,(T) := \alpha(T)\cdot(T-T_1)\,,\\
&\tilde f := \sum_{k=1}^{N}\frac{1}{n_k}\left(\frac{4I_k}{d_k^{\text{in}}\delta_k\pi}\right)^2 (\rho_0)_k\,(1-(\alpha_\rho)_k\,T_0)\;\mathbb{I}_{\Omega_k^{\text{core}}}\,.
\end{aligned} \tag{7.11}$$

7.3 Finite Element Approach

After the derivation of a weak formulation, we give some remarks about existence and uniqueness of a weak solution of problem (7.11). The necessity of a fixed geometry for the solution with finite elements requires the application of a modified circle packing algorithm.

7.3.1 Existence and Uniqueness of a Weak Solution

A weak formulation of (7.11) reads as follows:

Find $T \in H^1(\Omega^{\text{MC}})$ such that

$$\begin{aligned}
a(T,v) &= \int_{\Omega^{\text{MC}}} \tilde f\cdot v\,\mathrm{d}x \;\;\forall v \in H^1(\Omega^{\text{MC}}),\\
a(T,v) &:= \lambda\int_{\Omega^{\text{MC}}} \nabla T\cdot\nabla v\,\mathrm{d}x + \int_{\Omega^{\text{MC}}} c\,(T)\cdot v\,\mathrm{d}x + \int_{\Gamma^{\text{ex}}} \tilde\gamma\,(T)\cdot v\,\mathrm{d}s.
\end{aligned} \tag{7.12}$$

In order to get a bounded and coercive form a in (7.12), we apply $\tilde\alpha(T)$ defined in (2.31). We formulate analogously to Theorem 1

Theorem 15. *Assume that* $\max\limits_{1\le k\le N} \frac{(\rho_0)_k\,(\alpha_\rho)_k\,I_k^2}{\left(A_k^{ph}\right)^2} < \frac{\alpha_l}{d^{ex}}$ *holds. Then there exists a unique solution* $T \in H^1(\Omega^{MC})$ *of (7.12).*

7.3.2 Generation of the Geometry

Unlike the heat power balance approach (HBA) in Section 7.4, the finite element approach (FEA) necessarily needs a precise geometry of the multicable cross section. In the production process of a multicable, the single cables are placed in a template (see Figure 7.3) and pressed together. This makes it hard to determine the exact layout of the cross section of a multicable in advance.

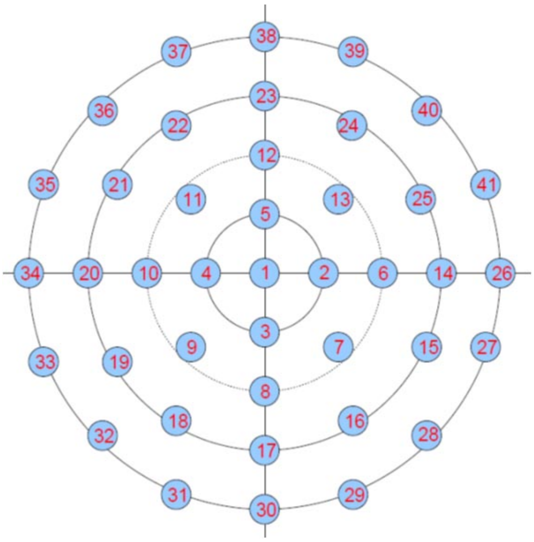

Fig. 7.3: *Template for initial positions of single cables to generate a multicable.*

To obtain an approximating geometry, we extend the circle packing algorithm in [7] to a cable squeezing algorithm. It computes the geometrical data of the multicable, starting from an initial configuration, and imitates the squeezing of the single cables. The objective of this preprocessing algorithm is not to optimally solve the circle packing problem or the layout optimization problem as in [140], proven to be NP-hard [41], but to quickly compute a realistic geometry. In the following, we briefly describe the main subroutines of this algorithm.

The k-th single cable is geometrically defined by a 'double circle' $c_k = \left(x_k, y_k, r_k^{\text{in}}, r_k^{\text{ex}}\right)$ with centre (x_k, y_k) in the Cartesian coordinate system, its inner radius r_k^{in} and the outer radius r_k^{ex}. Moreover, we define a multicable with N single cables by

$$MC = \left(\left(x_0, y_0, r_0^{\text{in}}, r_0^{\text{ex}},\right); c_1, \dots, c_N\right),$$

where (x_0, y_0) corresponds to the coordinates of its centre, $r_0^{\text{in}} = d^{\text{in}}/2$ to the interior radius of the exterior insulation Ω^{ex} and $r_0^{\text{ex}} = d^{\text{ex}}/2$ to the corresponding exterior radius. The abbreviations $c_1, \dots, c_N$ denote the N single cables in the multicable (cf. Figure 7.4a). Furthermore, we introduce tuples R and C consisting of all exterior radii of the single cables and of the entire single cables by $R = (r_1^{\text{ex}}, \dots, r_N^{\text{ex}})$, $C = (c_1, \dots, c_N)$.

An initial configuration C for the single cables is obtained via a simple procedure *init*(R, P). Therein, the mapping P assigns a position number of the template (cf. Figure 7.3) to every

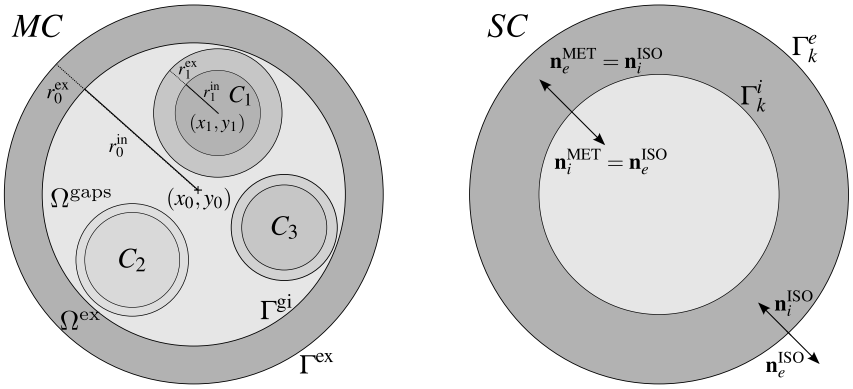

(a) Model of a multicable consisting of three single cables.

(b) Model of the k-th single cable.

Fig. 7.4: *Model of a multicable and a single cable with geometrical parameters.*

single cable. The squeezing of the single cables is interpreted as a repeated pushing to the centre (herein towards the origin of the coordinate system). Via a fixed damping factor $0 < \delta < 1$ and the maximal exterior radius $r_{\max} := \max\limits_{k=1,\dots,N} r_k^{\text{ex}}$ of the single cables, the new position of single cable c_k is computed in a routine *pushToCenter*$(c_k, \delta, r_{\max})$:

$$\begin{pmatrix} x_k \\ y_k \end{pmatrix} = \begin{pmatrix} x_k \\ y_k \end{pmatrix} (1 - \delta \frac{r_k^{\text{ex}}}{r_{\max}}). \tag{7.13}$$

Thus, all single cables are pushed towards the centre with respect to their distance from the origin. A sufficiently small parameter δ guarantees the smoothness of the repeated application of the routine, higher values provide better packing densities. The effect of factor $r_k^{\text{ex}}/r_{\max}$ is that single cables with larger exterior diameter move more quickly to the centre than thinner ones, also in order to get a better packing density.

It happens that circles overlap after application of the routine *pushToCenter*() to every single cable. To reduce overlappings, we calculate the distance of each cable to the centre by the procedure *dist*(c_k). Additionally, we introduce a single cable sorting function $L : \mathbb{N} \to \mathbb{N}$ that fulfils

$$L(k) < L(l), \quad \text{if} \quad \begin{cases} dist(c_k) < dist(c_l), \\ dist(c_k) = dist(c_l),\ k < l. \end{cases} \tag{7.14}$$

To separate overlapping circles c_k and c_l symmetrically on the connecting line of their centres, the following routine is applied:

```
separateCircles($c_k, c_l, dist$)
{
    $\vec{v} = \begin{pmatrix} x_k - x_l \\ y_k - y_l \end{pmatrix}$, $\begin{pmatrix} x_k \\ y_k \end{pmatrix} = \begin{pmatrix} x_k \\ y_k \end{pmatrix} + \frac{\vec{v}}{|\vec{v}|} \cdot \frac{r_k + r_l - |\vec{v}|}{2}$, $\begin{pmatrix} x_l \\ y_l \end{pmatrix} = \begin{pmatrix} x_l \\ y_l \end{pmatrix} - \frac{\vec{v}}{|\vec{v}|} \cdot \frac{r_k + r_l - |\vec{v}|}{2}$
}
Output($c_k, c_l$)
```

Having found all positions of the single cables, the radius r_0^{in} of the surrounding circle and the coordinates (x_0, y_0) of the centre are computed by solving the following optimization problem:

$$
\boxed{
\begin{aligned}
&r_0^{\text{in}} \to \ \min! \\
\text{s. t.}& \\
&(x_0 - x_k)^2 + (y_0 - y_k)^2 \le \left(r_0^{\text{in}} - r_k^{\text{ex}}\right)^2 , \quad k = 1, \dots, N, \\
&0 \le r_0^{\text{in}} \le \max_{k=1,\dots,N} \big(\sqrt{x_k^2 + y_k^2} + r_k^{\text{ex}}\big), \\
&\min_{k=1,\dots,N} (x_k - r_k^{\text{ex}}) \le x_0 \le \max_{k=1,\dots,N} (x_k + r_k^{\text{ex}}) , \\
&\min_{k=1,\dots,N} (y_k - r_k^{\text{ex}}) \le y_0 \le \max_{k=1,\dots,N} (y_k + r_k^{\text{ex}}) .
\end{aligned}
}
\tag{7.15}
$$

The exterior insulation radius r_0^{ex} of the multicable is prescribed by the thickness of the insulation and the interior insulation radius.

Finally, we state the Cable Squeezing Algorithm 4, abbreviated by CSA, that returns the geometrical data of multicable MC. Therein, the parameter $j_{\max}$ indicates the number of iterations for *pushToCenter*() and *separateCircles*() and $0 < \delta_0 < 1$ an initial damping factor.

Algorithm 4
(∗ CSA ∗)
Input: $r_k^{\text{ex}},\ k = 1, \dots, N,\ P,\ j_{\max},\ \delta_0$
Output: MC

```
Initialize:
    $r_{\max} = \max_{k=1,\dots,N} r_k^{\text{ex}}$, $C = Init\,(R, P)$.
Squeeze:
    for $j = 1, \dots, j_{\max}$
        $\delta = \delta_0 / \log(j + 1)$.
        for $k = 1, \dots, N$
            $c_k = pushToCenter\,(c_k, \delta, r_{max})$.
        Compute $L$ and $dist$ such that (7.14) is fulfilled.
        for $(k, l) \in \{1, \dots, N\} \times \{1, \dots, N\}$ and $k < l$
            $\vec{v} = \begin{pmatrix} x_{L(k)} - x_{L(l)} \\ y_{L(k)} - y_{L(l)} \end{pmatrix}$, $\Delta = r_{L(k)} + r_{L(l)} - |\vec{v}|$.
            if $\Delta > 0$
                $(c_{L(k)}, c_{L(l)}) = separateCircles\,\big(c_{L(k)}, c_{L(l)}, dist\big)$.
Minimize the surrounding cable radius:
    Solve (7.15).
return $MC = \big((x_0, y_0, r_0^{\text{in}}, r_0^{\text{ex}},) \,; c_1, \dots, c_N\big)$.
```

We define the radius $r_{0,j}^{\text{in}}$ of the surrounding circle after the j-th iteration of the squeezing in Algorithm 4. The repeated application of the procedures *pushToCenter*() and *separateCircles*() provides a monotonously decreasing sequence $(r_{0,j}^{\text{in}})_{j \in \mathbb{N}}$, bounded from below by $r_{\max}$. The proposed choice of the damping factor δ ensures that the algorithm converges to a fixed layout. Hence, the algorithm is convergent with respect to the radius of the surrounding circle. For reasons of efficiency, we renounce the computation of $r_{0,j}^{\text{in}}$ in every iteration step. Instead, the number of iterations $j_{\max}$ is chosen depending on a satisfying packing density, and the surrounding radius is solely computed at the end of the algorithm.

7.3.3 Numerical Solution and Implementation Details

To resolve problem (7.12) on a fixed domain Ω^{MC}, obtained via Algorithm 4, we use the finite element solver COMSOL Multiphysics 3.5a in combination with Matlab, version 7.10.0.499. The spatial discretization of the geometry is performed with the help of an automatic mesh generator in COMSOL, dividing the domain into triangular Lagrange elements with quadratic basis functions. To solve the nonlinear problem, a damped Newton method is applied. The Newton iteration stops as soon as the estimated relative error of the current solution is less than a predefined relative accuracy (1.0*e*-6). For the linear systems solved in each Newton iteration, we employ the direct solver PARDISO.

7.4 Heat Power Balance Approach

We briefly repeat the formulas to determine the differences of temperatures at characteristic positions of an insulated single-core cable with solid interior conductor. Afterwards, these results are transformed to the multicable by mean value formulas. Finally, we derive an adequate fixed point equation for the determination of the unknown temperatures.

7.4.1 Model for a Cable with Solid Conductor

For an insulated single-core cable with solid conductor (cf. Figure 7.5), we apply the temperature formulas derived in Section 5.2. As notation is different in this section, we rewrite the final formulas with the new names of the variables.

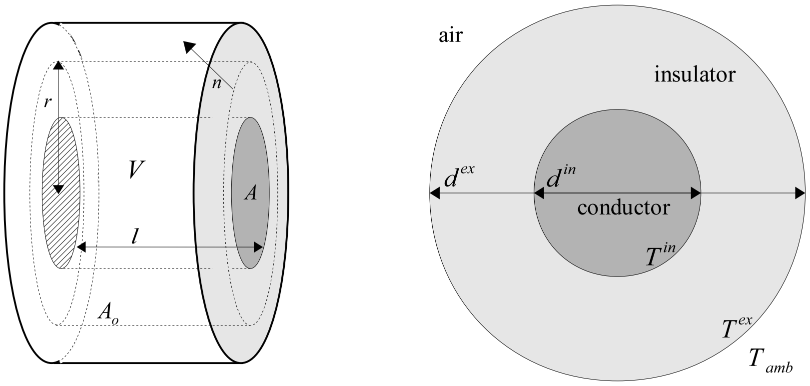

(a) Volume element. **(b)** Cross section.

Fig. 7.5: *Single cable with solid interior conductor.*

The difference in temperature $T^{\mathrm{in}} - T^{\mathrm{ex}}$ of the interior and exterior insulation boundary for a cable with diameter d^{ex} of the insulation and diameter d^{in} of the core is obtained by

$$T^{\mathrm{in}} - T^{\mathrm{ex}} = \frac{\rho\, I^2}{2\,\pi\,\lambda^{\mathrm{ex}}\,A^{\mathrm{in}}}\,\ln\left(\frac{d^{\mathrm{ex}}}{d^{\mathrm{in}}}\right). \tag{7.16}$$

Therein, we identify A^{in} with the cross sectional area of the core, ρ with its resistivity. Moreover, at the exterior boundary, there holds

$$T^{\mathrm{ex}} - T_1 = \frac{\rho\, I^2}{\pi\, d^{\mathrm{ex}}\,\alpha(T^{\mathrm{ex}})\,A^{\mathrm{in}}}. \tag{7.17}$$

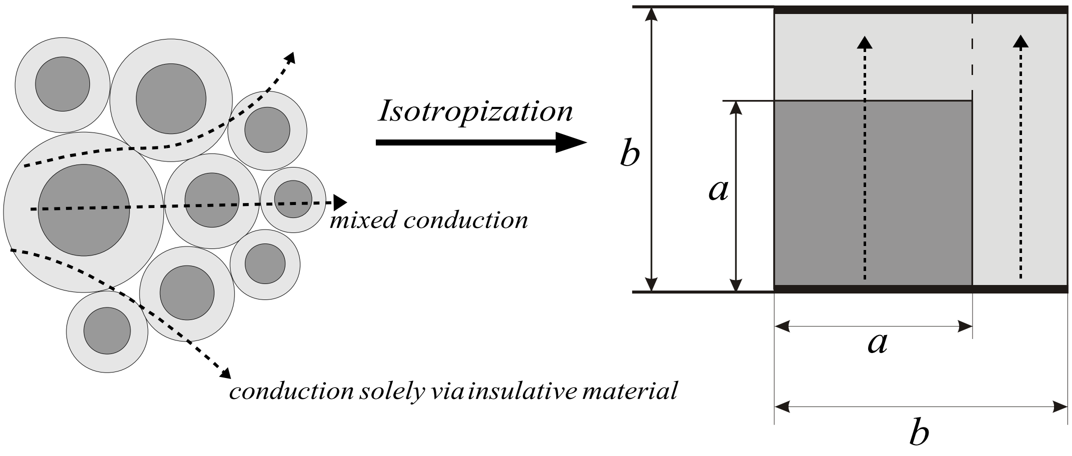

Fig. 7.6: *Geometrical model for the determination of a mean heat conductivity.*

7.4.2 Adaption for Application to a Multicable

To transform the formulas of Section 7.4.1 to a multicable, we derive a mean heat conductivity in the multicable and a heat power specific to the length, that depends on the distance from the centre of the multicable. By this procedure, in the following denoted by isotropization, we are able to compute temperatures T^{ex} at the exterior boundary of the insulation, T^{in} at interior boundary of the insulation and T^{cen} in the centre of the multicable. We define the following heat power specific to the length:

$$p \,= p(T) \,:=\, P/\ell \,=\, \sum_{k=1}^{N} \frac{\rho_k(T)\, I_k^2}{A_k^{\mathrm{ph}}}. \tag{7.18}$$

Furthermore, a mean heat conductivity λ^{mean} for the inner part of the multicable, similar to [81], is obtained via isotropization. We define the auxiliary diameters

$$D^{\mathrm{ex}} \,:=\, \sqrt{\sum_{k=1}^{N} \left(d_k^{\mathrm{ex}}\right)^2} \quad \text{and} \quad D^{\mathrm{in}} \,:=\, \sqrt{\sum_{k=1}^{N} \left(d_k^{\mathrm{in}}\right)^2} \tag{7.19}$$

and the auxiliary cross sectional areas

$$A^{\mathrm{cond}} := \sum_{k=1}^{N} A_k^{\mathrm{ge}}\,, \quad A^{\mathrm{iso}} := \frac{\pi}{4}\left(\left(D^{\mathrm{ex}}\right)^2 - \left(D^{\mathrm{in}}\right)^2\right) \;\text{ and }\; A^{\mathrm{air}} := \frac{\pi}{4}\left(\left(d^{\mathrm{in}}\right)^2 - \left(D^{\mathrm{ex}}\right)^2\right). \tag{7.20}$$

First, we calculate the auxiliary heat conductivities λ^{cond} and λ^{iso} as the weighted arithmetic means of the heat conductivities $(\lambda_k^{\mathrm{core}})_{k=1}^N$ and $(\lambda_k^{\mathrm{iso}})_{k=1}^N$:

$$\lambda^{\mathrm{cond}} := \frac{\sum\limits_{k=1}^{N} A_k^{\mathrm{ge}}\, \lambda_k^{\mathrm{core}}}{A^{\mathrm{cond}}}\,, \quad \lambda^{\mathrm{iso}} := \frac{\pi}{4}\, \frac{\sum\limits_{k=1}^{N} \left(\left(d_k^{\mathrm{ex}}\right)^2 - \left(d_k^{\mathrm{in}}\right)^2\right)\, \lambda_k^{\mathrm{iso}}}{A^{\mathrm{iso}}}\,. \tag{7.21}$$

Next, we define a mean heat conductivity $\lambda^{\mathrm{c/i}}$ for the composite material conductor-insulator. We assume a rotationally symmetric heat propagation from the centre of the multicable. Hence, a part of the heat is conducted through the insulation and the conductor material of the single cables, whereas the remaining part conducts solely through insulation (cf. Figure 7.6). Thus, we consider a unidirectional heat conduction, preserving the cross sectional areas $A^{\text{cond}} =: a^2$, $A^{\text{iso}} =: b^2 - a^2$. To obtain the entire heat conductivity in vertical direction of the left stripe in Figure 7.6, the inverse single resistivities are added by

$$\lambda^{\text{c/i}} = \frac{1}{r^{\text{left}}} + \frac{1}{r^{\text{right}}} = \frac{1}{\frac{1}{\lambda^{\text{cond}}} + \frac{b-a}{a} \frac{1}{\lambda^{\text{iso}}}} + \frac{b-a}{b} \lambda^{iso} \,. \tag{7.22}$$

Using the arithmetic mean, weighted with respect to the corresponding cross sections, we finally obtain

$$\lambda^{\text{mean}} = \frac{A^{\text{iso}} + A^{\text{cond}}}{A^{\text{ttl}}} \lambda^{\text{c/i}} + \frac{A^{\text{air}}}{A^{\text{ttl}}} \lambda^{\text{air}} \quad \text{with} \quad A^{\text{ttl}} = A^{\text{iso}} + A^{\text{cond}} + A^{\text{air}}. \tag{7.23}$$

After this preliminary work, it is possible to apply the formulas (7.16) and (7.17):

$$T^{\text{in}} - T^{\text{ex}} = \frac{p(T)}{2\,\pi\,\lambda^{\text{ex}}} \ln\left(\frac{d^{\text{ex}}}{d^{\text{in}}}\right), \tag{7.24}$$

$$T^{\text{ex}} - T_1 = \frac{p(T)}{\pi\, d^{\text{ex}}\, \alpha(T^{\text{ex}})} \,. \tag{7.25}$$

For geometrical reasons, the length specific heat power in the cross sectional area A_r depends on the radius r via $\tilde{p}(r) = \frac{A_r}{A}\, p(T) = \frac{4\,r^2}{(d^{\text{in}})^2}\, p(T)\,,\ r \leq \frac{d^{\text{in}}}{2}$. On the other hand, there holds $\tilde{p}(r) = -\,2\,\pi\,\lambda^{\text{mean}}\, r\, T'(r)$. Thus, integration over $r \in \left[0, d^{\text{in}}/2\right]$ finally yields

$$T^{\text{cen}} - T^{\text{in}} = \frac{p(T)}{4\,\pi\,\lambda^{\text{mean}}}, \tag{7.26}$$

with T^{cen} the temperature in the centre of the homogenized cable.

7.4.3 Temperature Dependent Parameters

In the calculation of $p(T)$ in (7.24), (7.25) and (7.26), we assume the electrical resistivities $\rho_k(T^{\text{mean}}) = (\rho_0)_k\ (1 + (\alpha_\rho)_k\, (T^{\text{mean}} - T_0))$ to depend only on the mean temperature

$$T^{\text{mean}} = \frac{T^{\text{cen}} + T^{\text{in}}}{2}. \tag{7.27}$$

in the core of the multicable. In contrast, the heat transfer coefficient $\alpha(T)$ depends on the boundary temperature T^{ex}. Consequently, its temperature dependency is completely incorporated.

7.4.4 Deployment towards a Fixed Point Mapping

In order to determine the temperatures $\mathcal{T} = (\mathcal{T}_1, \mathcal{T}_2, \mathcal{T}_3)^t := (T^{\text{ex}}, T^{\text{in}}, T^{\text{cen}})^t$ via a vector valued fixed point iteration, we define the temperature mapping $\mathbf{h} \in C^1(\mathbb{R}^3, \mathbb{R}^3)$ by

$$\mathbf{h}(\mathcal{T}) := \begin{pmatrix} T_0 + \frac{p(T^{\text{mean}})}{\pi\, d^{\text{ex}}\, \alpha(T^{\text{ex}})} \\ T^{\text{ex}} + \frac{p(T^{\text{mean}})}{2\,\pi\,\lambda^{\text{ex}}} \ln\left(\frac{d^{\text{ex}}}{d^{\text{in}}}\right) \\ T^{\text{in}} + \frac{p(T^{\text{mean}})}{4\,\pi\,\lambda^{\text{mean}}} \end{pmatrix}. \tag{7.28}$$

We set $\nabla \mathbf{h} = (\mathbf{h}_{ij})_{1\leq i,j\leq 3}$, $h_{ij}(\mathcal{T}) = \frac{\partial h_i(\mathcal{T})}{\partial \mathcal{T}_j}$, the Jacobian of $\mathbf{h}$. Furthermore, we define the iterative sequence $(\mathcal{T}^{(n)})_{n\in\mathbb{N}}$ by $\mathcal{T}^{(n+1)} = \mathbf{h}\left(\mathcal{T}^{(n)}\right)$ with $\mathcal{T}^{(n)} = \left((T^{\mathrm{ex}})^{(n)}, \left(T^{\mathrm{in}}\right)^{(n)}, (T^{\mathrm{cen}})^{(n)}\right)$, the matrix norm $\|\nabla\mathbf{h}(\mathcal{T})\| = \sup\limits_{x\in\mathbb{R}^3\setminus\{0\}} \frac{|\nabla\mathbf{h}(\mathcal{T})\cdot x|}{|x|}$ and apply a variant of Banach's fixed point theorem to this case.

Lemma 16. *Suppose that* $q := \sup\limits_{\mathcal{T}^{(1)},\mathcal{T}^{(2)}\in\mathbb{R}^3} \left\| \int\limits_0^1 \nabla\mathbf{h}(\mathcal{T}^{(1)} + s\,(\mathcal{T}^{(2)} - \mathcal{T}^{(1)}))\,ds \right\| < 1\,.$ *Then, the following assertions hold:*

1. *There exists a unique solution* $\mathcal{T}^* \in \mathbb{R}^3$ *of* $\mathbf{h}(\mathcal{T}) = \mathcal{T}$*.*
2. *For every initial vector* $\mathcal{T}^{(1)} \in \mathbb{R}^3$*, the recursively defined sequence* $\mathcal{T}^{(n+1)} = \mathbf{h}(\mathcal{T}^{(n)})$*,* $n \in \mathbb{N}$*, converges to the solution* $\mathcal{T}^*$ *with the following rate of convergence:*

$$\left|\mathcal{T}^{(n)} - \mathcal{T}^*\right| \leq \frac{q^n}{1-q}\left|\mathcal{T}^{(2)} - \mathcal{T}^{(1)}\right|.$$

Proof. Cf. Theorem 7 with $\mathbf{h} \in C^1(\mathbb{R}^3,\mathbb{R}^3)$ instead of $\mathbf{h} \in C^1(\mathbb{R}^2,\mathbb{R}^2)$. □

7.4.5 Physical Identification of the Constant of Contraction

We provide a sufficient condition for the convergence of $(\mathcal{T}^{(n)})_{n\in\mathbb{N}}$ in physical terms and determine an upper bound for the constant of contraction q, depending explicitly on the essential quantities.

Let $T_{\min}$ and $T_{\max}$ denote lower and upper bounds for the temperatures in the homogenized multicable, set a priori. We truncate α by (2.31) with $T_l = T_{\min}$ and $p(T)$ in (7.18) at $T = T_{\max}$ with the upper bound $p(T_{\max})$. Using these quantities for the fixed point mapping $\mathbf{h}$ in (7.28), we obtain

Proposition 17. *Assume* $\sum\limits_{k=1}^{N} \frac{(\rho_0)_k\,(\alpha_\rho)_k\,I_k^2}{A_k^{ph}} < \pi\,d^{ex}\,\alpha_l$*. Then the mapping* $\mathbf{h}$ *in Lemma 16 is contractive with*

$$q = \left(\sum_{k=1}^{N} \frac{(\rho_0)_k\,(\alpha_\rho)_k\,I_k^2}{A_k^{ph}}\right) / (\pi\,d^{ex}\,\alpha_l) < 1\,. \tag{7.29}$$

Proof. We define an auxiliary fixed point mapping $\bar{\mathbf{h}}$ which gives an upper bound on the Lipschitz constant of $\mathbf{h}$[1]:

$$\bar{\mathbf{h}}(\mathcal{T}) := \begin{pmatrix} T_0 + \frac{p(\mathcal{T}_3)}{\pi\,d^{\mathrm{ex}}\,\alpha_l} \\ \mathcal{T}_1 + \frac{p(T_{\max})}{2\,\pi\,\lambda^{\mathrm{ex}}}\ln\left(\frac{d^{\mathrm{ex}}}{d^{\mathrm{in}}}\right) \\ \mathcal{T}_2 + \frac{p(T_{\max})}{4\,\pi\,\lambda^{\mathrm{mean}}} \end{pmatrix}. \tag{7.30}$$

In the first component, we replace $\alpha(\mathcal{T}_1)$ by the smallest heat transfer coefficient $\alpha_l = \alpha(T_{\min})$. Moreover, we evaluate the heat power term $p = p(\mathcal{T}_3)$, where $\mathcal{T}_3 \geq T^{\mathrm{mean}}$. The remaining components $\bar{\mathbf{h}}_1$ and $\bar{\mathbf{h}}_2$ are evaluated at the largest temperature $T_{\max}$. Due to the monotonicity of p and α, these replacements yield a larger iterative increase of the components of $\bar{\mathbf{h}}$.

---

[1] Note that at this point, like in Proposition 8, a rigorous justification is outstanding.

Hence, we have $q \leq \bar{q} = \sup\limits_{\mathcal{T}^{(1)},\mathcal{T}^{(2)} \in \mathbb{R}^3} \left\| \int\limits_0^1 \nabla \bar{\mathbf{h}}(\mathcal{T}^{(1)} + s\,(\mathcal{T}^{(2)} - \mathcal{T}^{(1)}))\,\mathrm{d}s \right\|$. The definition of $\bar{\mathbf{h}}$ in (7.30) implies

$$\nabla \bar{\mathbf{h}} = \begin{pmatrix} 0 & 0 & C_{\bar{h}} \\ 1 & 0 & 0 \\ 0 & 1 & 0 \end{pmatrix} \quad \text{where } C_{\bar{h}} = \left(\sum_{k=1}^{N} \frac{(\rho_0)_k\,(\alpha_\rho)_k\,I_k^2}{A_k^{\mathrm{ph}}} \right) / (\pi\, d^{\mathrm{ex}}\, \alpha_l)\,.$$

Observe that $\nabla \bar{\mathbf{h}}$ is constant and diagonalizable. It has one real eigenvalue $\lambda_1 = \sqrt[3]{C_{\bar{h}}}$ and two complex ones $\lambda_{2,3}$ with $|\lambda_{2,3}| = \sqrt[3]{C_{\bar{h}}}$. There holds $\mathbb{C}^3 = E_{\lambda_1} \oplus E_{\lambda_2} \oplus E_{\lambda_3}$. Consequently, each vector $\mathbf{x} \in \mathbb{C}^3 \setminus \{0\}$ represents an eigenvector, belonging to λ_1, λ_2 or λ_3.

We define

$$\bar{q} := \|\nabla \mathbf{h}(\mathcal{T})\| = \sup_{\mathbf{x} \in \mathbb{R}^3 \setminus \{0\}} \frac{|\nabla \mathbf{h}(\mathcal{T}) \,\cdot\, \mathbf{x}|}{|\mathbf{x}|}.$$

As $\mathbb{R}^3 \setminus \{0\} \subset \mathbb{C}^3 \setminus \{0\}$, there holds on the one hand

$$\bar{q} \leq \sup_{\mathbf{x} \in \mathbb{C}^3 \setminus \{0\}} \frac{|\nabla \mathbf{h}(\mathcal{T}) \,\cdot\, \mathbf{x}|}{|\mathbf{x}|} = \max_{\lambda_i \in \{\lambda_1,\lambda_2,\lambda_3\}} |\lambda_i| = \lambda_1,$$

on the other hand

$$\bar{q} = \sup_{\mathbf{x} \in \mathbb{R}^3 \setminus \{0\}} \frac{|\nabla \mathbf{h}(\mathcal{T}) \,\cdot\, \mathbf{x}|}{|\mathbf{x}|} \geq \frac{|\nabla \mathbf{h}(\mathcal{T}) \,\cdot\, \mathbf{x}|}{|\mathbf{x}|} = \frac{|\lambda_i \,\cdot\, \mathbf{x}|}{|\mathbf{x}|} = |\lambda_i| = \lambda_1, \text{ with } \lambda_i \in \{\lambda_1, \lambda_2, \lambda_3\}\,.$$

Thus, $\bar{q}$ is given by the real eigenvalue of $\nabla \bar{\mathbf{h}}$, $\bar{q} = \sqrt[3]{C_{\bar{h}}}$. Identifying q with the upper bound $\bar{q}$ yields the result. □

Note that the sufficient condition for contractivity of **h** in Proposition 17 is already implied by the non-resonance condition in Theorem 15.

Proposition 18. *Suppose that the non-resonance condition in Theorem 15 is fulfilled. Then there holds $q < 1$, i.e. the fixed point iteration in Lemma 16 converges to the unique solution $\mathcal{T}^*$ of $\mathbf{h}(\mathcal{T}) = \mathcal{T}$.*

Proof. The non-resonance condition in Theorem 15 reads as $\max\limits_{1 \leq k \leq N} \left(\frac{(\rho_0)_k\,(\alpha_\rho)_k\,I_k^2}{(A_k^{\mathrm{ph}})^2} \right) \leq \frac{\alpha_l}{d_{\mathrm{ex}}}$ and the contractivity of **h** is ensured by $\frac{1}{\pi\, d_{\mathrm{ex}}^2} \sum\limits_{k=1}^{N} \frac{(\rho_0)_k\,(\alpha_\rho)_k\,I_k^2}{(A_k^{\mathrm{ph}})^2} \leq \frac{\alpha_l}{d_{\mathrm{ex}}}$. There holds

$$\begin{aligned} \frac{1}{\pi\, d_{\mathrm{ex}}^2} \sum_{k=1}^{N} \frac{(\rho_0)_k\,(\alpha_\rho)_k\,I_k^2}{A_k^{\mathrm{ph}}} &\leq \frac{1}{\pi\, d_{\mathrm{ex}}^2} \sum_{k=1}^{N} \max_{1 \leq k \leq N} \left(\frac{(\rho_0)_k\,(\alpha_\rho)_k\,I_k^2}{(A_k^{\mathrm{ph}})^2} \right) A_k^{\mathrm{ph}} \\ &= \frac{\sum\limits_{k=1}^{N} A_k^{\mathrm{ph}}}{\pi\, d_{\mathrm{ex}}^2} \max_{1 \leq k \leq N} \left(\frac{(\rho_0)_k\,(\alpha_\rho)_k\,I_k^2}{(A_k^{\mathrm{ph}})^2} \right) \leq \max_{1 \leq k \leq N} \left(\frac{(\rho_0)_k\,(\alpha_\rho)_k\,I_k^2}{(A_k^{\mathrm{ph}})^2} \right), \end{aligned}$$

which implies the assertion. □

Remark 19. *(i) For applications, it makes again sense to set* $T_{min} = T_{amb}$ *and* $T_{max} \leq 200\,^\circ\mathrm{C}$*, because the cables are at least as hot as the environment and insulation parts would not sustain temperatures higher than* $200\,^\circ\mathrm{C}$*.*
(ii) The a priori estimate on q *given by Proposition 17 may be too rough, i.e. there are currents violating the contractivity condition, nevertheless yielding convergence of* $(\mathcal{T}^{(n)})_{n\in\mathbb{N}}$*. Therefore, we introduce indicators of contractivity:*

$$q_n := \frac{\left|\mathbf{h}(\mathcal{T}^{(n)}) - \mathbf{h}(\mathcal{T}^{(1)})\right|}{\left|\mathcal{T}^{(n)} - \mathcal{T}^{(1)}\right|} = \frac{\left|\mathcal{T}^{(n+1)} - \mathcal{T}^{(2)}\right|}{\left|\mathcal{T}^{(n)} - \mathcal{T}^{(1)}\right|}\,.$$

If $\left(\mathcal{T}^{(n)}\right)_{n\in\mathbb{N}}$ *converges,* q_n *provides at least an a posteriori information about the convergence speed.*

7.5 Comparison of Calculations and Measurements

To compare the simulation results of both approaches, we determine the heat distribution in multicables consisting of 33 single cables.[2] The single cables are of different types Tp_k and each metallic part of a single cable consists of n_k^c conductors with diameter δ_k. The total number N_k^{Tp} of single cables of the corresponding type, their currents I_k in the multicables and the physical current density J_k^{ph} are listed in Table 7.1. All diameters are indicated in mm. More detailed information can be found in the Appendix in Table A.1.

Tab. 7.1: *Properties of single cables and currents in simulations and measurements of multicables.*

Tp_k	Name	d_k^{in}	d_k^{ex}	n_k	δ_k	N_k^{Tp}	I_k (A) [J_k^{ph} (A/mm^2)]
1	FLRY-A 10.0	4.30	5.80	80	0.40	1	$1 \times 53.0\,[5.30]$
2	FLRY-A 6.0	3.25	4.15	84	0.30	3	$1 \times 37.0\,[6.17]$, $1 \times 12.0\,[2.00]$, $1 \times 0.10\,[0.02]$
3	FLRY-A 4.0	2.70	3.55	56	0.30	4	$1 \times 23.0\,[5.75]$, $1 \times 16.2\,[4.05]$, $1 \times 14.9\,[3.72]$, $1 \times 0.10\,[0.03]$
4	FLRY-A 2.5	2.10	2.85	50	0.25	5	$2 \times 18.0\,[7.20]$, $1 \times 12.0\,[4.80]$, $2 \times 0.10\,[0.04]$
5	FLRY-A 1.0	1.30	2.00	32	0.20	6	$1 \times 12.0\,[12.0]$, $2 \times 9.50\,[9.50]$, $3 \times 0.10\,[0.10]$
6	FLRY-A 0.75	1.15	1.80	24	0.20	2	$2 \times 0.10\,[0.13]$
7	FLRY-A 0.50	0.93	1.60	16	0.20	2	$1 \times 7.00\,[14.0]$, $1 \times 4.50\,[9.00]$
8	FLRY-A 0.35	0.80	1.35	12	0.20	10	$2 \times 4.00\,[11.4]$, $2 \times 3.80\,[10.9]$, $1 \times 2.10\,[6.00]$, $3 \times 0.40\,[1.14]$, $2 \times 0.34\,[0.97]$

In order to examine the influence of the cable layout, we distinguish three scenarios with different initial configurations, dependent on the current density J_k^{ph} of each single cable:

1. Inner Layout (INL):
   Assignment of the single cables to template positions in descending order w.r.t. J_k^{ph}.
2. Outer Layout (OUL):
   Assignment of the single cables to template positions in ascending order w.r.t. J_k^{ph}.
3. Monte Carlo Layout (MCL):
   Stochastic placement of single cables in the template.

Furthermore, thermal measurements of the three multicables, composed for industrial application, were carried out in the laboratories of the Labco GmbH. One temperature for each single cable was measured via thermocouples. The exact layout of the cable cross section has

---

[2] The single cable data were provided by the automotive supplier Sumitomo Electric Bordnetze. The currents represent a current feed of a main strand in a VW Golf 5.

not been provided by the laboratory, only the initial positions for the production process, attached in Table A.1. Thus, we applied Algorithm 4, illustrated for MCL in Figure 7.7, to obtain an approximating cable configuration. In all three scenarios, the computed cable layouts are sufficiently realistic after 60 iterations of squeezing and separating for $\delta_0 = 0.5$. Finally, a cable layout like in Figure 7.8a is obtained. We apply FEM to this geometry, beginning with an automatic mesh generation (see Figure 7.8b).

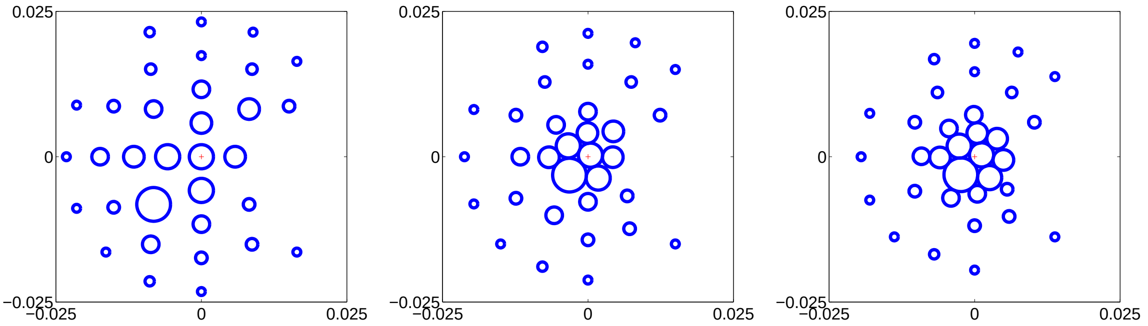

(a) Initial configuration **(b)** Config. iteration 1 **(c)** Config. iteration 2

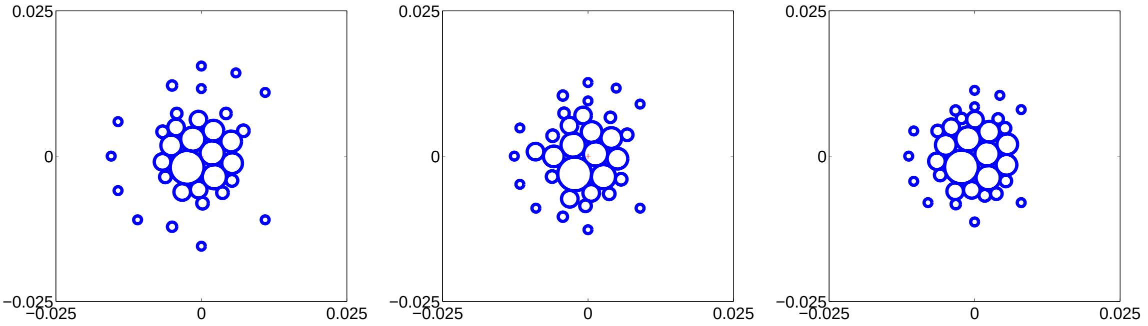

(d) Config. iteration 5 **(e)** Config. iteration 10 **(f)** Config. iteration 15

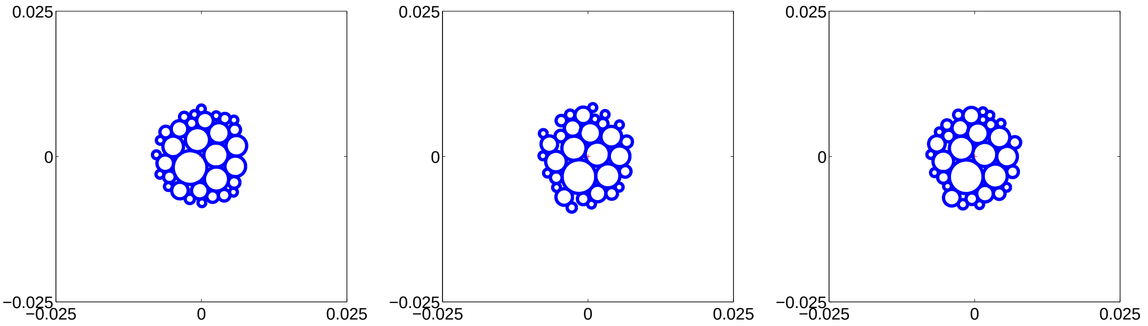

(g) Config. iteration 20 **(h)** Config. iteration 40 **(i)** Config. iteration 60

Fig. 7.7: *Cable Squeezing Algorithm 4 applied to 33 single cables with starting configuration MCL.*

In the simulations via both approaches, identical parameter values were used, cf. Table 7.2. The metallic parts of the single cables consist of copper, their insulation of PVC and the exterior multicable insulation of PET fleece. The parameter values were provided by the industrial partners. Since the measurements were carried out in different environments,

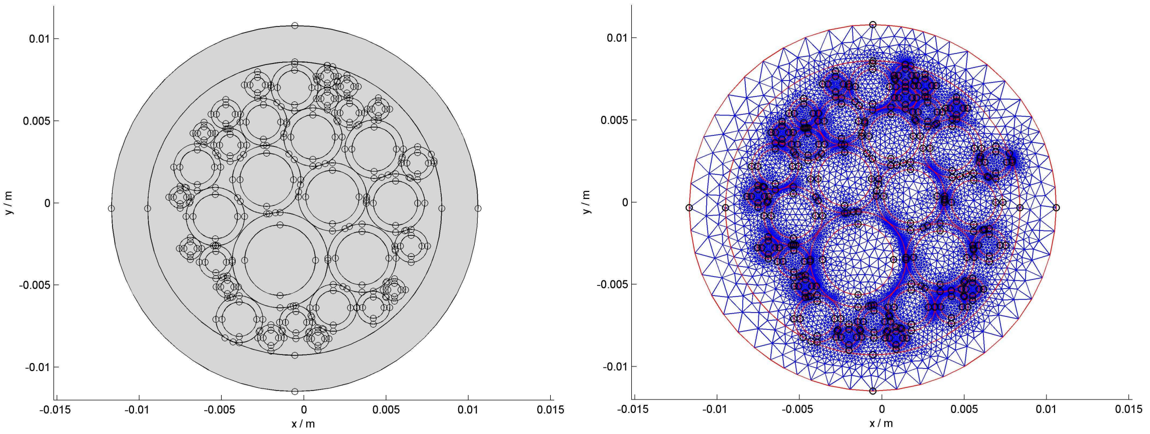

(a) Computed geometry for MCL. **(b)** Automatically generated mesh for MCL.

Fig. 7.8: *Computed geometry and generated mesh for Monte Carlo Layout.*

the ambient temperatures vary with respect to the three scenarios. This is considered in the evaluation of the results.

Tab. 7.2: *Parameter values in computations of temperatures in multicables.*

Parameter name	Symbol	Value	Unit
Heat conductivity of metallic conductors	λ_k^{met}	401	$\mathrm{W/(m \cdot K)}$
Heat conductivity of single cable insulation	λ_k^{iso}	0.19	$\mathrm{W/(m \cdot K)}$
Heat conductivity of outer insulation	λ^{ex}	0.08	$\mathrm{W/(m \cdot K)}$
Heat conductivity of air	λ^{air}	2.61e-2	$\mathrm{W/(m \cdot K)}$
Electr. resistivity at reftemperature	$(\rho_0)_k$	1.71e-8	$\Omega \cdot \mathrm{m}$
Temp. coefficient of the electr. resistivity	$(\alpha_\rho)_k$	4.04e-3	1/K
Emission coefficient	ϵ_{r}	0.93	
Reference temperature	T_0	20	°C
Ambient temperature	T_1	33.2(INL), 25.8(OUL), 36.5(MCL)	°C
Inner cable diameter	d^{in}	1.86 (INL), 1.79 (OUL), 1.79 (MCL)	cm
Outer cable diameter	d^{ex}	2.30 (INL), 2.23 (OUL), 2.23 (MCL)	cm

A summary of the calculation results for the three scenarios compared to the measurements (MES) is listed in Table 7.3 and further details are stated in Tables A.2 and A.3. Therein, we denote $\varnothing(T)$ the average temperature of the single cable cores, $\varnothing^{\mathrm{A}}(T)$ the average temperature in the single cable cores weighted with respect to the cross sectional area, $\max(T)$ the maximum and $\min(T)$ the minimum temperature in all single cables. We indicate these measures minus ambient temperatures to have a better comparability of the different scenarios. The varying ambient temperatures have an influence on the results, even on the differences of temperatures, but it is comparatively small. The finite element approach yields a detailed temperature profile of the multicable as depicted in Figure 7.9. For the HBA, we obtain temperatures at three characteristic points in a cable. We compare T^{cen} to the average temperatures and T^{in} to the minimum temperature. A maximum temperature cannot be provided, since we have no adequate quantity.

Both, the average and minimum temperature differences in the three layouts for HBA, hardly vary, cf. Table 7.3. This is not surprising, as HBA is invariant with respect to the configuration of the single cables. The minor differences can be explained by different

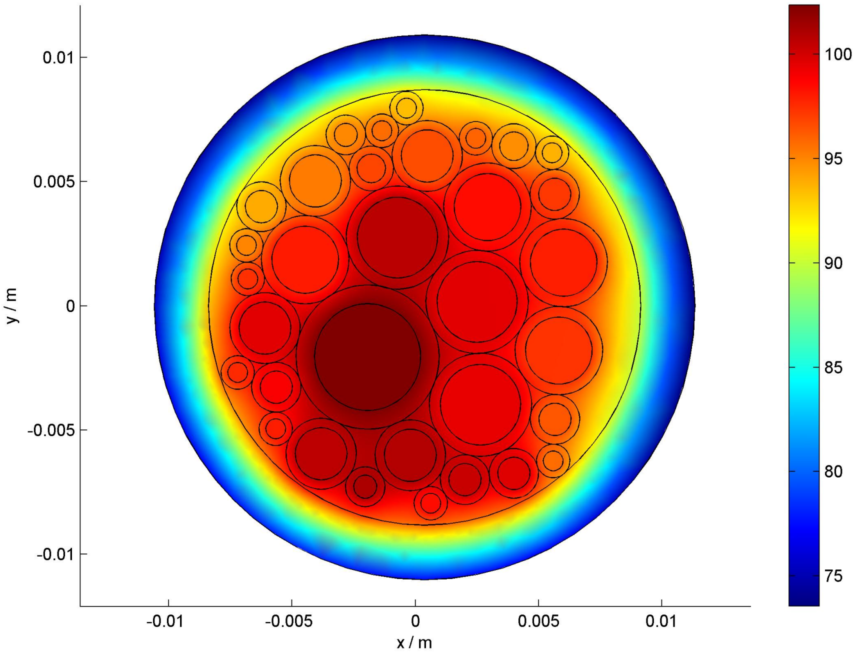

Fig. 7.9: *Temperature distribution in a multicable with starting configuration MCL.*

Tab. 7.3: *Measured and computed temperature differences for multicables in K.*

	Inner Layout			Outer Layout			Monte Carlo Layout		
	MES	FEA	HBA	MES	FEA	HBA	MES	FEA	HBA
$\varnothing^{\mathrm{A}}(T) - T_{\mathrm{amb}}$	61.6	65.6	60.8	63.0	61.7	61.8	61.0	63.6	62.2
$\max(T) - T_{\mathrm{amb}}$	69.7	74.2	-	66.6	65.2	-	64.5	67.2	-
$\min(T) - T_{\mathrm{amb}}$	55.0	57.2	53.5	57.4	58.0	55.1	54.6	57.9	55.2

ambient temperatures and the larger exterior diameters of the multicable for INL compared to OUL and MCL. Obviously, in OUL and MCL, the same exterior diameter is used, but the average temperature in OUL is slightly lower than in MCL. The reason is that the warmer ambient temperature in MCL effects a higher electrical resistivity of the metallic parts via $(\alpha_\rho)_k$. The slightly larger diameter of the multicable in INL yields a smaller packing density and a larger surface, which both result in comparatively lower temperatures[3].

Regarding the results of FEA, we notice that the maximum temperature in the multicable for INL is significantly higher than for the other scenarios. This observation is confirmed, albeit in weakened form, by the measurement results for the three scenarios. It is explained by the fact that single cables with higher values for J_k^{ph}, positioned closer to the exterior insulation, emit more heat to the ambience than in the centre. Consequently, the positioning of the single cables in the multicable essentially influences the maximum temperature.

Another consequence of this observation is the larger size of the temperature interval $[\min(T), \max(T)]$ for INL in FEA (17.0 K) and the measurements (14.7 K) than in OUL

---

[3] Comparatively lower in this context means in comparison to the same scenario with smaller diameters; it shall not mean compared to the other scenarios OUL and MCL.

(7.2 K respectively 8.8 K) and MCL (9.3 K respectively 9.9 K).

Tab. 7.4: *Absolute and relative deviations of simulations and measurements for multicables.*

	abs. deviation (K)						**rel. deviation (%)**					
	INL		OUL		MCL		INL		OUL		MCL	
	FEA	HBA	FEA	HBA	FEA	HBA	FEA	HBA	FEA	HBA	FEA	HBA
$\lvert \varnothing(\cdot) - \varnothing(\mathrm{MES}) \rvert$	2.7	2.3	1.2	0.8	3.4	3.4	4.3	3.6	1.9	1.3	5.8	5.8
$\lvert \varnothing^{\mathrm{A}}(\cdot) - \varnothing^{\mathrm{A}}(\mathrm{MES}) \rvert$	4.0	0.8	1.3	1.2	2.6	1.2	6.5	1.3	2.1	1.9	4.3	2.0
$\lvert \max(\cdot) - \max(\mathrm{MES}) \rvert$	4.5	-	1.4	-	2.7	-	6.5	-	2.1	-	4.2	-
$\lvert \min(\cdot) - \min(\mathrm{MES}) \rvert$	2.2	1.5	0.6	2.3	3.3	0.6	4.0	2.7	1.0	4.0	6.0	1.1
$\lvert \varnothing_k^{\mathrm{A}}(\Delta \mathrm{T}) \rvert$	4.1	3.9	1.6	2.6	2.7	2.5	6.7	6.3	2.5	4.1	4.4	4.1
$\lvert \max_{\mathrm{k}}(\Delta \mathrm{T}) \rvert$	8.5	-	5.1	-	6.5	-	13.5	-	8.1	-	11.1	-

In Table 7.4, the deviations of our simulations and measurements are shown. The measures with (MES) give the corresponding quantities of the measurements. Additionally, we denote $\max_{\mathrm{k}}(\Delta \mathrm{T})$ the maximal deviation in temperature of all single cables between measurement and simulation and $\varnothing_k^{\mathrm{A}}(\Delta \mathrm{T})$ the corresponding mean value. The relative deviation in Table 7.4 shows the ratio of deviation in temperature between measurement and computed temperature (in K) to the measured temperature (in °C).

Obviously, good agreement between measurements and simulations is obtained by FEA and HBA (cf. Tables 7.3 and 7.4). Keeping in mind that measuring inaccuracies, numerical errors and uncertainties in the parameter values are included, we see that both methods are appropriate for simulations, but they have different focuses. An absolute deviation of 8.5 K and a relative one of 13.5 % for $|\max_{\mathrm{k}}(\Delta \mathrm{T})|$ in INL is rather large. It is due to the fact that the cable squeezing algorithm can only provide an approximation of the real multicable cross section. Since we were not able to obtain the cross section of the measured cable, we cannot validate how well the computed layout corresponds to the real one. Single cables with very large current densities J_k^{ph}, positioned in a cold multicable region for the measurement and in a hot region for the simulation or vice versa, can imply deviations of this magnitude.

The isotropization in HBA suits ideally for cases where only small variations of J_k^{ph} occur. This is the normal case for practical applications with current loads over long periods. In Figure 7.10, the heat distribution of a multicable with only one single cable of higher current density ($J_k^{\mathrm{ph}} = 44.2\,\mathrm{A/mm^2}$) is depicted. The finite element simulation yields a maximum temperature of 178.8 °C. The fixed point approach provides only useless information ($T^{\mathrm{cen}} = 95.8\,°\mathrm{C}$, $T^{\mathrm{in}} = 88.2\,°\mathrm{C}$) for such an extreme case.

In both approaches, we observe fast convergence. The mentioned stopping criterion for FEA is in all cases reached after four to six Newton iterations. HBA requires about 20 iterations to fulfil $\left|\mathcal{T}^{(n)} - \mathcal{T}^*\right| \leq 1e\text{-}6$ with a posteriori contractivity indicators about 0.82[4]. Table 7.5 shows that calculation times for FEA on an Intel Core 2 Duo processor with 2.67 GHz and 3.00 GB RAM are short compared to the complexity of the calculation ($\approx$ 60 000 − 100 000 DOFs). Nevertheless, in context of applications, great numbers of parameter variations in complex parameter studies are necessary to find appropriate cable compositions. This effects a considerable increase of calculation times up to several hours. In contrast, the HBA allows extensive studies with several hundreds of variations in a few seconds, which makes the approach particularly interesting for industry.

---

[4] The a priori contractivity indicators are larger than 1 in this example and thus not helpful.

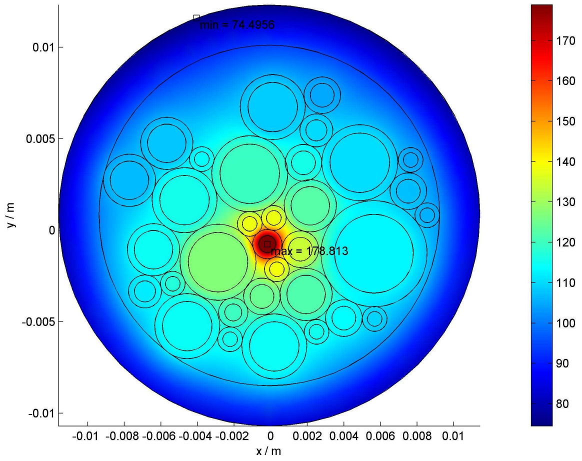

Fig. 7.10: *Heat distribution in a multicable with large variations in the current densities.*

	INL	OUL	MCL
t_{SQZ} (s)	4.83	4.92	4.85
t_{FEM} (s)	22.7	24.9	18.6
t_{FEA} (s)	27.6	29.8	23.4
t_{HBA} (s)	0.0103	0.0093	0.0094
NOE	43 652	51 069	30 900
DOFs	87 363	102 196	61 857
q_n	0.8209	0.8241	0.8246

Tab. 7.5: *Calculation times, degrees of freedom and contractivity indicators for the three test scenarios.*

7.6 Optimization

In the previous section, the dependence of the heat distribution in multicables on the configuration of the single cables was shown by numerical experiments and measurements. Figure 7.11 depicts two different multicables consisting of 33 single cables with the same current and cross sectional area for each single cable in both cases. Furthermore, the diameters of the multicable, ambient temperatures and all other parameters are equal. Both only differ in the positioning of the single cables in the multicable. Obviously, although the ambient temperature $T_1 = 33.2\,°\mathrm{C}$ and outer diameter $d^{\mathrm{ex}} = 1.86\,\mathrm{cm}$ are equal, the maximum temperature in the left multicable is lower than in the right one. It is 98.8 °C in the left multicable (created with OUL) and 107.4 °C in the right one (created with INL).

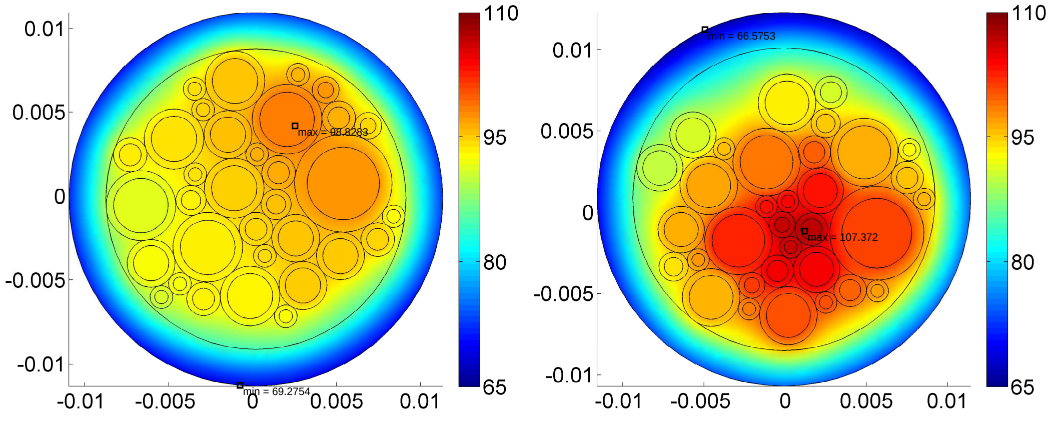

(a) Cable layout 1.

(b) Cable layout 2.

Fig. 7.11: *Temperature distributions for equally composed multicables varying in single cable positions.*

In this section, an algorithm to find an optimal multicable layout is developed. For each single cable, the current and the diameters are fixed a priori. Dependent on the number of single cables and available space, different strategies are recommended. Whereas for rather loosely packed cables the exclusive application of gradient based shape optimization is sufficient, we additionally have to couple it to a genetic algorithm for densely packed cables. For the shape optimization part, we point out the derivation of an adjoint system and the shape gradient as well as the local shape derivative. In addition, we present our genetic algorithm adapted to the problem.

We start by summarizing literature on the optimization of bundle wires and shape optimization. In [19], algorithms for the minimization of the total weight of cable bundles by given maximum temperature were developed. Therein, parallel multilevel methods are applied to heuristic strategies based on greedy type search methods. Our optimization problem is related. In contrast, we couple a non-gradient based strategy, namely a genetic algorithm, to a gradient based shape optimization approach. For introductions to the shape calculus and mathematical background, we recommend [26, 109, 122]. To derive the shape gradient and an adjoint system, we present two approaches. The alternative one attached in the Appendix A.2.4. Therein, like in [72], we formally obtain optimality conditions via the Lagrange technique (cf. [130]). The particularity in the Hadamard representation of our shape gradient is due to the jumps in the coefficients of different materials at the interfaces. In [49, 51, 54], methods to derive the corresponding shape gradient are explained.

This chapter is organized as follows: In Section 7.6.1, we formulate the optimal multicable layout problem. Our general optimization strategy combining the Cable Squeezing Algorithm 4, heuristics for good initial positions, shape optimization and a genetic algorithm is explained in Section 7.6.2. To perform gradient based shape optimization, we derive the local shape derivative, the shape gradient and an adjoint system for a sensitivity analysis in Section 7.6.3. Section 7.6.4 describes further numerical and computational details. Numerical experiments are carried out in Section 7.6.5 and we finally discuss our results and the practical applicability in Section 7.6.6.

7.6.1 Setting of the Problem

In this section, we introduce some additional mathematical notation and formulate the optimal multicable layout problem.

Notation

All vector valued functions are indicated by bold letters, e.g. the space variable $\mathbf{x} = (x, y)^T \in \mathbb{R}^2$ with norm $|\mathbf{x}|_{\mathbb{R}^2} = \left(x^2 + y^2\right)^{1/2}$ and inner product $(\mathbf{x}_1, \mathbf{x}_2)$. The operator Div denotes the tangential divergence of a tangential field and ∇_τ the tangential (surface) gradient of a scalar valued function. We identify $\mathbf{n} = \mathbf{n}_\mathrm{e}$ with the unit outer normal that points outward of the considered object, $\mathbf{n}_\mathrm{i}$ the inner normal pointing into the object (cf. Figure 7.4). Consequently, the notation $\frac{\partial}{\partial \mathbf{n}}$ corresponds to the normal derivative of a quantity in outer direction.

The interfaces between core and insulation of each single cable as well as between single cable insulation and surrounding gaps play an important role in the calculation of the shape gradient. Thus, we introduce the interface boundaries Γ_k^i and Γ_k^e for $k = 1, \ldots, N$. They are depicted in Figure 7.4b as well as corresponding normal vectors on the boundaries.

State System

Let the two dimensional cross sectional area of the multicable Ω^{MC} be a connected, bounded domain in $\mathbb{R}^2$ with regular exterior boundary $\partial\Omega^{\mathrm{MC}} = \Gamma^{\mathrm{ex}}$ and interface boundaries $\Gamma^{\mathrm{int}} = \bigcup_{k=1}^{N} \left(\Gamma_k^{\mathrm{i}} \cup \Gamma_k^{\mathrm{e}}\right) \cup \Gamma^{\mathrm{gi}}$. Therein, the boundary Γ^{gi} represents the interface between the exterior insulation and the core.

Due to the jumps of the heat conductivity, the temperature profile is continuous across the interface $\iota \in \Gamma^{\mathrm{int}}$ of different materials, but has kinks. We repeat the governing system that determines the temperature in the multicable and call it the *state system.* Although the mentioning of the interface conditions is not necessary for a concise problem presentation, we explicitly indicate them, since they are important for the Hadamard representation of the shape gradient:

$$\boxed{\begin{aligned} -\nabla \cdot (\lambda\, \nabla T) - c \cdot T = \tilde{f} \qquad & \text{in } \Omega^{\mathrm{MC}} \setminus \Gamma^{\mathrm{int}}, \\ \lambda^{\mathrm{ex}} \frac{\partial T}{\partial \mathbf{n}} + \alpha(T) \cdot (T - T_1) = 0 \qquad & \text{on } \Gamma^{\mathrm{ex}}, \\ [T]_{\pm} = 0 \quad \text{and} \quad \left[\lambda \frac{\partial T}{\partial \mathbf{n}}\right]_{\pm} = 0 \qquad & \text{on } \iota \in \Gamma^{\mathrm{int}}. \end{aligned}} \tag{7.31}$$

Optimization Problem

Let the dimensions of the exterior insulation and the single cables be given. The material parameters and the electric current of each single cable are fixed and known, such that λ, c and $\tilde{f}$ are determined a priori. What we vary is the positioning of the single cables, summarized by the domain

$$\Omega := \bigcup_{k=1}^{N} \Omega_k = \bigcup_{k=1}^{N} \left(\Omega_k^{\mathrm{core}} \cup \Omega_k^{\mathrm{iso}}\right), \tag{7.32}$$

with Ω_k the domain of single cable k. As the position of each single cable is determined by its centre, our optimization variables are the centre coordinates of the single cables $(x_1, y_1), \dots, (x_N, y_N)$. Consequently, the optimal multicable layout problem (OptMC) with dependent domain Ω reads as

$$\boxed{\begin{aligned} & J(\Omega) = \sum_{k=1}^{N} \int_{\Omega_k} j(\mathbf{x}, T(\mathbf{x}))\, \mathrm{d}\mathbf{x} + \int_{\Omega^{\mathrm{MC}} \setminus \cup_{k=1}^{N} \Omega_k} j(\mathbf{x}, T(\mathbf{x}))\, \mathrm{d}\mathbf{x} \to \text{ min!} \\ & \text{with} \\ & \quad -\nabla \cdot (\lambda\, \nabla T) - c \cdot T = \tilde{f} & & \text{in } \Omega^{\mathrm{MC}} \setminus \Gamma^{\mathrm{int}}, \\ & \quad \lambda^{\mathrm{ex}} \frac{\partial T}{\partial \mathbf{n}} + \alpha(T) \cdot (T - T_1) = 0 & & \text{on } \Gamma^{\mathrm{ex}}, \\ & \quad [T]_{\pm} = 0 \quad \text{and} \quad \left[\lambda \frac{\partial T}{\partial \mathbf{n}}\right]_{\pm} = 0 & & \text{on } \iota \in \Gamma^{\mathrm{int}}, \\ & \quad (x_k - x_0)^2 + (y_k - y_0)^2 < \left(r_k^{\mathrm{ex}} - r_0^{\mathrm{in}}\right)^2, & & k \in K = \{1, \dots, N\}, \\ & \quad (x_k - x_l)^2 + (y_k - y_l)^2 > \left(r_k^{\mathrm{ex}} + r_l^{\mathrm{ex}}\right)^2, & & (k, l) \in (K \times K) \setminus \{k = l\}, \\ & \quad x_1 = 0, \qquad 0 < y_1 < r_0^{\mathrm{in}}, \qquad 0 < x_2 < r_0^{\mathrm{in}}. \end{aligned}} \tag{7.33}$$

It is the objective to minimize the functional $J(\Omega)$ respectively the function $j\left(\mathbf{x}, T\left(\mathbf{x}\right)\right)$ over the domain Ω^{MC} subject to the state system (7.31) and geometrical constraints. We require that each single cable has to be inside the multicable and single cables must not overlap.[5] This problem is rotationally symmetrical because we apply the same boundary condition to the entire exterior boundary. Thus, we allow the first cable to be positioned only on the vertical upper line segment connecting the multicable centre and the point $(0, r_0^{\mathrm{in}})$. To avoid axial symmetry, the second cable has to be in the right sector of the multicable.

Note once more that the domain Ω of the single cables is composed of the subdomains $\Omega_k,\ k = 1, \ldots, N$, which themselves depend on the subdomains Ω_k^{core} and Ω_k^{iso}. We introduce the notation

$$B_r(\mathbf{c}) = \left\{\mathbf{x} \in \mathbb{R}^2 | d(\mathbf{c}, \mathbf{x}) < r\right\},$$

describing the open ball of radius $r > 0$ centered at a point $\mathbf{c} \in \mathbb{R}^2$. Thus, the core and the insulation of single cable k are determined by

$$\Omega_k^{\mathrm{core}} = B_{r_k^{\mathrm{in}}}\left((x_k, y_k)^t\right), \Omega_k^{\mathrm{iso}} = B_{r_k^{\mathrm{ex}}}\left((x_k, y_k)^t\right) \setminus \Omega_k^{\mathrm{core}}.$$

The dependence of the single cable k on the coordinates (x_k, y_k) is obvious and consequently the dependence of the entire domain Ω of the single cables on all centres, abbreviated by

$$\Omega = \Omega\left((x_1, y_1), \ldots, (x_N, y_N)\right).$$

We summarize the set of admissible domains by

$$\begin{aligned}\mathcal{O}_{\mathrm{ad}} = \big\{\Omega = \Omega\left((x_1, y_1), \ldots, (x_N, y_N)\right) \in \mathbb{R}^2 \mid \\ &(x_k - x_0)^2 + (y_k - y_0)^2 < \left(r_k^{\mathrm{ex}} - r_0^{\mathrm{in}}\right)^2,\ k \in K = \{1, \ldots, N\}, \\ &(x_k - x_l)^2 + (y_k - y_l)^2 > (r_k^{\mathrm{ex}} + r_l^{\mathrm{ex}})^2,\ (k, l) \in (K \times K) \setminus \{k = l\}, \\ &x_1 = 0,\ 0 < y_1 < r_0^{\mathrm{in}},\ 0 < x_2 < r_0^{\mathrm{in}}\big\}.\end{aligned}$$

The exterior insulation and thus the exterior boundary of the domain Ω^{MC} is fixed in this setting. However, we do not consider the domain entirely, but as a composition of several subdomains. Thus, the interface boundaries of Ω^{MC} vary for different shapes of the domain Ω of the single cables, which is indicated by the notation $\Omega^{\mathrm{MC}}(\Omega)$.

Throughout this chapter, we assume that all interface boundaries $\Gamma_k^{\mathrm{i}}, \Gamma_k^{\mathrm{e}},\ k = 1, \ldots, N$, Γ^{gi} and the exterior boundary Γ^{ex} are Lipschitz continuous and C^2-smooth.

7.6.2 Optimization Algorithm

Dependent on the number of single cables in the multicable and the available space, different optimization strategies have to be applied. In this section, we describe our general optimization strategy and how to find good initial positions.

Optimization Strategy

To solve the optimal multicable layout problem (7.33), we combine different algorithms and optimization techniques as shown in Figure 7.12. To approximate a global minimum, we use M different initial positions, obtained by heuristics and the application of the Cable Squeezing Algorithm 4.

---

[5] To avoid problems in the calculation with finite elements, we require in the numerical implementation that the distance between each single cable and the multicable insulation respectively pairwise between two single cables has to be larger than $\delta_m > 0$. The parameter δ_m is chosen such that there is sufficient space in between to create a feasible mesh.

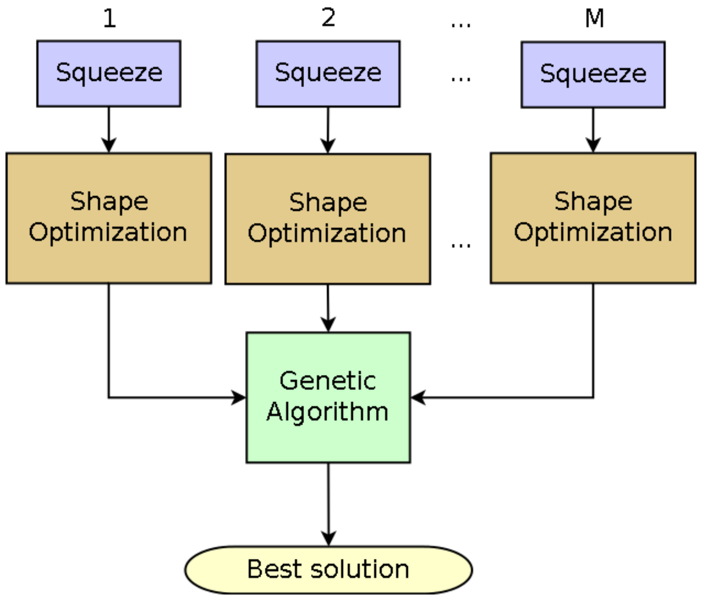

Fig. 7.12: *Optimization strategy to solve the optimal multicable layout problem.*

Using a gradient based strategy like shape optimization (cf. Section 4.2) does not always provide a satisfying solution, since for multicables consisting of a large number of single cables several local minima may exist. Therefore, we give our M local minima to a genetic algorithm (cf. Section 4.3) which tries to find an even better solution. The coupling of these different algorithms is adequate, as an exclusive use of the genetic algorithm is too time extensive and expensive. Furthermore, we obtain much better results in our simulations with the mixed strategies.

Initialization

As mentioned, different local minima can exist, especially for more than three single cables. In order to ensure feasibility of the cable configurations, we apply Algorithm 4. After a fixed number of squeezing steps, the diameter of the surrounding circle including all single cable circles has to be smaller than or equal to the given inner diameter of the exterior insulation. If this is not fulfilled, this initial template configuration cannot be used for the optimization.

The initial cable configuration has an important influence on the computed local minimum and is mainly determined by the initial assignment of single cables to template positions. Thus, we propose different heuristic strategies, dependent on the geometrical current density $J_k^{\text{ge}} = I_k/A_k^{\text{ge}}$, $k = 1, \dots, n$, to create good assignments of the single cables to their template positions[6]:

- The single cables are assigned to the template positions in descending order w.r.t. J_k^{ge}, denoted by INL;
- The single cables are assigned to the template positions in ascending order w.r.t. J_k^{ge}, denoted by OUL;

---

[6] The physical current density could also be chosen as criterion for the template assignments and would not change those in our example.

- The single cables are ordered ascendantly w.r.t. J_k^{ge}, but assigned to the template positions in steps of 2, 3, 4 respectively 5, denoted by OUL2, OUL3, OUL4 and OUL5. For example, in case of OUL2, we assign the cable with the lowest current density to position 1, the cable with the second lowest current density to position 3, etc. As soon as a single cable would be assigned to a template position larger than the number of all single cables, we start to fill the lacunas, meaning that the present single cable is assigned to position 2, the next to position 4, etc.;
- The single cables are assigned to template positions such that two cables following each other in order dependent on J_k^{ge} have the greatest possible distance in the template layer, denoted by OPP;
- Further template configurations are completely arbitrary and denoted by MCL1, MCL2, etc.

By tendency, hotter single cables can give more thermal energy to the ambience if they are nearer to the exterior border. Hence, especially OUL, OUL2–OUL5 and OPP seem promising to give good configurations, but they need not necessarily. As there exist cases for which other template configurations yield our best solution, we added INL and the arbitrary assignments.

7.6.3 Sensitivity Analysis

In the following, we apply an adjoint method to compute the shape gradient. Thus, we derive an adjoint system, the Hadamard representation of the shape gradient and the local shape derivative of the problem. An alternative approach which is only formal is attached in the Appendix A.2.4.

Local Shape Derivative

Before deriving the shape gradient, we state the system holding for the local shape derivative $\delta T[\mathbf{V}]$ of (OptMC). To this end, let $\mathbf{V} \in C^2(\overline{\Omega}; \mathbb{R}^2)$ be a smooth domain variation of Ω. Then, there holds:

$$\boxed{\begin{aligned} \nabla \cdot (\lambda \nabla \delta T[\mathbf{V}]) + c \cdot \delta T[\mathbf{V}] = 0 \ \text{ in } \ \Omega^{\mathrm{MC}} \setminus \Gamma^{\mathrm{int}}, \\ \lambda^{\mathrm{ex}} \frac{\partial \delta T\,[\mathbf{V}]}{\partial \mathbf{n}} + \big(\alpha'\,(T)\,(T - T_1) + \alpha(T)\big)\, \delta T\,[\mathbf{V}] = 0 \ \text{ on } \ \Gamma^{\mathrm{ex}}, \\ \left[\lambda \frac{\partial \delta T\,[\mathbf{V}]}{\partial \mathbf{n}}\right]_{\pm} = \operatorname{Div}\big(\langle \mathbf{V}, \mathbf{n}\rangle\,[\lambda]_{\pm}\, \nabla_{\tau} T\big) + \big([c]_{\pm}\, T + [f]_{\pm}\big)\, \langle \mathbf{V}, \mathbf{n}\rangle \\ \text{and } \ \Big[\delta T\,[\mathbf{V}]\Big]_{\pm} = -\,\langle \mathbf{V}, \mathbf{n}\rangle \left[\frac{\partial T}{\partial \mathbf{n}}\right]_{\pm} \ \text{ on } \ \iota \in \Gamma^{\mathrm{int}}. \end{aligned}} \tag{7.34}$$

Proof. The pointwise evaluation of the boundary value problem for T respectively $T_\epsilon[\mathbf{V}]$ on the domains $\Omega^{\mathrm{MC}}(\Omega)$ respectively $\Omega^{\mathrm{MC}}(\Omega_\epsilon[\mathbf{V}])$ in a point $\mathbf{x} \in \Omega^{\mathrm{MC}}(\Omega)$ provides

$$\lim_{\epsilon \to 0} \frac{\nabla \cdot (\lambda \nabla T_\epsilon[\mathbf{V}]) + c \cdot T_\epsilon[\mathbf{V}] - (\nabla \cdot (\lambda \nabla T) + c \cdot T)}{\epsilon} = -f + f = 0,$$

i.e. the partial differential equation

$$\nabla \cdot (\lambda \nabla \delta T[\mathbf{V}]) + c \cdot \delta T[\mathbf{V}] = 0 \ \text{ in } \ \Omega^{\mathrm{MC}} \setminus \Gamma^{\mathrm{int}}.$$

The boundary condition on the exterior boundary is

$$\lim_{\epsilon\to 0} \lambda^{\mathrm{ex}} \frac{\frac{\partial T_\epsilon[\mathbf{V}]}{\partial \mathbf{n}} - \frac{\partial T}{\partial \mathbf{n}}}{\epsilon} = -\lim_{\epsilon\to 0} \frac{\alpha(T_\epsilon[\mathbf{V}])(T_\epsilon[\mathbf{V}] - T_1) - \alpha(T)(T - T_1)}{\epsilon}.$$

Here, the term on the left hand side yields

$$\lim_{\epsilon\to 0} \lambda^{\mathrm{ex}} \frac{\frac{\partial T_\epsilon[\mathbf{V}]}{\partial \mathbf{n}} - \frac{\partial T}{\partial \mathbf{n}}}{\epsilon} = \lambda^{\mathrm{ex}} \frac{\partial \delta T\,[\mathbf{V}]}{\partial \mathbf{n}},$$

while the term on the right hand side provides

$$\begin{aligned}
&\lim_{\epsilon\to 0} \frac{\alpha(T_\epsilon[\mathbf{V}])(T_\epsilon[\mathbf{V}] - T_1) - \alpha(T)(T - T_1)}{\epsilon} \\
&= \lim_{\epsilon\to 0} \left(\frac{\alpha(T_\epsilon[\mathbf{V}]) - \alpha(T)}{\epsilon} (T_\epsilon[\mathbf{V}] - T_1) + \alpha(T) \frac{T_\epsilon[\mathbf{V}] - T}{\epsilon} \right) \\
&= \big(\alpha'\,(T)\,(T - T_1) + \alpha(T)\big)\, \delta T\,[\mathbf{V}]\,.
\end{aligned}$$

Putting the latter two identities together yields the desired boundary conditions at Γ^{ex}.

Finally, for the interface conditions of the local shape derivative, we refer to [54, 55]. ☐

Shape Gradient

For an optimal interior point, the necessary optimality condition

$$\delta J(\Omega)\,[\mathbf{V}] = 0$$

has to be fulfilled for all directions $\mathbf{V}$. The Hadamard representation of the shape gradient for (OptMC) reads as follows:

$$\boxed{\begin{aligned}
\delta J(\Omega)\,[\mathbf{V}] = \sum_{\iota\in\Gamma^{\mathrm{int}}} \int_{\iota} \langle \mathbf{V}, \mathbf{n}\rangle \Big\{ & \nabla_\tau p_{\mathrm{e}} \nabla_\tau T_{\mathrm{e}} [\lambda]_\pm \\
& - p^{\mathrm{e}} \left([c]_\pm T^{\mathrm{e}} + [f]_\pm\right) - \lambda^{\mathrm{e}} \frac{\partial p^{\mathrm{e}}}{\partial \mathbf{n}} \left[\frac{\partial T}{\partial \mathbf{n}}\right]_\pm \Big\}\,\mathrm{d}\sigma.
\end{aligned}} \tag{7.35}$$

with adjoint system

$$\boxed{\begin{aligned}
-\nabla\cdot(\lambda\nabla p) - c\cdot p &= -\frac{\partial j}{\partial T}\,(\cdot, T) && \text{in } \Omega^{\mathrm{MC}}\setminus\Gamma^{\mathrm{int}}, \\
\lambda^{\mathrm{ex}} \frac{\partial p}{\partial \mathbf{n}} + \big(\alpha'\,(T)\,(T - T_1) + \alpha(T)\big)\,p &= 0 && \text{on } \Gamma^{\mathrm{ex}}, \\
[p]_\pm = 0 \quad \text{and} \quad \left[\lambda \frac{\partial p}{\partial \mathbf{n}}\right]_\pm &= 0 && \text{on } \iota\in\Gamma^{\mathrm{int}}.
\end{aligned}} \tag{7.36}$$

Proof. Following [26], differentiation of $J(\Omega)$ in the direction $\mathbf{V}$ leads, in terms of the local shape derivative (7.34), to

$$\begin{aligned}
\delta J(\Omega)\,[\mathbf{V}] = & \int_{\Omega^{\mathrm{MC}}} \frac{\partial j}{\partial T}\,(\mathbf{x}, T)\cdot \delta T\,[\mathbf{V}]\;\mathrm{d}\mathbf{x} \\
& + \sum_{\iota\in\Gamma^{\mathrm{int}}} \int_{\iota} \langle \mathbf{V}, \mathbf{n}_{\mathrm{e}}\rangle\, j(\mathbf{x}, T) + \langle \mathbf{V}, \mathbf{n}_{\mathrm{i}}\rangle\, j(\mathbf{x}, T)\,\mathrm{d}\sigma.
\end{aligned}$$

With the adjoint system (7.36), we get

$$
\begin{aligned}
\delta J(\Omega)\left[\mathbf{V}\right] = & \int\limits_{\Omega^{\mathrm{MC}}} \left(\nabla \cdot (\lambda \nabla p) + c\, p\right) \delta T\left[\mathbf{V}\right]\, \mathrm{d}\mathbf{x} \\
& + \sum_{\iota \in \Gamma^{\mathrm{int}}} \int\limits_{\iota} \langle \mathbf{V}, \mathbf{n}_{\mathrm{e}} \rangle\, j(\mathbf{x}, T) + \langle \mathbf{V}, \mathbf{n}_{\mathrm{i}} \rangle\, j(\mathbf{x}, T)\, \mathrm{d}\sigma.
\end{aligned}
$$

As $\mathbf{n}_e = -\mathbf{n}_i$, the integrals over the interfaces $\iota \in \Gamma^{\mathrm{int}}$ cancel out each other. Application of Green's formula then provides

$$
\begin{aligned}
\delta J(\Omega)\left[\mathbf{V}\right] = & \int\limits_{\Omega^{\mathrm{MC}}} \underbrace{\left(\nabla \cdot \left(\lambda \nabla \delta T\left[\mathbf{V}\right]\right) + c \cdot \delta T\left[\mathbf{V}\right]\right) p}_{=0}\, \mathrm{d}\mathbf{x} \\
& + \int\limits_{\Gamma^{\mathrm{ex}}} \underbrace{\left(\lambda^{\mathrm{ex}} \frac{\partial p}{\partial \mathbf{n}} \delta T\left[\mathbf{V}\right] - \lambda^{\mathrm{ex}} \frac{\partial \delta T\left[\mathbf{V}\right]}{\partial \mathbf{n}} p \right)}_{=0} \mathrm{d}\sigma \\
& + \sum_{\iota \in \Gamma^{\mathrm{int}}} \Bigg[\int\limits_{\iota} \left(\lambda^{\mathrm{i}} \frac{\partial p^{\mathrm{i}}}{\partial \mathbf{n}_{\mathrm{i}}} \delta T^{\mathrm{i}}\left[\mathbf{V}\right] - \lambda^{\mathrm{i}} \frac{\partial \delta T^{\mathrm{i}}\left[\mathbf{V}\right]}{\partial \mathbf{n}_{\mathrm{i}}} p^{\mathrm{i}} \right) \mathrm{d}\sigma \\
& \qquad\qquad + \int\limits_{\iota} \left(\lambda^{\mathrm{e}} \frac{\partial p^{\mathrm{e}}}{\partial \mathbf{n}_{\mathrm{e}}} \delta T^{\mathrm{e}}\left[\mathbf{V}\right] - \lambda^{\mathrm{e}} \frac{\partial \delta T^{\mathrm{e}}\left[\mathbf{V}\right]}{\partial \mathbf{n}_{\mathrm{e}}} p^{\mathrm{e}} \right) \mathrm{d}\sigma \Bigg] \\
= & \sum_{\iota \in \Gamma^{\mathrm{int}}} \left[\int\limits_{\iota} \lambda^{\mathrm{e}} \frac{\partial p^{\mathrm{e}}}{\partial \mathbf{n}} \Big[\delta T\left[\mathbf{V}\right]\Big]_{\pm} \mathrm{d}\sigma - \int\limits_{\iota} p^{\mathrm{e}} \left[\lambda \frac{\partial \delta T\left[\mathbf{V}\right]}{\partial \mathbf{n}} \right]_{\pm} \mathrm{d}\sigma \right].
\end{aligned}
$$

Replacing the jumps in the Dirichlet data and the Neumann data by the interface conditions in (7.34) results in

$$
\begin{aligned}
\delta J(\Omega)\left[\mathbf{V}\right] = & \sum_{\iota \in \Gamma^{\mathrm{int}}} \int\limits_{\iota} -\lambda^{\mathrm{e}} \frac{\partial p^{\mathrm{e}}}{\partial \mathbf{n}} \langle \mathbf{V}, \mathbf{n} \rangle \left[\frac{\partial T}{\partial \mathbf{n}} \right]_{\pm} \\
& \qquad - p^{\mathrm{e}} \Big(\mathrm{Div}\left(\langle \mathbf{V}, \mathbf{n} \rangle [\lambda]_{\pm} \nabla_{\tau} T^{\mathrm{e}} \right) + \big([c]_{\pm}\, T^{\mathrm{e}} + [f]_{\pm} \big) \langle \mathbf{V}, \mathbf{n} \rangle \Big)\, \mathrm{d}\sigma.
\end{aligned}
$$

Integration by parts on the interface boundaries

$$
-\int\limits_{\iota} p^{\mathrm{e}} \mathrm{Div}\left(\langle \mathbf{V}, \mathbf{n} \rangle [\lambda]_{\pm} \nabla_{\tau} T^{\mathrm{e}} \right) \mathrm{d}\sigma = \int\limits_{\iota} \nabla_{\tau} p^{\mathrm{e}} \nabla_{\tau} T^{\mathrm{e}} \langle \mathbf{V}, \mathbf{n} \rangle [\lambda]_{\pm}\, \mathrm{d}\sigma
$$

finally implies the desired Hadamard representation of the shape gradient. ☐

7.6.4 Algorithmic and Numerical Implementation

We present how we calculate the objective function numerically, control the computation of our adjoint method by a finite difference approach and give insight to computational details of our implementation.

Shape Functional

Aim of our calculations is to minimize the maximum temperature in a multicable. As the functional

$$\min_{\Omega\in\mathcal{O}_{\mathrm{ad}}} \|T\|_{L^\infty(\Omega^{\mathrm{MC}}(\Omega))} = \min_{\Omega\in\mathcal{O}_{\mathrm{ad}}} \sup_{\bar{\mathbf{x}}\in\Omega^{\mathrm{MC}}(\Omega)} |T(\bar{\mathbf{x}})|$$

is not differentiable and thus the shape optimization approach would not be applicable, we define J by

$$J(\Omega) := \min_{\Omega\in\mathcal{O}_{\mathrm{ad}}} \frac{1}{q} \|T\|^q_{L^q(\Omega^{\mathrm{MC}}(\Omega))} = \min_{\Omega\in\mathcal{O}_{\mathrm{ad}}} \frac{1}{q} \int\limits_{\Omega^{\mathrm{MC}}(\Omega)} |T(\mathbf{x})|^q \,\mathrm{d}\mathbf{x}$$

for fixed values of $q > 0$. In (7.36), the derivative of the objective function appears on the right hand side of the PDE. For the sake of simplicity, we introduced the factor $1/q$, which does not influence the optimization routine. As for too high values of q, the right hand side could explode and result in numerical problems, we use values of $q = 2, 3, 4$ or 5 in general.

Computation of Jumps in Neumann Data and Control of the Gradient

In order to ensure the correctness of the gradient implementation based on the adjoint method, we verify it by a non-adjoint method. To simplify notation, we introduce the reduced objective functional $\tilde{J}$, being explicitly dependent on $x_1, y_1, \ldots, x_N, y_N$:

$$\tilde{J}(x_1, y_1, \ldots, x_N, y_N) = J\left(\Omega^{\mathrm{MC}}\left(\Omega\left(x_1, y_1, \ldots, x_N, y_N\right)\right)\right)$$

with the gradient

$$\nabla\tilde{J} = \left(\frac{\partial\tilde{J}}{\partial x_1}, \ldots, \frac{\partial\tilde{J}}{\partial y_N}\right)^T .$$

The partial derivative of $\tilde{J}$ to x_k is approximated via finite differences by

$$\frac{\partial\tilde{J}}{\partial x_k} \approx \lim_{\epsilon\to 0} \frac{\tilde{J}(\ldots, x_k+\epsilon, \ldots) - \tilde{J}(\ldots, x_k, \ldots)}{\epsilon},$$

where ϵ is a fixed and small value. In fact, the partial derivative of $\tilde{J}$ to x_k corresponds to a local translation of the position of single cable k in direction of the x-axis. For J, this could be described by the shape derivative $\delta J(\Omega)[\mathbf{V}]$ in direction of the (local) vector field

$$\mathbf{V} : \mathbb{R}^2 \to \mathbb{R}^2,\ \mathbf{x} \mapsto \mathbf{V}(\mathbf{x}) = \mathbb{I}_{\Omega_k}(\mathbf{x}) \begin{pmatrix} 1\,0 \\ 0\,0 \end{pmatrix} \mathbf{x}, \tag{7.37}$$

with $\mathbb{I}(\cdot)$ the indicator function.

We show the control of the gradient for one example in which the number of single cables is $N = 7$ and $q = 3$. Figure 7.13 illustrates the main quantities computed in the necessary steps to determine the jumps in the Neumann data (cf. Figure 7.13c) with COMSOL Multiphysics 3.5a. Apart from the calculation of the temperature profile (Figure 7.13a) and the adjoint (Figure 7.13b), we have to project the temperature distribution on the single cable core (Figure 7.14a), its complement (Figure 7.14b), the single cable insulation (Figure 7.15a) and its complement (Figure 7.15b) onto separate domains. This is required because we obtain completely wrong results if we directly compute the temperature distribution and the difference of the derivatives to the outer and inner normal in COMSOL. It is due

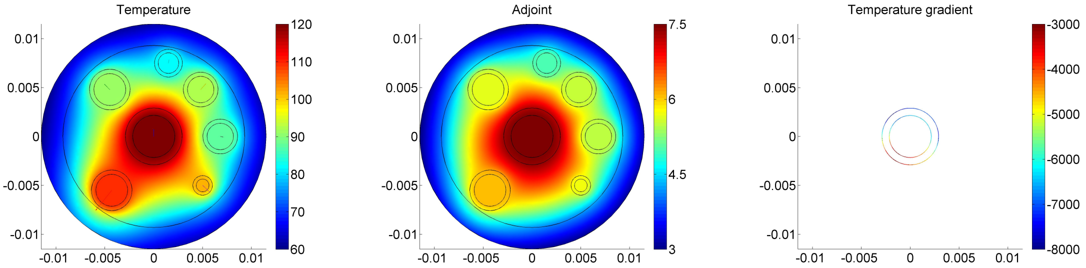

(a) Temperature. **(b)** Adjoint solution. **(c)** Temperature gradient on boundaries of a single cable.

Fig. 7.13: *Temperature distribution and associated adjoint solution in a multicable, and temperature gradient on the boundaries of a single cable.*

to an internal smoothing of the function in the software. To deal with the problem, the derivative to the outer normal is computed for the projected temperature on the domains (core respectively insulation of the single cable) and to the inner normal on their complements. Finally, this procedure yields correct gradients and has to be performed for every single cable.

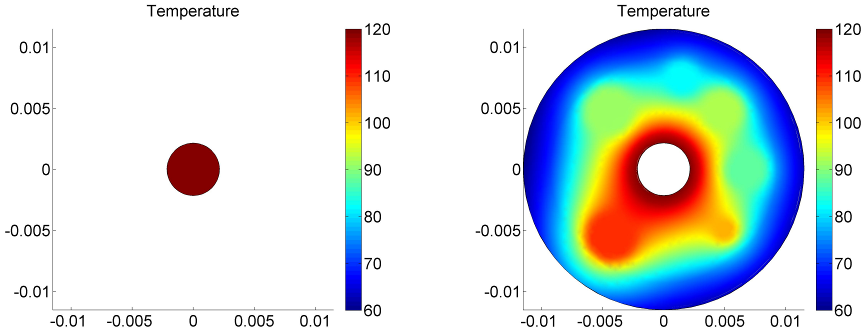

(a) Temperature on single cable core. **(b)** Temperature on core complement.

Fig. 7.14: *Temperature distribution in the core of a single cable and its complement.*

The partial derivatives obtained in this example, computed via the adjoint method, are

$$\begin{aligned}
&\frac{\partial J}{\partial\Omega(\tilde{x_1})} \approx -498.2, \; \frac{\partial J}{\partial\Omega(\tilde{y_1})} \approx -2123, \; \frac{\partial J}{\partial\Omega(\tilde{x_2})} \approx 1\,660, \; \frac{\partial J}{\partial\Omega(\tilde{y_2})} \approx -1\,668,\\
&\frac{\partial J}{\partial\Omega(\tilde{x_3})} \approx 5\,088, \; \frac{\partial J}{\partial\Omega(\tilde{y_3})} \approx 6\,291, \; \frac{\partial J}{\partial\Omega(\tilde{x_4})} \approx -181.4, \frac{\partial J}{\partial\Omega(\tilde{y_4})} \approx -1\,070,\\
&\frac{\partial J}{\partial\Omega(\tilde{x_5})} \approx -2\,334, \; \frac{\partial J}{\partial\Omega(\tilde{y_5})} \approx 2\,245, \; \frac{\partial J}{\partial\Omega(\tilde{x_6})} \approx -1\,650, \frac{\partial J}{\partial\Omega(\tilde{y_6})} \approx -1\,844,\\
&\frac{\partial J}{\partial\Omega(\tilde{x_7})} \approx -911.9, \; \frac{\partial J}{\partial\Omega(\tilde{y_7})} \approx 169.2.
\end{aligned}$$

Note that the correct notation for the local translation $\frac{\partial J}{\partial\Omega(\tilde{x_k})}$ of single cable k in direction of the x-coordinate is $\delta J(\Omega)\left[\mathbb{I}_{\Omega_k}(\mathbf{x})\begin{pmatrix}1\,0\\0\,0\end{pmatrix}\mathbf{x}\right]$. Furthermore, the translation $\delta J(\Omega)\left[\mathbb{I}_{\Omega_k}(\mathbf{x})\begin{pmatrix}0\,0\\0\,1\end{pmatrix}\mathbf{x}\right]$

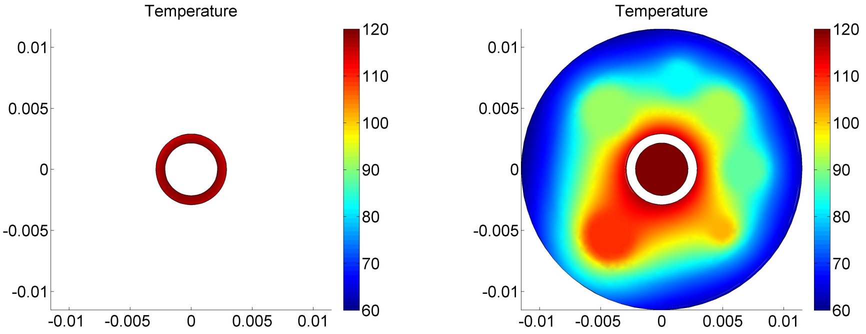

(a) Temperature on single cable insulation. **(b)** Temperature on insulation complement.

Fig. 7.15: *Temperature distribution on a single cable insulation and its complement.*

of cable k in direction of the y-coordinate is abbreviated by $\frac{\partial J}{\partial \Omega(\tilde{y_k})}$.

In Table 7.6, the parameters h and *hnumedg* represent measures for the mesh refinement on the entire domain of the multicable and for the refinement on the edges. Smaller values for h and larger values for *hnumedg*[7] result in finer grids and higher numbers of DOFs. The maximum of absolute discrepancies $\max(\text{err}_{\text{abs}})$ between adjoint and finite difference method is obtained in the partial derivative to the component *Comp*. The maximum relative error $\max(\text{err}_{\text{rel}})$ does not have to occur in the same component. It represents the maximum of deviations divided by the value of the derivative obtained via finite differences in all components. The quantities t_{ADJ} and t_{FD} specify the time in seconds necessary for the gradient determination with each method, Δt their difference in time.

h (hnumedg)	DOFs	$\max(\text{err}_{\text{abs}})$ [Comp]	$\max(\text{err}_{\text{rel}})$	$t_{\text{ADJ}}[s]$	$t_{\text{FD}}[s]$	$\Delta t[s]$
5 (10)	26 002	6.712 [x_5]	1.06e-2	25.8	560.4	534.6
5 (20)	70 842	2.050 [y_4]	3.75e-3	44.7	1 059.1	1 024.2
4 (30)	148 730	1.332 [y_4]	1.25e-3	98.9	2 704.2	2 605.3

Tab. 7.6: *Statistics for the mesh refinements, degrees of freedom, absolute resp. relative discrepancies between adjoint and non-adjoint method as well as calculation times for the specific example with seven single cables.*

We observe a good accordance of the gradients, calculated via the adjoint method and finite differences with $\epsilon = 1.0e\text{-}4$, especially for larger numbers of DOFs[8]. Thus, to have a reliable gradient approximation, we have to use fine meshes. Furthermore, the calculation times by the adjoint method are much shorter than those of the FDM. We have to admit that in the latter, neither the method itself, nor the implementation is optimized. Nevertheless, it is obvious that the adjoint method works much faster in this scope because, in addition to the one solution of the state system, the adjoint system, which is only linear, has to be solved once, independent of the number of single cables. In contrast, the nonlinear state

---

[7] The measure of refinement is a convention used in COMSOL Multiphysics 3.5a.

[8] When estimating sensitivities using FD, we are faced with the *step-size dilemma*, i.e. the desire to choose a small step size ϵ to minimize the truncation error, while avoiding the use of a step so small that errors due to subtractive cancellation become dominant [44]. By experience, $\epsilon = 1.0e\text{-}4$ yields a satisfying accordance of the gradients obtained via the FDM in this context.

system must be solved twice for each optimization variable with central differences (once if we used forward or backward instead of central differences), which corresponds to solving the PDE 28 times in this example.

Computational Algorithm

The implementation of the algorithm was performed in Matlab, where the entire optimization procedure is guided (cf. Fig 7.16). First, geometrical and physical parameters are read from input files and convergence criteria of the algorithm, if necessary of the shape optimization procedure and the genetic algorithm, are defined. Depending on the filling factor of the multicable and the number of single cables, different strategies are proposed.

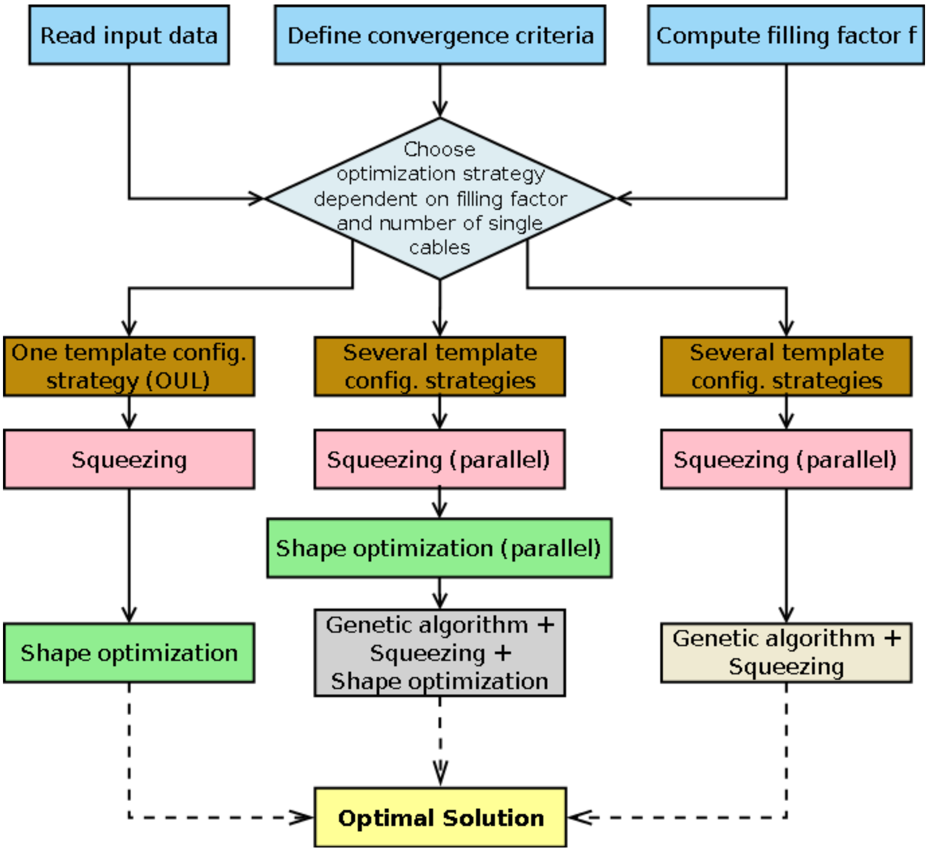

Fig. 7.16: *Entire optimization procedure for multicables.*

In case of low numbers of N and enough space in the multicable, we use only one initial template configuration. By experience, we recommend OUL. After the squeezing algorithm (implemented in Matlab), one shape optimization procedure in IPOPT is performed (cf. Figure 7.17), yielding the (approximately) best solution.

For cables that are packed very densely (filling factors larger than 90%), gradient based shape optimization does not make sense. Instead, we apply the presented initial template configurations to produce initial multicable configurations by running several instances of the squeezing algorithm in parallel. They are given to the genetic algorithm where new configurations are produced and made feasible by squeezing. This procedure, implemented in Matlab, takes a long time and in some cases, it does not provide a better solution than the best initial configuration.

Moderately packed multicables, which are common in practice, require a quite complex procedure. Initial configurations, generated by the proposed heuristics for template configurations, by application of the squeezing algorithm and finally by shape optimization, are passed on to the genetic algorithm. Therein, new configurations and the approximated global minimum are created by means of squeezing and shape optimization. The initial configurations, but also several ones during the genetic optimization, are evaluated in parallel in order to save time.

Implementation of Shape Optimization

The shape optimzation procedure, controlled via a Matlab script, for a given configuration of single cables first requires solutions of the state system (7.31) and the adjoint system (7.36). Both are computed with the help of COMSOL Multiphysics 3.5a.

Afterwards, the shape gradient (7.35) is evaluated for variations of each single cable in directions of the x- and y-axis (except for single cable 1 that only varies in the y-coordinate). The corresponding mapping $\mathbf{V}$ for variation of single cable k in the x-coordinate is indicated in (7.37), the mapping for variations in the y-coordinate was mentioned in Paragraph 7.6.4 (Computation of Jumps in Neumann Data and Control of the Gradient).

Shape gradient, solution of the state respectively adjoint system, the geometrical constraints of the optimization problem, defined in $\mathcal{O}_{\text{ad}}$, the constraints' derivatives and the initial configuration of the multicable are passed to IPOPT which normally computes a local minimum (cf. Figure 7.17).

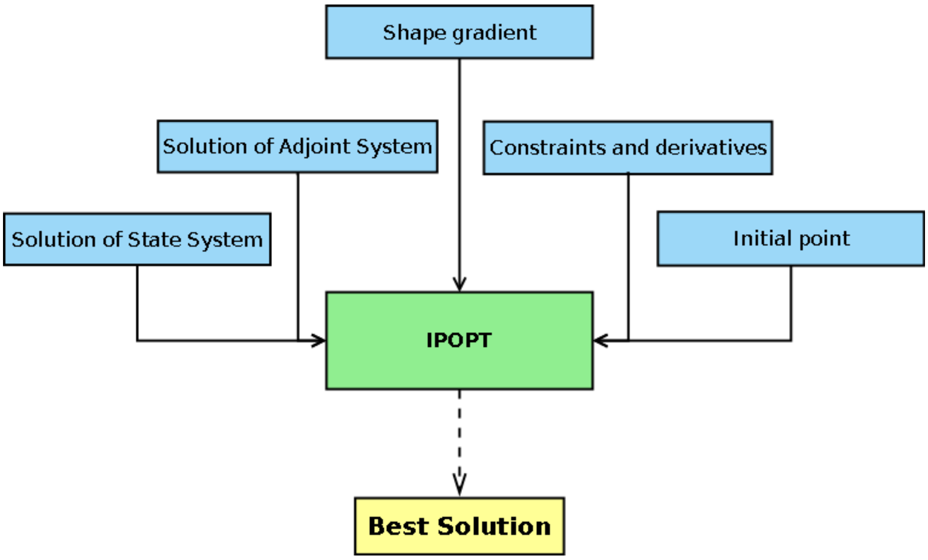

Fig. 7.17: *Input and output of the gradient based shape optimization algorithm.*

IPOPT is a software package for large-scale nonlinear optimization that implements an interior-point line-search filter method (cf. [135–137]). In our options, we use a monotone strategy for the barrier parameter μ of the logarithmic barrier function. If this barrier parameter is small enough and the KKT conditions are fulfilled satisfactorily, an optimum is reached. Else, if no (local) minimum is attained after a given number $n_{\max}$ of iterations, the procedure is interrupted.

Implementation of the Genetic Algorithm

We briefly state the main aspects of the implementation of the genetic algorithm for the second strategy (combination of shape optimization and genetic algorithm):

- **Initialization**:
  As shown in Section 7.6.2, several initial configurations are generated by squeezing of the single cables, which are positioned in the template of Figure 7.3. If for one of the presented assignment strategies the squeezing does not yield a feasible configuration after a fixed number of squeezing steps, the assignment strategy is skipped and replaced by a further stochastical one. If after trying a certain number of initial strategies, no feasible configuration is attained (e.g. if the exterior diameter is too small for the single cables), the algorithm is interrupted and the problem cannot be solved. However, if the number of computed feasible configurations is less than the intended number of individuals of each generation, we continue with fewer individuals.

- **Selection**:
  The best individual – the configuration with the smallest value of the objective function – is directly passed to the next generation as the elite. 70 % of the population of the next generation are created by crossover, the rest by mutation.

- **Genetic operators**:
  For crossover, we take the coordinates of two randomly selected parents of the previous generation. To generate one child of the next generation, we select a part of the genes (coordinates) from parent 1, the others from parent 2. To generate a certain coordinate of a child by mutation, we select a random number of individuals and compute the mean of this coordinate of the chosen individuals, supplemented by further, randomly generated coordinates. This procedure is performed for each coordinate of the child.

  Both, crossover and mutation, normally provide multicable configurations that are not feasible. Either, single cables are situated outside of the multicable domain (which is rather rare), or single cables overlapped (very frequent). Algorithm 4 does not only squeeze the single cables, but also reduces overlappings of single cables. Thus, after generation of coordinates by crossover and mutation, we apply the Cable Squeezing Algorithm to create feasible, hopefully better configurations.

- **Termination**:
  Normally, many generations are produced within a genetic algorithm. In our approach, a good solution is already approximated after a few generations in most cases. This is due to the combination with shape optimization. For that reason, our genetic algorithm finishes after a (small) number of generations (≤ 10).

7.6.5 Numerical Results

To test our proposed algorithm, we optimize the shape of different multicables, consisting of 1, 3, 15 and 33 single cables. In case of 1 and 3 single cables, the first strategy with exclusive application of shape optimization is sufficient. These two examples rather serve to confirm that the algorithm works as it should. In case of 15 and 33 single cables, we use the second strategy. An example for the third strategy is not presented because it employs no gradient based shape optimization and it is only applied to very specific multicables. All the following examples were carried out in Matlab, version 7.10.0.499, on a Pentium III Xeon processor with 4 cores (each 2.50 GHz) and 32 GB RAM.

First Example

We first optimize the position of only one single cable in the multicable with solid insulation material of low heat conductivity inside and the exterior insulation of PVC. This single cable carries a current of $I_1 = 102\,\mathrm{A}$ and its geometrical cross sectional area is $A_1^{\mathrm{ge}} \approx 14.5\,\mathrm{mm}^2$ ($Tp_1 = 1$ in Table 7.1). We suppose the ambient temperature to be 33.2 °C and the diameters $d_0^{\mathrm{in}} = 18.6\,\mathrm{mm}$, $d_0^{\mathrm{ex}} = 23.0\,\mathrm{mm}$. In the shape functional, we set $q = 2$.

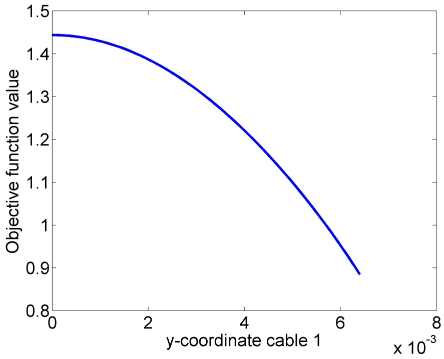

Fig. 7.18: *Objective function values for variation of the y-coordinate of one single cable.*

Iter	F-count	$J(\Omega)$	$\Delta\mathbf{x}$
0	1	1.4438692	
1	1	0.8963279	3.93e-2
2	1	1.2103676	8.38e-3
3	1	1.0596074	1.20e-3
4	1	0.9627317	7.63e-4
⋮	⋮	⋮	⋮
9	4	0.8868828	1.17e-5
10	4	0.8868126	1.03e-5
11	1	0.8865531	1.45e-7

Tab. 7.7: *Optimization progress for a multicable with one single cable.*

As the x-coordinate of the midpoint of the first single cable is fixed to zero and the y-coordinate ≥ 0, the objective function value is monotonically decreasing for larger values of the y-position of the first single cable (cf. Figure 7.18). The highest value is obtained at the origin of the coordinate system ($J \approx 1.4439$), the lowest at the exterior boundary ($J \approx 0.8866$). Table 7.7 shows the optimization progress in IPOPT with $\Delta\mathbf{x}$ denoting the Euclidean norm of the step size of the optimization variable in each iteration *Iter*. *F-count* indicates the number of function evaluations in each iteration. The computational time was about 328 s with ≈ 45 000 DOFs in the linear system of every Newton iteration.

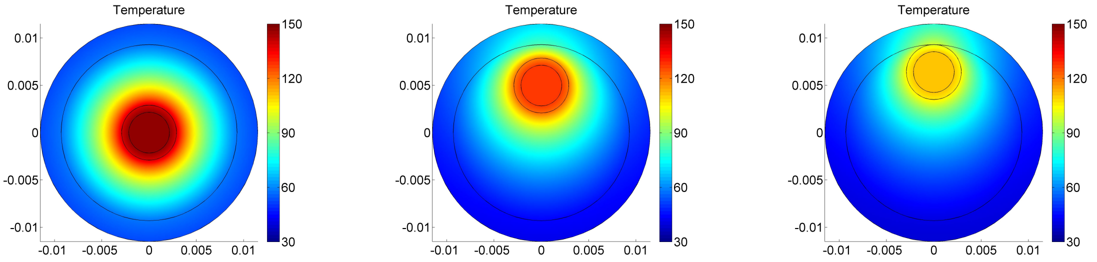

(a) Initial configuration. **(b)** Configuration iteration 3. **(c)** Optimal configuration.

Fig. 7.19: *Multicables with one single cable generated during the optimization process.*

Obviously, the optimization works very well. During the optimization process, the single cable, starting from the origin of the coordinate system (Figure 7.19a), moves towards the exterior boundary (Figure 7.19c). Figure 7.19 depicts the temperature distribution for three different configurations, each generated during the optimization process.

Although with $q = 2$, our objective function $J(\Omega)$ does not approximate the $L^\infty(\Omega)$-norm very accurately, the maximum temperature is much lower in the optimized multicable ($\approx 111.8\,^\circ\mathrm{C}$) than in the initial configuration ($\approx 147.9\,^\circ\mathrm{C}$). Indeed, if the single cable is situated nearer to the exterior boundary, more heat is emitted to the environment by convection and radiation than it is the case if the hotspot is situated in the centre of the multicable.

Second Example

Our algorithm is applied to multicables with three single cables. In the first multicable, the current densities are equal for the three single cables, in the second, they vary.

Multicable with Three Single Cables under Equal Current Loads

In our second example, we investigate a multicable of diameters $d_0^{\mathrm{in}} = 23.8\,\mathrm{mm}$ and $d_0^{\mathrm{ex}} = 28.2\,\mathrm{mm}$, consisting of three single cables with equal currents $I_1 = I_2 = I_3 = 89\,\mathrm{A}$ and cross sectional areas $A_1^{\mathrm{ge}} = A_2^{\mathrm{ge}} = A_3^{\mathrm{ge}} = 14.5\,\mathrm{mm}^2$. We set $q = 3$.

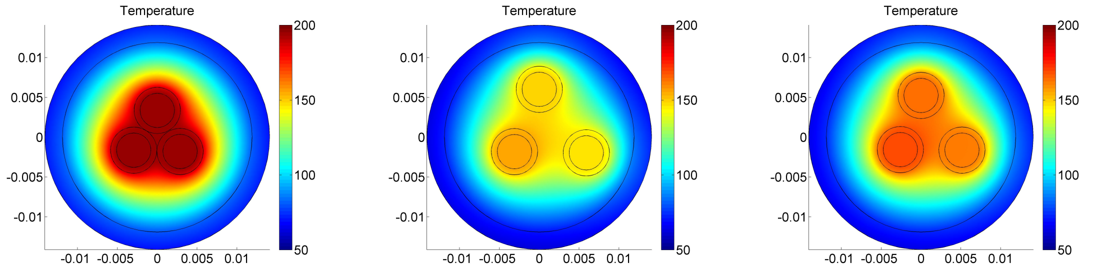

(a) Initial configuration. **(b)** Configuration iteration 1. **(c)** Configuration iteration 2.

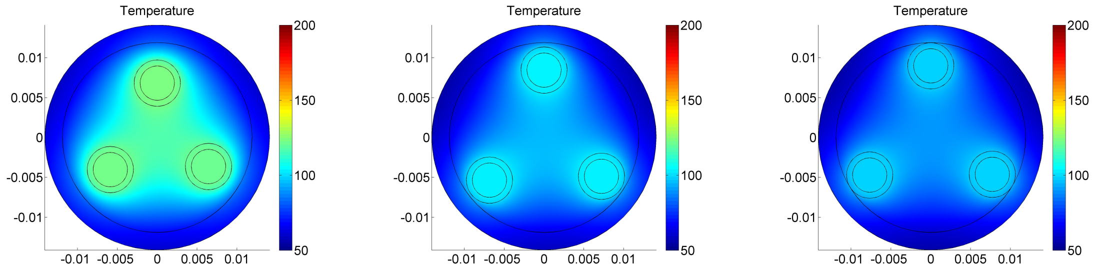

(d) Configuration iteration 5. **(e)** Configuration iteration 9. **(f)** Configuration iteration 30.

Fig. 7.20: *Cable configurations generated during the optimization process for a multicable which consists of three single cables that carry equal currents.*

Starting with an almost regular positioning, such that the midpoints of the single cables nearly form an equilateral triangle (cf. Figure 7.20a), the single cables move towards the exterior boundary (cf. Figures 7.20b-7.20d). Having reached the boundary (cf. Figure 7.20e), they are forced to find a configuration for which the cables have the largest possible distance from each other, i.e. an equilateral triangle of the midpoints with each single cable situated at the boundary of the multicable (cf. Figure 7.20f).

Iter	F-count	$J(\Omega)$	$\Delta\mathbf{x}$
0	1	5.0743619e+02	
1	2	3.0311155e+02	5.32e-01
2	1	3.6448495e+02	9.96e-03
3	1	2.0319573e+02	3.25e-03
4	1	2.1952290e+02	3.87e-04
5	1	1.9638202e+02	4.28e-04
⋮	⋮	⋮	⋮
8	1	1.3197190e+02	5.74e-05
9	1	1.3202247e+02	4.14e-05
10	1	1.2003736e+02	4.30e-04
⋮	⋮	⋮	⋮
28	11	1.1789933e+02	2.84e-04
29	13	1.1789923e+02	2.97e-04
30	14	1.1789918e+02	2.98e-04

Tab. 7.8: *Optimization progress for a multicable with three equally loaded single cables.*

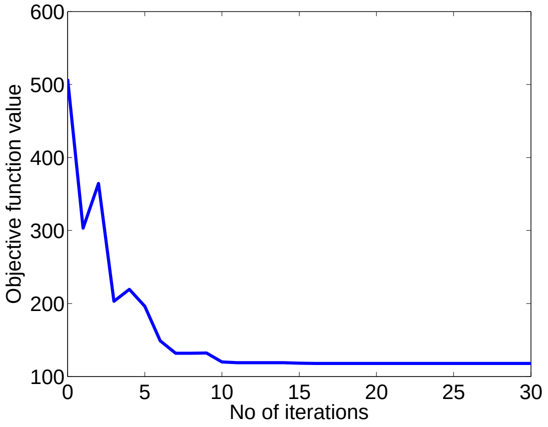

Fig. 7.21: *Convergence history of the optimizer for a multicable with three equally loaded single cables.*

In IPOPT, it sometimes happens that the objective function value increases in an iteration, e.g. in our case at the second iteration (cf. Table 7.8 and Figure 7.21). This is due to the interior-point algorithm, when the barrier parameter is modified [135]. The entire optimization is interrupted after thirty iterations, i.e. $n_{\max} = 30$.

Statistics			
Init $\max\limits_{\mathbf{x}\in\Omega^{\mathrm{MC}}} T(\mathbf{x})$	196.5 °C	Final $\max\limits_{\mathbf{x}\in\Omega^{\mathrm{MC}}} T(\mathbf{x})$	99.7 °C
No. of iterations	30	No. of function evaluations	63
Time optimizer	≈ 42 s	Time FEM solver	≈ 3 584 s
Time squeezing	≈ 1.1 s	Total time	≈ 3 632 s
DOFs	≈ 120 000	NOE	≈ 30 000

Tab. 7.9: *Statistics for optimization of a multicable with three equally loaded single cables.*

Obviously, the maximum temperature decreases from ≈ 197 °C to ≈ 100 °C during the optimization process (cf. Table 7.9). The reason for this diminution is again that more thermal energy can be emitted at the transition to air if the single cables are placed at the exterior boundary. In the final configuration, they have the greatest possible distances from each other.

The insulation material of the single cables and the exterior insulation is supposed to consist of PVC. Assumed a melting point of about 130 °C, the initial multicable would not be able to endure the given current loads, whereas the optimized one could without any problems.

Note that the heat conductivity of the inner insulation is computed according to formula (7.8). Thus, it is supposed to be a mixture of air and solid material. The modelling of the inner heat conductivity with such low filling factors ($\leq 30\,\%$) might be inadequate for real multicables. If we assume the inner material to consist entirely of solid material with heat conductivity $\lambda^{\text{gaps}} = 0.19\,\text{W}/(\text{m}\cdot\text{K})$, the maximum temperature decreases by shape optimization from 102.1 °C to 92.0 °C.

Concerning the calculation expense, most of the time is spent to solve state and adjoint systems during the 63 function evaluations (cf. Table 7.9 with further statistical information). The rather long evaluation times for the systems with about 120 000 DOFs and a number of elements (NOE) of $\approx 30\,000$ are explained by the nonlinearities. The squeezing time is nearly negligible and calculation time in the optimizer is very small. In fact, the optimization problem to be solved in the nonlinear optimizer is very small. Neglecting the x-coordinate of the first single cable as well as the lower and upper bounds for the other variables, it consists of 5 optimization variables and 6 geometrical constraints.

For higher values of q, it is even more expensive to solve the PDEs. With $q = 5$, we obtained nearly the same optimization process (with of course different values for $J(\Omega)$) and similar calculation times in the optimizer, but the solution of the PDEs took about four times longer for equal mesh refinements.

Multicable with Three Single Cables under Different Current Loads

We suppose again $N = 3$, $q = 3$, equal cross sectional areas for the single cables and the same material and ambient parameters as in the previous example. The only difference is that now the cables carry different current loads, namely $I_1 = 103\,\text{A}$ and $I_2 = I_3 = 80\,\text{A}$.

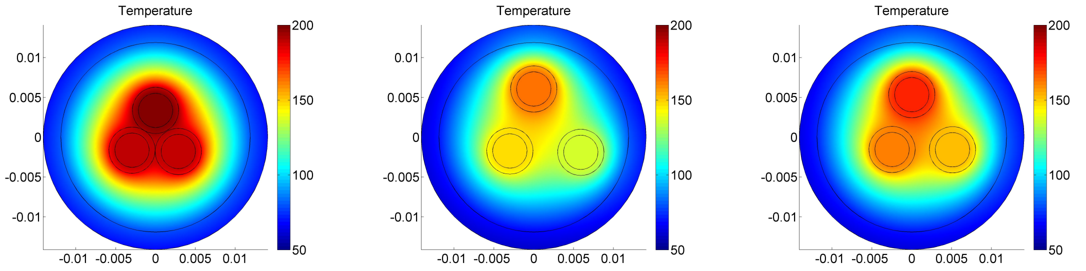

(a) Initial configuration. **(b)** Configuration iteration 1. **(c)** Configuration iteration 2.

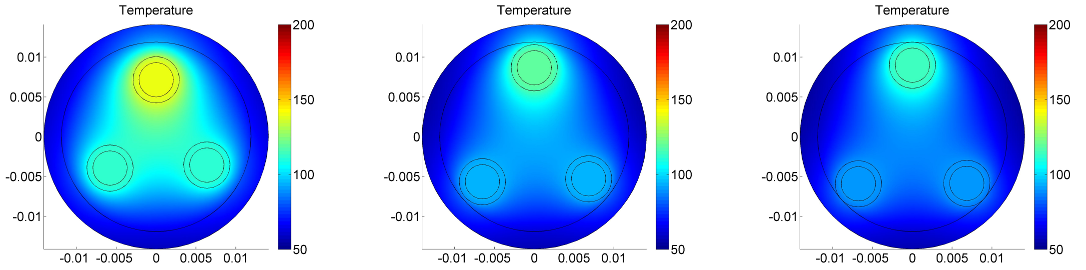

(d) Configuration iteration 5. **(e)** Configuration iteration 10. **(f)** Configuration iteration 30.

Fig. 7.22: *Cable configurations generated during the optimization process for a multicable which consists of three single cables carrying different currents.*

Starting from the same initial configuration as in Section 7.6.5, the single cables also move toward the exterior border (cf. Figure 7.22). In contrast to the previous example, they move until finally the centre coordinates form an isosceles triangle which is not equilateral (cf. Figure 7.22f). The distance to the single cable carrying a higher current is larger than between the cables with equal currents. The objective function value for $q = 3$ improves from $J(\Omega_{\text{init}}) \approx 486.3$ to $J(\Omega_{\text{opt}}) \approx 118.3$ and the maximum temperature decreases from $\max\limits_{\mathbf{x}\in\Omega_{\text{init}}} T(\mathbf{x}) \approx 199.2\,°\text{C}$ to $\max\limits_{\mathbf{x}\in\Omega_{\text{opt}}} T(\mathbf{x}) \approx 115.3\,°\text{C}$.

The entire optimization took 4 991 seconds with 30 optimization steps and 84 function evaluations. 42 seconds where required in the nonlinear optimizer, one second for squeezing, the rest to solve the PDEs. The NOE was about 30 000, corresponding to ≈ 120 000 DOFs in the linearized systems, which were solved by UMFPACK.

Third Example

We consider a multicable consisting of 15 single cables with different cross sectional areas and currents listed in the Appendix, Table A.4.

The filling factor of the multicable with diameters $d_0^{\text{in}} = 18.6\,\text{mm}$, $d_0^{\text{ex}} = 23.0\,\text{mm}$, is $\approx 47\,\%$, the ambient temperature $T_1 = 33.2\,°\text{C}$ and we use $q = 3$. The maximum temperatures of the depicted initial configurations, obtained by squeezing of the initial template configurations (cf. Figure 7.23), vary between $142.2 - 149.7\,°\text{C}$.

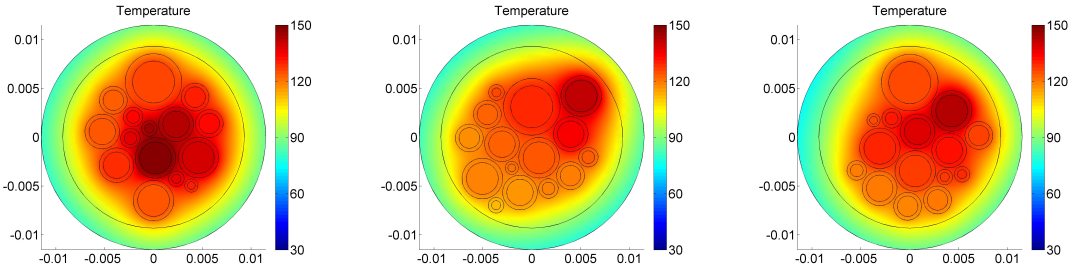

(a) INL ($J(\Omega) = 219.4$). **(b)** OUL ($J(\Omega) = 195.5$). **(c)** MCL1 ($J(\Omega) = 204.1$).

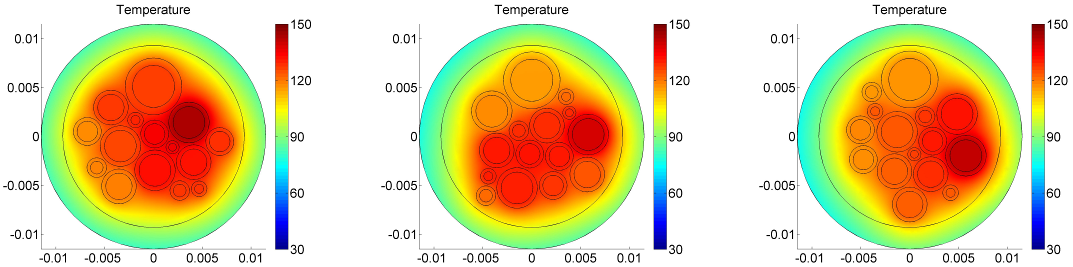

(d) OUL2 ($J(\Omega) = 207.2$). **(e)** OUL4 ($J(\Omega) = 198.0$). **(f)** OPP ($J(\Omega) = 193.8$).

Fig. 7.23: *Initial temperatures in multicables consisting of 15 single cables.*

The lowest maximum temperature after shape optimization applied to the initial template configurations, thus the maximum temperature of the best individual for the initial generation, is 127 °C. After a total calculation time of nearly 30 h with about 7 100 function evaluations[9], partly in parallel, we obtain our approximated (global) minimal maximum temperature (cf. Figure 7.24).

---

[9] Each function evaluation includes the solution of state and adjoint system.

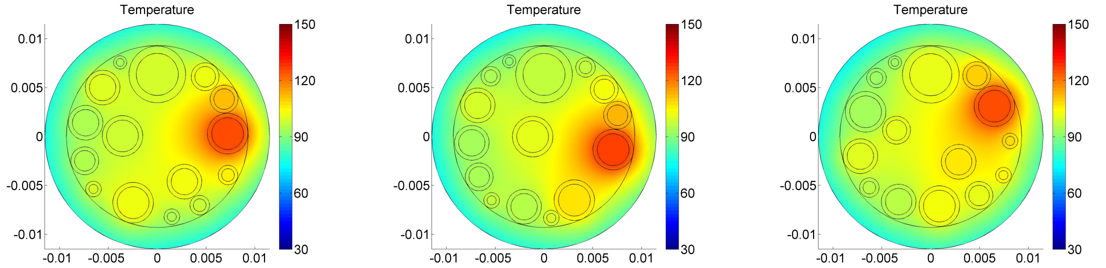

(a) Best config. ($J(\Omega) = 134.9$). **(b)** Second config. ($J(\Omega) = 135.0$). **(c)** Third config. ($J(\Omega) = 137.0$)

Fig. 7.24: *Cable configurations obtained via the genetic algorithm for multicables with 15 single cables.*

Therein, each shape optimization in IPOPT is interrupted after no later than 30 iterations. In each function evaluation, $30\,000 - 40\,000$ elements with $120\,000 - 160\,000$ DOFs are used for the finite element approximation. The linear solver is UMFPACK. The entire optimization problem has 29 optimization variables (x-coordinate of first single cable neglected) with 120 inequality constraints and 435 non-zero entries in the inequality constraint Jacobian.

The minimal maximum temperature of our best cable configuration is 125.9 °C. Hence, in this case with a rather low filling factor, most of the optimization is done by the gradient based shape optimization. The influence of the genetic algorithm is rather small in relation to the computational effort (see Figure 7.25a and Table A.5). But this also shows that the different template configuration strategies, combined with squeezing and shape optimization, already provide a good approximation of the best cable configuration.

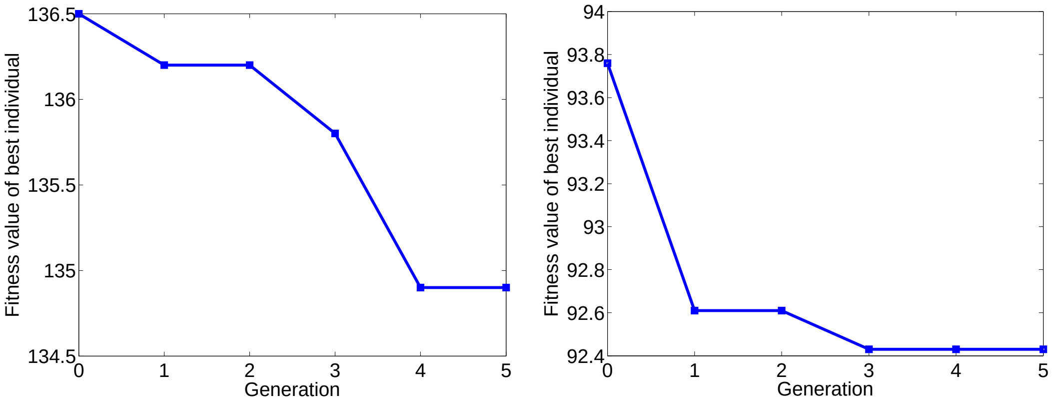

(a) Convergence history 15 single cables. **(b)** Convergence history 33 single cables.

Fig. 7.25: *Convergence history of the genetic algorithm for multicables with 15 and 33 single cables.*

Fourth Example

Finally, we optimize a multicable motivating this section, which consists of 33 single cables. All current loads and cross sectional areas are listed in Table A.1. We use the ambient temperature $T_1 = 33.2\,°\mathrm{C}$ and $q = 3$. The filling factor of the multicable is $\approx 63\,\%$ with an inner diameter of 19.2 mm and outer diameter of 23.6 mm for the exterior insulation.[10]

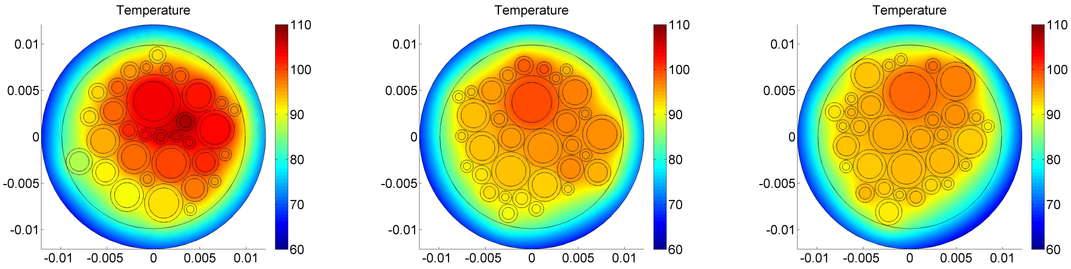

(a) INL ($J(\Omega) = 116.2$). **(b)** OUL ($J(\Omega) = 108.3$). **(c)** OPP ($J(\Omega) = 106.1$).

Fig. 7.26: *Temperature distributions in multicables with 33 single cables for different initial template assignments.*

Figure 7.26 shows that the maximum temperature obtained by the initial template configuration INL (Figure 7.26a) is 108.5 °C. In contrast, our optimized cable has a maximum temperature of 92.4 °C (Figure 7.27a). That means that the difference in maximum temperatures between a bad and good configuration for this case can be about 16.1 K. Thus, the reduction of maximum temperature of the optimized cable compared to that obtained with INL is $\approx 21\,\%$, if we consider the temperature in each cable minus ambient temperature.

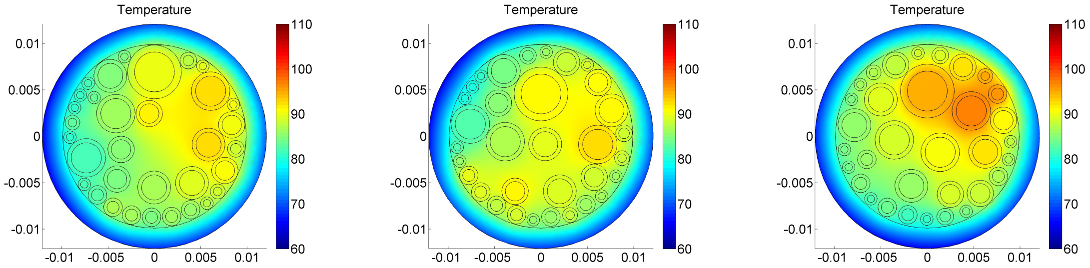

(a) Best config. ($J(\Omega) = 92.43$). **(b)** Second config. ($J(\Omega) = 93.81$). **(c)** Third config. ($J(\Omega) = 96.89$).

Fig. 7.27: *Cable configurations obtained via the genetic algorithm for multicables with 33 single cables.*

In the optimization procedure of the genetic algorithm, we determined 6 generations, each consisting of 9 individuals (cf. Table A.6). Therein, the objective function value was reduced from $J(\Omega_{\text{init}}) = 93.76$ to $J(\Omega_{\text{opt}}) = 92.43$ (cf. Figure 7.25b). The shape optimization of each individual in IPOPT was interrupted after latest $n_{\max} = 50$. The number of optimization variables was 65 with 561 inequality constraints and 2 145 non-zero entries in the inequality constraint Jacobian. The linearised systems in the evaluation with finite elements were solved with PARDISO and had between 250 000–350 000 unknowns.

Altogether, the state and adjoint systems were evaluated about 7 300 times. The entire optimization process took about 42 hours.

---

[10] Note that the exterior insulation has a slightly larger diameter than in the measurements. Furthermore, we used $\delta_0 = 0.3$ in Algorithm 4 for the optimization and $\delta_0 = 0.5$ in Section 7.5 for the simulation of multicables. This provides different configurations for INL.

7.6.6 Discussion

The goal of the present section was to derive an algorithm for the optimization of current carrying multicables. This was enabled by coupling our Cable Squeezing Algorithm that generates feasible cable configurations to a genetic algorithm and a gradient based shape optimization approach. The positive influence of the gradient based shape optimization for multicables consisting of several single cables, even for limited space, is surprising in this context. In fact, the gradient based approach runs into local minima that are numerous for larger numbers of single cables. In combination with the genetic algorithm, the global optimum is however well approximated in acceptable time, running several instances in parallel.

We showed how a well planned and exact production process of multicables could improve the thermal on-board management in cars, just by varying positions of the cables. Hardly any attention has been paid to this fact, yet. By now, the production process for multicables and cable harnesses is not as precise as necessary for an optimal design. Whether it is more valuable to change the production process in order to generate more precise and thermally optimal multicables or to maintain the old production process, lies beyond the author's scope. However, this research shows that there exists a great potential to reduce temperatures with an optimized cable design.

7.7 Conclusion

In this chapter, we compared two methods to compute the stationary temperatures in multicables and developed an algorithm to minimize their maximum temperatures.

The detailed temperature profile obtained via finite elements provides useful and reliable information about hotspot generation as well as average and maximum temperatures. An associated geometry is constructed via a cable squeezing algorithm. The comparison to measurement results shows good accordance. Discrepancies in some cases are explained by different positions of the single cables in simulations and measurements and by uncertainties in the parameter values.

Furthermore, formulas for characteristic temperatures in the multicable were derived and solved via a fixed point approach. The fixed point approach yields adequate mean value temperatures in the multicables, also shown by comparison to the measurements. But this approach does not provide appropriate results for extreme cases with very great variations in the current densities of the single cables, which are rare in practice.

The small calculation times qualify the fixed point approach for direct industrial application. However, a deeper analysis can only be performed by the finite element approach.

One main result of our extensive simulation and measuring study was that the positioning of the single cable has an essential impact on the temperature distribution and especially on the maximum temperature in the multicable. Hence, we developed an algorithm that computes the optimal cable layout for given current loads of the single cables and cable geometries. It was shown that, just by varying the inner layout, an optimal positioning of the single cables in a multicable can effect temperatures that are more than 20 % lower than those of arbitrary distributions.

8 Current Bars

Further components connecting electric devices, apart from cables and wires, are current bars. In contrast to cables, they do not have only two ends to which other electric devices can be attached, instead there exist several points where electric currents enter or leave the system (cf. Figure 8.1a with four cables connected to the current bar). Consequently, the electrical current passing the current bar varies from one section to another. The DIN standards 43 670 and 43 671 [29, 30] represent relevant protection specifications for thermal load capacities of current bars and give important advice for their construction. However, they do not provide information about how to correctly dimension current bars for attached components carrying different currents and thus, how intensively those contribute to the stress of the current bar. By now, the complex contexts of current bars have mainly been investigated by experimental knowledge and practical experience [114]. We developed first industrial applicable approaches for the fast computation of temperatures in current bars. In this thesis, we restrict to stationary investigations on current bars. Within the research project [82] in cooperation with the Dräxlmaier AG, a simulation tool for dimensioning of current bars was implemented (cf. Figure A.3 with a screenshot of the simulation tool). Its computations are entirely based on the methods we present in this chapter.

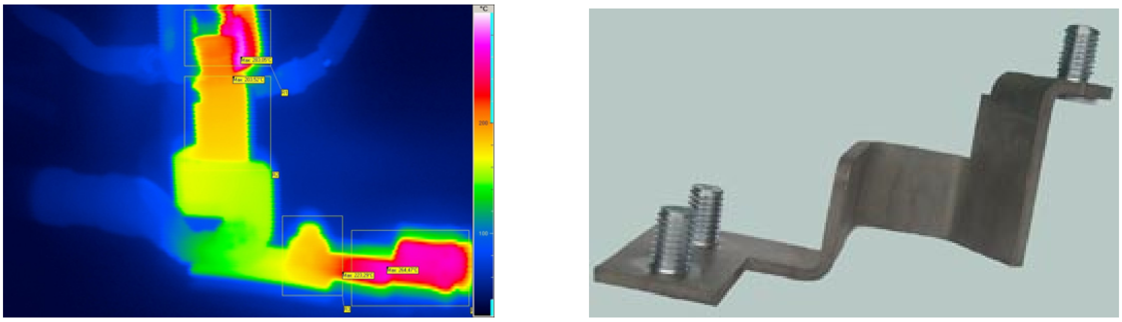

(a) Thermal image of a current bar under electric load.

(b) Current bar with three connecting screws.

Fig. 8.1: *Thermal image of a current bar under electric load and photography of the geometry (image source: Dräxlmaier Elektrotechnik GmbH).*

In [99], a prototype of the mentioned calculation tool has been tested and evaluated. To this purpose, experimental measurements were performed. They also serve as an indicator for the quality and applicability of our computational approach in industry. Moreover, we show comparisons to finite element computations and strengths and weaknesses of our method. Main parts of this chapter have been published in a peer reviewed IEEE conference proceeding [88].

8.1 Problem Formulation

It is the objective to develop a fast, robust and reliable computational method to determine temperatures in current bars with attached cables. Moreover, it shall enable a quick dimensioning of current bars for concrete current load scenarios, providing a priori estimates for more elaborative and expansive measurements or (FEM) computations. In this way, the total effort to dimension concrete current bars shall be reduced.

Figure 8.2 shows the model of a current bar with n attached cables. We suppose those to be insulated single-core cables, carrying electric currents I_k, $k = 1, \dots, n$. The entire current bar is subdivided into n input modules[1] of the form depicted in Figure 8.3a, numbered from left to right, and a metallic rest on the right of module n. Not to be confused with the temperature of the first module, the temperature of ambient air surrounding the current bar is abbreviated by T_{amb} in this chapter.

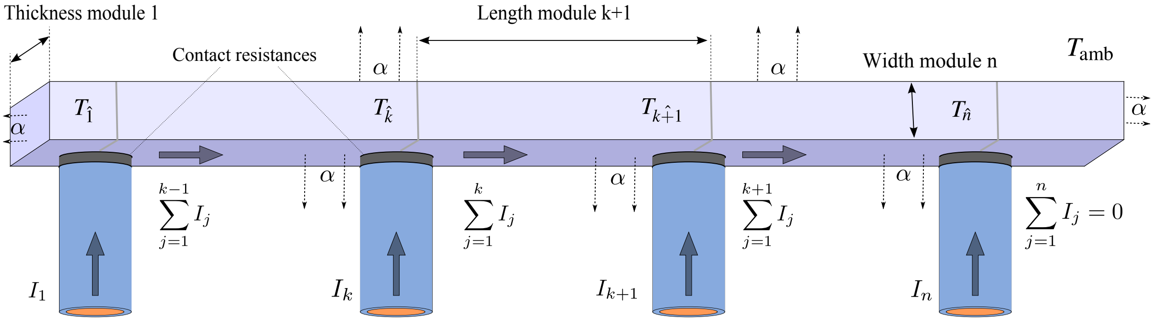

Fig. 8.2: *Model of a current bar with attached cables.*

The electric currents entering or leaving the system via attached cables have fixed direction. Those entering the system are taken into account by a positive sign, those leaving the current bar by a negative one. The resulting current $\hat{I}_k$ in module k represents the sum of electric currents entering and leaving the current bar by cables with numbers smaller than k. With $I_0 := 0$, we obtain

$$\hat{I}_k := \sum_{j=0}^{k-1} I_j, \; k = 1, \dots, n\,. \tag{8.1}$$

We require that for the sum of all currents in the current bar holds

$$\hat{I}_{n+1} := \sum_{j=0}^{n} I_j = 0. \tag{8.2}$$

The current bar is supposed to consist of homogeneous material with dimensions varying from one module to another. It is characterized by a heat conductivity λ_s, an electrical conductivity $\kappa_{0,s}$ at reference temperature and a linear coefficient $\alpha_{\rho,s}$ for the rise of electrical resistivity for higher temperatures. Since the contact of different conducting materials results in a higher electrical resistivity and thus in an additional heat source, we respect the contact resistance $R^c_{0,k}$ at cable k and a linear approximation with $\alpha^c_{\rho,k}$ of its growth for higher temperatures.

For the characterization of attached cables, we allow three different modes:

---

[1] The terms input/output refer to the computational description of the current bar subsections, not the electric current or energy entering and leaving the system.

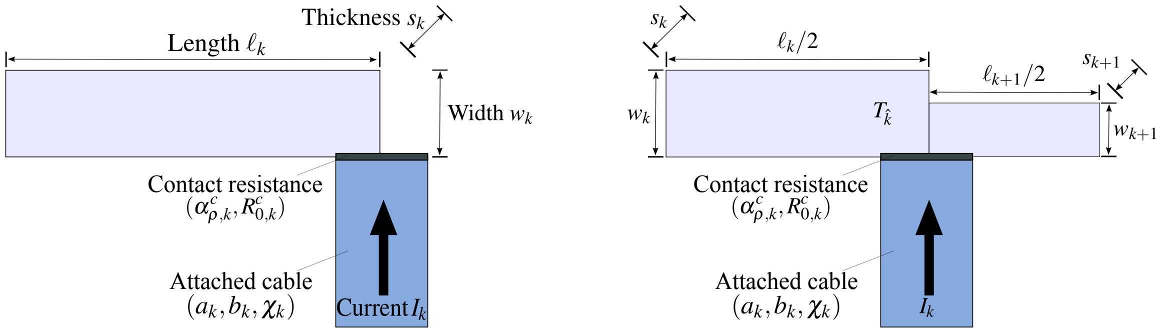

(a) Input module k.

(b) Output module $\hat{k}$.

Fig. 8.3: *Input and output modules of a current bar with attached cables.*

- **Wires of finite length with specification of all cable data**
  The cables are supposed to be of finite length $L_{f,k}$ with temperature $T_{\mathrm{f},k}$ at the end averted from the current bar. Then, the diameter $d_{2,k}$ of the insulation, the diameter $d_{3,k}$ of the core, the metallic cross sectional area A_k of the core, the ambient temperature $T_{\mathrm{amb},k}$ of the attached cable, the heat conductivity $\lambda_{3,k}$ of the metallic part, the heat conductivity $\lambda_{2,k}$ of the insulation, the emissivity ϵ_k of the insulation, the resistivity $\rho_{0,k}$ of the metallic part of the cable core and its linear temperature coefficient $\alpha_{\rho,k}$ are necessary for characterization.

- **Wires of finite length with reduced cable data**
  In Section 8.2.1, we describe an approach to characterize attached cables by simplified quantities, enabling an enormous reduction of parameters. Thus, for cables of finite length, only the parameters A_k, $T_{\mathrm{amb},k}$, Λ_k, $L_{f,k}$, $T_{\mathrm{f},k}$ and the cable characterizing quantities a_k, b_k and χ_k are required. We denote Λ_k the heat conductivity weighted with respect to the cross sectional area, a_k the linear characterizing constant, b_k analogously the quadratic one and χ_k the characterizing length of cable k.

- **Wires of infinite length with reduced cable data**
  For attached cables of infinite length, the input of data can also be reduced to a_k, b_k and χ_k. Then, the values for A_k, $T_{\mathrm{amb},k}$ and Λ_k have to be given in addition.

The mode *Wires of infinite length with specification of all cable data* is left out in this thesis, as it is not part of the mentioned calculation tool. Note that each cable attached to the current bar is characterized individually, and the mode of characterization may vary from one to another.

Heat power dissipates from the current bar by convection and radiation via the surface and possibly by conduction via attached cables of lower temperatures. Since we consider three dimensional current bars, we have to distinguish between upper, lower and vertical surfaces with different formulas for each surface type (cf. Section 2.3). In Figure 8.2, they are summarized by α without distinction, in the computations, they are denoted by α_u, α_l and α_v for the corresponding surfaces.

8.2 Simulation Methods

We first present a simplified computational approach based on heat power balances to determine temperatures at specific positions in the current bar. Afterwards, we explain how finite elements are used for this type of application.

8.2.1 Heat Power Balance Approach

The entire current bar in the steady state is considered to be a closed system of homogeneous material in which the heat power balance (2.1) holds with $\Delta E_{\mathrm{st}} = 0$. We derive a system of nonlinear equations, enabling the computation of one temperature in each output module of the current bar. This approach is based on heat power balances for each (output) module of the current bar (cf. Figure 8.3b).

We first explain how the different module types in Figure 8.3 are characterized and why we distinguish between *input* and *output* modules. An arbitrary current bar with possibly complex shape has to be transformed adequately in the model of Figure 8.2, before the present approach can be applied.

Input module k (cf. Figure 8.3a) consists of cable k, the contact resistance between cable k and the current bar as well as a certain subsection of the current bar. This subsection starts at the centre of the projected contact surface between current bar and cable $k-1$, and it ends at the corresponding centre of the projected contact surface at cable k. Input module 1 starts at the left end of the current bar. Dividing the current bar this way, there remains the current bar section between the right end of module n and the right end of the current bar. For the sake of simplicity, this subsection is denoted by module $n+1$, although there is no cable attached.

In contrast, an interior *output module $\hat{k}$* consists of the attached cable with index k and its contact resistance, the half current bar section of input module k and the half current bar section of input module $k+1$. For the left output module $\hat{1}$, the entire length of input module 1 is added and for the right output module $\hat{n}$, the rest of the entire length of current bar module $n+1$. Thus, for the lengths of output modules, there holds

$$\ell_{\hat{k}} = \begin{cases} \ell_1 + \frac{\ell_2}{2}, & \text{if } k = 1, \\ \frac{\ell_k}{2} + \frac{\ell_{k+1}}{2}, & \text{if } k = 2, \dots, n-1, \\ \frac{\ell_n}{2} + \ell_{n+1}, & \text{if } k = n. \end{cases} \tag{8.3}$$

In order to simplify notation, we additionally define the lengths

$$L_{\hat{k}} := \sum_{1}^{k} \ell_{\hat{k}}, \; k = 1, \dots n.$$

Manufacturers prefer to specify dimensions of current bars with input modules. However, stating a heat power balance for an input module would be difficult (or even impossible), since it is hard to determine a priori how much energy of the cable k is supplied to (or absorbed from) input module k and how much to (or from) module $k+1$. The introduction of output modules $\hat{k}$, $k = 1, \dots, n$, enables an adequate computation of the temperature $T_{\hat{k}}$, $k = 1, \dots, n$, in each module. With the contact of current bar and cables not being situated at the interface of two different (input) modules, we avoid the described problem.

Heat Power Balance for an Output Module

We identify $P_{\mathrm{s},\hat{k}}$ with the heat power generated in the current bar section of module $\hat{k}$ by Joule losses, $P_{\mathrm{w},\hat{k}}$ with the heat power supplied to or absorbed from the current bar by attached wire k, $P_{\mathrm{c},\hat{k}}$ with the heat power generated by the contact resistance between cable k and the current bar, $P_{\mathrm{a},\hat{k}}$ with the heat power exchanged with the adjacent module(s) via conduction and $P_{\alpha,\hat{k}}$ with the heat power emitted via convection and radiation. Thus, the following heat power balance for output module $\hat{k}$ holds:

$$P_{\mathrm{s},\hat{k}} + P_{\mathrm{w},\hat{k}} + P_{\mathrm{c},\hat{k}} + P_{\mathrm{a},\hat{k}} = P_{\alpha,\hat{k}},\ k = 1, \ldots, n. \tag{8.4}$$

Note that for the boundary modules $\hat{1}$ and $\hat{n}$, there exists only one adjacent module, but a further vertical surface where heat dissipates from via convection and radiation.

The heat power generated in module $\hat{k}$ computes by

$$P_{\mathrm{s},\hat{k}} = \frac{1}{\kappa_{0,s}} \cdot \left[1 + \alpha_{\rho,s}\left(T_{\hat{k}} - T_0\right)\right] \left(\frac{\ell_k/2}{w_k \cdot s_k}\hat{I}_k^2 + \frac{\ell_{k+1}/2}{w_{k+1} \cdot s_{k+1}}\hat{I}_{k+1}^2\right),\ k = 1, \ldots, n. \tag{8.5}$$

We remind that the resulting currents at the exterior modules are

$$\hat{I}_1 := I_0 = 0,\ \ \hat{I}_{n+1} = 0. \tag{8.6}$$

Heat power is supplied or dissipates by conduction via attached cables. Thus, there holds Fourier's law. Like in Section 6.3.1, we define the auxiliary quantity

$$\Lambda_k := (d_{2,k}^2 - d_{3,k}^2)\ \frac{\pi}{4} \cdot \lambda_{2,k} + A_k \cdot \lambda_{3,k}, \tag{8.7}$$

called the *heat conductivity with respect to the cross sectional area*. It enables to take into account that the heat exchange via the insulation is much smaller than that via the metallic parts of the cables[2]. By this simplification, we obtain

$$P_{\mathrm{w},\hat{k}} = \Lambda_k\ \frac{\mathrm{d}\tilde{T}_k}{\mathrm{d}\tilde{x}},\ k = 1, \ldots, n$$

with $\tilde{T}_k$ the temperature (distribution) in cable k and $\tilde{x}$ the (local) cable coordinate. The temperature in the current bar module $\hat{k}$ is essentially influenced by the temperature profile $\tilde{T}_k = \tilde{T}_k(\tilde{x})$ of the attached cable k in axial direction, in particular by the temperature change at the contact of current bar and cable (cf. Figure 8.4a for a qualitative temperature profile of an attached cable in axial direction). Note that $\tilde{x}$ is a local quantity, referred to the considered cable, with $\tilde{x} = 0$ the contact of the attached cable and the current bar. If cable k is of finite length, we additionally fix $\tilde{x} = L_{f,k}$ at the other end of cable k. Thus, the heat power contribution of cable k is summarized by

$$P_{\mathrm{w},\hat{k}} = \Lambda_k\ \tilde{T}_k'(0),\ k = 1, \ldots, n. \tag{8.8}$$

Analogously to Section 6, the consideration of a volume element with length $\mathrm{d}x$ (cf. Figure 8.4b) yields an ordinary differential equation for the temperature distribution in the insulated single-core cable k of finite length

$$\frac{\mathrm{d}^2\tilde{T}_k(\tilde{x})}{\mathrm{d}x^2} - B_k\,\tilde{T}_k(\tilde{x}) + C_k\ =\ 0, \tag{8.9}$$

---

[2] The heat power contribution of the air gaps in the cable core is neglected due to the extremely low heat conductivity of air.

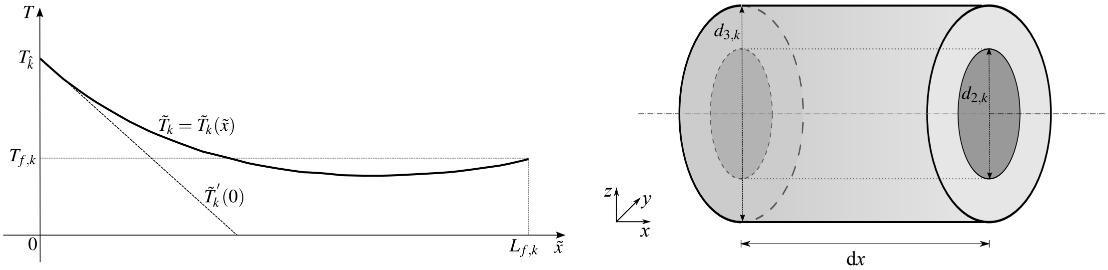

(a) Qualitative temperature profile in axial direction of cable k.

(b) Volume element of length dx for attached cable k.

Fig. 8.4: *Qualitative temperature profile and a volume element of the insulated single-core cable k.*

with

$$B_k = \frac{1}{\Lambda_k}\left(\frac{\pi}{\rho_{w,k}} - \frac{\rho_{0,k}\,\alpha_{\rho,k}\,I_{\hat{k}}^2}{A_k}\right), \quad C_k = \frac{1}{\Lambda_k}\left(\frac{\pi\,T_{\mathrm{amb},k}}{\rho_{w,k}} + \frac{\rho_{0,k}\,(1-\alpha_{\rho,k}\,T_0)\,I_{\hat{k}}^2}{A_k}\right) \tag{8.10}$$

and

$$\rho_{w,k} := \frac{1}{\alpha_k\,d_{2,k}} + \frac{1}{2\,\lambda_{2,k}}\,\ln(d_{2,k}/d_{3,k}). \tag{8.11}$$

The quantity α_k denotes the heat transfer coefficient for the cable k, which is in this context supposed to be constant over the length of the cable and evaluated for a mean temperature at its surface. We describe the determination in detail at the end of this paragraph. First, we define the *asymptotic core temperature of cable k*

$$T_{\infty,k} := \frac{C_k}{B_k}, \tag{8.12}$$

which represents a particular solution of Equation (8.9). Applying the boundary conditions

$$\tilde{T}_k(0) = T_{\hat{k}}, \quad \tilde{T}_k(L_{f,k}) = T_{f,k}, \tag{8.13}$$

provides the unique solution

$$\tilde{T}_k(x) = \vartheta_{1,k}\cdot e^{\sqrt{B_k}\,x} + \vartheta_{2,k}\cdot e^{-\sqrt{B_k}\,x} + \frac{C_k}{B_k}, \tag{8.14}$$

of Equation (8.9) with

$$\begin{aligned}\vartheta_{1,k} &= \frac{-\left(T_{\hat{k}} - T_{\infty,k}\right)\cdot e^{-\sqrt{B_k}\,L_{f,k}} + (T_{f,k} - T_{\infty,k})}{e^{\sqrt{B_k}\,L_{f,k}} - e^{-\sqrt{B_k}\,L_{f,k}}},\\ \vartheta_{2,k} &= \frac{\left(T_{\hat{k}} - T_{\infty,k}\right)\cdot e^{\sqrt{B_k}\,L_{f,k}} - (T_{f,k} - T_{\infty,k})}{e^{\sqrt{B_k}\,L_{f,k}} - e^{-\sqrt{B_k}\,L_{f,k}}}.\end{aligned} \tag{8.15}$$

Finally, we obtain for the heat power contribution by **wire** k **of finite length with specification of all cable data**

$$P_{\mathrm{w},\hat{k}} = \Lambda_k \frac{\mathrm{d}\tilde{T}_k(\tilde{x})}{\mathrm{d}\tilde{x}}\bigg|_{\tilde{x}=0} = \Lambda_k\,\sqrt{B_k}\,(\vartheta_{1,k} - \vartheta_{2,k}),\ k = 1,\ldots,n. \tag{8.16}$$

To reduce the enormous amount of input data, the theses [67, 123] show approaches to determine (a posteriori fitting) constants a_k, b_k, χ_k that describe the thermal characteristics of insulated single-core respectively shielded cables sufficiently accurately. Determining those a priori[3] for a current load I_k, the asymptotic temperature $T_{\infty,k}$ can be computed by

$$T_{\infty,k} = a_k \cdot |I_k| + b_k \cdot I_k^2 + T_{\mathrm{amb},k} \tag{8.17}$$

and the coefficient B_k by

$$B_k = 1/\chi_k^2. \tag{8.18}$$

Using Equation (8.15), the heat power contribution by **wire k of finite length with reduced cable data** is determined by

$$P_{\mathrm{w},\hat{k}} = \frac{\Lambda_k}{\chi_k} \left(\vartheta_{1,k} - \vartheta_{2,k}\right), \; k = 1, \dots, n. \tag{8.19}$$

If we consider an attached cable of infinite length with $L_{f,k} \to \infty$, the temperature $T_{f,k}$ at the end of the cable corresponds to the asymptotic temperature $T_{\infty,k}$ ($T_{f,k} = T_{\infty,k}$). Moreover, the structure of the coefficients $\vartheta_{1,k}$ and $\vartheta_{2,k}$ in (8.15) then implicates

$$P_{\mathrm{w},\hat{k}} = \Lambda_k \sqrt{B_k}\, (T_{\infty,k} - T_{\hat{k}}) \, \frac{e^{\sqrt{B_k}L_{f,k}} + e^{-\sqrt{B}L_{f,k}}}{e^{\sqrt{B_k}L_{f,k}} - e^{-\sqrt{B_k}L_{f,k}}} \xrightarrow[L\to\infty]{} \Lambda_k \sqrt{B_k}\, (T_{\infty,k} - T_{\hat{k}}). \tag{8.20}$$

Thus, for **wire k of infinite length with reduced cable data**, the heat power supplied to or emitted from the current bar computes by

$$P_{\mathrm{w},\hat{k}} = \frac{\Lambda_k}{\chi_k} \, (T_{\infty,k} - T_{\hat{k}}). \tag{8.21}$$

As mentioned, a main ingredient of B_k is the heat transfer coefficient $\alpha_k = \alpha_k(\tilde{T}_{2,k})$. Its value respectively the temperature $\tilde{T}_{2,k}$ at the surface of the insulation are determined iteratively. Starting with an initial value $\tilde{T}_{2,k}^{(1)} = T_{\mathrm{amb},k}$, we compute α_k and the corresponding solution $\tilde{T}_k = \tilde{T}_{3,k}$ according to Equation (8.14). Afterwards, we calculate a mean temperature of the cable core by

$$\tilde{T}_{3,k}^{\mathrm{av}} = \frac{1}{L_{f,k}} \int\limits_0^{L_{f,k}} \tilde{T}_k(\tilde{x}) \, \mathrm{d}\tilde{x} = \frac{\vartheta_{1,k}}{\sqrt{B_k}\, L_{f,k}} (e^{\sqrt{B_k}L_{f,k}} - 1) - \frac{\vartheta_{2,k}}{\sqrt{B_k} L_{f,k}} (e^{-\sqrt{B_k}L_{f,k}} - 1) + T_{\infty,k}, \tag{8.22}$$

and the temperature at the insulation for the the next iteration by

$$\tilde{T}_{2,k}^{(2)} = \tilde{T}_{3,k}^{\mathrm{av}} - \frac{\rho_{0,k}\, (1 + \alpha_{\rho,k}\, (\tilde{T}_{3,k}^{\mathrm{av}} - T_0))\, I_k^2}{2\pi\, \lambda_{3,k}\, A_k\, \ln(d_{2,k}/d_{3,k})}. \tag{8.23}$$

Repeating this iterative procedure until there holds $\left|\tilde{T}_{2,k}^{(i+1)} - \tilde{T}_{2,k}^{(i)}\right| < \epsilon$, $\epsilon > 0$ constant, we finally obtain an appropriate value for the temperature at the surface of cable k which then allows to evaluate the heat transfer coefficient α_k.

---

[3] We implemented calculation tools for the determination of characterizing quantities of insulated single-core cables and shielded cables. The latest versions are available on `http://cable.liess-physics.com`.

The heat power generated via the contact resistance at the connection of cable k to the current bar is

$$P_{\mathrm{c},\hat{k}} = R^c_{0,k} \left[1 + \alpha^c_{\rho,k} \left(T_{\hat{k}} - T_0\right)\right] \cdot I^2_{\hat{k}},\ k = 1, \ldots, n. \tag{8.24}$$

For the heat power contribution by adjacent modules, we have to distinguish between exterior modules with only one neighbour and interior modules with two neighbours:

$$P_{\mathrm{a},\hat{k}} = \begin{cases} \lambda_s \cdot w_2\ s_2 \cdot \left.\dfrac{\mathrm{d}T}{\mathrm{d}x}\right|_{L_{\hat{1}}}, & \text{if } k = 1, \\ \lambda_s \cdot \left(-w_k\ s_k \left.\dfrac{\mathrm{d}T}{\mathrm{d}x}\right|_{L_{\widehat{k-1}}} + w_{k+1}\ s_{k+1} \left.\dfrac{\mathrm{d}T}{\mathrm{d}x}\right|_{L_{\hat{k}}} \right), & \text{if } k = 2, \ldots, n-1, \\ -\lambda_s \cdot w_n\ s_n \cdot \left.\dfrac{\mathrm{d}T}{\mathrm{d}x}\right|_{L_{\widehat{n-1}}}, & \text{if } k = n. \end{cases} \tag{8.25}$$

The gradients in (8.25) at $L_{\hat{k}}$, the interface of output modules $\hat{k}$ and $\widehat{k+1}$, are approximated by difference quotients

$$\left.\frac{\mathrm{d}T}{\mathrm{d}x}\right|_{L_{\hat{k}}} \approx \frac{T_{\widehat{k+1}} - T_{\hat{k}}}{\ell_{\hat{k}}}. \tag{8.26}$$

Another distinction of interior and exterior modules has to be performed for the heat dissipation via the surface

$$P_{\alpha,\hat{k}} = \begin{cases} \Big[\left(\alpha_\mathrm{o}^{(1)} + \alpha_\mathrm{u}^{(1)}\right) \ell_1\, s_1 + \alpha_\mathrm{v}^{(1)} (2\, \ell_1\, w_1 + s_1\, w_1) \\ \quad + \left(\alpha_\mathrm{o}^{(2)} + \alpha_\mathrm{u}^{(2)}\right) \frac{\ell_2}{2}\, s_2 + \alpha_\mathrm{v}^{(2)}\, \ell_2\, w_2\Big] \left(T_{\hat{1}} - T_\mathrm{amb}\right), & \text{if } k = 1, \\ \Big[\left(\alpha_\mathrm{o}^{(k)} + \alpha_\mathrm{u}^{(k)}\right) \frac{\ell_k}{2}\, s_k + \alpha_\mathrm{v}^{(k)} \ell_k\, w_k + \\ \quad \left(\alpha_\mathrm{o}^{(k+1)} + \alpha_\mathrm{u}^{(k+1)}\right) \frac{\ell_{k+1}}{2}\, s_{k+1} + \alpha_\mathrm{v}^{(k+1)}\, \ell_{k+1}\, w_{k+1}\Big] \left(T_{\hat{k}} - T_\mathrm{amb}\right), & \text{if } k = 2, \ldots, n-1, \\ \Big[\left(\alpha_\mathrm{o}^{(n)} + \alpha_\mathrm{u}^{(n)}\right) \frac{\ell_n}{2}\, s_n + \alpha_\mathrm{v}^{(n)} \ell_n\, w_n + \left(\alpha_\mathrm{o}^{(n+1)} + \alpha_\mathrm{u}^{(n+1)}\right) \ell_{n+1}\, s_{n+1} \\ \quad + \alpha_\mathrm{v}^{(n+1)}\, (2\, \ell_{n+1}\, w_{n+1} + s_{n+1}\, w_{n+1})\Big] \left(T_{\hat{n}} - T_\mathrm{amb}\right), & \text{if } k = n. \end{cases} \tag{8.27}$$

Note that the heat transfer coefficients on upper, lower and vertical surfaces have to be determined separately for each module due to their temperature dependency.

Solution of the System of Nonlinear Equations

Putting the heat power terms (8.5), (8.24), (8.25) and (8.27) as well as (8.16), (8.19) or (8.21) into Equation (8.4) finally provides a system of nonlinear equations

$$\boxed{\begin{aligned} P_{\mathrm{s},\hat{1}}(T_{\hat{1}}) + P_{\mathrm{w},\hat{1}}(T_{\hat{1}}) + P_{\mathrm{c},\hat{1}}(T_{\hat{1}}) + P_{\mathrm{a},\hat{1}}(T_{\hat{1}}, T_{\hat{2}}) &= P_{\alpha,\hat{1}}(T_{\hat{1}}), \\ P_{\mathrm{s},\hat{k}}(T_{\hat{k}}) + P_{\mathrm{w},\hat{k}}(T_{\hat{k}}) + P_{\mathrm{c},\hat{k}}(T_{\hat{k}}) + P_{\mathrm{a},\hat{k}}(T_{\widehat{k-1}}, T_{\hat{k}}, T_{\widehat{k+1}}) &= P_{\alpha,\hat{k}}(T_{\hat{k}}), \quad k = 2, \ldots, n-1, \\ P_{\mathrm{s},\hat{n}}(T_{\hat{n}}) + P_{\mathrm{w},\hat{n}}(T_{\hat{n}}) + P_{\mathrm{c},\hat{n}}(T_{\hat{n}}) + P_{\mathrm{a},\hat{n}}(T_{\widehat{n-1}}, T_{\hat{n}}) &= P_{\alpha,\hat{n}}(T_{\hat{n}}), \end{aligned} \quad (8.28)}$$

with unknown temperature vector

$$\mathbf{T} = \begin{pmatrix} T_{\hat{1}} \\ \vdots \\ T_{\hat{n}} \end{pmatrix}.$$

As for each single output module a heat power balance is fulfilled, it is also valid for the entire current bar. The influences of heat powers by adjacent modules cancel each other out in a complete power balance.

To solve the system (8.28) of nonlinear equations, a fixed point approach like e.g. presented for shielded cables could be applied. In contrast to shielded cables, where we incorporate the influence by adjacent cable subsections via interface conditions, the influence by attached cables and adjacent modules in current bars is respected via the heat power balance. This changes the structure of the system of equations. An iterative method for the solution has not been implemented yet. Instead, the nonlinear system is solved (black box) in Matlab with the command *fsolve()*, which uses the Trust-Region dogleg method [142]. In this algorithm, Newton's method is combined with a Trust-Region method. Using Trust-Region techniques improves the robustness when starting far from the solution and handles the case when the Jacobian $\mathbf{J}$ is singular in Algorithm 2. In the second case, the Newton step $\delta\mathbf{x}^{(i+1)}$ would not be defined. The key feature of the Trust-Region dogleg implementation is the use of the Powell dogleg procedure [111] for the computation of the Newton step by minimizing an additionally introduced merit function. It is efficient, since it requires only one linear solution per iteration. Additionally, it can be more robust than using e.g. the Gauss-Newton method with linesearch [91].

For the initial vector, all temperatures $T_{\hat{1}}, \dots, T_{\hat{n}}$ are set to the ambient temperature of the current bar T_{amb}. Thus, in case of high currents in the current bar and small cross-sectional areas, this starting point can be quite far from the final solution, which makes it indispensable to have a robust solver.

Since our approach only provides an average temperature for each output module, we obtain an entire temperature profile along the current bar via interpolation between the discrete points. To this purpose, we apply the Matlab command *interp1()* with the interpolation option 'pchip'. Thus, a piecewise cubic Hermite interpolation is used to compute temperatures between the left and the right end of the current bar.

As the method to solve the nonlinear system has not been implemented by ourselves, we do not state any convergence properties of the applied iterative procedure. In fact, it may be supposed that an iterative algorithm like e.g. implemented for shielded cables nearly behaves in the same manner, because the stated problem respectively the ingredients of the systems of nonlinear equations are very similar. The implementation of the corresponding fixed point iteration and a deeper analysis is intended for the near future.

The close relationship of the convergence of an iterative procedure and the existence and uniqueness of a solution has been shown for all the three previously handled applications – insulated single-core cables, shielded cables and multicables. The structure of the given problem may lead to the conclusion that a condition like formulated for example in Theorem 1, which refers to the ratio of generated heat by the electrical resistance to the heat power emission via the surface in each subdomain, can be formulated in a similar way. Further analysis of this aspect is outstanding.

8.2.2 Finite Element Approach

The modelling with PDEs goes straightforward for the application of current bars with Equation (2.28). As the entire domain of a current bar is supposed to be of homogeneous material, its heat conductivity λ_s is constant. Furthermore, since the current bar is compact and, in contrast to cables, does not contain any air gaps, we do not have to distinguish between a geometrical and physical cross section. Thus, the following equation is used for the computation of temperature T in input module k of the current bar:

$$-\lambda_s \Delta T = \left(\frac{\hat{I}_k}{s_k w_k}\right)^2 \frac{1}{\kappa_{0,s}} \left(1 + \alpha_{\rho,s}\left(T - T_0\right)\right). \qquad (8.29)$$

We additionally apply Equation (2.24) at the interface of current bar and cable cores to respect the influence of contact resistances. Thus, for the area of the contact resistance, we use the metallic cross sectional area of the cables, denoted by the physical cross sectional area A_k.

To simulate a cable of infinite length in three dimensions, we replace it by a wire of finite length $L_{f,k} = 3\chi_k$. By experience, this length is sufficient to ensure that a loose cable[4] attains the asymptotic temperature computed in a two dimensional cross section, even though the temperature $T_{f,k}$ differs from $T_{\infty,k}$. In fact, for the comparison to finite element simulations, we set $T_{f,k} = T_{\infty,k}$, with $T_{\infty,k}$ determined a priori, either with the help of the mentioned cable simulation tool or with our computational approach presented in Chapter 5.

A geometry like depicted in Figure 8.5a is created in COMSOL Multiphysics 3.5a as well as an adaptive mesh which is automatically generated with a finer grid at the transition of cable to current bar (cf. Figure 8.5b). We use tetrahedrons with quadratic basis functions for discretization. Note that for reasons of better presentability, the current bar in Figure 8.5 is turned to the side, instead of all cables pointing to the floor.

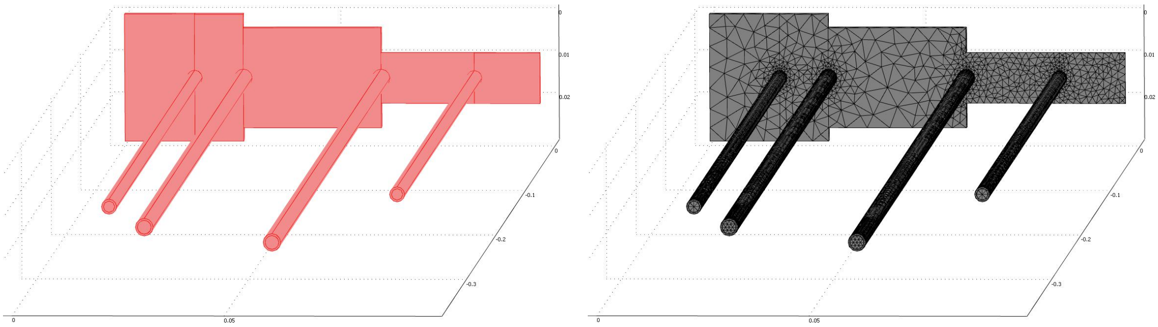

(a) Generated geometry. **(b)** Automatically generated mesh.

Fig. 8.5: *Geometry and mesh of a current bar with four attached cables.*

Finally, a damped Newton method is applied in combination with PARDISO to iteratively solve the system of nonlinear equations.

8.3 Numerical Results

In order to examine if our model for the simulation of temperatures in current bars is correct, we compare measurement and simulation results for a current bar with two attached cables. To investigate the error due to simplifications and discretization, more extensive computations with four wires are compared to finite element simulations. Finally, we show

---

[4] Loose cable means in this context that it is not attached to a current bar or any other electrical device. Thus, no further exterior thermal influences have to be taken into account than those respected in the considerations of the cross section in Chapter 5.

how the method can be used within a dimensioning tool of current bars for industrial application.

8.3.1 Comparison to Measurements

For the validation of practical applicability of the presented computational approach, the Dräxlmaier AG provided a current bar to be used in modern cars. Measurements under current loads were performed and documented in detail in thesis [99]. Two cables of nominal cross sectional area 35 mm^2 were attached to the current bar and for different current loads, measurements of temperatures were taken via thermocouples. The dimensions of the flat cuboid-shaped current bar are depicted in Figure 8.6 and the parameters of its material are summarized in Table 8.1.

Tab. 8.1: *Parameters of the current bar in the comparison of computations and measurements.*

Parameter name	Symbol	Value	Unit
Heat conductivity	λ_s	400	$\mathrm{W}/(\mathrm{m} \cdot \mathrm{K})$
Electrical conductivity	$\kappa_{0,s}$	5.85e7	$1/(\Omega \cdot \mathrm{m})$
Temperature coefficient of electr. resistivity	$\alpha_{\rho,s}$	3.93e-3	1/K
Emission coefficient of the current bar	ϵ_r	0.07	

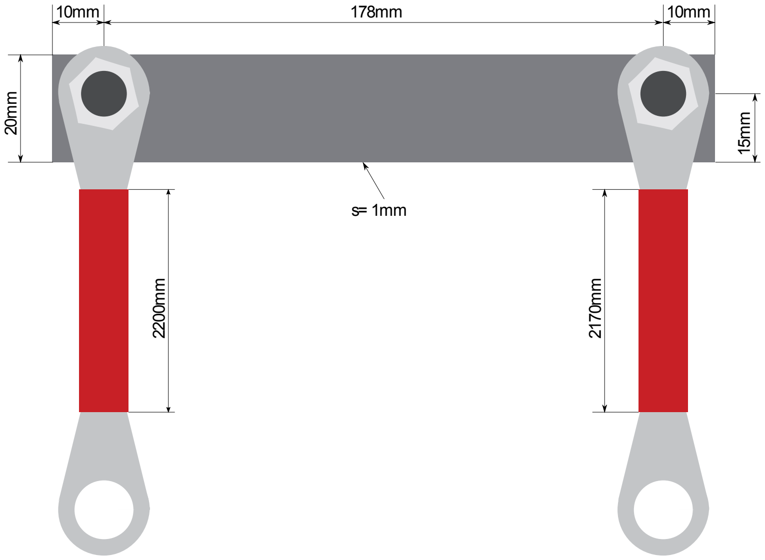

Fig. 8.6: *Dimensions of the current bar and attached cables of the measurements (Image source [99]).*

Five test cases were defined with electrical currents 100 A, 150 A, 175 A, 200 A, 225 A. As a rule of thumb, an arbitrary cross section of copper stands at least a current density of 10 A/mm^2 [99][5]. Since the cross sectional area of the entire current bar is $A_s = 20\,\mathrm{mm}^2$, this condition is fulfilled for $I = 200\,\mathrm{A}$. To cross this threshold, an even higher current was also chosen (225 A). The ambient temperatures were $T_\mathrm{amb} = T_\mathrm{amb,1} = T_\mathrm{amb,2} \approx 23\,°\mathrm{C}$.

Table 8.2 shows a summary of the measured parameters, i.e. the electric current I, the ambient temperature T_amb, the temperatures $T_{f,1}$, $T_{f,2}$ at the ends of attached cables and

---

[5] Note that this general statement should be used with caution, because properties of the surface, quality of contacts, etc. also essentially influence the heat distribution of a current bar.

the contact resistances R_1, R_2. All those represent mean values of three measurements. In Appendix A.3.2, the detailed results of the measurements are listed.

	Scenario				
	100 A	150 A	175 A	200 A	225 A
I(A)	100.3	150.5	175.6	200.7	225.5
T_{amb}(°C)	23.1	22.8	23.8	23.8	23.5
$T_{f,1}$(°C)	43.8	67.2	82.8	99.3	118.8
$T_{f,2}$(°C)	43.3	66.6	81.7	97.8	117.3
R_1($\mu\Omega$)	144.3	148.3	151.0	154.3	158.3
R_2($\mu\Omega$)	157.6	162.5	165.5	168.9	172.9

Tab. 8.2: *Mean values of measured parameters for a current bar with two attached cables.*

	Scenario				
	100 A	150 A	175 A	200 A	225 A
$T^s_{\hat{1}}$(°C)	52.2	85.7	109.3	135.6	165.3
$T^s_{\hat{2}}$(°C)	52.8	87.4	111.3	138.2	168.6
$T^m_{\hat{1}}$(°C)	49.9	80.1	100.7	123.0	147.9
$T^m_{\hat{2}}$(°C)	51.4	83.4	105.2	128.7	155.4
$E_{\hat{1}}$(K)	2.3	5.6	8.6	12.6	17.4
$e_{\hat{1}}$(%)	8.6	9.8	11.2	12.7	14.0
$E_{\hat{2}}$(K)	1.4	4.0	6.1	9.5	13.2
$e_{\hat{2}}$(%)	5.0	6.6	7.5	9.1	10.0

Tab. 8.3: *Simulation (s) and measurement (m) results and absolute respectively relative deviations for both modules of the current bar.*

The results of simulations and measurements to the given current bar for the five scenarios are listed in Table 8.3. The quantities $T^s_{\hat{1}}$ and $T^s_{\hat{2}}$ represent the computed temperatures in module one and two, $T^m_{\hat{1}}$ and $T^m_{\hat{2}}$ the corresponding measured values with

$$T^m_{\hat{1}} = \frac{1}{3}\sum_{i=1}^{3} T_{S_i} \text{ and } T^m_{\hat{2}} = \frac{1}{3}\sum_{i=3}^{5} T_{S_i}$$

and T_{S_i} the measured temperature at sensor i (cf. Table A.3.2 for details). The absolute differences between measurement and simulation for module one are given by $E_{\hat{1}}$ and those for module two by $E_{\hat{2}}$, the relative ones by $e_{\hat{1}}$ and $e_{\hat{2}}$. For the computation of relative deviations, the measured results serve as reference and ambient temperature are subtracted. It is worth mentioning that each simulation took less than 0.5 s in Matlab, version 7.10.0.499, on an Intel Core 2 Duo processor with 2.67 GHz and 3.00 GB RAM. Considering Table 8.3, we observe the following aspects:

1. The measuring and computational results are of the same magnitude (within a range of 15 % with regard to the relative error). However, discrepancies can be observed for larger current loads. In case of $I_1 = I_2 = 225$ A, the absolute deviation between simulation and measurement is 17.4 K for module $\hat{1}$ and 13.2 K for module $\hat{2}$.
2. The calculated temperatures are in all cases (slightly) higher than the measured ones.
3. In the simulations, the difference between the temperature in module $\hat{1}$ and module $\hat{2}$ is smaller than in the measurements for each scenario.
4. In both modules, the absolute and relative errors increase for larger current loads.
5. The discrepancy between simulation and measurement is smaller for module $\hat{2}$ than that of module $\hat{1}$ in each scenario.

We analyse and discuss reasons that may contribute to these discrepancies and observations:

1. The purpose of the presented method is to provide an estimate of temperature distributions in current bars that allows their pre-dimensioning before elaborative measurements or finite element computations are carried out. Considered from this point of view, the deviations between measurements and computations are acceptable.

   We have to take into account that the information provided about the measurements could be more precise. In [99], an indication about the state[6] of the current bar and the attached cables is missing. Thus, we supposed the current bar to be of pure copper of high quality. About the wires, we only knew that they had a nominal cross sectional area of $35\,\mathrm{mm}^2$, but the exact cable type was not provided. Due to the important influence of attached cables (by supplying heat power) on the current bar, differences in the cable parameters in simulations and measurements could entail these discrepancies.

A further reason for the discrepancies between simulations and measurements could be that the integration of contact resistances in the power balance, in the way it is implemented in our calculations, might involve an exaggerated influence of those. The high sensitivity of the computations to the contact resistances is investigated in detail in Section 8.3.3 (Influence of Contact Resistances).

Moreover, the values obtained via measurements might include inaccuracies and influence the temperatures themselves.

2. The quality of the material of the current bar affects the simulation results, among other parameters, by the emission coefficient ϵ_{r}. Its value was supposed to be $\epsilon_{\mathrm{r}} = 0.07$, which is only valid for pure copper of high quality. Higher values of ϵ_{r}, that are normal for copper of lower quality, would entail larger emissions of heat power via the surface and thus result in lower temperatures.
3. The more homogeneous heat distributions in the calculations with lower differences in temperatures of module $\hat{1}$ and $\hat{2}$ could allow to draw the conclusion that the supposed heat conductivity of the current bar is by far larger than in reality. As mentioned, we assumed the current bar to be of pure copper of high quality. If it was mixed with some other materials or degenerated by previously performed, intense current load scenarios, a smaller heat conductivity λ_s of the current bar would be more adequate. This would entail greater differences of temperatures between the modules in the simulations.
4. For the observation of increasing errors for larger currents, we refer once more to the discrepancies due to the contact resistances. Higher contact resistances were measured for larger current loads which seems plausible due to the temperature dependency of electrical resistivity. As the influence of contact resistances seems to be respected too intensely in simulations, the relative error rises with increasing contact resistances.
5. The three facts that our simulations by tendency overestimate the temperatures, the huge heat conductivity of the current bar and the minor contact resistances at module $\hat{1}$ imply that the errors at module $\hat{2}$ are smaller.

In conclusion, our results deviate from measurements to an acceptable level, although uncertainties in parameter values of current bar and cable types are included. The approach works extremely fast and is very robust, which makes it applicable for industrial use. However, contact resistances influence the heat distribution in current bars essentially and represent a problem for the correct dimensioning of industrial electrical components.

8.3.2 Comparison to Finite Element Simulations

In addition to the comparison of our simplified simulation approach to measurements, we investigate the accordance of results for a current bar with four cables carrying different currents to our finite element approach. Although the material of the current bar is copper,

---

[6] With the state of the current bar, we refer to its age and whether it was worn-out or not. In the mentioned work, only the dimensions of the current bar and its material, which was copper, were indicated.

some parameters used for both simulation approaches deviate from those in Table 8.1. The heat conductivity of the current bar is supposed to be 386 W/(m · K), the ambient temperature of cables and current bar is 24 °C. Detailed information about the dimensions of the modules, contact resistances and attached cables are summarized in Table 8.4. Cables number 1 and 4 are of type FLRY-B4, cables 2 and 3 of type FLRY-B6.

Tab. 8.4: *Parameter values used in the comparison of simulation results for current bars.*

k	$\ell_k(mm)$	$w_k(mm)$	$s_k(mm)$	$I_k(A)$	$\chi_k(cm)$	$a_k(K/A)$	$b_k(K/A^2)$	$A_k(mm^2)$	$R_{0_k}(m\Omega)$
1	16.5	30.0	2.50	+35	9.67	4.85e-2	1.92e-2	4.00	1.00
2	11.5	30.0	2.50	+45	11.20	4.03e-2	1.13e-2	6.00	1.50
3	32.5	23.6	2.50	-25	12.33	4.03e-2	1.13e-2	6.00	1.50
4	22.0	12.0	0.80	-55	8.72	4.85e-2	1.92e-2	4.00	1.00
5	15.5	12.0	0.80	-	-	-	-	-	-

Figure 8.7a shows the heat distribution computed with finite elements in the concrete current bar and attached cables. At the ends of the attached cables, we used Dirichlet boundary conditions with the temperature at the boundary corresponding to the asymptotic temperatures of the given cables. All wires have a cooling effect in this example, since the contact resistances are huge (cf. Table 8.4 for the parameter values of the current bar, of the contact resistances and of the attached cables. The cables are of finite length and described by reduced cable data.) and thus, the current bar gets hotter. In fact, the heat power generated by the contact resistances in sum is more than 10 W, whereas the power emitted via the surface is around 6.0 W and the heat power produced by the current is less than 1.0 W. Thus, it does not surprise that for the same simulation without contact resistances, the maximum temperature in the current bar is only 47.7 °C (HBA) respectively 46.9 °C (FEM). In the situation without contact resistances, the current bar serves as a heat sink, whereas the cables do in the present case with contact resistances.

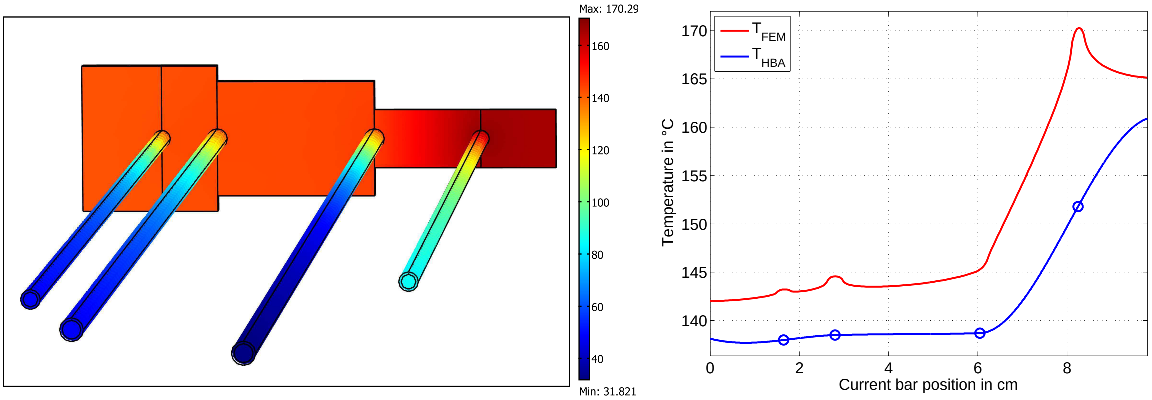

(a) Calculation results via FEM. **(b)** Comparison of simulation results.

Fig. 8.7: *Finite element results for a current bar and comparison to HBA.*

A cut through the temperature profile, computed by finite elements, of the current bar parallel to the x-axis, yields the red curve in Figure 8.7b. The smoothed peaks at the contacts to attached cables are, in contrast to the blue interpolation curve of HBA, obvious. Comparing both lines, one notes that in this example, the red line lies above the blue one, meaning that we obtain higher temperatures with finite elements than with the heat power balance approach (HBA). The maximum deviation of both approaches is 18.5 K at the position where the fourth cable is attached, and the average deviation over the entire current bar is 7.39 K. Taking the finite element results as reference and subtracting the ambient temperature, we have a maximum relative deviation of 12.6 % and an average relative deviation of 5.74 %.

Whereas for the HBA, a time of only 0.23 s is required to solve the nonlinear system in 9 Newton iterations with 51 function evaluations, 178.9 s are necessary via FEM with 192 228 DOFs in 4 Newton iterations. In both cases, the relative tolerance, which defines the stopping criterion, lies beneath $1e$-10.

The significantly lower computation time and costs are an obvious advantage of the heat power balance approach. On the other hand, we have to accept that these results are in most cases less accurate. The temperature rise in the blue curve at the right end of the current bar is due to the higher temperature at the fourth attached cable, and thus a consequence of the interpolation (respectively extrapolation). The flattening of the finite element curve towards the right end of the current bar is more realistic, as more heat dissipates from the current bar at the vertical surface by convection and radiation.

A main reason for the discrepancies of both approaches is the different incorporation of the influence by attached cables. Whereas the heat dissipation by conduction via attached cables might be simulated accurately via FEM, we use simplified models for the heat power balance approach ,which cannot respect influences around, at the end of or in the shape of attached cables in detail. Furthermore, a mean value of the temperature at the surface of the cable is used, whereas a local heat transfer coefficient is applied in FEM. The heat power dissipating via the surface of the current bar is also respected locally in the computations with finite elements. In contrast, only one temperature is computed for each current bar module in the HBA, which means that piecewise constant heat transfer coefficients have to be employed.

To summarize, the heat power balance excels by very short calculation times and minor computational effort. On the other hand, the computations in each module and inter-respectively extrapolation only provide an estimate of the temperature profile. Those inaccuracies require the correct interpretation by the user and have, in some cases, to be handled with care. The finite element approach enables to perform a detailed analysis of the heat distribution in the current bar and to investigate the influence of even curved, 'non-regular' shapes. More complex geometries as depicted in Figure 1.2 can be treated directly, whereas a conversion of the dimensions to the model of the HBA with modules has to be made in advance. Of course, this conversion is often associated with a loss of accuracy.

8.3.3 Further Calculations

The amount of parameters influencing the temperature distribution in a current bar would allow many parameter studies. We restrict to the investigation of the two following aspects:

- Influence of a varying thickness of one module to the temperature distribution and to the maximum temperature, and
- effects of contact resistances.

Other aspects like the dependency on the heat conductivity of the current bar are mentioned within these descriptions.

Example 1 (Variation of Module Thicknesses)

We consider a current bar of homogeneous material with eight attached cables. The physical properties of the current bar and its ambience are given in Table 8.1. The attached cables, the contact resistance and the dimensions of the current bar section are chosen equally for all modules (cf. Table 8.5 for parameter values), except of the length of each module and the electric current in the cables (cf. Table 8.6). We vary the thickness of module 7 in order to show the dependency of the maximum temperature in the current bar on the dimensions of this module.

Tab. 8.5: *Parameter values of all modules of the current bar of the first example.*

Parameter name	Symbol	Value	Unit
Width of each module	w_k	10	mm
Thickness of each module	s_k	5.0	mm
Contact resistance at each cable	$R^c_{0,k}$	1.0	mΩ
Temperature coefficient of the contact resistances	$\alpha^c_{\rho,k}$	3.93*e*-3	1/K
Metallic cross sectional area of each cable	A_k	3.0	mm^2
Ambient temperature of each cable	$T_{\text{amb},k}$	65	°C
Length of each cable	$L_{f,k}$	50	cm
Temperature at the end of each cable	$T_{f,k}$	60	°C
Resistivity of the metallic part of each cable	$\rho_{0,k}$	1.71e-8	$\Omega \cdot \text{m}$
Temperature coefficient of the metallic part of each cable	$\alpha_{\rho,k}$	3.93*e*-3	1/K
Exterior diameter of the attached cables	$d_{2,k}$	2.5	mm
Interior diameter of the attached cables	$d_{3,k}$	2.0	mm
Heat conductivity of the metallic part of attached cables	$\lambda_{3,k}$	386	$\text{W}/(\text{m} \cdot \text{K})$
Heat conductivity of the insulation of attached cables	$\lambda_{2,k}$	0.23	$\text{W}/(\text{m} \cdot \text{K})$
Emission coefficient of the insulation of attached cables	ϵ_k	0.93	–

Tab. 8.6: *Lengths of and electric currents in current bar modules of the first example.*

	Module No. (k)								
	1	2	3	4	5	6	7	8	9
ℓ_k(mm)	20	40	30	20	40	20	20	50	10
I_k(A)	40	-25	20	0	25	-10	-80	30	–
$\hat{I}_k$(A)	0	40	15	35	35	60	50	-30	0

Fig 8.8 depicts temperature distributions in axial direction of the current bar for a varying thickness of module 7. Obviously, the thickness of the current bar has an impact on the maximum temperature. If it is dimensioned too small (< 1.0 mm), too high temperatures (> 200 °C) might be generated. On the other hand, if the current bar module is thicker or equal to 2.0 mm, a further increase of the thickness has only a small effect. For example, the maximum temperature for a thickness of 3.5 mm is 151.8 °C, whereas for 10 mm, it attains 144.1 °C. Hence, we would propose to dimension the thickness with ≈ 2.0 mm, yielding a maximum temperature of 158.9 °C. Compared to a thickness of 3.5 mm, the temperature is only 7.0 K higher, but we save about 43 % of copper (or any other current bar material). In contrast, a further reduction to 1.0 mm would result in a temperature rise of 14.1 K.

Although the current densities vary significantly in the current bar from one module to another, the range from minimum to maximum temperature is in all cases rather small

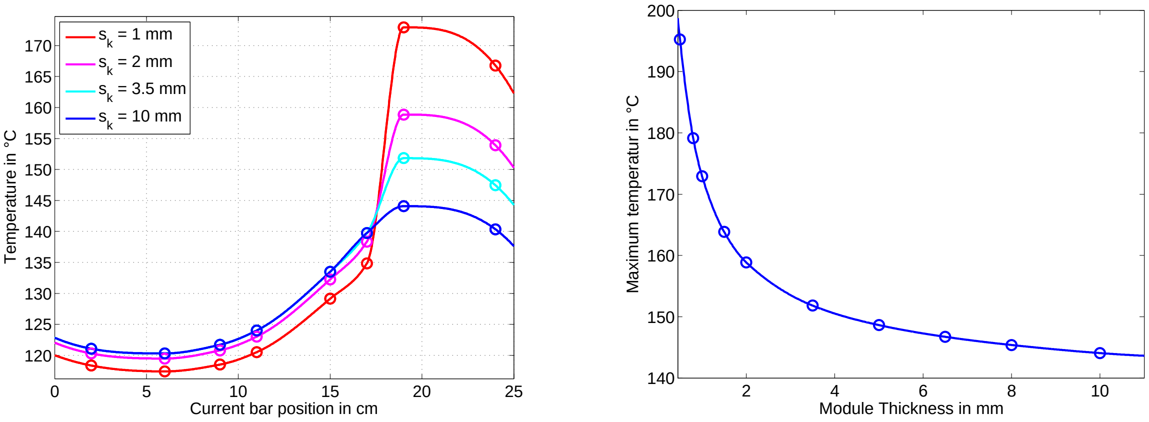

(a) Heat distributions in the current bar for different thicknesses of module 7.

(b) Module thickness vs. maximum temperature.

Fig. 8.8: *Variation of thickness of module 7 and effect on maximum temperature in current bar of second additional example.*

(cf. Figure 8.8a). If the thickness of module 7 corresponds to 10 mm, the minimum temperature is 120.3 °C, and the maximum temperature attains 144.1 °C. For $s_7 = 1.0\,\mathrm{mm}$, the temperature range is $117.4 - 172.9$ °C. These rather small differences are explained by the large heat conductivity of the current bar material ($386\,\mathrm{W/(m \cdot K)}$) which implies that heat entering the current bar at a specific point is distributed equally in the entire current bar. For lower heat conductivities, the temperature range would be much larger. Note in this context that the asymptotic temperature of the cable attached at the seventh module is, in case of $s_7 = 1.0\,\mathrm{mm}$, 226.7 °C and the minimum temperature of all attached cables corresponds to 71.7 °C.

Example 2 (Influence of Contact Resistances)

We consider the same current bar as in the previous example with a fixed thickness $s_7 = 5.0\,\mathrm{mm}$ of module 7 and vary the contact resistances at the cables attached at the third and the seventh module. These two modules are chosen for variation because the first carries a small electric current, the second a large one.

Figure 8.9a shows the heat distribution in the current bar for different contact resistances. The blue lines depict variations of the contact resistance at module 3, the red ones those at module 7. The contact resistances of $3.0\,\mathrm{m\Omega}$ are represented by solid lines, those of $0.0\,\mathrm{m\Omega}$ with dashed lines, the rest ($0.5\,\mathrm{m\Omega}$ to $2.5\,\mathrm{m\Omega}$ in steps of $0.5\,\mathrm{m\Omega}$) with dotted lines.

As expected, the contact resistance of module 3 has hardly any influence on the temperature profile in the current bar (cf. Figure 8.9b). Whereas for $R_{0,3} = 0.0\,\mathrm{m\Omega}$ the maximum temperature is 146.8 °C, it increases to 152.5 °C for $R_{0,3} = 3.0\,\mathrm{m\Omega}$. The low rise of temperature does not surprise, as the heat power produced by the contact resistance $P_{\mathrm{c},\hat{k}}$ mainly depends on the current I_k in the attached cable. Since the electric current of cable 3 is only 20 A, no rise of enormous temperature can be observed, even for huge contact resistances. On the other hand, the seventh cable carries a large current of 80 A. Obviously, the entire system is very sensitive to the contact resistance at cables carrying such high currents. Whereas the maximum temperature in the current bar remains below 100 °C for a perfect

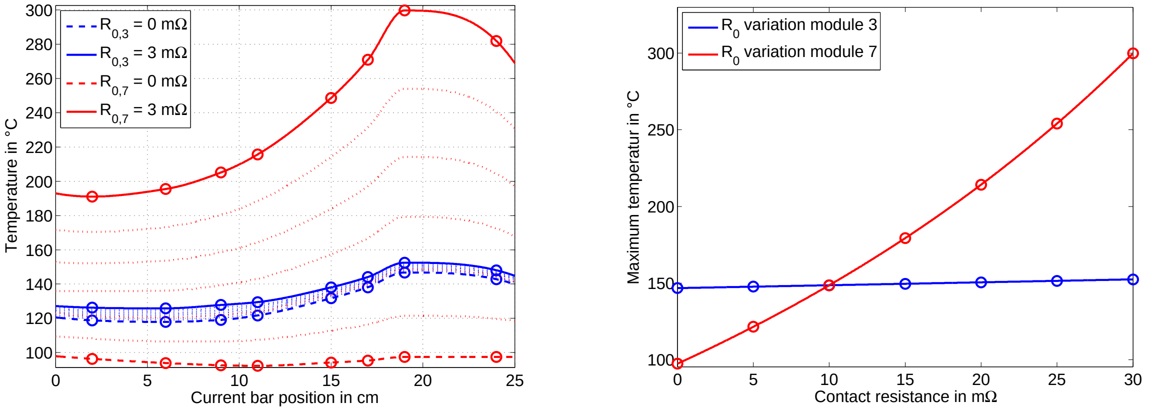

(a) Heat distributions in the current bar for different contact resistances of module 3 and 7.

(b) Impact of varying contact resistances on the maximum temperature for modules 3 and 7.

Fig. 8.9: *Variation of contact resistances of modules and effects on temperatures in current bars.*

thermal resistance at module seven, it exceeds 200 °C for $R_{0,7} \geq 2.0\,\mathrm{m\Omega}$.

Furthermore, Figure 8.9a shows that the range from minimum to maximum temperatures in one current bar is again small due to the large heat conductivity. For $R_{0,7} = 3.0\,\mathrm{m\Omega}$, the difference between minimum (191.1 °) and maximum temperature (299.7 °) is 108.6 K which might seem a lot. But it relativises in comparison to the computation of the same current bar with heat conductivity $\lambda_s = 100\,\mathrm{W/(m \cdot K)}$, where the temperature range (theoretically) extends from 151.9 °C to 488.1 °C.

8.4 Conclusion

In this chapter, we presented an approach to compute the heat distributions in current bars that allows to perform a fast analysis of their geometry. Comparison to measurements showed discrepancies in the range of $5 - 15\,\%$, which are on the one hand due to the simplified model, on the other hand due to the inaccuracies of the provided data and of the measurements. It is interesting that the computed temperatures lie above the measured ones, but those of the finite element analysis are, for another example, even higher.

The variation of single parameters leads to the conclusion that the temperature in the current bars is very sensitive to the contact resistances at attached cables. We proposed a way to take these aspect into account. Further investigations on this topic are necessary and a current research subject. The variation of the thickness of only one module shows that there exists only a small range of plausible current bar thicknesses. If the thickness is below this range, the temperatures increase intensely, even for low currents; above it, there is hardly any change in temperature for thicker current bars. Thus, material and space would be wasted.

For more complex geometries, the proposed method provides a rough estimate. A more detailed analysis, e.g. with finite elements, is required in this context for most cases. Nevertheless, the purpose of the presented method is fulfilled: giving the current bar manufacturers a first, fast 'shot' how to dimension current bars, before a more elaborate and expensive computation or measurement is performed that respects even more details.

9 Fuses

Further Joule heating applications are fuses. Their important function consists in protecting electric devices and connecting structures from overheating and irreparable damages in case of too large electric currents. Since they heat up more intensely than the rest of the electric circuit due to a partially higher resistance, they represent therein a bottle neck. If the electric current is too high, the fuse element melts and interrupts the electric circuit.

9.1 Problem Formulation

In order to protect components of different thermal loads, there exists a great number of fuse types, whose blowing characteristic is affected by the shape and the (composition of) materials. A nominal current assigned to each fuse allows the classification of different fuse types (cf. Figure 9.1a). This nominal current denotes the minimal current a fuse still resists for long times; for higher currents it blows. Practical experiences show that for currents less than 120 % of the nominal current, the fuses often blow after more than ten minutes, whereas for 200 % and more, it takes less than three seconds.

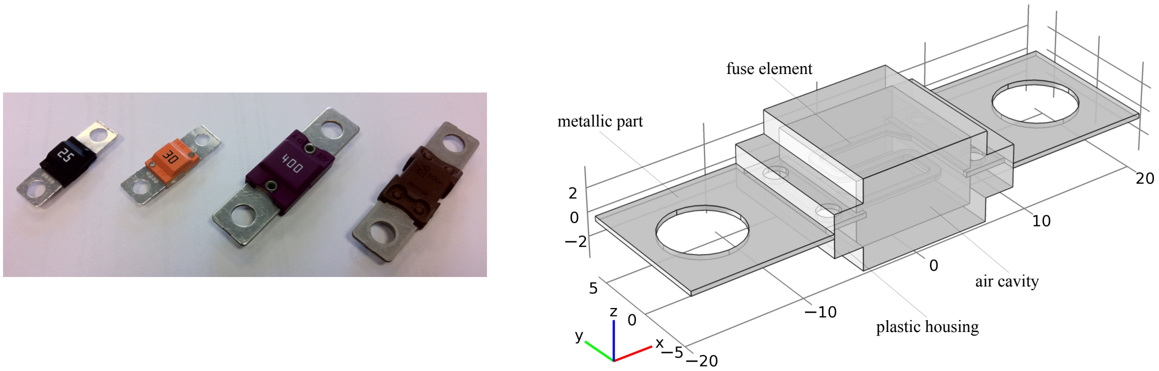

(a) Different types of fuses with nominal currents 25 A, 30 A, 400 A and 500 A.

(b) Geometry of a fuse (fuse type: Midi 25).

Fig. 9.1: *Fuses of different nominal currents and their general geometry.*

Most fuses are composed of four components (cf. Figure 9.1b): a metallic part that connects the fuse to other devices like cables, a fuse element with the mentioned partially higher resistance, a plastic housing that surrounds the fuse element and an air cavity between the fuse element and the plastic housing. The material, the thickness and the length of the fuse element determine the blowing characteristics of fuses. It is the challenge for manufacturers to create fuses that would ideally carry their rated current indefinitely, and melt on a small excess, at least before attached devices or cables are affected. Furthermore, the fuse element must not be damaged by minor harmless surges of current, and must not oxidise or change its behaviour after possibly years of service.

Fuse manufacturers provide characteristic curves for the blowing behaviour of each type of fuse, as depicted for fuse type Midi 25 in Figure 9.2. The red curves provide lower and upper bounds for the blowing times, the blue one represents an exemplary blowing curve.

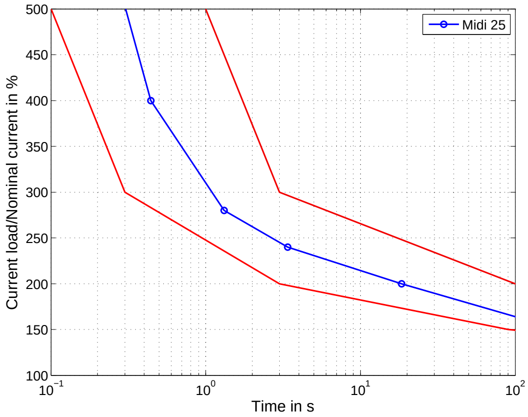

Fig. 9.2: *Characteristic curve of Midi 25 (blue) and its validity corridor (red).*

The objective of this chapter is to set up an appropriate simulation model to determine the blowing characteristics of fuses a priori, without elaborative and expensive measurements. As in the previous sections, we derive a simplified approach based on heat power balances, solve the derived equations by an implicit Euler scheme[1] and finite differences and compare the results for some examples to measurements and finite element computations. In contrast to the previous chapters, we describe measurements performed to investigate experimentally the blowing characteristics of fuses. Finally, we present a design proposition that improves the blowing behaviour of fuses and allows more precise predictions of their blowing characteristics.

In literature, there exist many approaches to compute the heat generation and blowing characteristics of fuses, e.g. [2, 39, 45, 57, 67, 73, 94, 118, 129, 132, 133]. We give a short overview of the mentioned works and show the differences to our approaches. The authors of [57] employ an analogy of the electrical and thermal flow field to derive a thermal network that is solved iteratively. This approach is widespread in the field of electrical engineering. It enables a one dimensional calculation of the different parts of the fuses, but has the drawback that each thermal and continuous effect has to be represented by a discrete element. In [132, 133], a technique called *conservative averaging method* is applied to transform the governing PDEs in three ODEs that are partly solved by finite differences. Like in our heat power balance approaches, this method also uses reduced models and mathematical means to derive simplified equations. Contrary to our approach, starting point of these consideration is not an energy or heat power balance, but the full PDE system. Other authors like those of [2, 45] directly use finite differences to solve the full thermal problem. In both articles as well as in [94], the main focus remains on the validation of experimental data and practical methods to measure temperatures in different kinds of fuse types. Thus, the computations remain rather superficial and only serve as an indicator, whether the measuring results can be correct or not. The characteristic blowing curves of fuse types are

---

[1] We implemented an explicit and implicit Euler scheme to compute blowing times of fuses. Applying finer discretizations of the space, we observed stability problems for the explicit Euler, which were compensated by a large number of discretization point in time (cf. CFL condition). As the implicit Euler scheme is unconditionally stable, we applied the implicit scheme in this context.

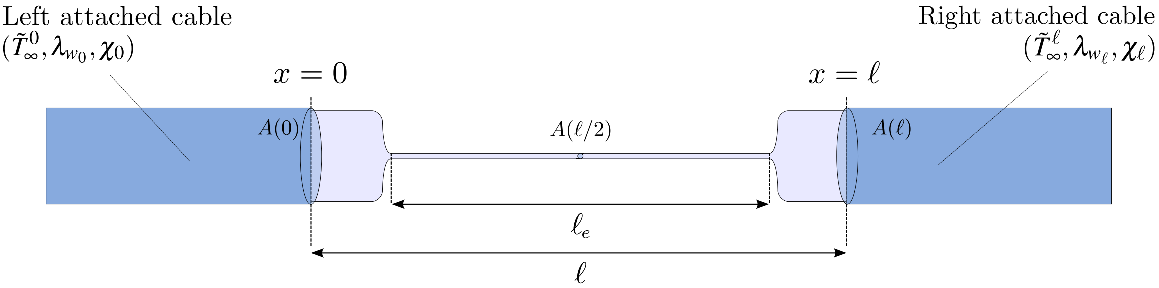

Fig. 9.3: *Model of a fuse element and attached cables for computation of blowing times with the HBA.*

not determined within all the mentioned articles.

To solve Joule heating problems with the help of finite elements and commercial solvers, we refer to the publications [39, 73, 129]. Especially the authors of [39, 129] use models that are quite similar to ours, but in both works, other commercial tools than COMSOL Multiphysics are applied. A good (updated) tutorial that helped us to start our simulations of fuses is [97].

A general difference of our approach to all these works is that the temperature dependence of the heat transfer coefficients is taken into account. In the mentioned investigations using analytical methods, the heat transfer coefficient is supposed to be constant and set a priori; in the numerical works, an information about this subject is missing in most of the cases. The first theses applying a temperature dependent heat transfer coefficient are [67, 118]. Whereas in [118] the computations and the methods are only hinted and practical results represent the main contribution, the author of [67] also describes some details about his numerical approaches. In contrast to our work, the author applies finite volumes for the solution of governing equations and uses different computational formulas.

9.2 Simulation Methods

In this section, we first describe how the blowing characteristics of fuses can be computed by a reduced numerical approach that involves simplifications concerning the geometry. Afterwards, we introduce a more elaborative model solved with finite elements.

9.2.1 Heat Power Balance Approach

We state an energy balance in the metallic part of the fuse for an infinitesimal period of time $\mathrm{d}t$, involving heat power provided by the attached cables. To this purpose, we consider a simplified geometry of the fuse as depicted in Figure 9.3, which restricts to the metallic part of the fuse, neglecting the plastic housing and the air cavity. Moreover, we suppose the fuse element to be cylindrical of length ℓ_e and to have a cross sectional area $A_e = A(\ell/2)$.

Governing Equation

We abbreviate the heat power generated in the metallic part of the fuse by P_ρ, the heat power that dissipates via the surface by P_α, the heat power contribution via conduction by P_x and the stored energy within the time interval by $\mathrm{d}E_\gamma$. Thus, for the metallic part of the fuse, there holds the energy balance

$$P_\rho \, \mathrm{d}t \;=\; P_\alpha \, \mathrm{d}t + P_x \, \mathrm{d}t + \mathrm{d}E_\gamma \; . \tag{9.1}$$

We suppose that the entire metallic part is of identical material with resistivity ρ_0, linear temperature coefficient α_ρ and cross sectional area $A = A(x),\ x \in (0, \ell)$, that varies along the length ℓ. With a constant current I, there holds

$$P_\rho = \frac{\rho_0\,(1 + \alpha_\rho\,(T - T_0))\,I^2}{A(x)}\,\mathrm{d}x \tag{9.2}$$

for the heat power generated in the fuse. Moreover, the heat power emitted via convection and radiation with ambient temperature T_1, heat transfer coefficient $\alpha(T)$ and space dependent perimeter $u(x)$, computes by

$$P_\alpha = \alpha(T)\,(T - T_1)\,u(x)\,\mathrm{d}x\ . \tag{9.3}$$

According to Fourier's law, the heat power supplied or emitted via conduction is given by

$$P_x = -\lambda\,A(x)\,\frac{\mathrm{d}^2T}{\mathrm{d}x}, \tag{9.4}$$

with λ the heat conductivity of the metal in the fuse element. Finally, for the energy stored during the time interval $\mathrm{d}t$, there holds

$$\mathrm{d}E_\gamma = \gamma\,A(x)\,\mathrm{d}x\,\mathrm{d}T, \tag{9.5}$$

with γ the specific heat capacity per volume of the metallic part of the fuse and $\mathrm{d}T$ the change of temperature during the time interval.[2]

Thus, inserting formulas (9.2)-(9.5) into Equation (9.1), we obtain

$$-\frac{\mathrm{d}^2T}{\mathrm{d}x^2} + \frac{\gamma}{\lambda}\,\frac{\mathrm{d}T}{\mathrm{d}t} = \underbrace{\frac{\rho_0\,(1 + \alpha_\rho\,(T - T_0))\,I^2}{\lambda\,A(x)^2} - \frac{\alpha(T)\,(T - T_1)\,u(x)}{\lambda\,A(x)}}_{=:f(T)}\ . \tag{9.6}$$

Boundary and Initial Conditions

In these considerations, we restrict to cables of infinite length, attached on the left ($x = 0$) and right ($x = \ell$) end of the fuse. We introduce local coordinates $\tilde{x} \in (0, \infty)$ and the temperature profile $\tilde{T}(\tilde{x}, \hat{t})$ of the cable core with $\hat{t} \in [0, t_{\max}]$. For simplification, we assume that the temperature distribution in the cable at fixed time $\hat{t}$ corresponds to that of a stationary one. Thus, equivalently to Equation (8.9), there holds

$$\tilde{T}''(\tilde{x}, \hat{t}) - B\tilde{T}(\tilde{x}, \hat{t}) + C = 0,\ \tilde{x} \in (0, \infty), \tag{9.7}$$

with B and C defined in (8.10). Additionally, we apply the boundary conditions

$$\tilde{T}(0, \hat{t}) = T(x = 0, \hat{t}),\ \lim_{\tilde{x}\to\infty} \tilde{T}(\tilde{x}, \hat{t}) = \tilde{T}_\infty(\hat{t}). \tag{9.8}$$

Note that the point $x = 0$ of the coordinate system for T and $\tilde{x} = 0$ for $\tilde{T}$ represents the connecting point of both systems.[3] The solution of this boundary value problem, with χ the characteristic length of the cable, is

$$\tilde{T}(\tilde{x}, \hat{t}) = (T(0, \hat{t}) - \tilde{T}_\infty(\hat{t}))\ e^{-\sqrt{B}\tilde{x}} + \tilde{T}_\infty(\hat{t}) = (T(0, \hat{t}) - \tilde{T}_\infty(\hat{t}))\ \exp\left(-\frac{\tilde{x}}{\chi}\right) + \tilde{T}_\infty(\hat{t}). \tag{9.9}$$

---

[2] Note that contact resistances possibly occurring at the interface of the metallic part of the fuse and attached cables have not been taken into account, yet.

[3] We confine at first to the left attached cable. The corresponding equation for the right attached cable would be obtained by replacing 0 by ℓ for the x-coordinate. Observe that for the gradient determination, different signs have to be applied in case of left and right attached cables.

Its derivative at the point $\tilde{x} = 0$ finally yields

$$\tilde{T}'(0,\hat{t}) = \frac{\tilde{T}_\infty(\hat{t}) - T(0,\hat{t})}{\chi}.$$

The equality of the heat fluxes at the connection of attached cables and fuse is expressed by

$$\begin{aligned} \lambda_{w_0}\, A_{w_0}\, \tilde{T}_0'(0,\hat{t}) &= -\lambda\, A(0)\, T'(0,\hat{t}), \\ \lambda_{w_\ell}\, A_{w_\ell}\, \tilde{T}_\ell'(0,\hat{t}) &= \lambda\, A(\ell)\, T'(\ell,\hat{t}), \end{aligned} \tag{9.10}$$

with λ_{w_0} the heat conductivity, A_{w_0} the cross sectional area, $\tilde{T}_0'$ the temperature gradient at $x = 0$, $\tilde{T}_\infty^0$ the asymptotic temperature and χ_0 the characteristic length of the *left* attached cable; the parameters λ_{w_ℓ}, A_{w_ℓ}, $\tilde{T}_\ell'$, $\tilde{T}_\infty^\ell$, χ_ℓ represent the corresponding quantities of the *right* attached cable. It follows for $\hat{t} = t \in [0, t_{\max}]$:

$$\begin{aligned} T'(0,t) &= -\frac{\lambda_{w_0}\, A_{w_0}}{\lambda\, A(0)}\, \frac{\tilde{T}_\infty^0(t) - T(0,t)}{\chi_0}, \\ T'(\ell,t) &= \frac{\lambda_{w_\ell}\, A_{w_\ell}}{\lambda\, A(\ell)}\, \frac{\tilde{T}_\infty^\ell(t) - T(\ell,t)}{\chi_\ell}. \end{aligned} \tag{9.11}$$

The asymptotic temperatures $\tilde{T}_\infty^\ell(0)$, $\tilde{T}_\infty^\ell(t)$, in the core of the attached cables are determined a priori via the formulas presented in Section 5.2.2. For each time step, the asymptotic temperature corresponds to the temperature we obtain computationally for the cross section of a cable of infinite length.

As usual, we suppose the entire system – fuse and attached cables – to have the same temperature as the ambience at the beginning $t = 0$:

$$T(x,0) = T_1,\ x \in (0,\ell), \quad \tilde{T}_0(\tilde{x},0) = \tilde{T}_\ell(\tilde{x},0) = T_1,\ \tilde{x} \in (0,\infty). \tag{9.12}$$

Fuse Heating Problem

We summarize the entire problem by

$$\boxed{\begin{aligned} -\frac{\mathrm{d}^2 T}{\mathrm{d}x^2} + \frac{\gamma}{\lambda}\frac{\mathrm{d}T}{\mathrm{d}t} &= f(T(x,t)),\ x \in (0,\ell),\ t \in [0,t_{\max}], \\ T'(0,t) &= -\frac{\lambda_{w_0}\, A_{w_0}}{\lambda\, A(0)}\, \frac{\tilde{T}_\infty^0(t) - T(0,t)}{\chi_0},\ t \in [0,t_{\max}], \\ T'(\ell,t) &= \frac{\lambda_{w_\ell}\, A_{w_\ell}}{\lambda\, A(\ell)}\, \frac{\tilde{T}_\infty^\ell(t) - T(\ell,t)}{\chi_\ell},\ t \in [0,t_{\max}], \\ T(x,0) &= T_1,\ x \in [0,\ell]\,. \end{aligned}} \tag{9.13}$$

Numerical Solution of the Fuse Heating Problem

We first divide the time interval $[0, t_{\max}]$ into $n_t + 1$ time steps and apply an implicit Euler scheme for time discretization by

$$\frac{\mathrm{d}T}{\mathrm{d}t} \approx \frac{T^{(i+1)} - T^{(i)}}{\delta_t} \text{ with } \delta_t := t_{i+1} - t_i = \frac{t_{\max}}{n_t}. \tag{9.14}$$

Hence, we obtain for the governing equation

$$\frac{\gamma}{\lambda}\,\frac{T^{(i+1)}-T^{(i)}}{\delta_t}=f(T^{(i+1)})+(T^{(i+1)})'',\ i=0,\dots,n_t-1. \tag{9.15}$$

For discretization in space, we apply the same principle to the derivative of second order, with n_x+2 the number of space discretization points:

$$\frac{\mathrm{d}^2T}{\mathrm{d}x^2}\approx\frac{T_{(j+1)}-2T_{(j)}+T_{(j-1)}}{\delta_x^2},\ j=1,\dots,n_x, \tag{9.16}$$

with $\delta_x := x_{j+1}-x_j=\frac{\ell}{n_x+1}$. This yields the following system, discretized in time and space:

$$\begin{aligned}
\frac{\gamma}{\lambda}\frac{T_{(j)}^{(i+1)}-T_{(j)}^{(i)}}{\delta_t}-\frac{T_{(j+1)}^{(i+1)}-2T_{(j)}^{(i+1)}+T_{(j-1)}^{(i+1)}}{\delta_x^2}&=f(T_{(j)}^{(i+1)}), && i=0,\dots,n_t-1,\ j=1,\dots,n_x,\\
\frac{T_{(1)}^{(i)}-T_{(0)}^{(i)}}{\delta_x}&=-\frac{\lambda_{w_0}\ A_{w_0}}{\lambda\ A(0)\ \chi_0}\,(\tilde{T}_\infty^0(i\delta_t)-T_{(0)}^{(i)}), && i=1,\dots,n_t,\\
\frac{T_{(n_x+1)}^{(i)}-T_{(n_x)}^{(i)}}{\delta_x}&=\frac{\lambda_{w_\ell}\ A_{w_\ell}}{\lambda\ A(\ell)\ \chi_\ell}\,(\tilde{T}_\infty^\ell(i\delta_t)-T_{(n_x+1)}^{(i)}), && i=1,\dots,n_t,\\
T_{(j)}^{(0)}&=T_1, && j=0,\dots,n_x+1.
\end{aligned} \tag{9.17}$$

Additionally, we define the vector $\mathbf{T}^{(i)}$ of temperatures at time step i and the matrix $\mathcal{T}$ of temperatures for time and space:

$$\mathbf{T}^{(i)}=\left(T_{(0)}^{(i)}\dots T_{(n_x+1)}^{(i)}\right)^t,\ \mathcal{T}=\left(\mathbf{T}^{(0)}\dots\mathbf{T}^{(n_t)}\right).$$

We summarize how the system (9.17) is solved in Matlab and refer to [103] for further details. The temperature distribution $\mathbf{T}^{(0)}$ for $t=0$ is given by the initial condition. Afterwards, for each time step $i=0,\dots,n_t-1$, a large *sparse* block matrix $M^{(i)}$ and temperature dependent right hand side are set up. The corresponding system (9.18) is solved with the help of the command *fsolve* and yields the temperature distribution $T_{(j)}^{(i+1)}$, $j=0,\dots,n_{x+1}$.

$$\boxed{M^{(i)}\,\mathbf{T}^{(i+1)}=b^{(i)}(\mathbf{T}^{(i+1)}),\ i=0,\dots,n_t-1,} \tag{9.18}$$

with

$$M^{(i)}=\begin{pmatrix}
-\frac{1}{\delta_x}-\frac{\lambda_{w_0}\ A_{w_0}}{\lambda\ A(0)\ \chi_0} & \frac{1}{\delta_x} & & & (0)\\
-\frac{1}{\delta_x^2} & \frac{2}{\delta_x^2}+\frac{\gamma}{\lambda\delta_t} & -\frac{1}{\delta_x^2} & & \\
 & \ddots & \ddots & \ddots & \\
 & & -\frac{1}{\delta_x^2} & \frac{2}{\delta_x^2}+\frac{\gamma}{\lambda\delta_t} & -\frac{1}{\delta_x^2}\\
(0) & & & -\frac{1}{\delta_x} & \frac{1}{\delta_x}+\frac{\lambda_{w_\ell}\ A_{w_\ell}}{\lambda\ A(\ell)\ \chi_\ell}
\end{pmatrix},$$

$$b^{(i)} = \begin{pmatrix} -\frac{\lambda_{w_0}\ A_{w_0}}{\lambda\ A(0)\ \chi_0}\ \tilde{T}^0_\infty(i\delta_t) \\ f\left(T^{(i+1)}_{(1)}\right) + \frac{\gamma}{\lambda\delta_t}\ T^{(i)}_{(1)} \\ \\ \vdots \\ \\ f\left(T^{(i+1)}_{(n_x)}\right) + \frac{\gamma}{\lambda\delta_t}\ T^{(i)}_{(n_x)} \\ \frac{\lambda_{w_\ell}\ A_{w_\ell}}{\lambda\ A(\ell)\ \chi_\ell}\ \tilde{T}^\ell_\infty(i\delta_t) \end{pmatrix}.$$

The system (9.18) of nonlinear equations is solved iteratively for each time step in Matlab. Matlab internally takes advantage of the sparse structure of the matrices by adequate matrix storage formats like CSR (*Compressed Sparse Row*) or CSC (*Compressed Sparse Column*) and adapted algorithms for solution. This explains why we get comparatively fast computational times with the presented calculation method.

Melting Time of the Fuse Element

The numerical results in Section 9.3 will exhibit that by tendency, the heating of the fuse element up to the melting temperature T_{melt} provides characteristic curves with smaller blowing times than the measured ones. The reason for this observation is that the electric circuit is not interrupted as soon as the melting point is attained, but when the fuse element is entirely melted (at least at one slice). For this reason, we introduce the term *melting time* t_{melt}, which denotes the time necessary for the melting of the fuse element. The blowing time t_{blow} then consists of two parts, the *heating time* t_{heat} until the fuse element has reached the melting temperature and the melting time, which is necessary to transform the fuse element from solid into liquid:

$$t_{\text{blow}} = t_{\text{heat}} + t_{\text{melt}}. \tag{9.19}$$

Note that the process of melting starts as soon as the temperature in the fuse element attains the melting temperature ($T = T_{melt}$). Afterwards, the cross sectional area of the fuse element reduces in time. In order to determine the melting time, we state an energy balance for the melting process in a slice of the fuse element. Therein, the parameter Θ (unit: J/m^3) denotes the specific melting energy per volume of the material of the fuse element material, and the quantity $\mathrm{d}E_\Theta$ the stored melting energy during the time interval $\mathrm{d}t$. It holds

$$P_\rho\ \mathrm{d}t = P_\alpha\ \mathrm{d}t + \mathrm{d}E_\Theta. \tag{9.20}$$

For the identification of the heat power P_ρ generated during the melting process, the emitted heat power P_α and the stored melting energy $\mathrm{d}E_\Theta$, we introduce the quantities κ_1 and A_1, which represent the electrical conductivity of the solid part of the fuse element and its cross sectional area. The parameters κ_2 and A_2 denote the corresponding quantities for the liquid part of the fuse element. Thus, we obtain the electrical resistivity

$$R = \frac{\ell_e}{\kappa_1\ A_1 + \kappa_2\ A_2}$$

in the fuse element. As we assume $A_e = A_1 + A_2$[4], we obtain

$$P_\rho = \frac{\ell_e I^2}{\kappa_1 A_e + (\kappa_2 - \kappa_1) A_2}. \tag{9.21}$$

The heat power P_α emitted via the surface of the fuse element computes by

$$P_\alpha = \alpha(T_{\text{melt}})(T_{\text{melt}} - T_1)\ 2\sqrt{\pi A_e}\ \ell_e. \tag{9.22}$$

We implicitly suppose that the fuse element maintains the temperature T_{melt} during the process of melting. Finally, for the stored melting energy, there holds

$$\mathrm{d}E_\Theta = \Theta\ \mathrm{d}A_2\ \ell_e. \tag{9.23}$$

Putting the terms (9.21)-(9.23) into Equation (9.20) and resolving the resulting equation for $\mathrm{d}t$, yields

$$\begin{aligned}\mathrm{d}t &= \frac{\Theta\ \mathrm{d}A_2}{\frac{I^2}{\kappa_1 A_e + (\kappa_2 - \kappa_1) A_2} - \alpha(T_{\text{melt}})\ (T_{\text{melt}} - T_1)\ 2\sqrt{\pi A_e}} \\ &= \frac{\Theta\ (\kappa_1 A_e + (\kappa_2 - \kappa_1) A_2)\ \mathrm{d}A_2}{I^2 - \alpha(T_{\text{melt}})\ (T_{\text{melt}} - T_1)\ 2\sqrt{\pi A_e}\ (\kappa_1 A_e + (\kappa_2 - \kappa_1) A_2)}.\end{aligned}$$

Thus, integration of the expression over the time interval $[0, t_{\text{melt}}]$ (details cf. Appendix A.4)

$$\int_0^{t_{\text{melt}}} 1\,\mathrm{d}t = \int_0^{A_e} \frac{\Theta\ (\kappa_1 A_e + (\kappa_2 - \kappa_1) A_2)\ \mathrm{d}A_2}{I^2 - \alpha(T_{\text{melt}})\ (T_{\text{melt}} - T_1)\ 2\sqrt{\pi A_e}\ (\kappa_1 A_e + (\kappa_2 - \kappa_1) A_2)}$$

and definition of the heat power $P'_\alpha := \alpha(T_{\text{melt}})\ (T_{\text{melt}} - T_1)\ 2\sqrt{\pi A_e}$ per length finally provides

$$\boxed{t_{\text{melt}} = \frac{\Theta I^2}{P'^2_\alpha\ (\kappa_1 - \kappa_2)} \ln\left(\frac{I^2 - P'_\alpha\ \kappa_2\ A_e}{I^2 - P'_\alpha\ \kappa_1\ A_e}\right) - \frac{\Theta A_e}{P'_\alpha}.} \tag{9.24}$$

Note that fuses might blow, even though the cross section of the fuse element has not been melted entirely. This modelling error is accepted and the numerical results in Section 9.3.1 show that the introduced model corresponds well with the measurements.

9.2.2 Finite Element Approach

Computing the heat generated by flow of electric current through a fuse represents a classical Joule heating problem. Hence, from version 4.1, COMSOL Multiphysics offers the module 'Joule Heating' [96] which is applied for computations of temperatures in this context. In contrast to all other applications of this thesis, we do not enter the constituting PDEs directly, but use the mentioned module as a 'black box'.

---

[4] For the sake of simplicity, we neglect that the volume of the material expands when it transforms from solid into liquid.

Computational Model

To approximate our simulations to the experimental setup (cf. Section 9.3.1), we perform the following procedure[5]:

On one side of the fuse element, the electric potential is set to the value U_0, that is calculated as a product of the electric current I and the resistance R of the fuse element. On the other end of the fuse element, we set the boundary condition to 'ground', i.e., the electric potential at the boundary is zero. Consequently, the entire resistive loss is in the fuse element:

$$U_0 = I \cdot R = I \cdot \frac{\ell_e}{A_e} \cdot \rho_0 \ \left(1 + \alpha_\rho \left(T - T_0\right)\right). \tag{9.25}$$

The resistance of the fuse element depends, among others, on its length ℓ_e and its cross sectional area A_e. Since not all fuse elements are of homogeneous material, their electrical resistivity has to be computed appropriately. For example, the fuse elements of Midi 25 and Midi 30 consist of copper and a tinny layer. Hence, we determine the electric potential by

$$U_0 = I \ \ell_e \cdot \frac{\rho_{Cu} \, \rho_{Sn}}{A_{Cu}\rho_{Sn} + A_{Sn}\rho_{Cu}}. \tag{9.26}$$

Therein, the parameters ρ_{Cu} and ρ_{Sn} represent the resistivity of copper and tin, the quantities A_{Cu} and A_{Sn} the corresponding cross sectional areas of the materials in the fuse element.

Moreover, materials and their parameter values are chosen from a material library for each subdomain of the fuse. In particular, we assign tin to the upper layer of the fuse element (which represents 40 % of the volume of the fuse element for Midi 25 and Midi 30), copper to the lower one. At the exterior surfaces, we apply our heat transfer coefficients and, to respect the heat exchange in the air cavity by radiation, which is essential for higher temperatures, we employ the option 'Surface-to-Surface Radiation' [96].

The interaction of temperature and electric potential is implemented by the option 'Total Power Dissipation Density' as general heat source for the thermal calculation.

Computational Details

Precise information about the geometry and composition of the fuses, provided by the fuse manufacturers, allow to build an exact geometry (cf. [102]). An associated mesh is generated automatically in COMSOL and has been sufficient for our considerations in all simulations. For example, in case of the fuse Midi 30, a mesh with 54 101 tetrahedral elements was created.

For the time-dependent solver, a generalized α-method with time step adapted to the estimated blowing time, an amplification of 0.75 for high frequency and a linear predictor is applied. To solve the linear systems of each iteration, we use PARDISO with the nested dissection multithreaded preordering algorithm and a pivoting perturbation of 1e-8 [95, 96].

With the presented model and computing procedure, we can determine heat distributions in fuses at any time (cf. Figure 9.4). To obtain a characteristic curve of a fuse, we have to calculate the blowing times for several currents. Starting with lower values, we increase the electric currents in simulations for the stationary case until the melting point is attained. Afterwards, we perform simulations for the transient case with rising currents and note the

---

[5] Attached cables have not yet been respected in the simulation with finite elements. We investigate their influence explicitly by means of the HBA in Section 9.3.3 (Example 1).

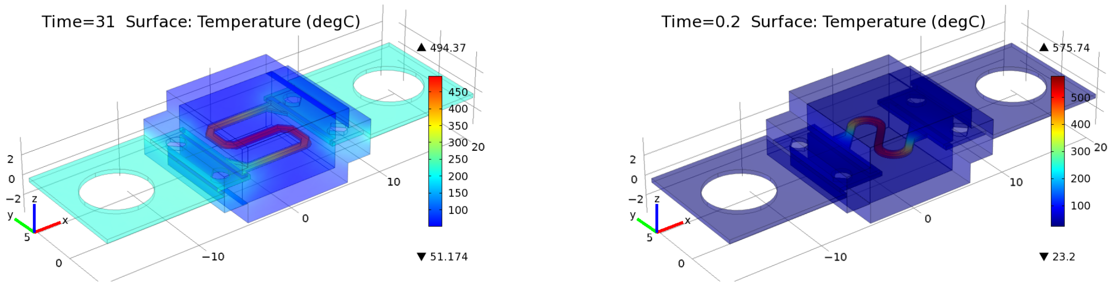

(a) Heat distribution in Midi 25 after 31 seconds with 32.5 A and ambient temperature 50 °C.

(b) Heat distribution in Midi 30 after 0.2 seconds with 90 A and ambient temperature 20 °C.

Fig. 9.4: *Heat distribution in Midi fuses computed with finite elements.*

heating times of the fuse element until the melting temperature is reached. Finally, these heating times are connected by a piecewise linear interpolation.

9.3 Numerical Results

We show how we performed measurements on fuses and compare the experimental results to those of our simplified calculation model and the computations with finite elements.

9.3.1 Comparison to Measurements

In [107, 108], a great number of measurements, performed to determine the blowing characteristics of several fuses, is documented. We briefly describe our experimental setup and compare our computational to the measuring results.

Experimental Setup

We measured the blowing times of fuses in an experimental setting, depicted in Figure 9.5a. Therein, a virtual oscilloscope, connected to a computer, measures the voltage at a shunt. Since the resistance of the shunt is known, the electric current in the fuse can be computed by Ohm's law. The current source is also connected to the computer, such that the magnitude of voltage and current can be controlled by the user (cf. Figure 9.5b).

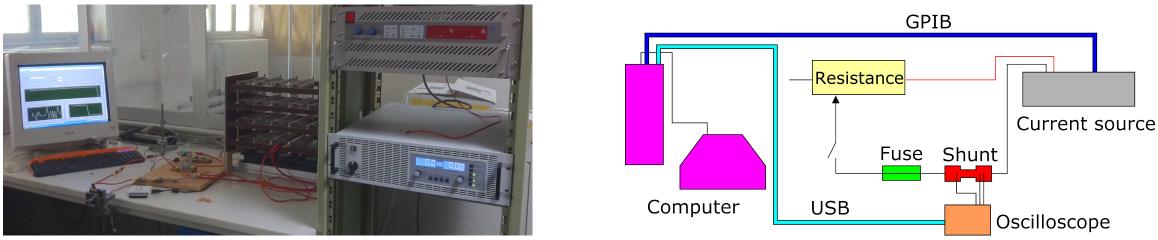

(a) Experimental setup for measurements of blowing times of fuses.

(b) Basic circuit diagram of experimental setup.

Fig. 9.5: *Setup and basic diagram for measurements of blowing characteristics of fuses.*

To be able to measure the correct blowing times, we have to know the moment when the flank of the current edge rises most intensely. This moment represents the start of the measuring of time and it ends as soon as the fuse blows. Both, beginning and stopping of the current flow in the fuse element, are determined automatically by a computer programme, implemented in LabVIEW®. This procedure is performed once or several times for each type of fuse with minimally 120 % of the nominal current, up to maximally 500 % in several steps. For each current, up to three measurements are carried out and fitting of the average values for each current experimentally yields the characterising blowing curve of a fuse type.

Measurement and Simulation Results

We compare the results of our simulations to measurements for self-made fuses, consisting of a metallic strand, and for fuses obtained by a manufacturer that have a more complex geometry.

Self-Made Fuses

First, we performed measurements and simulations on simple, self made fuses that consist of a single strand of copper. The strand has a diameter of 0.3 mm and the length of the fuse element varies from 2.5 mm to 15.0 mm. Figure 9.6 shows the results obtained by simulations (blue and green curves) and measurements (red curves). The attached cables were both of type FLRY-A 2.5.

Regarding Figure 9.6, we state the following observations:

- The short time behaviour ($< 1\,\mathrm{s}$) is described very well by our computational approach. The heating times t_{heat} are obviously shorter than the measured blowing times t_{meas}. Thus, we additionally introduced the melting time t_{melt}. The sum of both times, t_{heat} and t_{melt}, summarized in t_{blow}, yields an almost perfect accordance of computed and measured blowing times in all six cases for the short time behaviour.

- In contrast, for the mean time (1-10 s) and long time behaviour ($> 10\,\mathrm{s}$), the accordance seems to be improvable. In all cases, the computed times are shorter than the actually measured ones.

- All computed curves show an asymptotic behaviour with a horizontal asymptote towards an electric current, in the following called the asymptotic current I_{asym}. It holds $\lim\limits_{I \to I_{\mathrm{asym}}} t_{\mathrm{blow}}(I) = \infty$. For currents $I < I_{\mathrm{asym}}$, the fuse does not blow; however, for larger currents, it does after sufficiently long time. Note that the asymptotic currents of computations and measurements are very close for all cases.

- Especially for the strands of lengths 2.5 cm, 5.0 cm and 12.5 cm (cf. Figures 9.6a, 9.6b and 9.6e), the convergence towards the horizontal asymptote is attained more quickly by the computed curves than by the measured ones. This effect is optically reinforced by a linear interpolation between the measured values, whereas more smooth curves are calculated for the interpolation of the computed values. It means that for currents (slightly) above I_{asym}, the blowing time is still short and for currents even closer to I_{asym}, the blowing times increase significantly. For example, the strand of length 5.0 mm blows after 8.27 s in our measurements with 23.2 A and after 563.5 s for 20.0 A. In the computations with 18.0 A, it blows after 6.5 s and after 621 s for 17.65356 A.

This means that for a decrease of time in the same magnitude, the current has to be reduced about 13.8 % in the measurements, but only 1.96 % in computations.

- The blowing curves move downwards for longer strands in computations and measurements. Whereas the asymptotic current load of the strands with a length of 2.5 mm is nearly exactly 20.0 A, it is ≈ 14.6 A for the strands of length 15.0 mm. This tendency is also recognizable for the measurements.

The following reasons contribute to the observations and discrepancies of measurements and computations:

- The discrepancy between simulation and measurement results for the mean and long time behaviour can mainly be explained by different (chemical) processes that influence the blowing times of fuses, starting only after a certain time of operation. Whereas for high currents, the blowing time is essentially determined by the heat capacity of the fuse element, the metallic surface of the fuse element starts to oxidise after longer times of current load. We suppose that it forms an oxide pipe that prevents the melted material of the fuse element to drop off. These (chemical) reactions imply longer blowing times, but they have not yet been respected in our model. We reinforce our explanation by an improved fuse design which is the subject of Section 9.4.

- As in all previous sections of this thesis, errors of measurements contribute to the discrepancies. For the fuse types Midi 25 and Midi 30, we performed several measurements with equal current loads. Although we used the same types of fuses, we often observed great deviations in the long time behaviour. For example for Midi 25, the blowing time with a current load of 38.41 A varied between 43.6 – 73.8 s (cf. Section A.4.2).

- Additionally and also mentioned in all previous comparisons of this thesis, inaccuracies of material parameters (length and width of e.g. the fuse element) have an impact on the real blowing times of fuses. Furthermore, we experimentally observed (cf. [27]) that fuses also *deteriorate*, meaning that fuses which had to carry (larger) current loads several times before without blowing, can be damaged and consequently blow faster than new ones. These fatigue effects, which are well known in mechanics by Wöhler's curve [69], have to be taken into account to obtain precise predictions for the blowing behaviour of fuses, but they have not yet been respected in the present model.

- The longer heating times for fuse elements of shorter length can be explained by the increasing influence of the attached cables, which normally have a cooling effect on the temperature of the fuse element. We go more into detail to this aspect in Section 9.3.3 (Variation of Attached Cables).

Midi 25/30

Figure 9.7 shows comparisons of measurement (MEAS) and simulation results (HBA) for the fuse types Midi 25 (cf. Figure 9.7a) and Midi 30 (cf. Figure 9.7b), with red curves for the measurements and blue curves for the simulations. Note that measurements have only been performed up to 70 A due to technical reasons, which corresponds to 280 % of the

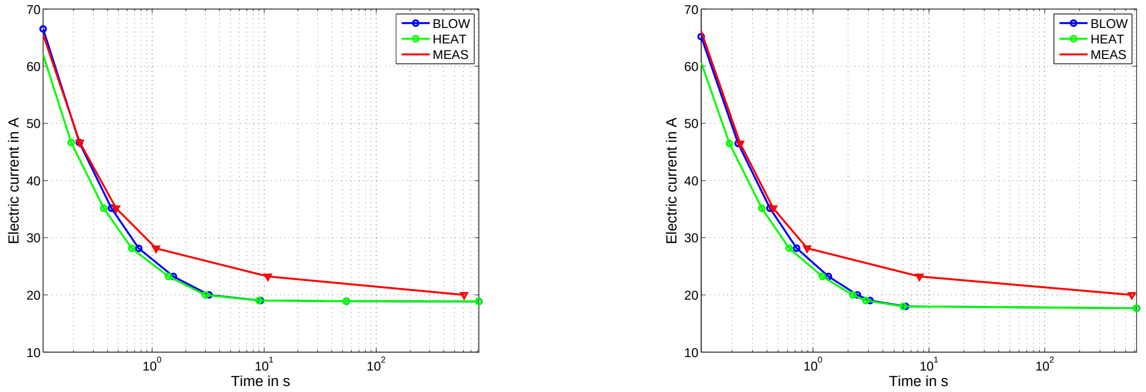

(a) Measured and computed blowing curve with a strand as fuse element of length 2.5 mm.

(b) Measured and computed blowing curve with a strand as fuse element of length 5.0 mm.

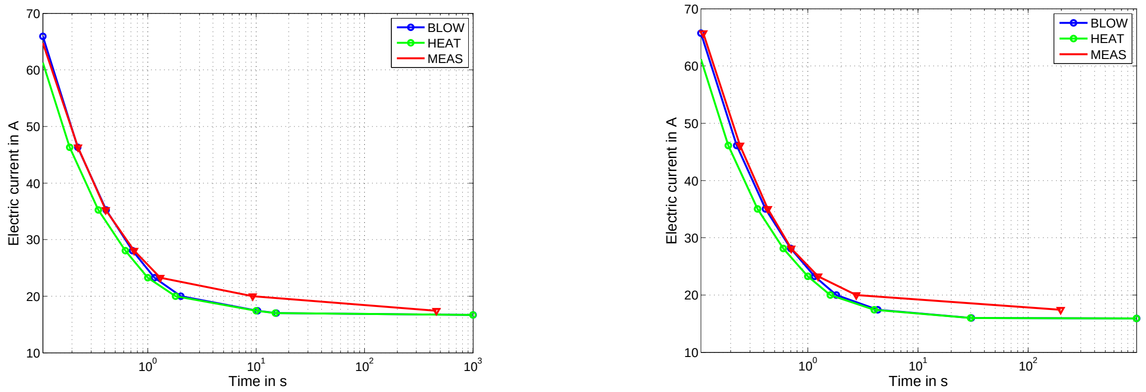

(c) Measured and computed blowing curve with a strand as fuse element of length 7.5 mm.

(d) Measured and computed blowing curve with a strand as fuse element of length 10.0 mm.

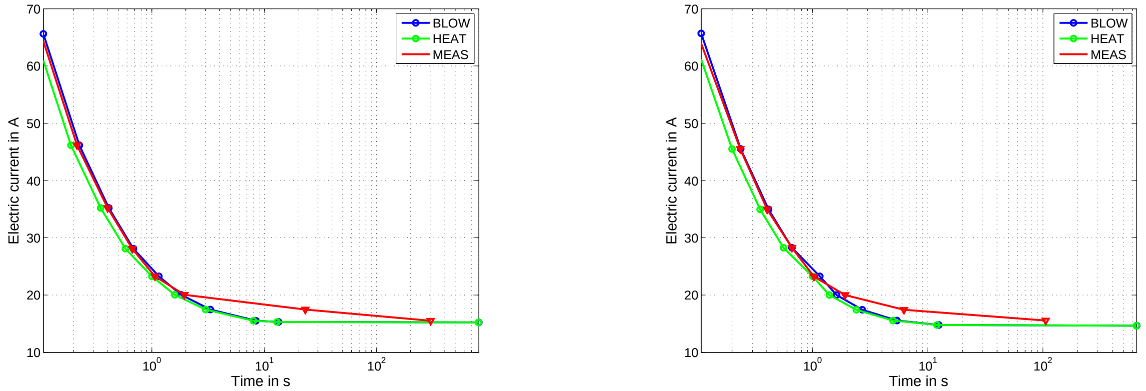

(e) Measured and computed blowing curve with a strand as fuse element of length 12.5 mm.

(f) Measured and computed blowing curve with a strand as fuse element of length 15.0 mm.

Fig. 9.6: *Measured (red lines) and computed blowing curves (green, blue lines) for a strand with fuse element of diameter 0.3 mm and varying lengths. In each subfigure, the green curve shows only the heating time, the blue one the blowing time which consists of heating and melting time.*

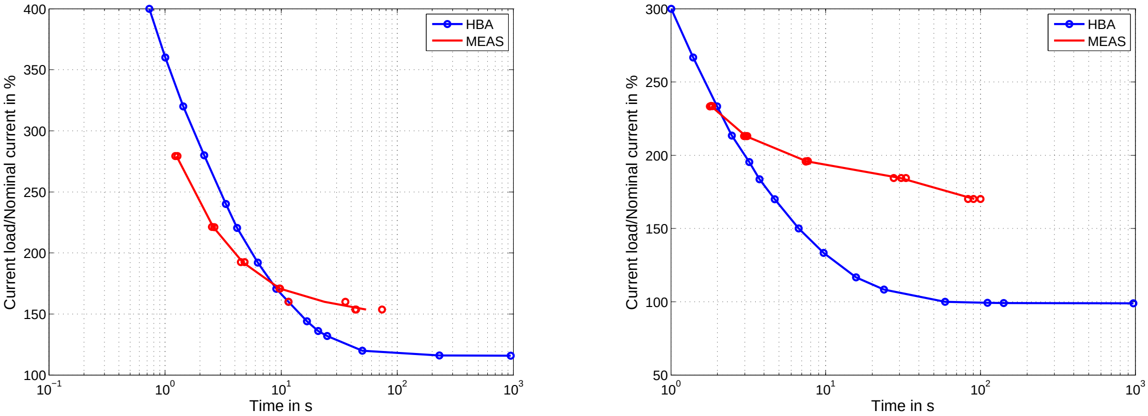

(a) Midi 25. **(b)** Midi 30.

Fig. 9.7: *Measured and computed blowing characteristics of Midi fuses.*

nominal current for Midi 25 and 233 % for Midi 30. Thus, all measured points refer to the mean and long time behaviour.

We observe that the measured and computed curves do not correspond very well for both fuse types. In both cases, the curves of the measurements are, for the long time behaviour, above those of the simulations and both curves cross after a few seconds. In the following, we explain these discrepancies that are much larger than those of the self made fuses.

The fuse elements of both fuse types consist of not only one material, but of two different layers. The upper layer, which represents 40 % of the fuse element volume, is made of tin, the lower part, which thus represents 60 %, of copper. Note that the melting point of copper is 1083 °C and that of tin 231 °C. In our HBA simulations, we acted as if the material of the fuse was a homogeneous mixture of copper and tin. Hence, we applied a weighted mean value for all parameters, including the melting point, which then results in 730 °C. It seems that our computational approach is not sufficiently adequate for these types of fuses with a heterogeneous fuse element. In reality, the tin part of the fuse element starts to melt before the part of copper reaches the melting temperature. The melted part of the fuse element influences the copper part by a chemical reaction and also by the jump of electric resistance, when it turns from solid into liquid. Thus, the distribution of the current density changes fundamentally from one moment to another.

As stated in the theoretical part, we assume that the melting of the fuse element starts as soon as the melting temperature is attained. For a fuse element composed of different materials, this assumption is not true and the heating and melting processes run partly in parallel. In our computations, however, we still simply add the heating and melting time to compute the blowing time.

Moreover, the fuse element is of curved shape (cf. FEM simulations in Figure 9.4), whereas in our computational model, we suppose it to be straight-line. We show in the computations with finite elements that this curved shape of the fuse element influences the distribution of the current density in the fuse element and consequently the blowing characteristics of fuses. Finally, the plastic housing of the fuse is not respected in the simplified approach. This influence seems to be rather small and was investigated by finite element simulations in [89].

9.3.2 Comparison to Finite Element Simulations

In contrast to the previous chapters, the main focus of this subsection is on the comparison of computations with finite elements to measurements for fuses of type Midi 25 and Midi 30. Besides, we compare the finite element simulations with those obtained via the HBA.

Figure 9.4 shows that we generated a very precise geometry of both fuse types with concrete dimensions directly obtained from the manufacturer. Using the Joule heating module of COMSOL Multiphysics 4.3 and applying the formulas explained in Section 9.2.2, we obtain the blowing characteristics of both types of fuses, depicted in Figure 9.8. Therein, we distinguish between a layer of copper and one of tin in the fuse element, but do not respect the influence of attached cables. The criterion when the fuse blows is that the maximum temperature reaches the average melting temperature, which is supposed to be 730 °C.

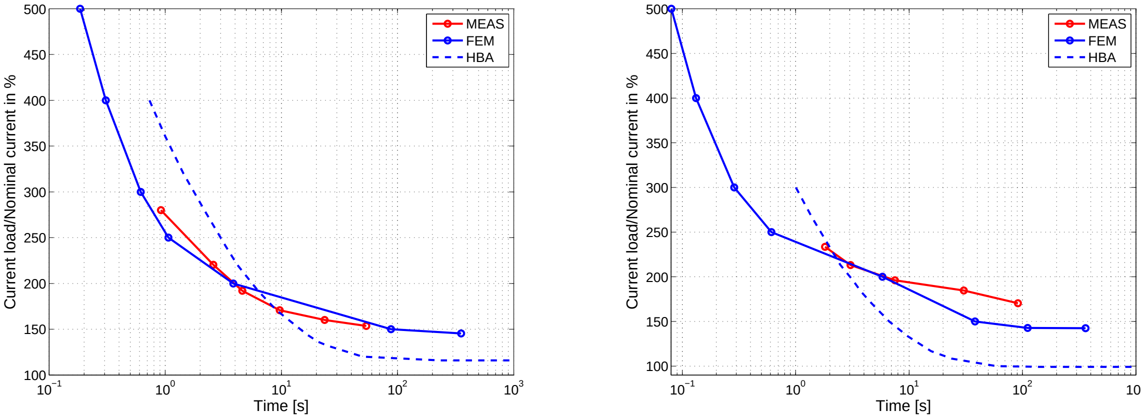

(a) Midi 25. **(b)** Midi 30.

Fig. 9.8: *Blowing behaviour of Midi fuses, computed with finite elements.*

The finite element simulations correspond quite well to the measurements, whereas the results of the HBA deviate significantly from both. The reasons why the HBA results do not coincide with those of the measurements and the finite element simulations are numerous and were mentioned in the previous section. One main argument was that the current density varies in the fuse element. We examined this in our finite element simulations, cf. Figure 9.9. The slice through the fuse of Midi 30 for an electric current of $I = 60\,\mathrm{A}$

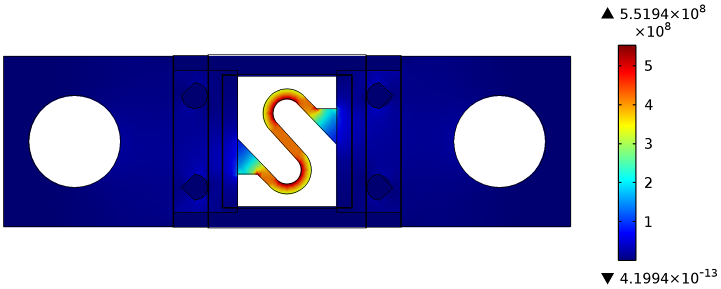

Fig. 9.9: *Slice through a Midi 30 for an electric current of 60 A with current density in* A/m^2.

shows that the current density in the fuse element is not equally distributed. In fact, the current tries to find the shortest way possible, thus the heat distribution at the inner curves ($\approx 5.5e8\,\mathrm{A/m^2}$) is significantly higher than at the exterior ones ($\approx 3.5e8\,\mathrm{A/m^2}$).

The mentioned effect of unequal distributions of the current density is to the largest part compensated by the huge heat conductivity of the fuse element. Nevertheless, varying current densities can result in different maximum temperatures in the fuse element and have to be taken into account for more precise computations.

This example shows once more the advantages and drawbacks of our two kinds of approaches for thermal analysis of devices carrying electric current. The simplifications we use for our HBA implicate much faster computational times – generating the blowing curve of a fuse type takes only a few minutes. In contrast, setting up the complex geometry, solving repeatedly the nonlinear systems with a large number of DOFs and finally creating the blowing curves required several hours in Matlab, version 7.10.0.499, on a Pentium III Xeon processor with 4 cores (each 2.50 GHz) and 32 GB RAM. However, the simplified models make it very hard to take into account all essential effect. This is where a more elaborative method, based e.g. on the solution with finite elements, excels.

9.3.3 Further Calculations

Example 1 (Variation of Attached Cables)

To investigate the influence of attached cables on the blowing behaviour of fuses, we take a strand of copper (cf. Section 9.3.1 (Measurement and Simulation Results – Self-Made Fuses)) and vary the cable types attached on the left and on the right end[6]. The strand has a diameter of 0.3 mm and a length of 2.5 mm We attach insulated single-core cables of nominal cross sectional area 0.35 mm^2, 1.0 mm^2, 2.5 mm^2 and 25 mm^2. In Figure 9.10, the dependency of the blowing characteristics of fuses is presented.

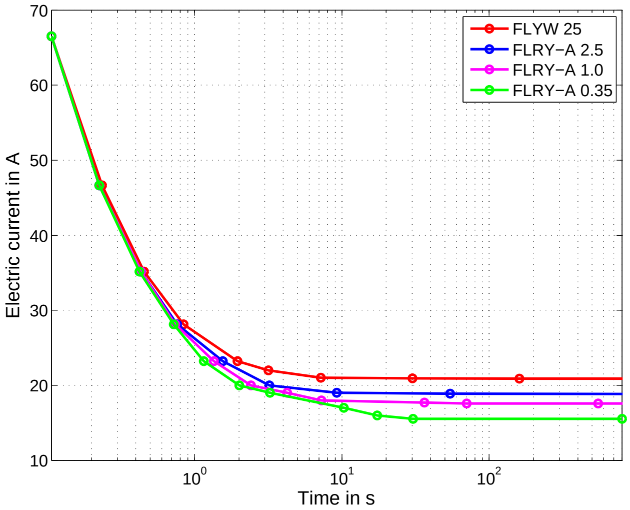

Fig. 9.10: *Characteristic curves for a strand of diameter 0.3 mm and a length of the fuse element of 2.5 mm. The attached cable types have cross sectional areas of 0.35, 1.0, 2.5 and 25 mm^2.*

It turns out that the short time behaviour of fuses is nearly completely independent of the

---

[6] Note that in these considerations, we attach the same cable type on the left and right end, although different cable types at both ends can be respected in our calculations.

attached cable type, whereas for longer times, the heat emitted to the ambience plays a main role. For more than 28 A, the four curves and thus the blowing times are nearly identical for all attached cable types. This changes for the mean and long time behaviour, where the influence of the heat emitted by the surface via convection and radiation and especially at the ends of the fuse via conduction is significant. For attached cables of nominal cross sectional area 0.35 mm^2, the asymptotic current has a value of $\approx$ 15.547 A, whereas for those of 25 mm^2, it is $I_{\text{asym}} = 20.905$ A.

The reason is simply that a huge attached cable heats up less intensively than a thin one for the same current and hence, it can absorb more heat from the fuse. Consequently, the fuse does not blow for certain currents in case of thick cables, whereas it does in case of thinner ones. This might not be dangerous for the attached cables, but for the device attached at the other end of the cable.

Our study shows that each fuse with its certain blowing behaviour has to be dimensioned directly with the concrete cable and, if possible, also with the device attached at the other end of the cable. Neglecting the influence of attached cables might involve very different behaviours of fuse types, which could result in overheating of the main components.

Example 2 (Variation of Lengths of Fuse Elements)

It is evident that the blowing characteristics of fuses are essentially determined by the thickness of the fuse elements, since its cross sectional area represents a main ingredient of the current density. In this example, we examine the influence of the length of the fuse element.

Our simulations and measurements in Section 9.3.1 (Measurement and Simulation Results – Self-Made Fuses) confirm that the length of the fuse element has a strong impact on the blowing characteristic, which is shown in Figure 9.11 for a strand of diameter 0.3 mm and attached cables of type FLRY-A 2.5. The lengths of the fuse elements vary and are 1.0 mm, 5.0 mm, 12.5 mm, 25 mm and 50 mm.

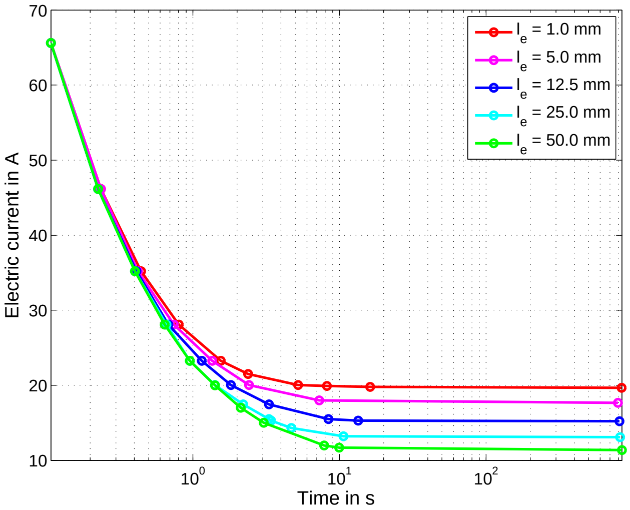

Fig. 9.11: *Characteristic blowing curves for a copper strand of diameter 0.3 mm with varying lengths of the fuse element from 1.0 to 50.0 mm.*

The green curve in Figure 9.11, representing the blowing characteristic of the strand with length $\ell_e = 50$ mm of the fuse element, is significantly lower than that of the strand with for example $\ell_e = 1.0\,\mathrm{mm}$. In case of $\ell_e = 50\,\mathrm{mm}$, the asymptotic current load is 11.355 A, in case of $\ell_e = 1.0\,\mathrm{mm}$, it is 19.676 A.

The reason for this observation is of course the same as mentioned in the previous example. The cooling effect of attached cables is more significant for shorter fuse elements than for longer ones. Nevertheless, it is surprising that the influence of varying lengths of the fuse element is so enormous.

Example 3 (Variation of Fuse Element Materials)

The comparison of measurements and simulations for the Midi fuses revealed significant deviations. One probable reason is that the fuse element of both types are composed of different materials. In this example, we investigate by numerical experiments how the material of the fuse element influences the blowing characteristic of a fuse. To this purpose, we examine four fuses of equal geometrical dimensions, which only differ in the material of the fuse element. Electric currents are applied to strands with a diameter of 0.3 mm and a length of 7.5 mm of the fuse element, for fuse elements consisting of copper (Cu), tin (Sn), zinc (Zn) and aluminium (Al). For each created fuse type, we determine the blowing curve, starting with an electric current of 70 A up to the asymptotic current I_{asym}. The attached cables are of type FLRY-A 2.5.

In Figure 9.12, the blowing curves of our four fuse types are depicted. Obviously, the blowing behaviour varies enormously for different materials of the fuse element. In contrast to our previous examinations, not only the mean and long time behaviour is concerned, but also the short time behaviour. All material parameters vary from one fuse material to another, but probably the most important quantity in this context is the melting point, which is 1083 °C for Cu, 231 °C for Sn, 420 °C for Zn and 660 °C for Al. The blowing curve belonging to the fuse of copper lies above all others, whereas the one of the tin fuse represents the lowest. The order of blowing curves coincides exactly to the value of the corresponding melting point.

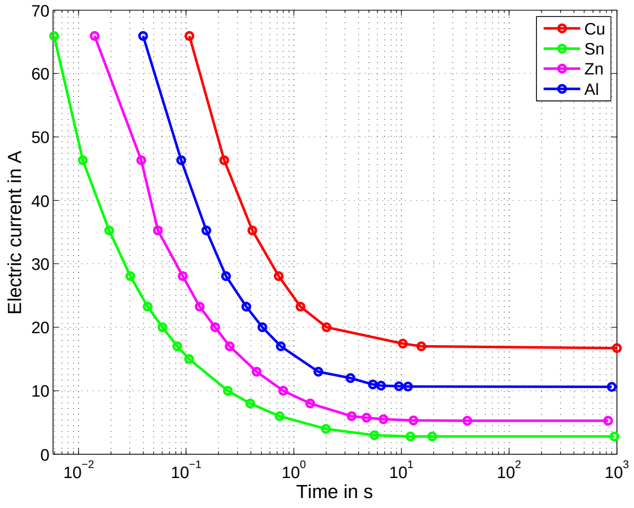

Fig. 9.12: *Influence of different materials of the fuse element on the blowing characteristics.*

This fact allows to draw the conclusion that it is not surprising that for the fuses of types Midi 25 and Midi 30, the computed blowing curves do not correspond well to the measured ones. The blowing behaviour of different materials is not similar at all and also completely different for a mixture of copper and tin.

9.4 An Improved Fuse Design

We performed further measurements on self-made fuses of zinc[7] [108]. The main interest of these measurements was to examine how magnets near the fuse elements influence the blowing behaviour of fuses. We noticed that the heating times until the blowing of fuses are shortened for fuses with magnets. This is also shown in Figure 9.13 for a strand of tin with diameter 0.643 mm, length 25 mm of the fuse element and attached cables of type FLRY-A 2.5.

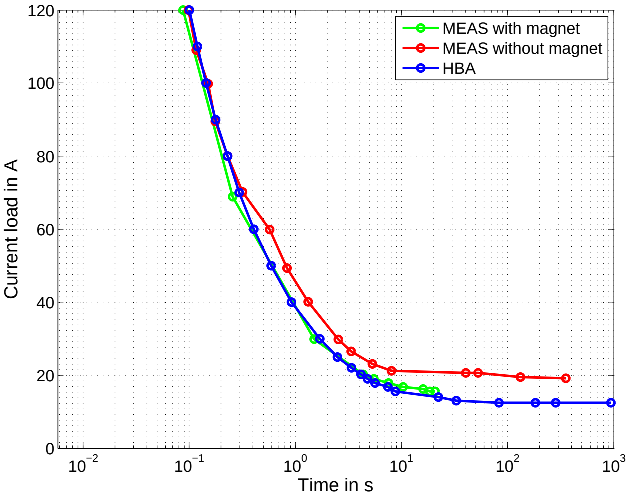

Fig. 9.13: *Influence of magnets on blowing characteristics of a fuse made of zinc.*

Interesting in this context is that the computed blowing curve corresponds much better to that of the measurements, especially for the mean time behaviour, if we add magnets near the fuse element. We obtained this tendency not only for the presented fuse type, but for further ones not mentioned in this thesis. Concerning the long time behaviour with magnets, we did not have any adequate results for comparison. As mentioned, it is difficult to predict the long time behaviour precisely, since in particular there, the measurements often yield results that vary enormously for the same fuse type. Furthermore, they depend significantly on the state of the fuse.

The observation that our computational results coincide better with the measurements if we add magnets, especially for the mean time behaviour, can be explained by the described theory in Section 9.3.1 (Measurement and Simulation Results - Self-Made Fuses). The oxidation process at the surface of the fuse element generates a tube around the melted material, which forces the material not to drop off immediately and not to interrupt the electric circuit. The attraction of the magnets prevents the generation of this oxidation tube, because the melted material is directly pulled out.

---

[7] In fact, these fuses consist of zinc, copper and titanium. Since the percentage of copper represents only 1.2 % and that of titanium only 0.2 %, the influence of these two materials is nearly negligable.

Thus, we propose to construct fuses with magnets near the fuse element in order to guarantee a better predictability of their blowing behaviour and to get more reliable information by our simplified computational approach without elaborative measurements.

9.5 Conclusion

Subject of this chapter was the computation and experimental validation of the blowing characteristics of fuses. We presented a simplified method based on heat power balances, and a more elaborative approach with exact geometries and finite elements. To validate those with experimental results, we performed measurements and determined characteristic curves of different fuse types. Furthermore, we examined the influence of attached cables, of the lengths of the fuse elements and their materials. Finally, we proposed an improved fuse design which excels by a better predictability of blowing times for larger electric currents.

The comparison to self-made fuses showed that our simplified model coincides well with our measurements, especially for the short time behaviour, if we add the melting time of a fuse to the heating time. Some discrepancies were detected for the mean and long time behaviour, which could practically be compensated, to the largest part, by integration of magnets near the fuse element.

On the other hand, we observed that, in contrast to the finite element simulations, for fuses composed of different materials, our simplified computational approach exhibits substantial defects. The behaviour of different layers, in particular heterogeneous materials, distinguishes enormously from that of homogeneous materials, which makes predictions of blowing times very difficult.

For future work, we intend to extend our simplified computational approach to take varying current densities into account as well as chemical reactions that occur for longer operation times. Furthermore, we will have to find a solution on how to handle non-homogeneous materials and how to predict their influence on the blowing behaviour. Via the finite element simulations which respect the geometry of the fuse element, we could try to find an improved design of the fuse element. This requires the application of shape optimization. For example, the fuse elements of the type Midi 25 have an S-form, those of Midi 30 a Z-form. It would be interesting to find out which of these shapes or others excel by a better blowing behaviour. A final research subject already in progress is how to determine the ageing process of fuses, which also has an impact on the heating and blowing characteristics.

10 Conclusion

In this thesis, we have introduced several techniques to model, to simulate and to optimize heat generation in cables and cable related components, caused by electric currents. These methods enable fast, accurate and robust thermal analysis of electric connecting structures of automotive applications. We first derived problem specific approaches for temperature determination in insulated single-core cables and transformed those to more complex systems like shielded cables and cable bundles. In addition, the influence of attached cables has been taken into account for computation of temperatures in current bars and fuses.

New aspects of this work were to analyse the mentioned cable specific approaches, to respect varying ambient temperatures and influences at the end of the wires on the temperature distribution in axial direction as well as to consider non-constant, time-dependent current profiles. Most of these approaches have been investigated concerning mathematical plausibility and compared to experimental measurements in order to ensure practical applicability. Since not all interesting effects could be examined by measurements, we additionally validated our computational approaches by finite element simulations. Thus, taking the example of cable bundles, we showed how our simplified approaches, which mostly excel by very short calculation times, can be used profitably and how to gain deeper insight by analysis with finite elements. Moreover, a new algorithm that allows to optimize the composition of multicables has been developed. Concerning thermal analysis of current bars and fuses, we presented adequate computational approaches, showed for concrete examples how to apply those and investigated influences of materials, dimensions, contact resistances, etc. For fuses, we concluded with a design proposition which enables more precise predictions of the blowing characteristics.

A main objective of this thesis was to demonstrate the benefits that simulation methods offer in the analysis of cables, compared to elaborative measurements. In fact, many measurements have already been replaced by simulations in different branches of engineering and industry. However, the cable industry behaves conservatively, still holds on to old, established norms and often rather believes in practical experiments. The complexity of the considered problems makes it necessary to reduce the effort of computations which is realized by simplified computational methods and adapted models in this work. Since reducing a model requires the knowledge of relevant and negligible influences, we always tried to plausibly justify our simplifications and to show how those affect the simulation results.

Further motivation to write this thesis was that, although cables and connecting structures often represent components of only secondary interest, they offer an enormous potential for optimization. In thermal analyses for cable manufacturers, we observed that many connecting structures exceed required dimensions by far in order to be on the safe side. Our presented computational methods contribute to find more appropriate dimensions of cables, cable harnesses and other components. Moreover, the analysis of multicables in this thesis and the application of our developed optimization algorithm show that decreases of maximum temperatures up to more than 20 % are possible just by simple means like varying the inner cable design. Additionally, the rise of the copper price in the last years forces manufacturers to diminish copper consumption, which could either be realized by a reduction of cross sections or by a replacement with other materials like aluminium.

The present work relates nearly exclusively to the thermal analysis of connecting structures. Further physical influences like the skin effect, electromagnetic compatibility (EMC), etc., are not respected, but they are often directly coupled. Taking those into account, investigating their influence and introducing adequate models as well as reduced computational methods will be subjects of future research. A further aspect to which hardly any attention has been paid yet, is the ageing of cables and fuses. Similar to Wöhler's curve in mechanics, we noticed that the blowing characteristics of fuses essentially depend on their state. A similar effect can also be observed for cables. It will be our next task to analyse the process of ageing of cables respectively of fuses and to describe it by appropriate, possibly reduced systems of equations.

For the analysis of cables, but also for the blowing behaviour of fuses and especially for current bars, contact resistances will have to be taken into account to guarantee more precise, realistic results. In particular, if we consider larger and more complex systems like current distribution boxes and entire motor systems, their influence has to be respected properly. Nevertheless, we will also try to find reduced models for these complex systems with the main challenge to be still sufficiently adequate. Optimizing current boxes or entire car sections will be an interesting task for the future as well as the application of our shape optimization approach for an optimized fuse design. We hope to be able to answer the question whether the S-, Z- or any other shape of a fuse element works most reliably.

A Appendix

A.1 Insulated Single-Core Cables

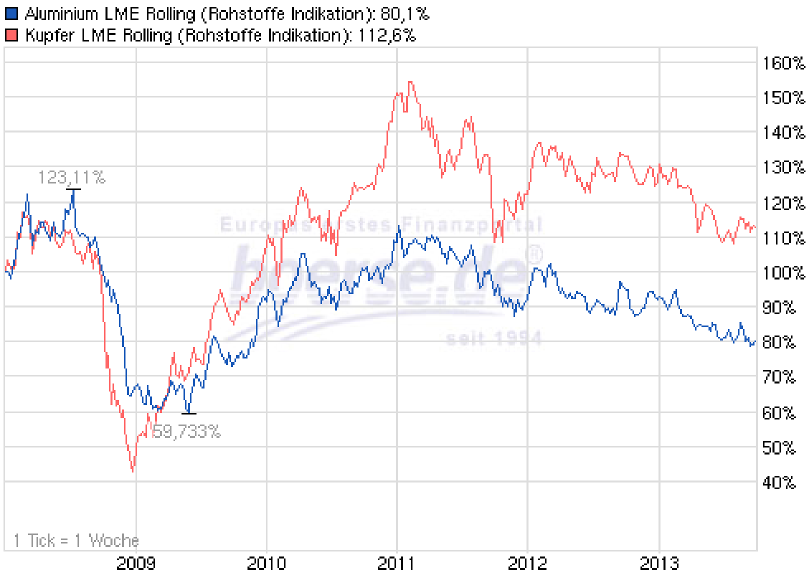

Fig. A.1: *Relative evolutions of copper (red line) and aluminium (blue line) prices in the years 2008-2013*[7] *(Image source: boerse.de).*

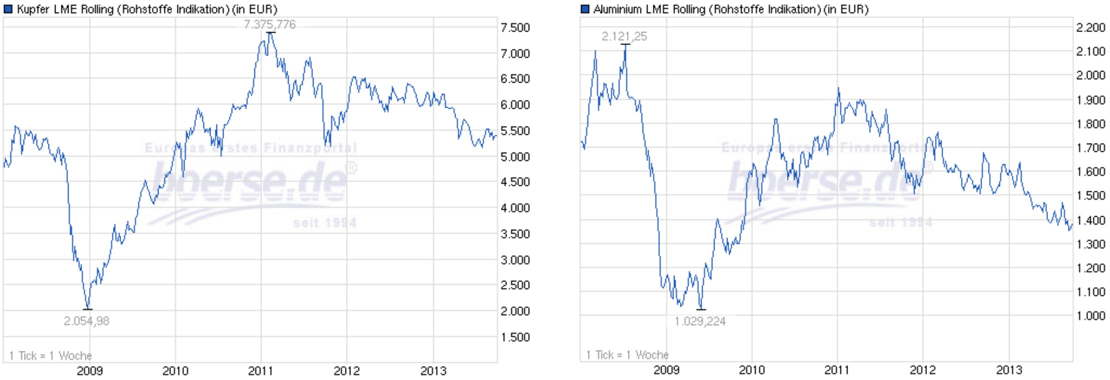

(a) Evolution of the copper price (Image source: boerse.de).

(b) Evolution of the aluminium price (Image source: boerse.de).

Fig. A.2: *Evolution of the copper and aluminium prices in the years 2008-2013*[7].

A.2 Multicables

A.2.1 Single Cable Parameters in Simulations and Measurements

In the scenarios INL, OUL and MCL, the single cable k is of type Tp_k, carries the electric current I_k, has a physical respectively geometrical cross sectional area A_k^{ph} respectively A_k^{ge}, a current density J_k^{ph} respectively J_k^{ge} and the initial template position P_k.

k	Tp_k	I_k (A)	A_k^{ph} (mm^2)	A_k^{ge} (mm^2)	J_k^{ph} (A/mm^2)	J_k^{ge} (A/mm^2)	$\mathrm{P}_k^{\mathrm{INL}}$	$\mathrm{P}_k^{\mathrm{OUL}}$	$\mathrm{P}_k^{\mathrm{MCL}}$
1	1	53.0	10.0	14.5	5.30	3.66	14	14	9
2	2	37.0	6.00	8.30	6.17	4.46	10	24	4
3	2	12.0	6.00	8.30	2.00	1.45	22	20	1
4	4	12.0	2.50	3.46	4.80	3.47	20	15	8
5	5	12.0	1.00	1.33	12.0	9.02	2	35	16
6	3	23.0	4.00	5.73	5.75	4.01	17	23	13
7	3	14.9	4.00	5.73	3.72	2.60	23	17	2
8	3	16.2	4.00	5.73	4.05	2.83	21	21	5
9	4	18.0	2.50	3.46	7.20	5.20	7	19	20
10	4	18.0	2.50	3.46	7.20	5.20	13	16	18
11	5	9.50	1.00	1.33	9.50	7.14	12	27	25
12	5	9.50	1.00	1.33	9.50	7.14	8	31	17
13	7	7.00	0.50	0.68	14.0	10.3	1	40	31
14	7	4.50	0.50	0.68	9.00	6.62	9	25	37
15	8	0.34	0.35	0.50	0.97	0.68	19	8	35
16	8	0.34	0.35	0.50	0.97	0.68	25	6	32
17	8	0.40	0.35	0.50	1.14	0.80	18	10	38
18	8	0.40	0.35	0.50	1.14	0.80	16	12	40
19	8	0.40	0.35	0.50	1.14	0.80	15	18	28
20	8	2.10	0.35	0.50	6.00	4.20	11	22	30
21	8	4.00	0.35	0.50	11.4	8.00	4	37	23
22	8	4.00	0.35	0.50	11.4	8.00	3	39	39
23	8	3.80	0.35	0.50	10.9	7.60	5	32	33
24	8	3.80	0.35	0.50	10.9	7.60	6	29	34
25	2	0.10	6.00	8.30	0.02	0.01	40	9	3
26	3	0.10	4.00	5.73	0.03	0.02	32	1	10
27	4	0.10	2.50	3.46	0.04	0.03	35	11	12
28	4	0.10	2.50	3.46	0.04	0.03	36	7	11
29	5	0.10	1.00	1.33	0.10	0.08	28	13	7
30	5	0.10	1.00	1.33	0.10	0.08	39	5	19
31	5	0.10	1.00	1.33	0.10	0.08	41	3	21
32	6	0.10	0.75	1.04	0.13	0.10	33	4	24
33	6	0.10	0.75	1.04	0.13	0.10	24	2	22

Tab. A.1: *Cable type, electric current, cross sectional area, current density and position of each single cable in the multicables of the three experimental setups INL, OUL, MCL.*

A.2.2 Computed and Measured Temperatures

The calculation results for the three scenarios compared to those of the measurements (MES) are listed in Table A.2, where $\varnothing$ summarizes the average temperature in the single cable cores ($\varnothing(T) := 1/N \sum_{k=1}^{N} T_k$ with T_k the measured resp. computed temperature in the centre of the single cable core), $\varnothing^{\mathrm{A}}$ the average temperatures of the single cable core weighted w.r.t. the cross sectional area ($\varnothing^{\mathrm{A}}(T) := \left(\sum_{k=1}^{N} T_k \cdot A_k^{\mathrm{ph}}\right) / \left(\sum_{k=1}^{N} A_k^{\mathrm{ph}}\right)$), max the maximum and min the minimum temperature in all single cables.

	Inner Layout			Outer Layout			Monte Carlo Layout		
k	MES	FEA	FPA	MES	FEA	FPA	MES	FEA	FPA
1	97.1	101.5	T^{cen} 94.0	92.4	90.0	T^{cen} 87.6	101.0	103.7	T^{cen} 98.7
2	101.2	102.9		91.4	91.0		100.4	102.3	
3	90.6	99.1		84.0	84.2		98.8	100.7	
4	91.4	96.7		87.1	87.7		97.3	101.4	
5	102.9	107.4		86.9	86.2		94.8	100.7	
6	96.0	100.8		91.0	88.0		95.1	99.3	
7	92.3	93.7		85.8	85.8		97.6	98.4	
8	95.0	97.1		85.0	86.6		97.4	99.5	
9	101.2	104.9		87.0	85.2		93.8	98.7	
10	100.1	103.6		88.5	87.6		97.8	101.4	
11	99.2	100.2		86.4	87.3		92.9	97.6	
12	100.3	104.9	T^{in} 86.7	84.0	85.9	T^{in} 80.9	96.6	103.1	T^{in} 91.7
13	102.6	106.9		90.0	90.0		96.6	102.6	
14	99.6	101.8		91.7	87.1		91.1	94.9	
15	96.3	97.6		89.0	87.0		92.5	95.9	
16	95.6	93.1		90.5	85.4		94.3	100.6	
17	99.2	98.9		87.7	86.6		93.2	94.4	
18	97.0	100.8		90.8	88.9		94.5	95.5	
19	97.5	97.4		87.0	85.1		94.1	97.5	
20	98.3	95.8		88.4	87.4		96.6	99.7	
21	101.3	103.8		87.1	86.7		93.8	97.4	
22	100.3	106.7		90.4	88.7		93.1	95.7	
23	101.4	104.4		83.2	83.8		93.1	98.1	
24	101.8	96.2		83.8	85.3		93.3	97.9	
25	88.5	96.7		88.4	86.0		100.2	99.7	
26	92.9	96.4		90.6	87.5		96.4	99.8	
27	89.5	90.4		88.8	88.1		93.1	95.4	
28	88.2	91.4		88.5	87.9		95.3	97.7	
29	93.1	100.0		92.2	88.9		95.8	96.1	
30	91.9	91.3		90.5	89.1		94.6	99.7	
31	89.0	95.8		89.8	87.2		92.9	98.3	
32	92.4	94.2		89.1	86.0		94.4	97.5	
33	93.0	95.5		91.5	88.1		92.3	95.3	
$\varnothing$	96.3	99.0	94.0	88.4	87.2	87.6	95.3	98.7	98.7
$\varnothing^{\mathrm{A}}$	94.8	98.8	94.0	88.8	87.5	87.6	97.5	100.1	98.7
max	102.9	107.4	-	92.4	91.0	-	101.0	103.7	-
min	88.2	90.4	86.7	83.2	83.8	80.9	91.1	94.4	91.7

Tab. A.2: *Comparison of measurement and simulation results, computed with finite elements (FEA) and the fixed point approach (FPA) for the three test scenarios. All quantities are indicated in* °C.

A.2.3 Computed and Measured Temperature Differences

In Table A.3, the single cables are ordered according to their initial template positions. E.g., this means in the first line that the single cables with number 13 for INL, number 26 for OUL and number 3 for MCL are assigned to template position 1. The measured resp. via FEM computed temperatures are indicated minus ambient temperatures and ΔT denotes the absolute difference between measurement and simulation for each single cable. The notations $\varnothing$, $\varnothing^{\mathrm{A}}$, max and min are defined like in Table A.2.

	Inner Layout				Outer Layout				Monte Carlo Layout		
k	MES	FEA	ΔT	k	MES	FEA	ΔT	k	MES	FEA	ΔT
13	69.4	73.7	4.3	26	64.8	61.7	3.1	3	62.3	64.2	1.9
5	69.7	74.2	4.5	33	65.7	62.3	3.4	7	60.9	63.0	2.1
22	67.1	73.5	6.4	31	64.0	61.4	2.6	25	63.7	63.2	0.5
21	68.1	70.6	2.5	32	63.3	60.2	3.1	2	63.9	65.8	1.9
23	68.2	71.2	3.0	30	64.7	63.3	1.4	8	60.9	63.0	2.1
24	68.6	63.0	5.6	16	64.7	59.6	5.1	29	59.3	59.6	0.3
9	68.0	71.7	3.7	28	62.7	62.1	0.6	4	60.8	64.9	4.1
12	67.1	71.7	4.6	15	63.2	61.2	2.0	1	64.5	67.2	2.7
14	66.4	68.6	2.2	25	62.6	60.2	2.4	26	59.9	63.3	3.4
2	68.0	69.7	1.7	17	61.9	60.8	1.1	28	58.8	61.2	2.4
20	65.1	62.6	2.5	27	63.0	62.3	0.7	27	56.6	58.9	2.3
11	66.0	67.0	1.0	18	65.0	63.1	1.9	6	58.6	62.8	4.2
10	66.9	70.4	3.5	29	66.4	62.1	4.3	5	58.3	64.2	5.9
1	63.9	68.3	4.4	1	66.6	64.2	2.4	12	60.1	66.6	6.5
19	64.3	64.2	0.1	4	61.3	61.9	0.6	10	61.3	64.9	3.6
18	63.8	67.6	3.8	10	62.7	61.8	0.9	30	58.1	63.2	5.1
6	62.8	67.6	4.8	7	60.0	60.0	0.0	9	57.3	62.2	4.9
17	66.0	65.7	0.3	19	61.2	59.3	1.9	31	56.4	61.8	5.4
15	63.1	64.4	1.3	9	61.2	59.4	1.8	33	55.8	58.8	3.0
4	58.2	63.5	5.3	3	58.2	58.4	0.2	21	57.3	60.9	3.6
8	61.8	63.9	2.1	8	59.2	60.8	1.6	32	57.9	61.0	3.1
3	57.4	65.9	8.5	20	62.6	61.6	1.0	11	56.4	61.1	4.7
7	59.1	60.5	1.4	6	65.2	62.2	3.0	19	57.6	61.0	3.4
33	59.8	62.3	2.5	2	65.6	65.2	0.4	20	60.1	63.2	3.1
16	62.4	59.9	2.5	14	65.9	61.3	4.6	13	60.1	66.1	6.0
29	59.9	66.8	6.9	11	60.6	61.5	0.9	16	57.8	64.1	6.3
26	59.7	63.2	3.5	24	58.0	59.5	1.5	23	56.6	61.6	5.0
32	59.2	61.0	1.8	12	58.2	60.1	1.9	24	56.8	61.4	4.6
27	56.3	57.2	0.9	23	57.4	58.0	0.6	15	56.0	59.4	3.4
28	55.0	58.2	3.2	5	61.1	60.4	0.7	14	54.6	58.4	3.8
30	58.7	58.1	0.6	21	61.3	60.9	0.4	17	56.7	57.9	1.2
25	55.3	63.5	8.2	22	64.6	62.9	1.7	22	56.6	59.2	2.6
31	55.8	62.6	6.8	13	64.2	64.2	0.0	18	58.0	59.0	1.0
$\varnothing$	63.1	65.8	3.5		62.6	61.4	1.7		58.8	62.2	3.4
$\varnothing^{\mathrm{A}}$	61.6	65.6	4.1		63.0	61.7	1.6		61.0	63.6	2.7
max	69.7	74.2	8.5		66.6	65.2	5.1		64.5	67.2	6.5
min	55.0	57.2	0.1		57.4	58.0	0.0		54.6	57.9	0.3

Tab. A.3: *Comparison of measured temperatures and (relative) temperatures computed by FEM for the three test scenarios. All temperatures minus ambient temperatures are indicated in K.*

A.2.4 Sensitivity Analysis with the Formal Lagrange Approach

We present an alternative approach to derive an optimality system for problem (7.33), applying the formal Lagrange technique [72, 130]. By taking corresponding variations to zero, one obtains an adjoint system and the necessary condition for a stationary point, namely the shape gradient to be equal to zero. In the following, we suppose the underlying functions to be sufficiently smooth to ensure well-posedness of all operations.

This derivation of an optimality system is formal. Thus, some mathematical details like e.g. existence of and function spaces for the adjoint variables $p,\ p_1,\ p_2$ are not investigated in detail. However, the approach enables to systematically derive an adjoint system. For that reason, we show this alternative approach.

Formal Lagrange Approach

We define the Lagrangian $\mathcal{L}$ for (7.33) by subtracting integrals over the equation on the domain and the exterior boundary from the objective function $J(\Omega)$. As mentioned, the interface conditions are not necessary for a concise problem formulation. Consequently, they and also the geometrical constraints are not considered in the Lagrangian. Denoting the Lagrange multipliers by p_1, p_2, the Lagrangian reads as

$$\begin{aligned}\mathcal{L}\left(T,\Omega,p_1,p_2\right) = J\left(\Omega\right) &- \int\limits_{\Omega^{\mathrm{MC}}} \left(\nabla\cdot\left(\lambda\,\nabla T\right) + cT + f\right) p_1 \,\mathrm{d}\mathbf{x} \\ &- \int\limits_{\Gamma^{\mathrm{ex}}} \left(\lambda^{\mathrm{ex}}\frac{\partial T}{\partial \mathbf{n}} + \alpha(T)\left(T - T_1\right)\right) p_2 \,\mathrm{d}\sigma.\end{aligned}$$

Dividing Ω^{MC} into subdomains and applying Green's formula on each subdomain leads, in view of the given jump conditions at the interfaces, to

$$\begin{aligned}&\mathcal{L}\left(T,\Omega,p_1,p_2\right) \\ &= J(\Omega) - \int\limits_{\Omega^{\mathrm{MC}}} \left(\nabla\cdot\left(\lambda\,\nabla p_1\right) + c\,p_1\right) T \,\mathrm{d}\mathbf{x} - \int\limits_{\Omega^{\mathrm{MC}}} f\,p_1 \,\mathrm{d}\mathbf{x} - \int\limits_{\Gamma^{\mathrm{ex}}} \lambda^{\mathrm{ex}}\frac{\partial T}{\partial \mathbf{n}} p_2 \,\mathrm{d}\sigma \\ &- \int\limits_{\Gamma^{\mathrm{ex}}} \alpha\left(T\right)\left(T - T_1\right) p_2 \,\mathrm{d}\sigma - \int\limits_{\Gamma^{\mathrm{ex}}} \lambda^{\mathrm{ex}}\frac{\partial T}{\partial \mathbf{n}} p_1 \,\mathrm{d}\sigma + \int\limits_{\Gamma^{\mathrm{ex}}} \lambda^{\mathrm{ex}}\frac{\partial p_1}{\partial \mathbf{n}} T \,\mathrm{d}\sigma \\ &- \sum_{\iota\in\Gamma^{\mathrm{int}}} \left[\int\limits_{\iota} \lambda^{\mathrm{e}}\frac{\partial T^{\mathrm{e}}}{\partial \mathbf{n}} \left(p_1^{\mathrm{e}} - p_1^{\mathrm{i}}\right) \,\mathrm{d}\sigma - \int\limits_{\iota} T^{\mathrm{e}}\left(\lambda^{\mathrm{e}}\frac{\partial p_1^{\mathrm{e}}}{\partial \mathbf{n}} - \lambda^{\mathrm{i}}\frac{\partial p_1^{\mathrm{i}}}{\partial \mathbf{n}}\right) \,\mathrm{d}\sigma \right].\end{aligned}$$

In this expression, taking the outer trace at the interior interface $\iota\in\Gamma^{\mathrm{int}}$ is indicated by the suffix $\cdot^{\mathrm{e}}$, whereas taking the inner trace at the interior interface $\iota\in\Gamma^{\mathrm{int}}$ is indicated by the suffix $\cdot^{\mathrm{i}}$.

Let $\left(\bar{T},\bar{\Omega}\right)$ be an optimal pair of (7.33). Then, the first variations of $\mathcal{L}$ w.r.t. p_1, p_2, T and Ω in the directions h_{p_1}, h_{p_2}, h_T and h_Ω are all zero, i.e., the following first order optimality conditions hold:

$$\begin{aligned}\mathcal{L}_{p_1}\left(\bar{T},\bar{\Omega},p_1,p_2\right) h_{p_1} &= 0,\\ \mathcal{L}_{p_2}\left(\bar{T},\bar{\Omega},p_1,p_2\right) h_{p_2} &= 0,\\ \mathcal{L}_{T}\left(\bar{T},\bar{\Omega},p_1,p_2\right) h_{T} &= 0,\\ \mathcal{L}_{\Omega}\left(\bar{T},\bar{\Omega},p_1,p_2\right) h_{\Omega} &= 0.\end{aligned} \tag{A.1}$$

The variation of $\mathcal{L}$ w.r.t. the Lagrange multipliers yields the state system (7.31), the variation w.r.t. the temperature provides the adjoint system and, by the variation w.r.t. the domain, we obtain the necessary optimality condition for stationary points (cf. [72]).

Adjoint System

Taking the first variation of $\mathcal{L}$ w.r.t. the temperature T in the direction $h_T \in H^1(\Omega^{\mathrm{MC}})$ to zero provides the identity

$$\begin{aligned}
0 &= \mathcal{L}_T\left(\bar{T}, \bar{\Omega}, p_1, p_2\right) h_T \\
&= \int\limits_{\Omega^{\mathrm{MC}}} \frac{\partial j}{\partial T}(\mathbf{x}, \bar{T}) h_T \,\mathrm{d}\mathbf{x} - \int\limits_{\Omega^{\mathrm{MC}}} \left(\nabla \cdot (\lambda\, \nabla p_1) + c\, p_1\right) h_T \,\mathrm{d}\mathbf{x} \\
&- \int\limits_{\Gamma^{\mathrm{ex}}} \lambda^{\mathrm{ex}} \frac{\partial h_T}{\partial \mathbf{n}} p_2 \,\mathrm{d}\sigma - \int\limits_{\Gamma^{\mathrm{ex}}} \left(\alpha'(\bar{T})\left(\bar{T} - T_1\right) + \alpha(\bar{T})\right) h_T\, p_2 \,\mathrm{d}\sigma \\
&- \int\limits_{\Gamma^{\mathrm{ex}}} \lambda^{\mathrm{ex}} \frac{\partial h_T}{\partial \mathbf{n}} p_1 \,\mathrm{d}\sigma + \int\limits_{\Gamma^{\mathrm{ex}}} \lambda^{\mathrm{ex}} \frac{\partial p_1}{\partial \mathbf{n}} h_T \,\mathrm{d}\sigma \\
&- \sum_{\iota \in \Gamma^{\mathrm{int}}} \left[\int\limits_{\iota} \lambda^{\mathrm{e}} \frac{\partial h_T^{\mathrm{e}}}{\partial \mathbf{n}} \left(p_1^{\mathrm{e}} - p_1^{\mathrm{i}}\right) \mathrm{d}\sigma - \int\limits_{\iota} h_T^{\mathrm{e}} \left(\lambda^{\mathrm{e}} \frac{\partial p_1^{\mathrm{e}}}{\partial \mathbf{n}} - \lambda^{\mathrm{i}} \frac{\partial p_1^{\mathrm{i}}}{\partial \mathbf{n}}\right) \mathrm{d}\sigma \right].
\end{aligned}$$

If it holds $h_T \in C_0^\infty(\Omega^{\mathrm{MC}})$ with $h_T = \frac{\partial h_T}{\partial \mathbf{n}} = 0$ on all $\iota \in \Gamma^{\mathrm{int}}$, one obtains

$$\int\limits_{\Omega^{\mathrm{MC}}} \frac{\partial j}{\partial T}(\mathbf{x}, \bar{T}) h_T \,\mathrm{d}\mathbf{x} = \int\limits_{\Omega^{\mathrm{MC}}} \left(\nabla \cdot (\lambda \nabla p_1) + c\, p_1\right) h_T \,\mathrm{d}\mathbf{x},$$

which implies that p_1 satisfies the partial differential equation

$$\nabla \cdot (\lambda \nabla p_1) + c\, p_1 = \frac{\partial j}{\partial T}(\cdot, \bar{T}) \;\text{ in }\; \Omega^{\mathrm{MC}} \setminus \Gamma^{\mathrm{int}}. \tag{A.2}$$

To derive the associated boundary conditions, we consider $h_T \in H_0^1(\Omega^{\mathrm{MC}})$ such that $h_T = \frac{\partial h_T}{\partial \mathbf{n}} = 0$ on all $\iota \in \Gamma^{\mathrm{int}}$ and $\frac{\partial h_T}{\partial \mathbf{n}}$ arbitrary on Γ^{ex}. This yields

$$-\int\limits_{\Gamma^{\mathrm{ex}}} \lambda^{\mathrm{ex}} \frac{\partial h_T}{\partial \mathbf{n}} p_1 \,\mathrm{d}\sigma - \int\limits_{\Gamma^{\mathrm{ex}}} \lambda^{\mathrm{ex}} \frac{\partial h_T}{\partial \mathbf{n}} p_2 \,\mathrm{d}\sigma = 0,$$

which means that $p_1 = -p_2$. We define $p := p_1 = -p_2$ and apply next an arbitrary $h_T \in H^1(\Omega^{\mathrm{MC}})$ and $h_T = \frac{\partial h_T}{\partial \mathbf{n}} = 0$ on all $\iota \in \Gamma^{\mathrm{int}}$ to provide

$$\int\limits_{\Gamma^{\mathrm{ex}}} \lambda^{\mathrm{ex}} \frac{\partial p}{\partial \mathbf{n}} h_T \,\mathrm{d}\sigma + \int\limits_{\Gamma^{\mathrm{ex}}} \left(\alpha'(\bar{T})\left(\bar{T} - T_1\right) + \alpha(\bar{T})\right) h_T\, p \,\mathrm{d}\sigma = 0.$$

Hence, we arrive at the Robin boundary condition

$$\lambda^{\mathrm{ex}} \frac{\partial p}{\partial \mathbf{n}} + \left(\alpha'(\bar{T})\left(\bar{T} - T_1\right) + \alpha(\bar{T})\right) p = 0 \;\text{ on }\; \Gamma^{\mathrm{ex}}. \tag{A.3}$$

Let $\iota \in \Gamma^{\text{int}}$ be an arbitrary, but fixed and connected interface boundary. By choosing $h_T \in H^1(\Omega^{\text{MC}})$ such that $h_T = 0$ on ι and $h_T = \frac{\partial h_T}{\partial \mathbf{n}} = 0$ on all $\tilde{\iota} \in \Gamma^{\text{int}} \setminus \iota$, we get the Dirichlet jump condition

$$p^{\text{e}} = p^{\text{i}} \quad \Leftrightarrow \quad \big[p\big]_{\pm} = 0 \qquad \text{on } \iota \in \Gamma^{\text{int}}. \tag{A.4}$$

Finally, for $\iota \in \Gamma^{\text{int}}$ arbitrary, fixed and connected, the choice $h_T \in H^1(\Omega^{\text{MC}})$ such that $h_T = \frac{\partial h_T}{\partial \mathbf{n}} = 0$ on all $\tilde{\iota} \in \Gamma^{\text{int}} \setminus \iota$ yields the Neumann jump condition at the interface ι

$$\lambda^{\text{e}} \frac{\partial p_1^{\text{e}}}{\partial \mathbf{n}} = \lambda^{\text{i}} \frac{\partial p_1^{\text{i}}}{\partial \mathbf{n}} \quad \Leftrightarrow \quad \left[\lambda \frac{\partial p}{\partial \mathbf{n}}\right]_{\pm} = 0 \quad \text{on } \iota \in \Gamma^{\text{int}}. \tag{A.5}$$

Since $\iota \in \Gamma^{\text{int}}$ is arbitrary, the interface conditions (A.4) and (A.5) hold for all $\iota \in \Gamma^{\text{int}}$. Thus, combining (A.2)–(A.5), the adjoint p solves the following system and corresponds to $p = p_1 = -p_2$:

$$\boxed{\begin{aligned} -\nabla \cdot (\lambda \nabla p) - c \cdot p &= -\frac{\partial j}{\partial T}(\cdot, T) \quad \text{in } \Omega^{\text{MC}} \setminus \Gamma^{\text{int}}, \\ \lambda^{\text{ex}} \frac{\partial p}{\partial \mathbf{n}} + \big(\alpha'(T)(T - T_1) + \alpha(T)\big) p &= 0 \quad \text{on } \Gamma^{\text{ex}}, \\ \big[p\big]_{\pm} = 0 \quad \text{and} \quad \left[\lambda \frac{\partial p}{\partial \mathbf{n}}\right]_{\pm} &= 0 \quad \text{on } \iota \in \Gamma^{\text{int}}. \end{aligned}} \tag{A.6}$$

Shape Gradient

We reformulate (7.33) equivalently (cf. [72]) by

$$\min_{\Omega \in \mathcal{O}_{\text{ad}}, T} \Big\{ \max_{p} \mathcal{L}(T, \Omega, p) \Big\}. \tag{A.7}$$

The theory of min-max problems [109] provides

$$\delta J(\Omega)\,[\mathbf{V}] = \mathcal{L}_{\Omega}\,(T, \Omega, p)\, h_{\Omega} \;\; \text{with} \;\; \mathbf{V} = h_{\Omega}$$

at the solution of the min-max formulation (A.7). For an optimal interior point, the necessary optimality condition

$$\delta J(\Omega)\,[\mathbf{V}] = 0$$

has to be fulfilled for all directions $\mathbf{V}$. The Hadamard representation of the shape gradient for (OptMC) reads as follows and is derived in the same manner as in Section 7.6.3 (Shape Gradient):

$$\boxed{\begin{aligned} \delta J(\Omega)\,[\mathbf{V}] = \sum_{\iota \in \Gamma^{\text{int}}} \int_{\iota} \langle \mathbf{V}, \mathbf{n} \rangle \Big\{ & \nabla_{\tau} p_{\text{e}} \nabla_{\tau} T_{\text{e}} [\lambda]_{\pm} \\ & - p^{\text{e}} \left([c]_{\pm}\, T^{\text{e}} + [f]_{\pm} \right) - \lambda^{\text{e}} \frac{\partial p^{\text{e}}}{\partial \mathbf{n}} \left[\frac{\partial T}{\partial \mathbf{n}} \right]_{\pm} \Big\}\, \mathrm{d}\sigma. \end{aligned}} \tag{A.8}$$

A.2.5 Optimization of Multicables – Statistics

Single Cable No.	I_k (A)	A_k^{ge} (mm^2)	J_k^{ge} (A/mm^2)
1	53.00	14.5	3.65
2	82.00	8.30	9.89
3	12.00	8.30	1.45
4	12.00	3.46	3.46
5	52.00	8.30	6.27
6	43.00	5.73	7.51
7	14.88	5.73	2.60
8	16.20	5.73	2.83
9	18.00	3.46	5.20
10	18.00	3.46	5.20
11	9.50	1.33	7.16
12	9.50	1.33	7.16
13	10.00	0.68	14.72
14	4.50	0.68	6.62
15	0.34	0.50	0.68

Tab. A.4: *Currents and cross sectional areas of a multicable with 15 single cables.*

Generation	Individual No.								
No.	1	2	3	4	5	6	7	8	9
0	154.0	136.7	137.7	139.8	147.0	141.0	157.5	136.5	140.7
1	136.5	143.6	140.3	141.5	147.9	142.8	142.4	136.2	143.1
2	136.2	141.7	142.3	147.8	140.3	142.0	137.0	142.3	142.8
3	136.2	135.8	137.6	142.6	135.8	150.8	147.8	144.2	149.6
4	135.8	134.9	138.8	140.6	138.8	140.1	146.4	146.1	137.3
5	134.9	137.0	141.8	135.0	146.6	141.7	140.4	143.4	140.2

Tab. A.5: *Fitness values of all individuals for 6 generations in the genetic algorithm for multicables with 15 single cables.*

Generation	Individual No.								
No.	1	2	3	4	5	6	7	8	9
0	99.05	96.59	99.64	96.48	97.53	96.76	95.81	97.37	93.76
1	93.76	95.39	96.30	99.12	93.09	95.68	92.61	95.13	98.45
2	92.61	99.65	98.34	94.54	96.37	97.87	97.88	97.33	98.70
3	92.61	96.90	97.92	92.43	96.00	95.86	94.92	95.04	98.16
4	92.43	95.97	95.50	95.75	96.59	96.09	99.61	96.75	95.79
5	92.43	98.18	98.11	93.81	97.45	99.12	98.65	97.04	96.89

Tab. A.6: *Fitness values of all individuals for 6 generations in the optimization progress of the genetic algorithm for a multicable with 33 single cables.*

A.3 Current Bars

A.3.1 Calculation Tool

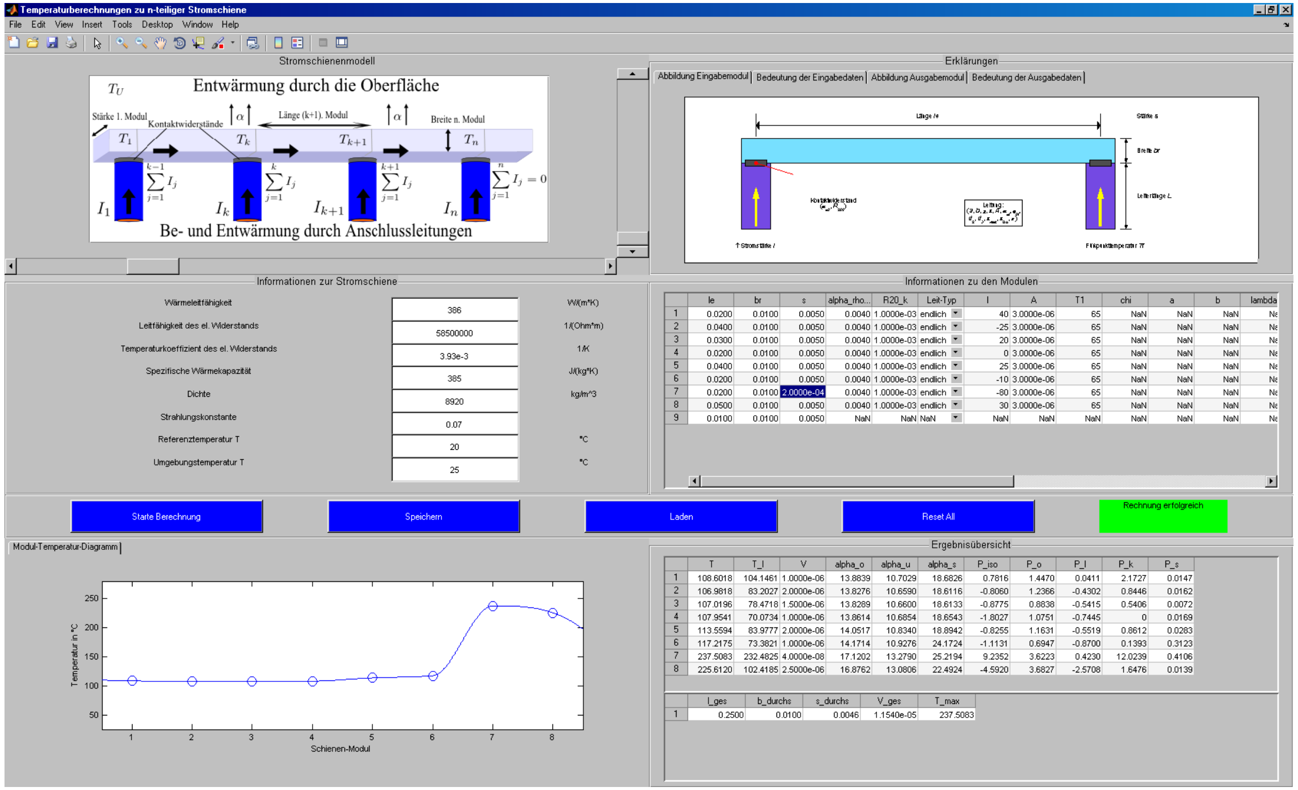

Informationen zur Stromschiene

Wärmeleitfähigkeit	386	W/(m*K)
Leitfähigkeit des el. Widerstands	58500000	1/(Ohm*m)
Temperaturkoeffizient des el. Widerstands	3.93e-3	1/K
Spezifische Wärmekapazität	385	J/(kg*K)
Dichte	8920	kg/m^3
Strahlungskonstante	0.07	
Referenztemperatur T	20	°C
Umgebungstemperatur T	25	°C

Informationen zu den Modulen

	le	br	s	alpha_rho...	R20_k	Leit-Typ	I	A	T1	chi	a	b	lambda
1	0.0200	0.0100	0.0050	0.0040	1.0000e-03	endlich	40	3.0000e-06	65	NaN	NaN	NaN	Na
2	0.0400	0.0100	0.0050	0.0040	1.0000e-03	endlich	-25	3.0000e-06	65	NaN	NaN	NaN	Na
3	0.0300	0.0100	0.0050	0.0040	1.0000e-03	endlich	20	3.0000e-06	65	NaN	NaN	NaN	Na
4	0.0200	0.0100	0.0050	0.0040	1.0000e-03	endlich	0	3.0000e-06	65	NaN	NaN	NaN	Na
5	0.0400	0.0100	0.0050	0.0040	1.0000e-03	endlich	25	3.0000e-06	65	NaN	NaN	NaN	Na
6	0.0200	0.0100	0.0050	0.0040	1.0000e-03	endlich	-10	3.0000e-06	65	NaN	NaN	NaN	Na
7	0.0200	0.0100	2.0000e-04	0.0040	1.0000e-03	endlich	-80	3.0000e-06	65	NaN	NaN	NaN	Na
8	0.0500	0.0100	0.0050	0.0040	1.0000e-03	endlich	30	3.0000e-06	65	NaN	NaN	NaN	Na
9	0.0100	0.0100	0.0050	NaN	NaN	NaN	NaN	NaN	NaN	NaN	NaN	NaN	Na

Ergebnisübersicht

	T	T_l	V	alpha_o	alpha_u	alpha_s	P_iso	P_o	P_l	P_k	P_s
1	108.6018	104.1461	1.0000e-06	13.8839	10.7029	18.6826	0.7816	1.4470	0.0411	2.1727	0.0147
2	106.9818	83.2027	2.0000e-06	13.8276	10.6590	18.6116	-0.8060	1.2366	-0.4302	0.8446	0.0162
3	107.0196	78.4718	1.5000e-06	13.8289	10.6600	18.6133	-0.8775	0.8838	-0.5415	0.5406	0.0072
4	107.9541	70.0734	1.0000e-06	13.8614	10.6854	18.6543	-1.8027	1.0751	-0.7445	0	0.0169
5	113.5594	83.9777	2.0000e-06	14.0517	10.8340	18.8942	-0.8255	1.1631	-0.5519	0.8612	0.0283
6	117.2175	73.3821	1.0000e-06	14.1714	10.9276	24.1724	-1.1131	0.6947	-0.8700	0.1393	0.3123
7	237.5083	232.4825	4.0000e-08	17.1202	13.2790	25.2194	9.2352	3.6223	0.4230	12.0239	0.4106
8	225.6120	102.4185	2.5000e-06	16.8762	13.0806	22.4924	-4.5920	3.6827	-2.5708	1.6476	0.0139

	l_ges	b_durchs	s_durchs	V_ges	T_max
1	0.2500	0.0100	0.0046	1.1540e-05	237.5083

Fig. A.3: *Graphical user interface of the temperature calculation tool for current bars.*

A.3.2 Measurement Results

		100 A		
Meas. No.	1	2	3	Mean Value
$I(\mathrm{A})$	100.00	100.40	100.40	**100.27**
$T_{\mathrm{amb}}(^\circ\mathrm{C})$	22.98	23.30	22.98	**23.09**
$T_{\mathrm{f},1}(^\circ\mathrm{C})$	44.27	43.65	43.53	**43.82**
$T_{\mathrm{f},2}(^\circ\mathrm{C})$	43.66	43.14	43.06	**43.29**
$T_{S_1}(^\circ\mathrm{C})$	50.12	50.08	48.74	**49.65**
$T_{S_2}(^\circ\mathrm{C})$	50.07	50.12	49.02	**49.74**
$T_{S_3}(^\circ\mathrm{C})$	50.87	50.66	49.35	**50.29**
$T_{S_4}(^\circ\mathrm{C})$	52.16	52.16	51.07	**51.80**
$T_{S_5}(^\circ\mathrm{C})$	52.24	52.38	51.41	**52.01**
$R_1(\mu\Omega)$	144.74	144.12	144.04	**144.30**
$R_2(\mu\Omega)$	158.02	157.35	157.29	**157.55**

Tab. A.7: *Measurement results for 100 A.*

		150 A		
Meas. No.	1	2	3	Mean Value
$I(\mathrm{A})$	150.20	150.70	150.60	**150.50**
$T_{\mathrm{amb}}(^\circ\mathrm{C})$	21.45	23.05	23.81	**22.77**
$T_{\mathrm{f},1}(^\circ\mathrm{C})$	66.70	66.72	68.07	**67.16**
$T_{\mathrm{f},2}(^\circ\mathrm{C})$	65.64	65.56	68.66	**66.62**
$T_{S_1}(^\circ\mathrm{C})$	77.99	79.48	81.03	**79.50**
$T_{S_2}(^\circ\mathrm{C})$	77.93	80.11	81.31	**79.78**
$T_{S_3}(^\circ\mathrm{C})$	80.19	80.81	82.41	**81.14**
$T_{S_4}(^\circ\mathrm{C})$	83.41	84.65	85.59	**84.55**
$T_{S_5}(^\circ\mathrm{C})$	83.27	84.83	85.42	**84.51**
$R_1(\mu\Omega)$	148.40	148.15	148.33	**148.29**
$R_2(\mu\Omega)$	162.69	162.35	162.35	**162.46**

Tab. A.8: *Measurement results for 150 A.*

		175 A		
Meas. No.	1	2	3	Mean Value
$I(\mathrm{A})$	175.70	175.60	175.60	**175.63**
$T_{\mathrm{amb}}(^\circ\mathrm{C})$	23.68	23.59	24.00	**23.76**
$T_{\mathrm{f},1}(^\circ\mathrm{C})$	81.56	82.77	84.11	**82.81**
$T_{\mathrm{f},2}(^\circ\mathrm{C})$	78.92	80.65	85.40	**81.66**
$T_{S_1}(^\circ\mathrm{C})$	99.37	99.42	100.31	**99.70**
$T_{S_2}(^\circ\mathrm{C})$	100.55	100.15	101.06	**100.58**
$T_{S_3}(^\circ\mathrm{C})$	101.05	101.43	103.34	**101.94**
$T_{S_4}(^\circ\mathrm{C})$	106.99	106.15	107.67	**106.93**
$T_{S_5}(^\circ\mathrm{C})$	106.54	106.02	107.55	**106.70**
$R_1(\mu\Omega)$	151.02	150.89	151.07	**151.00**
$R_2(\mu\Omega)$	165.48	165.46	165.66	**165.53**

Tab. A.9: *Measurement results for 175 A.*

		200 A		
Meas. No.	1	2	3	Mean Value
$I(\mathrm{A})$	200.70	200.80	200.70	**200.73**
$T_{\mathrm{amb}}(^\circ\mathrm{C})$	24.27	23.47	23.74	**23.83**
$T_{\mathrm{f},1}(^\circ\mathrm{C})$	98.89	98.08	100.87	**99.28**
$T_{\mathrm{f},2}(^\circ\mathrm{C})$	97.14	98.08	98.30	**97.84**
$T_{S_1}(^\circ\mathrm{C})$	122.09	121.39	121.34	**121.61**
$T_{S_2}(^\circ\mathrm{C})$	123.66	122.44	122.90	**123.00**
$T_{S_3}(^\circ\mathrm{C})$	126.26	124.23	122.78	**124.42**
$T_{S_4}(^\circ\mathrm{C})$	132.39	130.71	130.83	**131.31**
$T_{S_5}(^\circ\mathrm{C})$	131.43	129.80	129.90	**130.38**
$R_1(\mu\Omega)$	154.48	154.14	154.21	**154.28**
$R_2(\mu\Omega)$	169.06	168.82	168.72	**168.87**

Tab. A.10: *Measurement results for 200 A.*

		225 A		
Meas. No.	1	2	3	Mean Value
$I(\mathrm{A})$	224.90	225.90	225.70	**225.50**
$T_{\mathrm{amb}}(^\circ\mathrm{C})$	23.35	22.96	24.14	**23.48**
$T_{\mathrm{f},1}(^\circ\mathrm{C})$	115.49	119.30	121.71	**118.83**
$T_{\mathrm{f},2}(^\circ\mathrm{C})$	114.42	115.19	122.22	**117.28**
$T_{S_1}(^\circ\mathrm{C})$	144.27	144.54	147.19	**145.34**
$T_{S_2}(^\circ\mathrm{C})$	148.28	147.42	149.04	**148.25**
$T_{S_3}(^\circ\mathrm{C})$	151.49	147.75	151.11	**150.12**
$T_{S_4}(^\circ\mathrm{C})$	159.73	157.57	158.99	**158.76**
$T_{S_5}(^\circ\mathrm{C})$	158.31	156.17	157.25	**157.24**
$R_1(\mu\Omega)$	158.78	157.93	158.25	**158.32**
$R_2(\mu\Omega)$	173.56	172.55	172.66	**172.92**

Tab. A.11: *Measurement results for 225 A.*

A.4 Fuses

A.4.1 Melting Time of the Fuse Element

The integral

$$t_{\text{melt}} = \int\limits_{0}^{A_e} \frac{\Theta \; (\kappa_1 A_e + (\kappa_2 - \kappa_1) A_2) \; \mathrm{d}A_2}{I^2 - P'_\alpha \; (\kappa_1 A_e + (\kappa_2 - \kappa_1) A_2)}$$

has to be computed. Written equivalently by

$$t_{\text{melt}} = \int\limits_{0}^{A_e} \frac{\Theta(\kappa_2 - \kappa_1) A_2 + \Theta \kappa_1 A_e}{P'_\alpha (\kappa_1 - \kappa_2) A_2 + I^2 - P'_\alpha \kappa_1 A_e} \; \mathrm{d}A_2,$$

we have the same structure as given in [13, p. 298]

$$\int \frac{ax + b}{fx + g} = \frac{ax}{f} + \frac{bf - ag}{f^2} \; \ln{(fx + g)} + C.$$

Thus, we obtain

$$\begin{aligned} t_{\text{melt}} &= \Bigg[\frac{\Theta(\kappa_2 - \kappa_1) A_2}{(\kappa_1 - \kappa_2) P'_\alpha} + \frac{\Theta \kappa_1 (\kappa_1 - \kappa_2) P'_\alpha A_e + I^2 \Theta (\kappa_1 - \kappa_2) - \Theta \kappa_1 (\kappa_1 - \kappa_2) P'_\alpha A_e}{(\kappa_1 - \kappa_2)^2 P'^2_\alpha} \\ &\qquad \ln \left(I^2 - P'_\alpha \kappa_1 A_e + (\kappa_1 - \kappa_2) P'_\alpha A_2 \right) \Bigg]_0^{A_e} \\ &= -\frac{\Theta A_e}{P'_\alpha} + \left[\frac{I^2 \Theta}{(\kappa_1 - \kappa_2) P'^2_\alpha} \; \ln \left(I^2 - P'_\alpha \kappa_1 A_e + (\kappa_1 - \kappa_2) P'_\alpha A_2 \right) \right]_0^{A_e} \\ &= -\frac{\Theta A_e}{P'_\alpha} + \frac{I^2 \Theta}{(\kappa_1 - \kappa_2) P'^2_\alpha} \; \ln \left(\frac{I^2 - P'^2_\alpha \kappa_2 A_e}{I^2 - P'^2_\alpha \kappa_1 A_e} \right). \end{aligned}$$

□

A.4.2 Measured Blowing Times of Midi 25 and 30

		MIDI 25			
Theoretical Current I_{th}(A)	Measured Current I_{meas}(A)	Time t(s)	Voltage U(V)	Mean current I_{m}(A)	Mean Time t_{m}(s)
70.00	69.83	1.2225	35	69.83	1.2525
70.00	69.83	1.2825	35		
55.10	55.26	2.6650	32	55.30	2.5975
55.10	55.34	2.5300	32		
48.00	48.13	4.8400	32	48.14	4.6650
48.00	48.14	4.4900	32		
42.66	42.71	9.6675	32	42.71	9.7213
42.66	42.70	9.7750	32		
40.00	39.98	35.6850	30	39.98	23.6350
40.00	39.97	11.5850	30		
38.40	38.42	73.8450	32	38.42	53.8967
38.40	38.42	43.5675	32		
38.40	38.41	44.2775	32		

Tab. A.12: *Measured currents, blowing times and voltages for Midi 25.*

		MIDI 30			
Theoretical Current I_{th}(A)	Measured Current I_{meas}(A)	Time t(s)	Voltage U(V)	Mean current I_{m}(A)	Mean Time t_{m}(s)
70.00	69.99	1.7875	35	70.05	1.8208
	70.11	1.8175			
	70.05	1.8575			
64.00	63.91	3.0600	32	63.92	3.0508
	63.92	2.9725			
	63.94	3.1200			
58.62	58.80	7.6800	34	58.76	7.5258
	58.73	7.4625			
	58.75	7.4350			
55.10	55.36	33.0600	32	55.35	30.4483
	55.36	30.7225			
	55.34	27.5625			
51.00	51.05	100.2075	34	51.05	91.1292
	51.05	83.0275			
	51.06	90.1525			

Tab. A.13: *Measured currents, blowing times and voltages for Midi 30.*

Bibliography

[1] R.A. Adams, *Sobolev Spaces*, Academic Press, Boston, MA, 1975.

[2] M.S. Agarwal, A.D. Stokes, and P. Kovitya, *Pre-arcing behaviour of open fuse wire*, J. Phys. D: Appl. Phys **20** (1987), 1237–1242.

[3] G.J. Anders, *Rating of Electric Power Cables: Ampacity Computations for Transmission, Distribution, and Industrial Applications*, IEEE Press Power Engineering Series, McGraw-Hill, 1997.

[4] ———, *Rating of Electric Power Cables in Unfavorable Thermal Environment*, IEEE Press Series on Power Engineering, Wiley, 2005.

[5] W.T. Ang, *A Beginner's Course in Boundary Element Methods*, Universal Publishers, 2007.

[6] T. Apel, *Numerik für Differentialgleichungen*, Lecture notes, Universität der Bundeswehr München, 2014.

[7] I. Ayucar, *2D Circle Packing algorithm ported to C#*, Available online at `http://www.codeproject.com/Articles/42067/2D-Circle-Packing-algorithm-ported-to-C#`, March 2012.

[8] H.M. Badr, *Laminar combined convection from a horizontal cylinder - parallel and contra flow regimes*, International Journal of Heat and Mass Transfer **27** (1984), no. 1, 15–27.

[9] T. Becks, *Elektrofahrzeuge ermöglichen neue Fahrzeugformen und Mobilitätskonzepte*, VDE Verband der Elektrotechnik Elektronik Informationstechnik e.V., `http://www.vde.com/de/e-mobility/fahrzeugtechnik/seiten/default.aspx`, June 2013.

[10] boerse.de, *boerse.de Finanzportal*, Available online at `http://www.boerse.de/chart-tool/Aluminium/XC0009677839`, September 2013.

[11] D. Braess, *Finite Elemente*, 2nd ed., Springer-Verlag, Heidelberg, 1997.

[12] S.C. Brenner and L.R. Scott, *The Mathematical Theory of Finite Element Methods*, Texts in Applied Mathematics, Springer-Verlag, 2002.

[13] I.N. Bronstein and K.A. Semendjajew, *Taschenbuch der Mathematik*, 19th ed., Teubner Verlagsgesellschaft, Nauka-Verlag, Leipzig, Moskau, 1979.

[14] P. Brown, A. Hindmarsh, and L. Petzold, *Using Krylov Methods in the Solution of Large-Scale Differential-Algebraic Systems*, SIAM Journal on Scientific Computing **15** (1994), no. 6, 1467–1488.

[15] C. Büskens, *Linienmethode*, Lecture notes, Universität Bayreuth, 2002.

[16] J. Chung and G.M. Hulbert, *A Time Integration Algorithm for Structural Dynamics With Improved Numerical Dissipation: The Generalized-alpha Method*, Journal of Applied Mechanics **60** (1993), no. 2, 371–375.

[17] S.W. Churchill and H.S. Chu, *Correlating equations for laminar and turbulent free convection from a horizontal cylinder*, International Journal of Heat and Mass Transfer **18** (1975), no. 9, 1049–1053.

[18] S.W. Churchill and R. Usagi, *A general expression for the correlation of rates of transfer and other phenomena*, AIChE Journal **18** (1972), no. 6, 1121–1128.

[19] R. Čiegis, A. Ilgevičius, G. Jankevičiūtė, and M. Meilūnas, *Determination of Heat Conductivity Coefficient of a Cable Bundle by Inverse Problem Solution Method*, Electron. Electr. Eng. **2** (2009), 77–80.

[20] R. Čiegis, A. Ilgevičius, H.-D. Ließ, M. Meilūnas, and O. Suboč, *Numerical simulation of the heat conduction in electrical cables*, Math. Model. Anal. **12** (2007), no. 4, 425–439.

[21] Coroplast GmbH, *Fahrzeugleitungen*, Kabelkatalog, 2012.

[22] M. Cuesta, J.-P. Gossez, and P. Omari, *Nonresonance to the right of the first eigenvalue for the one-dimensional p-Laplacian*, Nonlinear Anal. **38** (1999), no. 4, Ser. A: Theory Methods, 481–496.

[23] W. Dahmen and A. Reusken, *Numerik für Ingenieure und Naturwissenschaftler*, Springer-Lehrbuch, Springer-Verlag, 2008.

[24] T.A. Davis, *Algorithm 832: UMFPACK V4.3 – an Unsymmetric-Pattern Multifrontal Method*, ACM Trans. Math. Softw. **30** (2004), no. 2, 196–199.

[25] T.A. Davis and I.S. Duff, *An Unsymmetric-Pattern Multifrontal Method for Sparse LU Factorization*, SIAM Journal on Matrix Analysis and Applications **18** (1997), no. 1, 140–158.

[26] C. Delfour and J.P. Zolésio, *Shapes and Geometries: Metrics, Analysis, Differential Calculus, and Optimization*, 2nd ed., Advances in Design and Control, Society for Industrial and Applied Mathematics (SIAM), Philadelphia, 2011.

[27] S. Dessort, *Studie zum Verhaltens von Sicherungen bei Stromimpulsen*, Internship report, Universität der Bundeswehr München, 2012.

[28] P. Deuflhard, *A Modified Newton Method for the Solution of Ill-Conditioned Systems of Nonlinear Equations with Application to Multiple Shooting*, Numer. Math. **22** (1974), 289–315.

[29] DIN 43 670, *Stromschienen aus Aluminium, Bemessung für Dauerbetrieb.*, December 1975.

[30] DIN 43 671, *Stromschienen aus Kupfer, Bemessung für Dauerbetrieb.*, December 1975.

[31] B. Démoulin and L. Koné, *Shielded Cable Transfer Impedance Measurements*, IEEE Electromagnetic Compatibility Society Newsletter (2010), 30–37.

[32] ———, *Shielded Cable Transfer Impedance Measurements High frequency range 100 MHz to 1 GHz*, IEEE Electromagnetic Compatibility Society Newsletter (2010), 8–16.

[33] ———, *Shielded Cable Transfer Impedance Measurements in the Microwave Range of 1 GHz to 10 GHz*, IEEE Electromagnetic Compatibility Society Newsletter (2011), 52–61.

[34] Y. Du and X.H. Wang, *Electrical and Thermal Analysis of Parallel Single-Conductor Cable Installations*, Industry Applications Society Annual Meeting 2009, IEEE, 2009, pp. 1–6.

[35] K. Dvorsky, *Analysis of a Nonlinear Boundary Value Problem with Application to Heat Transfer in Electric Cables*, Ph.D. thesis, Universität der Bundeswehr München, Fakultät für Luft- und Raumfahrttechnik, Neubiberg, 2012.

[36] ———, *Fehlerabschätzung zur quasistationären Approximation*, Internal Report, October 2013.

[37] J. Engbring, *Leichtbau-Strategien im Hochvolt-Bordnetz*, ATZelektronik **6** (2011), 48–53.

[38] R. Eymard, T. Gallouët, and R. Herbin, *Finite Volume Methods*, Handb. Numer. Anal., VII, North-Holland, Amsterdam, 2000.

[39] H. Feshki Farahani, M. Asadi, and A. Kazemi, *Analysis of Thermal Behavior of Power System Fuse Using Finite Element Method*, Proceedings of the 4th International Power Engineering and Optimization Conference, 2000, pp. 189–195.

[40] M.P. Filippakou, C.G. Karagiannopoulos, D.P. Agoris, and P.D. Bourkas, *Electrical contact overheating under short-circuit currents* , Electric Power Systems Research **57** (2001), no. 2, 141–147.

[41] R.J. Fowler, M. Paterson, and S.L. Tanimoto, *Optimal Packing and Covering in the Plane are NP-Complete*, Inf. Process. Lett. **12** (1981), no. 3, 133–137.

[42] M. Gerdts and F. Lempio, *Mathematische Optimierungsverfahren des Operations Research*, De Gruyter Studium, Gruyter, Walter de GmbH, 2011.

[43] D.C. Giancoli, *Physik: Lehr- und Übungsbuch*, Pearson Studium - Physik, Pearson Deutschland, 2010.

[44] P.E. Gill, W. Murray, and M.H. Wright, *Practical Optimization*, Academic Press Inc., London, 1981.

[45] V. Giurgiu, G. Oarga, and S. Purdel, *Analysis of Thermal Phenomena in High-Voltage Fuse-Links Based on Thermovision Equipment*, Proceedings of the International Conference on Electrical Fuses and their Applications, 1999, pp. 65–68.

[46] J. Grandvuillemin, *Electro-thermal phenomena study governing the power lines of an electrical vehicle network - application to the modelling and design of electrical harnesses and protections*, Ph.D. thesis, Université de Franche-Comté, 2009.

[47] C. Großmann and H.G. Roos, *Numerische Behandlung Partieller Differentialgleichungen*, Teubner Studienbücher Mathematik, Teubner B.G. GmbH, 2005.

[48] K. Gärtner, *Solving unsymmetric sparse systems of linear equations with PARDISO*, Journal of Future Generation Computer Systems **20** (2004), 475–487.

[49] H. Harbrecht, *On analytical derivatives for geometry optimization in the polarizable continuum model*, J. Math. Chem. **49** (2011), 1928–1936.

[50] H. Harbrecht and F. Loos, *Optimization of Current Carrying Multicables*, Preprint, Available online at `http://jones.math.unibas.ch/~harbrech/publications/ShapeOptMulticable.pdf`, 2013.

[51] H. Harbrecht and J. Tausch, *An efficient numerical method for a shape-identification problem arising from the heat equation*, Inverse Problems **27** (2011), 065013.

[52] J. Haslinger and R.A.E. Mäkinen, *Introduction to Shape Optimization: Theory, Approximation, and Computation*, Advances in Design and Control, Society for Industrial and Applied Mathematics (SIAM), Philadelphia, 2003.

[53] R.L. Haupt and S.E. Haupt, *Practical Genetic Algorithms*, John Wiley & Sons, Inc., New York, 1998.

[54] F. Hettlich and W. Rundell, *The determination of a discontinuity in a conductivity from a single boundary measurement*, Inverse Problems **14** (1998), 67–82.

[55] ______, *Identification of a discontinuous source in the heat equation*, Inverse Problems **17** (2001), no. 5, 1465.

[56] A.C. Hindmarsh, P.N. Brown, K.E. Grant, S.L. Lee, R. Serban, D.E. Shumaker, and C.S. Woodward, *SUNDIALS: Suite of Nonlinear and Differential/Algebraic Equation Solvers*, ACM Trans. Math. Softw. **31** (2005), no. 3, 363–396.

[57] G. Hoffmann and U. Kaltenborn, *Thermal modeling of high voltage H.R.C. fuses and simulation of tripping characteristic*, 7th Int. Conf. on Electrical Fuses & Their Appl., 2003, pp. 174–180.

[58] G.G.C. Hsiao and W.W.L. Wendland, *Boundary Integral Equations*, Applied Mathematical Sciences Series, Springer-Verlag, Berlin, Heidelberg, 2008.

[59] S.Y. Huang and F. Mayinger, *Wärmeübergang bei freier Konvektion um elliptische Rohre*, Wärme- und Stoffübertragung, 3, Springer-Verlag, 18th ed., 1984, pp. 175–183.

[60] IEC Standard 60287, *Calculation of the Continuous Current Rating of Cables (100% load factor)*, International Electrotechnical Commission, 1st ed., 1969.

[61] ______, *Calculation of the Continuous Current Rating of Cables (100% load factor)*, International Electrotechnical Commission, 2nd ed., 1982.

[62] ______, *Calculation of the Continuous Current Rating of Cables (100% load factor)*, International Electrotechnical Commission, 3rd ed., 1994.

[63] IEC Standard 60287-1-1, *Electrical cables - Calculation of the current rating - part 1 - current rating equations (100% load factor) and calculation of losses - General*, International Electrotechnical Commission, 2nd ed., 2006.

[64] IEC Standard 60287-1-2, *Electrical cables - Calculation of the current rating - part 2 - Thermal resistance*, International Electrotechnical Commission, 2nd ed., 2006.

[65] IEC Standard 60853-1, *Calculation of the Cyclic and Emergency Current Ratings of Cables. Part I : Cyclic Rating Factor for Cables up to and Including 18/30 (36) kq*, International Electrotechnical Commission, 1985, Publication 853-1.

[66] IEC Standard 60853-2, *Calculation of the Cyclic and Emergency Current Ratings of Cables. Part 2: Cyclic Rating Factor of Cables Greater than 18/30 (36) kV and Emergency Ratings for Cables of All Voltages*, International Electrotechnical Commission, 1989, Publication 853-2.

[67] A. Ilgevičius, *Analytical and numerical analysis and simulation of heat transfer in electrical conductors and fuses*, Ph.D. thesis, Universität der Bundeswehr München, 2004.

[68] F.P. Incropera, D.P. DeWitt, T.L. Bergman, and A.S. Lavine, *Fundamentals of Heat and Mass Transfer*, 8th ed., John Wiley & Sons, 2007.

[69] J. Köhler, *Versuchen oder rechnen – Betriebsfestigkeit und Nullbruchlinie. To try or to calculate – Operating fatigue strength and zero fracture line*, Mat.-wiss. u. Werkstofftech. **41** (2010), 150–153.

[70] K.E. Jansen, C.H. Whiting, and G.M. Hulbert, *A generalized-alpha method for integrating the filtered Navier-Stokes equations with a stabilized finite element method*, Comput. Methods Appl. Mech. Engrg. **190** (2000), 305–319.

[71] M. Jung and U. Langer, *Methode der Finiten Elemente für Ingenieure*, 1st ed., Teubner, 2001.

[72] H. Kasumba and K. Kunisch, *On free surface PDE constrained shape optimization problems*, Appl. Math. Comput. **218** (2012), 11429–11450.

[73] Y. Kawase, T. Miyatake, and S. Ito, *Heat Analysis of a Fuse for Semiconductor Devices Protection Using 3-D Finite Element Method*, IEEE Transactions on Magnetics **36** (2000), no. 4, 1377–1380.

[74] P. Knabner and L. Angerman, *Numerical Methods for Elliptic and Parabolic Partial Differential Equations*, Texts in Applied Mathematics, Springer, New York, 2003.

[75] K. Küpfmüller, W. Mathis, and A. Reibiger, *Theoretische Elektrotechnik*, Springer-Lehrbuch, Springer-Verlag, 2008.

[76] E.M. Landesman and A.C. Lazer, *Nonlinear Perturbations of Linear Elliptic Boundary Value Problems at Resonance*, J. Math. Mech. **19** (1970), no. 4, Ser. A: Theory Methods, 609–623.

[77] H.P. Langtangen, *Computational Partial Differential Equations: Numerical Methods and Diffpack Programming*, 2 ed., Springer New York, Inc., Secaucus, NJ, USA, 2003.

[78] Leonische Drahtwerke, *Automotive Wires and Cables*, 1997, Kabelkatalog.

[79] R. LeVeque, *Finite Difference Methods for Ordinary and Partial Differential Equations: Steady-State and Time-Dependent Problems (Classics in Applied Mathematics Classics in Applied Mathemat)*, Society for Industrial and Applied Mathematics (SIAM), Philadelphia, 2007.

[80] R.J. LeVeque, *Finite-Volume Methods for Hyperbolic Problems*, Cambridge University Press, 2002.

[81] H.-D. Ließ and A. Ilgevičius, *Analytical versus numerical calculations of physical problems. The benefits of its combination*, Mathematical Modelling and Analysis **8** (2003), no. 4, 291–302.

[82] H.-D. Ließ, F. Loos, and K. Dvorsky, *Abschlussbericht zum Forschungsprojekt Auslegung elektrischer Komponenten im Fahrzeugbordnetz*, Research project of Dräxlmaier AG and Universität der Bundeswehr München, Sponsored by the Bayerische Forschungsstiftung, Aktenzeichen AZ-756-07, January 2007–September 2011.

[83] J.H. Lienhard, *A Heat Transfer Textbook*, 3rd ed., Phlogiston Press, 2006.

[84] Y. Liu, N. Phan-Thien, R. Kemp, and X.-L. Luo, *A coupled conduction convection and radiation problem for three insulated cables suspended in air*, Computational Mechanics **22** (1998), no. 4, 326–336.

[85] F. Loos, K. Dvorsky, and H.-D. Ließ, *Determination of Stationary Temperature Distribution in Shielded Cables of Finite Length*, I.RE.M.E. **7** (2013), no. 2, 282–292.

[86] ______, *Determination of temperature in automotive high-voltage cables of finite length with dynamic current profiles*, Accepted for publication in Mathematical and Computer Modelling of Dynamical Systems, Taylor & Francis, Available online at `http://www.tandfonline.com/doi/abs/10.1080/13873954.2013.833120#.Urf-LfuQOF8`, 2013.

[87] ______, *Two Approaches for Heat Transfer Simulation of Current Carrying Multicables*, Accepted for publication in Mathematics and Computers in Simulation, Elsevier, 2014.

[88] F. Loos, H.-D. Ließ, and K. Dvorsky, *Simulation methods for heat transfer processes in mechanical and electrical connections*, 1st International Electric Drives Production Conference (EDPC), IEEE, 2011, pp. 214–220.

[89] F. Loos, H.-D. Ließ, and B. Philippe, *Transient Analysis of the Triggering Behaviour of Safety Fuses*, COMSOL Conference, Stuttgart, 2011.

[90] J. Mahwin and J.R. Ward, *Variational Methods and Semi-linear Elliptic Equations*, Nonlinear Analysis, Theory, Methods and Applications (1981), 677–684.

[91] Matlab, *Version 7.10.0 (R2010a): Optimization Toolbox*, The MathWorks Inc., Natick, Massachusetts, 2010.

[92] ______, *Version 7.10.0 (R2010a): Using the Genetic Algorithm*, The MathWorks Inc., Natick, Massachusetts, 2010.

[93] J.M. Miller and P.R. Nicastri, *The next generation automotive electrical power system architecture: issues and challenges*, Digital Avionics Systems Conference, Proceedings, vol. 2, Oct 1998, pp. I15/1–I15/8.

[94] A. Münzenmaier, *Einsatz von Hochvoltsicherungen bei Fahrzeugen mit elektrischem Hauptantrieb*, Bachelor's thesis, Hochschule Esslingen – University of Applied Sciences, 2010.

[95] COMSOL Multiphysics, *Reference Guide Version 3.5a*, 2008.

[96] ______, *User's Guide, Version 4.1*, 2010.

[97] ______, *Joule Heating in a Fuse on a Circuit Board Tutorial*, Available online at `http://www.youtube.com/watch?v=p0eXEPP9Aao`, January 2014.

[98] F. Murat and J. Simon, *Etude de Problème d'Optimal Design*, Optimization Techniques: Modeling and Optimization in the Service of Man, Part 2 - Proceedings, 7th IFIP Conference, Nice, September 8-12, 1975 (Jean Céa, ed.), Lecture Notes in Computer Science, vol. 41, Springer-Verlag, 1975, pp. 54–62.

[99] T. Neddersen, *Validierung und Weiterentwicklung eines Berechnungstools zur thermischen Auslegung stromdurchflossener Kuperschienen*, Bachelor's thesis, Hochschule Rosenheim, 2012.

[100] J.H. Neher, *The Transient Temperature Rise of Buried Cable Systems*, IEEE Transactions on Power Apparatus and Systems **83** (1964), 102–114.

[101] J.H. Neher and M.H. McGrath, *The Calculation of the Temperature Rise and Load Capability of Cable Systems*, Transactions of The American Institute of Electrical Engineers. Part III: Power Apparatus and Systems **76** (1957), 752–764.

[102] B. Nolet, *Thermische Simulation elektrischer Bauteile und messtechnische Überprüfung*, Internship report, Universität der Bundeswehr München, 2011.

[103] ______, *Implementierung eines Ansatzes zur Simulation des Auslöseverhaltens von Schmelzsicherungen*, Internship report, Universität der Bundeswehr München, 2012.

[104] A.J. Nowak, *Numerical Methods in Heat Transfer*, 1st ed., Papierflieger Verlag Clausthal-Zellerfeld, 2009.

[105] N. Özişik, *Finite Difference Methods in Heat Transfer*, Taylor & Francis, 1994.

[106] J. Peiro and S. Sherwin, *Finite difference, finite element and finite volume methods for partial differential equations*, pp. 1–32, Springer-Verlag, 2005.

[107] B. Philippe, *Studie zum Auslöseverhalten von Automobilsicherungen I*, Internship report, Universität der Bundeswehr München, 2010.

[108] ______, *Studie zum Auslöseverhalten von Automobilsicherungen II*, Internship report, Universität der Bundeswehr München, 2011.

[109] O. Pironneau, *Optimal Shape Design for Elliptic Systems*, Springer Series in Computational Physics, Springer-Verlag, 1984.

[110] A.D. Polianin, *Handbook of Linear Partial Differential Equations for Engineers and Scientists*, Chapman & Hall/CRC, 2002.

[111] M.J.D. Powell, *A Fortran Subroutine for Solving Systems of Nonlinear Algebraic Equations*, Atomic Energy Res. Estab. Report, H. M. Stationery Office, 1968.

[112] L. Pryor, R. Schlabohm, and B. Brownell, *A Comparison of Aluminium vs. Copper as Used in Electrical Equipment*, Available online at `www.geindustrial.com`, 2012.

[113] G.D. Raithby and K.G.T. Hollands, *A General Method of Obtaining Approximate Solutions to Laminar and Turbulent Free Convection Problems*, Advances in Heat Transfer, vol. 11, Elsevier, 1975, pp. 265–315.

[114] R.-D. Rogler, H. Löbl, and J. Schmidt, *A diagnostic system for live electrical joints in power transmission systems*, European Transaction on Electrical Power, vol. 7, September 1997, pp. 331–336.

[115] M. Schanz and O. Steinbach, *Boundary Element Analysis: Mathematical Aspects and Applications*, Lecture Notes in Applied and Computational Mechanics, 29, Springer-Verlag, Berlin, Heidelberg, 2007.

[116] O. Schenk and K. Gärtner, *On fast factorization pivoting methods for symmetric indefinite systems*, Electronic Transactions on Numerical Analysis **23** (2006), no. 1, 158–179.

[117] S. Schmidt, *Efficient Large Scale Aerodynamic Design Based on Shape Calculus*, Ph.D. thesis, Universität Trier, 2010.

[118] T. Schulz, *Grundsatzuntersuchung zum Temperaturverhalten elektrischer Leitungen und deren Schutzelemente auf Schmelzleiterbasis in Kfz-Bordnetzen*, Ph.D. thesis, Universität der Bundeswehr München, 2002.

[119] H.R. Schwarz and N. Köckler, *Numerische Mathematik*, Vieweg+Teubner Verlag, 2011.

[120] R. Siegel and J.R. Howell, *Thermal Radiation Heat Transfer*, Taylor & Francis, 2002.

[121] D.M. Simmons, *Calculation of the electrical problems of underground cables*, General Cable Corporation, 1932.

[122] J. Sokolowski and J.-P. Zolésio, *Introduction to Shape Optimization*, Springer-Verlag, 1992.

[123] M. Stahl, *Rechnergestützte Wärmeleitungsberechnung in stromdurchflossenen, abgeschirmten Einzelleitungen*, Bachelor's thesis, Universität der Bundeswehr München, Fakultät für Elektrotechnik und Informationstechnik, Neubiberg, 2010.

[124] J. Taler and P. Duda, *Solving Direct and Inverse Heat Conduction Problems*, Springer-Verlag, Dordrecht, 2006.

[125] Technology Review, *Alu statt Kupfer*, Heise Zeitschriften Verlag, April 2011, pp. 10–11.

[126] N. Tesla, *The Transmission of Electrical Energy Without Wires As a Means for Furthering Peace*, Electrical World and Engineer **45** (1905), no. 1, 21–24.

[127] A.N. Tikhonov and A.A. Samarskii, *Equations of Mathematical Physics*, Dover Books on Physics, Dover Publications, 1990.

[128] P.A. Tipler, G. Mosca, and D. Pelte, *Physik: Für Wissenschaftler und Ingenieure*, Sav Physik/Astronomie, Elsevier, Spektrum Akad. Verlag, 2004.

[129] E. Torres, A.J. Mazon, E. Fernandez, and I. Zamora, *New FEM Model for thermal analysis of medium voltage fuses*, 19th International Conference on Electricity Distribution, Vienna, 2007.

[130] Fredi Tröltzsch, *Optimale Steuerung partieller Differentialgleichungen - Theorie, Verfahren und Anwendungen*, Vieweg, 2005.

[131] VDI-Gesellschaft V. und Chemieingenieurwesen GVC (ed.), *VDI-Wärmeatlas. Berechnungsunterlagen für Druckverlust, Wärme- und Stoffübergang*, 10th ed., Springer, Berlin, 2006.

[132] R. Vilums and A. Buikis, *Conservative Averaging and Finite Difference Methods for Transient Heat Conduction in 3D Fuse*, WSEAS Transactions on Heat and Mass Transfer **3** (2008), 111–124.

[133] R. Vilums, H.-D. Ließ, A. Buikis, and A. Rudevics, *Cylindrical Model of Transient Heat Conduction in Automotive Fuse Using Conservative Averaging Method*, Proceedings of the 13th WSEAS International Conference on Applied Mathematics, 2008, pp. 355–360.

[134] P. von Böckh and T. Wetzel, *Wärmeübertragung: Grundlagen und Praxis*, 3rd ed., Springer-Verlag, Berlin, 2009.

[135] A. Wächter, *Short Tutorial: Getting Started With Ipopt in 90 Minutes*, Combinatorial Scientific Computing (Leibniz-Zentrum für Informatik) (U. Naumann, O. Schenk, H.D. Simon, and S. Toledo, eds.), Dagstuhl Seminar Proceedings, no. 09061, Schloss Dagstuhl, 2009.

[136] A. Wächter and L.T. Biegler, *Line Search Filter Methods for Nonlinear Programming: Local Convergence*, SIAM Journal on Optimization **16** (2005), no. 1, 32–48.

[137] A. Wächter and L.T. Biegler, *On the implementation of an interior-point filter line-search algorithm for large-scale nonlinear programming*, Mathematical Programming **106** (2006), 25–57.

[138] N. Wongyala, *Erwärmung elektrischer Leiter*, Diploma thesis, Universität der Bundeswehr München, Fakultät für Elektrotechnik und Informationstechnik, Neubiberg, 1999.

[139] L.C. Wrobel and M.H. Aliabadi, *The Boundary Element Method*, Wiley, 2002.

[140] R.-B. Xiao, Y.-C. Xu, and M. Amos, *Two hybrid compaction algorithms for the layout optimization problem*, BioSystems **90** (2007), 560–567.

[141] E. Zeidler, *Nonlinear Functional Analysis and its Applications II/B*, Springer-Verlag, Berlin, 1990.

[142] J. Zhang and D. Zhu, *A trust region typed dogleg method for nonlinear optimization*, Optimization **21** (1990), no. 4, 543–557.

List of Figures

List of Tables

List of Symbols and Abbreviations

Abbreviations

BDF	Backward differentiation formulas
BE	Boundary elements
BVP	Boundary value problem
CFD	Computational fluid dynamics
CFL	Courant-Friedrichs-Lewy
Comp	Component of the maximal absolute discrepancy between adjoint and finite difference method
CSA	Cable squeezing algorithm
CSC	Compressed sparse column
CSR	Compressed sparse row
DC	Direct current
DIN	Deutsches Institut für Normung
DOF	Degree of freedom
e.g.	exempli gratia
EMC	Electromagnetic compatibility
F-count	Number of functions
FD	Finite differences
FDM	Finite difference method
FE	Finite elements
FEA	Finite element approach
FEM	Finite element method
FVM	Finite volume method
HBA	Heat power balance approach
IDA	Implicit differential-algebraic solver
i.e.	id est
IEC	International electrotechnical commission
INL	Inner layout
IPOPT	Interior point optimizer
KKT	Karush-Kuhn-Tucker (conditions)
LME	London metal exchange
MC	Multicable
MCL	Monte Carlo layout

ME, MEA, MEAS, MES	Measurements
NOE	Number of elements
nz	non-zero elements
ODE	Ordinary differential equation
OPP	Opposed layout
OptMC	Optimal multicable layout problem
OUL	Outer layout
PARDISO	Parallel direct sparse solver
PDE	Partial differential equation
SQZ	Squeezing
UMFPACK	Unsymmetric multifrontal sparse LU factorization package
VDI	Verein Deutscher Ingenieure
w.r.t.	with respect to

Chemical Elements and Compounds

Al	Aluminium
Cu	Copper
PET	Polyethylene terephthalate
PVC	Polyvinyl chloride
Sn	Tin
Zn	Zinc

Physical Variables

α	Heat transfer coefficient in $W/(m^2 \cdot K)$
$\tilde{\alpha}$	Truncated heat transfer coefficient in $W/(m^2 \cdot K)$
α_{conv}	Convective heat transfer coefficient in $W/(m^2 \cdot K)$
α_l	Lower bound for the heat transfer coefficient in $W/(m^2 \cdot K)$
α_{rad}	Radiative heat transfer coefficient in $W/(m^2 \cdot K)$
α_ρ	Linear temperature coefficient of electrical resistance in 1/K
α_{ρ_c}	Linear temperature coefficient of electrical resistance at contact in 1/K
$\alpha_{\rho,k}$	Linear temperature coefficient of electrical resistance in k-th subdomain in 1/K
β	Thermal extension coefficient of air in 1/K
c	Specific heat capacity per weight in $J/(kg \cdot K)$
$\tilde{c}$	Auxiliary quantity in $W/(K \cdot m^3)$
ΔE_{st}	Rate of heat energy stored within a closed system in J
ΔT	Temperature difference in K
E_{g}	Heat energy generated in a closed system in J

E_{in}	Heat energy entering a closed system in J
E_{out}	Heat energy dissipating from a closed system in J
E_{surf}	Heat energy flowing across the surface in J
ϵ_{r}	Emissivity of radiating element
$\eta(t)$	Temperature ratio dependent on time
η_{res}	Temperature ratio for currents above the resonance current
η_s	Temperature ratio for the stationary case
$\eta^{(j)}$	Temperature ratio at a discrete time step j
$\tilde{f}$	Auxiliary quantity in W/m^3
g	Gravitational acceleration in N/kg
γ	Specific heat capacity per volume in $\text{J}/(\text{m}^3 \cdot \text{K})$
$\tilde{\gamma}(\cdot)$	Auxiliary quantity (function) in W/m^2
Gr	Grashof number
I	Electric current in A
I_k	Electric current of k-th subdomain in A
I_{lim}	Limiting current in A
$I_{\text{lim},k}$	Limiting current of k-th subdomain in A
I_{res}	Resonance current in A
$\mathcal{I}$	Vector of electric currents
κ	Electrical conductivity in $1/(\Omega \cdot \text{m})$
κ_0	Electrical conductivity at reference temperature in $1/(\Omega \cdot \text{m})$
$\kappa_{0,k}$	Electrical conductivity of k-th subdomain at reference temperature in $1/(\Omega \cdot \text{m})$
λ	Heat conductivity in $\text{W}/(\text{m} \cdot \text{K})$
λ_a	Heat conductivity of a fluid in $\text{W}/(\text{m} \cdot \text{K})$
λ_{air}	Heat conductivity of air in $\text{W}/(\text{m} \cdot \text{K})$
λ_{ex}	Heat conductivity at the exterior surface in $\text{W}/(\text{m} \cdot \text{K})$
λ_i	Heat conductivity in direction of i-th space coordinate in $\text{W}/(\text{m} \cdot \text{K})$
λ_k	Heat conductivity of k-th subdomain in $\text{W}/(\text{m} \cdot \text{K})$
Nu	Nusselt number
ν	Kinematic viscosity of air in m^2/s
P_c	Heat power generated at a contact surface in W
Pr	Prandtl number of air
$P'_{\alpha}(T_2)$	Heat power density per length at the insulation surface in W/m
q_r	Radiation rate per unit surface area and unit time in W/m^2
R	Electrical resistance in Ω
R_c	Electrical contact resistance in Ω
$R_{c,0}$	Electrical contact resistance at reference temperature in Ω
Ra	Rayleigh number
ρ	Electrical resistivity in $\Omega \cdot \text{m}$

ρ_0	Electrical resistivity at reference temperature in $\Omega \cdot \mathrm{m}$
$\rho_{0,k}$	Electrical resistivity of k-th subdomain at reference temperature in $\Omega \cdot \mathrm{m}$
ϱ	Density in $\mathrm{kg/m^3}$
σ	Stefan-Boltzmann constant in $\mathrm{W/(m^2 \cdot K^4)}$
σ_i	Heat flux in direction x_i in $\mathrm{W/m^2}$
T	Temperature in °C
T_{init}	Initial temperature in °C
T_l	Lowest temperature of a concrete scenario in °C
T_m	Average temperature in °C
$T_{\max}$	Maximum temperature in °C
$T_{\min}$	Minimum temperature in °C
T_ϵ	Temperature distribution on perturbed domain in °C
T_0	Reference temperature in °C
$T_1,\ T_{\mathrm{amb}}$	Ambient temperature in °C
T_2	Temperature at the exterior (insulation) surface in °C
T_{1K}, T_{2K}	Absolute temperature of the surface and ambient air in K
$T^{(i)}$	Temperature at a discrete time step i in °C

Space and Time Variables

a	Length of a rectangular horizontal surface in m
A	Cross sectional area in $\mathrm{m^2}$
A_k	Cross sectional area of k-th subdomain in $\mathrm{m^2}$
A^{ge}	Geometrical cross sectional area in $\mathrm{m^2}$
A^{ph}	Physical cross sectional area in $\mathrm{m^2}$
b	Width of a rectangular horizontal surface in m
$\beta,\ \beta_f$	Filling factor
d	Diameter of a (horizontal) cylinder in m
d_{ex}	Maximum distance of two arbitrary points of a domain in m
$\mathrm{d}t$	Infinitesimal time interval in s
δ	Length of time step in s
$\Delta t,\ \Delta t^*$	Length of time interval in s
Δx_i^*	Edge lengths of a volume element in i-th space direction
Γ	Boundary of a domain
Γ^{ex}	Exterior boundary
Γ^{gi}	Interface boundary between the exterior insulation and air gaps
Γ^{int}	Set of interface boundaries
Γ_k^e, Γ_k^i	Exterior and interior interface boundaries of domain Ω_k
ℓ	Length of a conductor in m
ℓ_0	Characteristic length in m

Ω	Spacial domain
Ω_ϵ	Perturbed domain
Ω_k	k-th subdomain
Ω_{init}	Initial domain in shape optimization
Ω_{opt}	Optimal domain in shape optimization
Ω_{ref}	Reference domain
P	Centre of a volume element
$\mathcal{Q}$	Cylinder of space and time
S	Boundary of a volume element
t	Time in s
t_j	Discrete time step in s
$t_{\max}$	Maximum time in s
t_1, t_2	Start and ending of time interval in s
V	Volume element
$\mathbf{x}$	(Higher dimensional) space coordinate
x_i	(One dimensional) space coordinate
$\tilde{x}$	(Local) space coordinate of attached cables

Coefficients, Constants and Function(-al)s

$a(\cdot,\cdot)$	(Non-)Bilinear form in the weak formulation
$b(\cdot)$	Linear form in the weak formulation
$C_{\bar{h}}$	Entry in the Jacobian of an auxiliary temperature mapping $\bar{\mathbf{h}}$
δ_{ij}	Kronecker's delta
ϵ	Small real constant > 0
$f(\cdot)$	General function, e.g. to describe the Nusselt number
$f_1,\ f_2$	Right hand side of a general equation of boundary condition in shape optimization
F	Nonlinear system in the finite element approximation
$\mathbf{F}$	Vector valued mapping
$\widetilde{\mathbf{F}}$	Modified vector valued mapping
φ_i	Ansatz function
$\mathbf{g}$	Mapping of restrictions
$g(\Gamma)$	Scalar distribution on the boundary
γ_Γ^*	Adjoint of the trace operator on Γ
G	General function discretized via the θ-method
$G(\Omega)$	General shape gradient
h	Step length of the discretization in space
$\mathbf{h}$	Temperature mapping
$\bar{\mathbf{h}}$	Auxiliary fixed point mapping
$i_{\max}$	Maximum number of iterations

$J(\cdot)$	Shape functional
$j_1(\cdot),\ j_2(\cdot)$	Real functions to define the shape functional
K_{ij}	Symmetric matrix in the finite element approximation
$\mathcal{L}(\cdot)$	Lagrange function
M_{ij}	Mass matrix
M_k	Element in the finite element mesh
N	Number of basis functions, but also number of subdomains
n_c	Number of conductors
n_d	Number of discretization points of a current interval
n_t	Number of time steps
n_x	Number of space discretization points
$p,\ p_1,\ p_2$	Adjoint variables
q	Contraction constant
$\bar{q}$	Contraction constant of an auxiliary temperature mapping
T_h	Approximation of the temperature (function) with finite elements
T_j	Coefficient of basis functions in the finite element approximation
$\mathcal{T}$	Temperature vector or matrix
$\mathcal{T}^*$	Temperature vector as fixed point of an iteration
θ	Weight for determination of the time discretization method
v	Test function
v_h	Functions of function space V_h
v_j	Coefficients of basis functions in finite element approximation
$\mathbf{V}$	Vector/perturbation field
w	Minimum value of an optimization problem
$\mathbf{x}^*$	Optimal solution of an optimization problem, but also root of a vector valued function or fixed point
$x^{(i)}$	i-th value of an iterative sequence
$\left(x^{(i)}\right)_{i\in\mathbb{N}}$	Sequence
ζ	Intermediate point

Operators, Norms and other Notations

$[\cdot]_\pm$	Difference of the traces of a function at an interface boundary
$(\cdot,\cdot)\,,\ \langle\cdot,\cdot\rangle$	Inner product
$\lvert\lvert\cdot\rvert\rvert$	Non-specified vector or matrix norm
$\lvert\cdot\rvert_{\mathbb{R}^2}$	Euclidean norm
$\lvert\lvert\cdot\rvert\rvert_{L^q}$	L^q-norm
$\lvert\lvert\cdot\rvert\rvert_{L^\infty}$	L^∞-norm
$\cdot^{\mathrm{e}}$	Suffix for outer trace at an interface
$\cdot^{\mathrm{i}}$	Suffix for inner trace at an interface
$\cdot^{-1}$	Inverse function or operator

∇	Gradient operator
Δ	Laplace operator
∇_τ	Tangential (surface) gradient of a scalar valued function
$\nabla\cdot$	Divergence operator
$\mathcal{A}$	Arbitrary operator in a domain
$\mathcal{B}$	Arbitrary operator on a boundary
Div	Tangential divergence of a tangential field
$d(\cdot,\cdot)$	Distance of two points
D_i^+	Forward difference operator
D_i^-	Backward difference operator
D_i^0	Central difference operator
$\partial\cdot$	Boundary of a domain
$\frac{\partial\cdot}{\partial x}$	Partial derivative of a function to x
$\delta J(\Omega)[\mathbf{V}]$	Derivative of shape functional J at domain Ω in direction of vector field $\mathbf{V}$
$\delta T(\cdot)$	Local shape derivative of T
$\mathbf{e}_i$	Unit vector pointing in direction of i-th coordinate axis
$\mathbf{H}$	Hessian
$\mathbb{I}(\cdot)$	Indicator function
$\mathbf{J},\ J_{ij}$	Jacobian and its entries
$\mathbf{M}(\cdot,\cdot)$	Approximating linear function in Newton iteration
$\mathbf{n}$	Normal vector
$\mathbf{n}_\mathrm{e}$	Unit outer normal that points away from the surface of the considered object
$\mathbf{n}_\mathrm{i}$	Unit inner normal pointing into the object
$\mathcal{O}(\cdot)$	Error order
$\mathcal{O}_{loc}(\cdot)$	Local error order
$\mathrm{supp}(\cdot)$	Support

Mathematical Spaces and other Sets

$B_r(\mathbf{p})$	Open (metric) ball of radius r centered at point $\mathbf{p}$
$C^1(\cdot)$	Space of continuously differentiable functions
$C^1(\cdot, C^2(\cdot))$	Space of functions twice continuously differentiable in space and continuously differentiable in time
$C_0^\infty(\cdot)$	Space of infinitely differentiable functions with compact support
D	Spacial domain, sometimes called holdall
$\mathcal{D}^{-k}(\cdot)$	Function space of scalar distributions
$H^1(\cdot)$	Space of functions with square integrable weak derivatives
$H_0^1(\cdot)$	Space of functions with square integrable weak derivatives and compact support

K	Index set
$\mathbf{K_1}$	Set of implicit restrictions
$\mathbf{K_2}$	Set of explicit restrictions
$L^q(\cdot)$	Space of Lebesgue measurable and q-integrable functions
$L^\infty(\cdot)$	Space of Lebesgue measurable and essentially bounded functions
$\mathcal{M}_h$	Finite element mesh
$\mathcal{O}_{\text{ad}}$	Set of admissible domains
$\mathbf{S}$	Feasible set of an optimization problem
U	Vicinity of a fixed point
$V(\cdot)$	(Infinite dimensional) space of test functions
$V_h(\cdot)$	Finite dimensional space of test functions
$\mathbf{X}$	Arbitrary set
$(\mathbf{X}, d)$	Complete metric space
$\mathbf{Z}$	Arbitrary set

Insulated Single-Core Cables

A_3	Cross sectional area of the core in m^2
A_3^{ph}	Physical cross sectional area of the core in m^2
A_3^{ge}	Geometrical cross sectional area of the core in m^2
d_2	Diameter of the outer insulation in m
d_3	Diameter of the core in m
d_4	Diameter of the conductors in m
$\mathrm{d}E_{\text{in}}^{\text{co}}$	Increase of stored energy of the cable core during infinitesimal time $\mathrm{d}t$ in J
$\mathrm{d}E_{\text{in}}^{\text{is}}$	Increase of stored energy of the insulation during infinitesimal time $\mathrm{d}t$ in J
γ_2	Specific heat capacity per volume of the insulation in $\mathrm{J/(m^3 \cdot K)}$
γ_3	Specific heat capacity per volume of the core in $\mathrm{J/(m^3 \cdot K)}$
γ_4	Specific heat capacity per volume of the conductors in $\mathrm{J/(m^3 \cdot K)}$
λ_2	Heat conductivity of the outer insulation in $\mathrm{W/(m \cdot K)}$
λ_3	Heat conductivity of the core in $\mathrm{W/(m \cdot K)}$
λ_4	Heat conductivity of the metallic conductors in $\mathrm{W/(m \cdot K)}$
P_{g}	Heat power generated in the core of an insulated single-core cable in W
P_{in}	Heat power entering into an insulated single-core cable in W
P_{out}	Heat power emitted via the surface in W
ρ_3	Electrical resistivity of the core in $\Omega \cdot \mathrm{m}$
$\rho_{0,3}$	Electrical resistivity of the core at reference temperature in $\Omega \cdot \mathrm{m}$
T_3	Temperature in the core in °C

Shielded Cables

A_2	Cross sectional area of the exterior insulation in m^2
A_3	Cross sectional area of the shielding in m^2
A_4	Cross sectional area of the interior insulation in m^2
A_5	Cross sectional area of the core in m^2
A_k	Cross sectional area relevant for contact resistances in m^2
A_s	Cross sectional area for a circle with radius s in m^2
α_i	Heat transfer coefficient of cable subsection i in $\mathrm{W}/(\mathrm{m}^2 \cdot \mathrm{K})$
$\mathbf{b_1},\ \mathbf{b_2}$	Right hand sides of linear systems for temperatures in shielded cable subsections
B	Coefficient of term of zeroth order in stationary equation of axial heat transfer in $1/\mathrm{m}^2$
B_d	Two dimensional circle with diameter d
B_i	Coefficient of term of zeroth order in stationary equation of axial heat transfer of subsection i in $1/\mathrm{m}^2$
$\beta(\cdot)$	Auxiliary function in $\mathrm{W}/(\mathrm{m}^2 \cdot \mathrm{K})$
$\tilde{\beta}$	Value of $\beta(\cdot)$ for the stationary temperature in the core in $\mathrm{W}/(\mathrm{m}^2 \cdot \mathrm{K})$
C	Temperature independent term in the stationary equation for the axial heat transfer in K/m^2
C_i	Temperature independent term in the stationary equation for axial heat transfer of subsection i in K/m^2
$\mathrm{d}E_{\gamma_{3,5}}$	Energy per length of the core and shielding in J/m
$\mathrm{d}P_k$	Heat power generated in the core in W
$\mathrm{d}P_r,\ P_r$	Heat power conducted in radial direction in W
$\mathrm{d}P_{\rho_{3,5}}$	Heat power per length generated in the core and shielding in W/m
$\mathrm{d}P_s$	Heat power generated in the shielding in W
$\mathrm{d}P_x$	Heat power conducted in axial direction in W
d_2	Diameter of the exterior insulation in m
d_3	Diameter of the shielding in m
d_4	Diameter of the interior insulation in m
d_5	Diameter of the core in m
d_6	Diameter of the conductors in m
$\Delta T_{\max}$	Absolute deviation of measured and computed maximum temperatures in K
ΔU	Voltage drop in V
$e,\ \epsilon_{\mathrm{rel}}$	Relative deviation between measured and computed temperatures
e_1	Auxiliary interpolation factor to approximate temperature evolutions in the instationary state
E	Absolute deviation between measured and computed temperatures in K

$f(\cdot)$	Function for the heat flux description in K/m
$f(\cdot,\cdot)$	Temperature independent part of the power density in the cable core in $\mathrm{W/m^3}$
$\tilde{f}$	Auxiliary function to describe the power density in $\mathrm{W/m^3}$
γ_3	Heat capacity of the shielding specific to the volume in $\mathrm{J/(m^3 \cdot K)}$
γ_5	Heat capacity of the core specific to the volume in $\mathrm{J/(m^3 \cdot K)}$
$I,\ I_5$	Current in the cable core in A
I_3	Current in the shielding in A
ℓ_i	Length of subsection i in m
$\ell_x,\ L$	Length of a shielded cable in m
L_i	Length from left to right end of cable subsection i in m
λ_2	Heat conductivity of the exterior insulation in $\mathrm{W/(m \cdot K)}$
λ_3	Heat conductivity of the shielding in $\mathrm{W/(m \cdot K)}$
λ_4	Heat conductivity of the interior insulation in $\mathrm{W/(m \cdot K)}$
λ_5	Heat conductivity of the core in $\mathrm{W/(m \cdot K)}$
$\lambda_{ad}^l,\ \lambda_{ad}^r$	Heat conductivity of left resp. right attached object in $\mathrm{W/(m \cdot K)}$
Λ	Heat conductivity specific to the cross section of the cable in axial direction in $\mathrm{W \cdot m/K}$
P_{cab}	Heat power emitted by the cable at the contact boundary in W
P_{out}	Heat power emitted via the surface in W
$P_{\mathrm{ad}}^l,\ P_{\mathrm{ad}}^r$	Heat power absorbed by attached material at the left resp. right end of the cable in W
$P_{\mathrm{k}}^l,\ P_{\mathrm{k}}^r$	Heat power generated by the contact resistance to material attached at the left resp. right end of the cable in W
$\mathbf{\Pi_1},\ \mathbf{\Pi_2}$	Matrices of the linear systems to determine temperatures in the subsections of shielded cables
$\phi,\ \tilde{\phi},\ \phi_{\mathrm{inst}}$	Interpolation factors in 1/s
$r(\cdot,\cdot)$	Temperature dependent part of the power density in the cable core in $\mathrm{W/m^3}$
$\tilde{r}(\cdot)$	Auxiliary function to describe the power density in $\mathrm{W/m^3}$
$\rho,\ \rho_5$	Electrical resistivity of the core in $\Omega \cdot \mathrm{m}$
ρ_w	Heat resistance of the cable core to the environment in radial direction in $\mathrm{m \cdot K/W}$
ρ_0	Electrical resistivity of the core at reference temperature in $\Omega \cdot \mathrm{m}$
ρ_3	Electrical resistivity of the shielding in $\Omega \cdot \mathrm{m}$
$R_k^l,\ R_k^r$	Contact resistance of the left resp. right attached object in Ω
$\sigma_{ij},\ \sigma_{-ij}$	Matrix entries of the linear systems to determine temperatures in the subsections of a shielded cable
T_{s}	Stationary temperature in the core in °C
T_{sj}	Stationary temperature in the j-th cable layer in °C
T_{1i}	Ambient temperature of subsection i in °C
T_3	Temperature at the interface of the exterior insulation and the shielding in °C

T_4	Temperature at the interface of the shielding and the interior insulation °C
T_5	Temperature in the core in °C
T^{com}	Computed temperature in °C
$T^l,\ T^r$	Fixed temperature at left resp. right end of the cable in °C
T^{me}	Measured temperature in °C
$T^{(i)}$	Axially variable temperature in the core of subsection i in °C
$T^l_{ad},\ T^r_{ad}$	Asymptotic temperature of the left resp. right attached object in °C
$T^{\text{com}}_{\text{max}}$	Computed maximum temperature in °C
$T^{\text{mes}}_{\text{max}}$	Measured maximum temperature in °C
$T^{\text{com}}_{\text{S}}$	Computed temperature with shielding current in °C
T^{me}_{S}	Measured temperature with shielding current in °C
$T^{(i)}_{2,as}$	Asymptotic temperature at the surface of the shielded cable in subsection i in °C
$\bar{T}^{(i)}$	Mean temperature in the cable core of subsection i in °C
$\bar{T}^{(i)}_2$	Mean temperature at the exterior surface of the cable in subsection i in °C
$\bar{T}^{(i)}_{2,start}$	Initial temperature of the fixed point iteration to determine temperatures of shielded cables in subsection i in °C
$\big(\bar{T}^{(i)}_{2,k}\big)_{k\in\mathbb{N}}$	Sequence of mean temperatures in subsection i
$\tau_{ij},\ \tau_{-ij}$	Matrix entries of the linear systems to determine temperatures in the subsections of shielded cables
ϑ_i	Temperature coefficient in °C
Z^L_i	Cylinder with diameter d_i and length L

Multicables

$.^{\text{core}}$	Quantities referred to the core of the single cables
$.^{\text{gaps}}$	Quantities referred to the air gaps
$.^{\text{iso}}$	Quantities referred to the exterior insulation
$.^{\text{met}}$	Quantities referred to the metallic conductors
A^{air}	Auxiliary cross sectional area of multicable cores in m^2
A^{cond}	Auxiliary cross sectional area of the insulation domains in m^2
A^{iso}	Auxiliary cross sectional area of the air gap domains in m^2
A^{ttl}	Auxiliary cross sectional area of the total cross sectional area in m^2
c_k	Geometrical definition of single cable k as a circle resp. double circle
C	Tuple of single cable circles
d^{ex}	Exterior diameter of a multicable in m
d^{in}	Interior diameter of a multicable in m

d_k^{ex}	Exterior diameter of single cable k in m
d_k^{in}	Interior diameter of single cable k in m
D^{ex}	Auxiliary exterior diameter for the transformation of a multicable to an insulated single-core cable in m
D^{in}	Auxiliary interior diameter for the transformation of a multicable to an insulated single-core cable in m
$dist(\cdot)$	Distance of a single cable from the centre of a multicable
δ_0	Initial damping factor in the cable squeezing algorithm
δ	Damping factor in the cable squeezing algorithm
δ_k	Diameter of conductors in single cable k in m
Δ	Auxiliary quantity in the cable squeezing algorithm
Δt	Difference in time to compute the shape gradient with an adjoint resp. FD method in s
$\Delta \mathbf{x}$	Euclidean norm of the step size of the optimization variable(s)
f	Heat power density in $\mathrm{W/m^2}$
$\tilde{f}$	Temperature independent part of the power density of a multicable in $\mathrm{W/m^2}$
Γ^{ex}	Exterior boundary of a multicable
$\tilde{\gamma}$	Right hand side of the exterior boundary condition in $\mathrm{W/m^2}$
h	Measure for the mesh refinement of the multicable domain
h_{p_1}, h_{p_2}, h_T, h_Ω	Directions of first variations of Lagrangian w.r.t. p_1, p_2, T, Ω
$hnumedg$	Measure for the refinement of multicable domain edges
$j_{\max}$	Maximum number of iterations in the cable squeezing algorithm
J_k^{ge}	Geometrical current density of single cable k in $\mathrm{A/mm^2}$
J_k^{ph}	Physical current density of single cable k in $\mathrm{A/mm^2}$
$L(\cdot)$	Single cable sorting function
$\lambda^{\mathrm{c,i}}$, λ^{cond}	Auxiliary heat conductivities for the transformation of a multicable to an insulated single-core cable in $\mathrm{W/(m \cdot K)}$
λ^{ex}	Heat conductivity of the exterior insulation in $\mathrm{W/(m \cdot K)}$
λ^{gaps}	Heat conductivity of the air gaps in $\mathrm{W/(m \cdot K)}$
λ^{iso}, λ^{mean}	Auxiliary heat conductivities for the transformation of a multicable to an insulated single-core cable in $\mathrm{W/(m \cdot K)}$
$\lambda_k^{\mathrm{core}}$	Heat conductivity in the core of the k-th single cable in $\mathrm{W/(m \cdot K)}$
μ	Barrier parameter in the interior point optimizer
$\max(\mathrm{err_{abs}})$	Absolute value of the maximal discrepancy between adjoint and FD method in K
$\max(\mathrm{err_{rel}})$	Relative value of the maximal discrepancy between adjoint and FD method
$\max_{\mathrm{k}}(\Delta \mathrm{T})$	Maximum of the temperature deviations between measurement and simulation over all single cables in K
n_k	Number of conductors in single cable k

$n_{\max}$	Number of maximum iterations in the interior point algorithm
N	Number of single cables in a multicable
N_k^{Tp}	Number of single cables of the corresponding type in a multicable
Ω^{ex}	Exterior insulation domain of a multicable
Ω^{gaps}	Domain of the air gaps in a multicable
Ω^{MC}	Entire multicable domain
Ω_k^{core}	Cable core domain of k-th single cable
Ω_k^{iso}	Insulation domain of k-th single cable
p	Heat power specific to the length in W/m
q	Exponent in the L^q-norm for the approximation of the L^∞-norm
q_n	Indicator of contraction
$r_{\max}$	Maximum of the exterior radii of all single cables in m
r^{left}, r^{right}	Heat resistivity of the left resp. right part of an auxiliary heat distribution model in $\mathrm{K} \cdot \mathrm{m/W}$
r_k^{ex}	Exterior core radius of single cable k in m
r_0^{ex}	Exterior core radius of a multicable in m
r_k^{in}	Interior core radius of single cable k in m
r_0^{in}	Interior core radius of a multicable in m
R	Tuple of exterior single cable radii
t_{ADJ}	Time to compute the shape gradient with the adjoint method in s
t_{FD}	Time to compute the shape gradient with finite differences in s
T^{cen}	Temperature in the centre of a homogenized multicable in °C
T^{ex}	Temperature at the exterior insulation boundary of a multicable in °C
T^{in}	Temperature at the interior insulation boundary of a multicable in °C
T^{mean}	Mean temperature in a multicable in °C
U	Voltage drop in V
$\vec{v}$	Auxiliary vector in the cable squeezing algorithm
V_k^{core}	Volume of the core of the k-th single cable in m^3
V_k^{met}	Volume of the metallic part of the k-th single cable in m^3
$(\bar{T}, \bar{\Omega})$	Optimal pair of problem (OptMC)
(x_0, y_0)	Centre coordinates of a multicable
$\varnothing(T)$	Average temperature of single cable cores in a multicable in °C
$\varnothing^{\mathrm{A}}(T)$	Average temperature of single cable cores weighted w.r.t. the cross sectional area in °C
$\varnothing_k^{\mathrm{A}}\,(\Delta\mathrm{T})$	Mean value of the temperature deviations of all single cables between measurement and simulation in K

Current Bars

a_k	Linear characterizing constant of attached cable k in K/A
A_k	Metallic cross sectional area of the core of attached cable k in m^2
α_l	Heat transfer coefficient at the lower surfaces in $\mathrm{W}/(\mathrm{m}^2 \cdot \mathrm{K})$
α_u	Heat transfer coefficient at upper surfaces in $\mathrm{W}/(\mathrm{m}^2 \cdot \mathrm{K})$
α_v	Heat transfer coefficient at vertical surfaces in $\mathrm{W}/(\mathrm{m}^2 \cdot \mathrm{K})$
$\alpha_{\rho,k}$	Linear temperature coefficient of the electrical resistivity of metallic parts of attached cable k in 1/K
$\alpha_{\rho,s}$	Linear coefficient of the electrical resistivity of a current bar in 1/K
$\alpha^c_{\rho,k}$	Linear coefficient for the rise of the electrical resistivity at the contact to cable k in 1/K
b_k	Quadratic characterizing constant of attached cable k in K/A^2
B_k	Coefficient of the term of zeroth order in the stationary equation for the axial heat transfer of attached cable k in $1/\mathrm{m}^2$
C_k	Temperature independent term in the stationary equation for the axial heat transfer of attached cable k in K/m^2
$d_{2,k}$	Exterior diameter of attached cable k in m
$d_{3,k}$	Diameter of the core of attached cable k in m
$E_{\hat{1}},\ E_{\hat{2}}$	Absolute deviation between measurement and simulation results at the first and second output module in K
$e_{\hat{1}},\ e_{\hat{2}}$	Relative deviation between measurement and simulation results at the first and second output module
ϵ_k	Insulation emissivity of attached cable k
$\vartheta_{1,k}$, $\vartheta_{2,k}$	Coefficient in the temperature defining equation of attached cable k in °C
I_k	Electric current in attached cable k in A
$\hat{I}_k$	Resulting electric current in output module k in A
k	Index of input modules
$\hat{k}$	Index of output modules
$\kappa_{0,s}$	Electrical conductivity of the current bar at reference temperature in $1/(\Omega \cdot \mathrm{m})$
ℓ_k	Length of input module k in m
$\ell_{\hat{k}}$	Length of output module k in m
$L_{f,k}$	Length of attached cable k in m
$L_{\hat{k}}$	Sum of lengths of output modules with number smaller than or equal k in m
$\lambda_{2,k}$	Heat conductivity of the insulation of attached cable k in $\mathrm{W}/(\mathrm{m} \cdot \mathrm{K})$
$\lambda_{3,k}$	Heat conductivity of the metallic part of attached cable k in $\mathrm{W}/(\mathrm{m} \cdot \mathrm{K})$

λ_s	Heat conductivity of the current bar in $\mathrm{W/(m \cdot K)}$
Λ_k	Heat conductivity weighted w.r.t. the cross sectional area of attached cable k in $\mathrm{W \cdot m/K}$
n	Number of modules
$P_{\mathrm{a},\hat{k}}$	Heat power at output module k absorbed from or emitted to adjacent modules in W
$P_{\mathrm{c},\hat{k}}$	Heat power generated by the contact resistance to cable k in W
$P_{\mathrm{s},\hat{k}}$	Heat power generated in the current bar section of module $\hat{k}$ in W
$P_{\mathrm{w},\hat{k}}$	Heat power emitted to or absorbed from attached cable k in W
$P_{\alpha,\hat{k}}$	Heat power emitted by convection/radiation at module $\hat{k}$ in W
$R^c_{0,k}$	Contact resistance at cable k in Ω
$\rho_{w,k}$	Heat resistance of the cable core to the environment in radial direction for attached cable k in $\mathrm{m \cdot K/W}$
$\rho_{0,k}$	Resistivity of the metallic part of attached cable k in $\Omega \cdot \mathrm{m}$
s_k	Thickness of current bar module k in m
$\mathbf{T}$	Vector of temperatures
$T_{\mathrm{amb},k}$	Ambient temperature of attached cable k in °C
$T_{\mathrm{f},k}$	Temperature of attached cable k at the end averted from the current bar in °C
$T_{\hat{k}}$	Temperature in output module k in °C
T_{S_i}	Measured temperature in current bar subsection i in °C
$T_{\infty,k}$	Asymptotic temperature of attached cable k in °C
$T^m_{\hat{1}}$, $T^m_{\hat{2}}$	Measured average temperature for output module 1 and 2 in °C
$T^s_{\hat{1}}$, $T^s_{\hat{2}}$	Computed average temperature for output module 1 and 2 in °C
$\tilde{T}_{2,k}$	Temperature of the exterior insulation surface of attached cable k in °C
$\tilde{T}_k,\ \tilde{T}_{3,k}$	Temperature in the core of attached cable k in °C
$\tilde{T}^{\mathrm{av}}_{3,k}$	Average temperature of attached cable k over the length in °C
$\tilde{T}^{(i)}_{2,k}$, $\tilde{T}^{(i)}_{3,k}$	Insulation and core temperature of cable k at iteration i in °C
w_k	Width of current bar module k in m
χ_k	Cable characterizing length of attached cable k in m

Fuses

$A,\ A(x)$	Space dependent cross sectional area in the fuse in m^2
A_1	Cross sectional area of the solid part of the fuse element in m^2
A_2	Cross sectional area of the liquid part of the fuse element in m^2
A_e	Cross sectional area of the fuse element in m^2
A_{Cu}	Cross sectional area of the copper part in the fuse element in m^2
A_{Sn}	Cross sectional area of the tin part in the fuse element in m^2
$A_{w_0},\ A_{w_\ell}$	Cross sectional area of the left resp. right attached cable in m^2

$b^{(i)}$	Right hand side of the discretized system in the i-th iteration
B	Linear coefficient of the stationary heat equation for attached cables in $1/\mathrm{m}^2$
C	Constant of the stationary heat equation for attached cables in K/m^2
$\mathrm{d}E_\gamma$	Stored energy in the fuse element during infinitesimal time $\mathrm{d}t$ in J
$\mathrm{d}E_\Theta$	Stored melting energy during infinitesimal time $\mathrm{d}t$ in J
δ_t	Time discretization interval in s
δ_x	Space discretization interval in m
I_{asym}	Asymptotic electric current of a fuse in A
κ_1	Electrical conductivity of the solid part of the fuse element in $1/(\Omega \cdot \mathrm{m})$
κ_2	Electrical conductivity of the liquid part of the fuse element in $1/(\Omega \cdot \mathrm{m})$
ℓ	Length of the metallic part of the fuse in m
ℓ_e	Length of the fuse element in m
λ_w	Heat conductivity of an attached cable in $\mathrm{W}/(\mathrm{m} \cdot \mathrm{K})$
$\lambda_{w_0},\ \lambda_{w_\ell}$	Heat conductivity of the left resp. right attached cable in $\mathrm{W}/(\mathrm{m} \cdot \mathrm{K})$
$M^{(i)}$	Sparse block matrix for the solution of a discretized system in the i-th iteration
P_α	Heat power emitted via the surface in W
P_ρ	Heat power generated in the fuse element in W
P_x	Heat power conducted in axial direction in W
P'_α	Auxiliary quantity for the computation of the melting time in W/m
R	Electrical resistance of the fuse element in Ω
ρ_0	Resistivity of the material of the fuse element in $\Omega \cdot \mathrm{m}$
ρ_{Cu}	Resistivity of the copper part in the fuse element in $\Omega \cdot \mathrm{m}$
ρ_{Sn}	Resistivity of tin part in the fuse element in $\Omega \cdot \mathrm{m}$
t_{blow}	Computed blowing time of a fuse in s
t_{heat}	Computed heating time of a fuse in s
t_{mea}	Measured blowing time of a fuse in s
t_{melt}	Melting time of the fuse element in s
$\hat{t}$	Fixed time step in s
T_{melt}	Melting temperature of the fuse element in °C
$T^{(i)}_{(j)}$	Temperature in the fuse at the discrete time step i and space point j in °C
$\tilde{T}$	Temperature in an attached cable in °C
$\tilde{T}_\infty$	Asymptotic temperature of an attached cable in °C
$\tilde{T}^0_\infty,\ \tilde{T}^\ell_\infty$	Asymptotic temperature of the left resp. right attached cable in °C

Θ	Volume specific melting energy of the fuse element material in $\mathrm{J/m^3}$
$u(x)$	Space dependent perimeter of the metallic part of the fuse in m
U_0	Electric potential of the fuse element in V
$\chi_0,\ \chi_\ell$	Characteristic length of the left resp. right attached cable in m